Three Little Superconducting Quantum Gates and how to Apply Them

Stig Elkjær Rasmussen

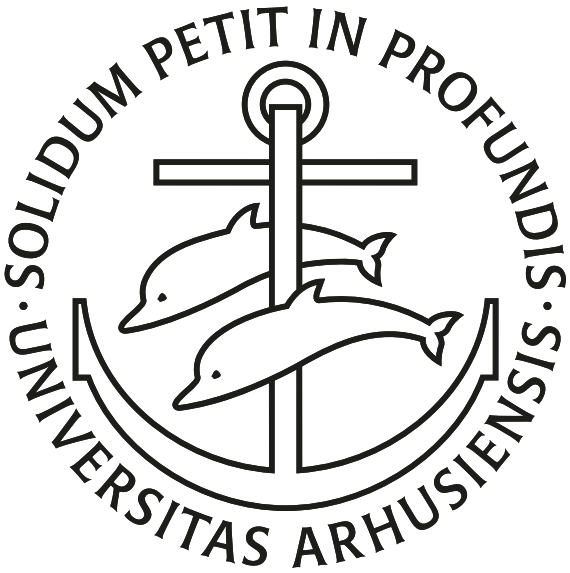

Dissertation for the degree of Doctor of Philosophy
Aarhus University
Department of Physics and Astronomy

Supervisor: Nikolaj Thomas Zinner

Department of Physics and Astronomy
Aarhus University
Ny Munkegade 120
DK-8000 Aarhus C
Denmark
Email: stig@phys.au.dk
Google scholar: https://scholar.google.com/citations?user=djrmrggAAAAJ&hl=da
ORCID: https://orcid.org/0000-0001-7917-0309
LinkedIn: https://www.linkedin.com/in/s-e-rasmussen/

2nd edition, March 21, 2022

Note on the title: The title of this thesis refers to the fable of the "Three Little Pigs". Much like the little pigs built houses of increasing quality, I believe that the gates/research I have been conducting during my PhD studies have been increasing in quality (as it should). Hopefully, this also implies that any reviewers/the big bad wolf will have a hard time tearing it apart. As with any good fairy tale, the reader will notice that this thesis is divided into three parts and seven chapters (not including the conclusion).
The title is also an homage to the song "Three Little Birds" by Bob Marley and the Wailer, reminding the reader that even though the content of this thesis might be frustrating to understand, every little thing is gonna be alright.

Layout and typography chosen and implemented by the author.
Font: 9pt Palatino and mathpazo.
Typesetting done with LaTeX 2_ε, Biber, and the MEMOIR class.
Compiled using pdfLaTeX.
Figures in Python and InkScape.
Printed by AU TRYK, Aarhus University.

I am the person, if any, who controls the "motion of the atoms" according to the Laws of Nature.

— Erwin Schrödinger (1887 - 1961)

Abstract

About a century ago, the field of quantum mechanics emerged when pioneering physicists developed a formulation for describing the world of the very small. The theory successfully describes physical properties at the scale of atoms and subatomic particles. Since then, the field has undergone many breakthroughs and significant development, and in the last few decades, a related field has been emerging from descriptive quantum mechanics, namely quantum technologies. Rather than trying to explain and describe the quantum world, the field of quantum technologies aims to control and engineer. Rapid advances within this field have led to the belief that we will be able to harvest the fruits of quantum mechanics and exploit them commercially within the next couple of years.

This dissertation explores some recent quantum technology advances within superconducting circuits and hybrid quantum-classical algorithms. Specifically, it outlines the theory behind superconducting circuit design needed for tailoring quantum mechanical systems controlled by macroscopic parameters. Following this introduction, three controlled quantum gates are presented: An n-bit iToffoli gate, a controlled iSWAP gate, and a linear controlled swapping gate. As these gates are introduced and explained, possible implementations in superconducting circuits are also proposed.

In the ensuing chapters, we zoom out and focus on applying such quantum gates in hybrid quantum-classical algorithms, to obtain a quantum advantage. In particular, parameterized quantum circuits are discussed, and it is shown that the number of single-qubit rotations can be decreased. The variational quantum eigensolver is explored as an example of a hybrid quantum-classical algorithm, and it is used for approximating the ground state of molecules and Heisenberg chains. The effect of entangling gates in the variational quantum eigensolver is also considered. Lastly, a quantum version of the highly successful generative adversarial networks is considered. It is shown that it can be used to approximate the ground state without knowing the Hamiltonian.

Dansk resumé

For omkring et århundrede siden opstod feltet kvantemekanik da pionerer indenfor fysikken udviklede en formulering til at beskrive de allermindste ting i verden. Teorien beskrev succesfuldt de fysiske egenskaber for atomer og mindre partikler. Siden da har feltet oplevet mange gennembrudt og betydeligt udvikling. I de sidste par årtier er et relateret felt begyndt at opstå fra den deskriptive kvantemekanik; nemlig kvanteteknologi. Fremfor at forsøge at forklare og beskrive kvanteverdenen, så forsøger kvanteteknologi at kontrollere og skabe. Hurtige fremskridt i dette felt har ført til troen på at man inden for de næste par år vil kunne høste frugterne af kvantemekanikken og udnytte dem kommercielt.

Denne afhandling udforsker nogle nylige kvanteteknologi fremskridt inden for superledende kredsløb og hybrid kvante-klassiske algoritmer. Specifikt så opridser den teorien bag superledende kredsløbs design, som er nødvendigt for at kunne skræddersy kvantemekaniske systemer som kan kontrolleres af makroskopiske parametre. Efter denne introduktion præsenteres tre kontrollerede kvantemekaniske porte: en n-bit iToffoli port, en kontrolleret iSWAP port og en lineær kontrolleret bytte port. I takt med at disse porte bliver introduceret, forslås mulige implementation i superledende kredsløb.

I de følgende kapitler zoomer vi ud og fokusere på, hvordan man vil anvende sådanne kvanteporte i hybrid kvante-klassiske algoritmer for at opnå en kvantefordel. Særligt diskuteres parameteriserede kvantekredsløb og det vises at antallet af single-qubit rotationer kan mindskes. Som et eksempel på en hybrid kvante-klassisk algoritme udforskes den variationelle kvante-egenløser. Den bruges til at approksimere grundtilstandene i molekyler og Heisenberg kæder. Effekten af sammenfiltringsporte i den variationelle kvante-egenløser undersøges også. Til sidst undersøges en kvante version af den yderst succesfulde generative modstander netværk og det vises at dette kan bruges til at approksimere grundtilstanden af en Hamilton-funktion uden at Hamilton-funktionen skal være kendt for netværket.

Contents

Preface

The seeming megalomania quote by Schödinger at the cover of this thesis is taken very much out of context. The proper quote from his book "What is Life?" [1] reads:

> My body functions as a pure mechanism according to the Laws of Nature. Yet I know, by incontrovertible direct experience, that I am directing its motions, of which I foresee the effects, that may be fateful and all-important, in which case I feel and take full responsibility for them. The only possible inference from these two facts is, I think, that I – I in the widest meaning of the word, that is to say, every conscious mind that has ever said or felt "I" – am the person, if any, who controls the "motion of the atoms" according to the Laws of Nature.

Schrödinger did not claim to be the one godly entity that controls all atoms. Instead, he followed the long line of German philosophers, such as Kant and Schopenhauer. They thought that all worldly voices referring to themselves as "I" were referring to the same universal I, rather than independent I's. His point was that we control the atoms since we are the atoms and the atoms are us.

These philosophical ponderings were typical for physicists such as Schrödinger, Einstein, or Bohr, who founded quantum mechanics. Their objective was to understand how the world's smallest components make sense in relation to the classical world. Today, almost a century later, the focus has changed. Most physicists are no longer concerned with the philosophical aspects of the quantum world – notwithstanding, I[1] believe that this is still the main appeal for young quantum physicists *in spe*, myself included – but are instead focused on actually doing quantum mechanics. Due to many experimental and technical breakthroughs since the conception of quantum mechanics, a new field has emerged as quantum technologies. Within this field, physicists are no longer just trying to explain and describe the world of quantum mechanics; instead, we are trying to engineer and control. We are now able to do things quantum-mechanically that the founding fathers of quantum mechanics through only possible in their wildest *gendanken* experiments. This has also opened up for a more literal interpretation of the initial quote in this thesis: Any quantum engineer can now, in good faith, utter the words: "I am the person, if any, who controls the 'motion of the atoms' according to the Laws of Nature", regardless of whether these atoms are trapped ions, ultracold atoms, quantum dots, or artificial atoms in superconducting circuits.

[1] Here the "I" refers to the independent author and not the universal I.

This thesis concludes my PhD studies at the Department of Physics and Astronomy at Aarhus University under the supervision of Nikolaj Zinner. My studies have revolved around the theoretical aspects of quantum technologies and quantum engineering. My initial focus was on superconducting circuits as a tool for creating quantum bits, or qubits, and interactions among these. During this initial part of my PhD studies, I spent a lot of time trying to engineer different circuits to do as I wanted, something I had also done during my master's. Therefore this thesis opens up with an introduction to superconducting circuits in Chapter 1. This chapter is based on a tutorial written to introduce students and researchers who are new to the field [**VIII**].

In the second part of this thesis, we continue the quest in superconducting circuits, and I introduce three different controlled quantum gates, which all can be implemented in superconducting circuits following the approach in Chapter 1. Specifically, in Chapter 2, I introduce the n-bit iToffoli gate, which flips the state of a single qubit depending on the state of n control qubits. The chapter is based on Ref. [**V**]. In Chapter 3 I discuss the controlled iSWAP, which swaps the state of two qubits at the expense of an i phase, depending on several control qubits. This chapter is based on Ref. [**VI**]. In Chapter 4, I introduce a linear controlled swapping gate, where the swapping is dependent on a superposition state of the control qubits. This chapter is based on Ref. [**III**], and is significantly shorter than the previous two chapters as part of the work on this gate was done during my master's and is therefore not included here.

In the third and last part of this thesis, we change gear and consider some algorithms which could be used on a near-term quantum chip. We concentrate on the concept of hybrid quantum-classical algorithms, which, as the name suggests, combines quantum resources with classical computational resources. In Chapter 5 I present parameterized quantum circuits that serve as the base element in many hybrid quantum-classical algorithms. I discuss how the number of single-qubit rotations can be reduced without loss of expressibility or entangling capability, something which was first presented in Ref. [**VII**]. In Chapter 6, I introduce the variational quantum eigensolver, which is a hybrid quantum-classical algorithm, that can be used to find approximate eigenvalues. I also present results of different simulations of a variational quantum eigensolver, some related to Ref. [**VII**], and some unpublished. In Chapter 7, I present a, so far, less successful hybrid quantum-classical algorithm, namely the quantum generative adversarial network. The classical version of this has been quite successful, and I discuss different approaches for the quantum version and present some unpublished simulation results.

Finally, in Chapter 8, I summarize and present some final remarks regarding the entire work presented in this thesis and discuss points for further investigation.

In addition to the papers discussed in this thesis, I have produced four other papers, which do not fit into the scope of this thesis. My first paper was based on my bachelor's thesis on Efimov physics and utterly unrelated to the subject discussed here [**I**]. During my master's thesis, I worked a bit with time crystals, and possible implementations in superconducting circuits [**II**]. I have also been part of a paper discussing a possible implementation of a coherent router in superconducting circuits [**IV**]. Finally, I have helped co-supervise a master's student, which led to a manuscript that has just been

accepted in Physical Review Applied [**IX**].

My supervisor Nikolaj T. Zinner deserves a big thank you for the opportunity to do a PhD and his continued support during my studies. Also, thank you for letting me teach advanced particle physics, despite having followed the course myself just a few years earlier. I especially appreciated that Nikolaj's criteria of success for a PhD student seem to be "as long as you answer your e-mails". I thoroughly enjoyed this freedom with responsibility, and I can honestly say that I do not think I would have done a PhD with any other supervisor.

I would also like to thank the rest of our research group for always being available to discuss various topics (physics-related or not), answering or asking questions, and challenging me to do better.

A big thank goes out to my office mates, Andreas, Christian, and Kasper. It has been a pleasure to work next to you, despite the noise of your coffeemaker. I will miss being able to discuss every matter that we could think of throughout the working day.

Especially Andreas deserves a big thank you. We have studied physics together for the last eight and a half years, and in much of this time, we have shared an office. I always knew it would be a good day when I arrived in the morning (around noon), and you were sitting at your desk. We have spent a significant time together at sober activities and possibly an even more significant amount of time doing less sober activities. I do enjoy our friendship.

A special thanks go out to my home office mate, Martin, who managed to keep me somewhat sane during the Corona lockdowns. Though I enjoyed it, I never hope any pandemic forces us to share an office again.

Also a big thank you to Mogens who kindly proofreading part of this thesis.

Finally, I would like to thank everyone else that has been part of my university life; my friends, FFB, the kroket group, FC LFP. It has been a very joyful ride.

List of Publications

[I] **S. E. Rasmussen**, A. S. Jensen, and D. V. Fedorov. "Window for Efimov physics for few-body systems with finite-range interactions". *Journal of Physics B: Atomic, Molecular and Optical Physics* **51**.2 (2017), 025302.

[II] R. E. Barfknecht, **S. E. Rasmussen**, A. Foerster, and N. T. Zinner. "Realizing time crystals in discrete quantum few-body systems". *Phys. Rev. B* **99** (2019), 144304.

[III] **S. E. Rasmussen**, K. S. Christensen, and N. T. Zinner. "Controllable two-qubit swapping gate using superconducting circuits". *Phys. Rev. B* **99** (2019), 134508.

[IV] K. S. Christensen, **S. E. Rasmussen**, D. Petrosyan, and N. T. Zinner. "Coherent router for quantum networks with superconducting qubits". *Phys. Rev. Research* **2** (2020), 013004.

[V] **S. E. Rasmussen**, K. Groenland, R. Gerritsma, K. Schoutens, and N. T. Zinner. "Single-step implementation of high-fidelity n-bit Toffoli gates". *Phys. Rev. A* **101** (2020), 022308.

[VI] **S. E. Rasmussen** and N. T. Zinner. "Simple implementation of high fidelity controlled-$i$swap gates and quantum circuit exponentiation of non-Hermitian gates". *Phys. Rev. Research* **2** (2020), 033097.

[VII] **S. E. Rasmussen**, N. J. S. Loft, T. Bækkegaard, M. Kues, and N. T. Zinner. "Reducing the Amount of Single-Qubit Rotations in VQE and Related Algorithms". *Advanced Quantum Technologies* **3**.12 (2020), 2000063. ISSN: 2511-9044.

[VIII] **S.E. Rasmussen**, K.S. Christensen, S.P. Pedersen, L.B. Kristensen, T. Bækkegaard, N.J.S. Loft, and N.T. Zinner. "Superconducting Circuit Companion—an Introduction with Worked Examples". *PRX Quantum* **2** (2021), 040204.

[IX] E. Bahnsen, **S.E. Rasmussen**, N.J.S. Loft, and N.T. Zinner. "Application of the Diamond Gate in Quantum Fourier Transformations and Quantum Machine Learning". *Phys. Rev. Applied* **17** (2022), 024053.

PART I

First Steps into the World of Superconducting Circuitry

CHAPTER 1

Introduction to Superconducting Circuits

*During my master's studies, I learned the craftmanship of analyzing superconducting circuits. This learning process was difficult since there were no introductory-level texts on the subject. As I progressed as a PhD student, I have seen countless students having to go through the same struggles without any suitable introduction text. Our group, therefore, decided to write such a text, which ended up as a tutorial on superconducting circuits. While this tutorial was one of the last things I did during my PhD studies, it does describe some of the first scientific methods I encountered, and it lays the groundwork for much of my work during my PhD studies. I, therefore, open this thesis with this introduction to superconducting circuits based on Ref. [**VIII**]. Text and figures have been edited to fit into the thesis.*

A particularly prominent platform for scalable quantum technology is superconducting circuits that implement qubits or even higher-dimensional qudits. Compared to other quantum technology schemes, such as trapped ions [2–7], ultracold atoms [8–12], electron spins in silicon [13–18] and quantum dots [19–23], nitrogen vacancies in diamonds [24, 25], or polarized photons [26–29], which all encode quantum information in microscopic systems, such as ions, atoms, electrons, or photons, superconducting circuits are quite different. They are macroscopic in size and printed lithographically on wafers much similar to classical computer chips [30–34]. The fact that these systems exhibit microscopic behavior, i.e., quantum-mechanical effects, while being macroscopic in size has led to the notion of mesoscopic physics in order to describe this intermediate scale [35–37]. A mesoscopic advantage of superconducting circuits is that microscopic features such as energy spectra, coupling strengths, and coherence rates depend on macroscopic circuit parameters. This means that one can design circuits such that the properties of the resulting quantum-mechanical system, sometimes called an artificial atom [38–42], can be more or less tailormade to exhibit a particular behavior.

In this chapter, we aim to introduce circuit analysis of superconducting qubits intended for researchers who are new to the field. We aim to give the tools needed for tailoring macroscopic circuits to a desired qubit behavior. We refer to a (superconducting) qubit as the two lowest energy levels of a superconducting circuit or subcircuit, denoted by the Fock states $|0\rangle$ and $|1\rangle$. There are several examples of superconducting qubits which

exploit higher-lying states for coupling [43] or control [44, 45]. The present chapter can be viewed as an introduction to more advanced field reviews, such as Refs. [37, 38, 41, 46–55], and is by no means a review of current state-of-the-art technology or practices, but rather a detailed introduction to the theoretical methods needed to analyze superconducting circuits to produce and manipulate qubits. We do not discuss the actual experimental production of superconducting circuits, but limit the tutorial to theoretical analysis of such circuits. The interested experimentalist should refer to the tutorial by Ref. [56].

The following chapter is organized as follows: First, we present the basic circuit variables and components used in the analysis in Section 1.1. Then we present the classical analysis used for finding the Hamiltonian of a given superconducting circuit in Section 1.2, where we use the method of nodes. In Section 1.3 we quantize the Hamiltonian and in Section 1.4 we recast the Hamiltonian as interacting oscillators. In Section 1.5 we discuss time-averaged dynamics using the interaction picture. The truncation of anharmonic oscillators is discussed in Section 1.6. The use of microwave driving for control and single-qubit gates is presented in Section 1.7, and the simple coupling of modes is presented in Section 1.8, where two-qubit gates are discussed as well. In Section 1.9 we introduce a method for treating noise in open two-level quantum systems. Finally, in Section 1.10 we present a variety of examples ranging from single qubit implementations to tunable couplers and multibody interactions. In Section 1.11 we give an overview of the methods and presents a perspective to the rest of this thesis.

1.1 Lumped-element circuit diagrams

In this section, we introduce the dynamical variables used when analyzing superconducting circuits and then present the basic components of the circuits.

Our analysis takes its starting point in the lumped-element model. This model simplifies the description of a spatially distributed system (in our case, a superconducting electrical circuit) into a topology of discrete entities. We assume that the circuit attributes (capacitance, inductance, and resistance) are idealized into electrical components (capacitors, inductors, and resistors) joined by a network of perfectly conducting wires. An example of a lumped circuit can be seen in Fig. 1.1(a). We discuss the different components in Section 1.1.2.

We assume all the circuits discussed in this chapter to be superconducting, meaning that there is no electrical resistance in the circuit, and all magnetic fields are expelled from the wires (the Meissner effect). We, therefore, ignore losses to the external environment in the following analysis. In other words, we will consider closed quantum systems for most of this chapter. However, a realistic description of any quantum system should include some interactions with the environment, as these can never be completely ignored in an experiment. Notwithstanding, it is an excellent description to treat losses to the external environment as a correction to the dynamics of the system, something which we discuss in Section 1.9.

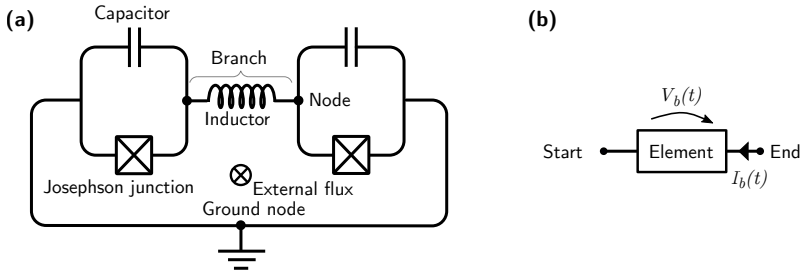

Figure 1.1: (a) *Example of a lumped-element circuit consisting of a Josephson junction and a capacitor in parallel connected by an inductor to another Josephson junction and capacitor pair. Such a Josephson junction and capacitor pair is considered a transmonlike qubit, see Section 1.10.1. An external flux is threading the inductive loop of the circuit.* **(b)** *Arbitrary two-terminal component on a branch, b, between two nodes (dots). The voltage, $V_b(t)$, over the component is defined from the branch's start to the branch's end. The current, $I_b(t)$, through the branch is defined in the opposite direction.*

1.1.1 Circuit variables

Circuit analysis aims at finding the equations of motion of an electrical circuit. Typically this means determining the current and voltage through all circuit components. For simplicity, we consider only circuit networks containing two-terminal components, i.e., components connected to two wires. Each such component is said to lie on a *branch*, b, and is characterized by two variables at any given time t: The voltage, $V_b(t)$, across it and the current, $I_b(t)$, through it. We define the orientation of the voltage to be opposite to the direction of the current, see Fig. 1.1(b). Thus these two are defined by the underlying electromagnetic field by

$$V_b(t) = \int_{\text{start of } b}^{\text{end of } b} \boldsymbol{E}(t) \cdot \mathrm{d}\boldsymbol{\ell}, \tag{1.1a}$$

$$I_b(t) = \frac{1}{\mu_0} \oint_b \boldsymbol{B}(t) \cdot \mathrm{d}\boldsymbol{\ell}, \tag{1.1b}$$

where μ_0 is the vacuum permeability, and $\boldsymbol{E}$ and $\boldsymbol{B}$ are the electric field inside the wire and the magnetic field outside the wire, respectively. The closed loop in the second integral is in vacuum encircling the given element. As we describe the circuits in the lumped-element model, the voltage and current are independent of the precise path the fields are integrated along in the following sense. For the line integral of the electric field in Eq. (1.1a) we take the integration path to be well outside the wire of the inductors, meaning that the magnetic field is zero along the path. Similarly, for the loop integral of the magnetic field in Eq. (1.1b), we take the integration path to be well outside the dielectric of the capacitors, meaning that the electric field is zero along the path. For more details on the integration of electromagnetic fields, see, e.g., Ref. [57].

We define the branch flux and branch charge variables as

$$\Phi_b(t) = \int_{-\infty}^{t} V_b(t')\,\mathrm{d}t', \tag{1.2a}$$

$$Q_b(t) = \int_{-\infty}^{t} I_b(t')\,\mathrm{d}t', \tag{1.2b}$$

where it is assumed that the system is at rest at $t' = -\infty$ with zero voltages and currents. As there are fewer degrees of freedom in the circuit than there are branches in the circuit, these are, just as the currents and voltages, not completely independent but related through Kirchhoff's laws

$$\sum_{\substack{\text{all } b \text{ arriving} \\ \text{at } n}} Q_b = q_n, \tag{1.3a}$$

$$\sum_{\text{all } b \text{ around } l} \Phi_b = \tilde{\Phi}_l, \tag{1.3b}$$

where q_n is the charge accumulated at node n and $\tilde{\Phi}_l$ is the external magnetic flux through the loop l. A *node* can be understood as a point where components, or branches, converge, see Fig. 1.1(a), where we denote nodes with a dot. We can define any circuit as a set of nodes and a set of branches.

The notion of nodes and branches comes from graph theory, which is the natural mathematical language for analyzing circuits. The interested reader can find more details of fundamental graph theory and its application to electrical circuits in Appendix A.1.

1.1.2 Circuit components

We primarily consider three components of a superconducting circuit: linear capacitors, linear inductors, and nonlinear Josephson junctions. The two linear components should be well known to most readers, and we, therefore, introduce them only briefly. On the other hand, the Josephson junction is a nonlinear component that is specific to superconducting circuits, and it is the main component when working with superconducting qubits.

As we consider superconducting circuits, we do not consider resistors or other losses. Such dissipative components are not easily included in the Hamiltonian formalism presented in this chapter due to their irreversible nature. However, it can be done using, for instance, the Caldeira-Leggett model [48, 58].

Capacitors

The first component we consider is the capacitor. For a general capacitor, the charge on the capacitor is determined as a function of the voltage, $q(t) = f[V(t)]$. In this chapter, we consider only linear capacitors where the voltage is proportional to the charge stored on the capacitor plates

$$V(t) = \frac{q(t)}{C}, \tag{1.4}$$

where C is the capacitance of the capacitor, this linear relationship is the defining property of the linear capacitor. In reality, this is merely an approximation, as small nonlinearities

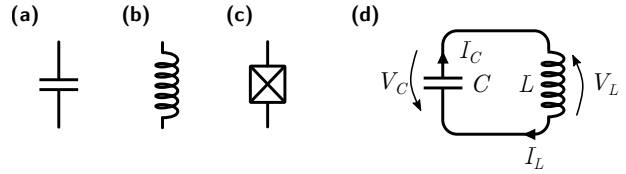

Figure 1.2: (a) *Capacitor.* **(b)** *Linear inductor.* **(c)** *Josephson junction.* **(d)** *Simple LC-oscillator circuit. A capacitor with capacitance C is connected in a closed circuit with an inductor of inductance L. The voltages over the two components are V_C and V_L, respectively, while the currents are I_C and I_L. The resulting equation of motion is a harmonic oscillator.*

make C a function of q and V. These effects are usually small, and therefore it is standard to neglect them. Equation (1.4) can be rewritten to the flux-charge relation using Eq. (1.2a) as

$$\dot{\Phi}(t) = V(t) = \frac{q(t)}{C}, \tag{1.5}$$

where the dot indicates differentiation with respect to t. The charge $q(t)$ is equal to the branch charge, and using Eq. (1.2b) we find the branch current

$$I(t) = C\ddot{\Phi}(t). \tag{1.6}$$

The energy stored in the capacitor is found by integrating the power $P = V(t)I(t)$ from $t = -\infty$ to t

$$E = \frac{1}{2}C\dot{\Phi}^2(t). \tag{1.7}$$

For superconducting circuits, typical values of the capacitances are of the order 10 fF. In lumped-circuit diagrams we denote the capacitor as a pair of parallel lines, see Fig. 1.1(a) or Fig. 1.2(a).

Inductors

The time-dependent current flowing through a general inductor is a function of the flux through it, $I(t) = f[\Phi(t)]$. For a linear inductor, the current is proportional to the magnetic flux,

$$I(t) = \dot{q}(t) = \frac{1}{L}\Phi(t), \tag{1.8}$$

where L is the inductance of the inductor. Integrating over the power as before, the energy stored in the inductor is then

$$E = \frac{1}{2L}\Phi^2(t). \tag{1.9}$$

For superconducting qubits, typical values of linear inductances are of the order 1 nH. In lumped-circuit diagrams, we denote the linear inductor as a coil, see Fig. 1.1(a) or Fig. 1.2(b).

As a short clarifying example we consider the classical LC oscillator shown in Fig. 1.2(d). From Kirchhoff's current law in Eq. (1.3a) we know that $I_C = I_L$, where I_C and I_L are the currents through the capacitor and inductor, respectively. Kirchhoff's voltage

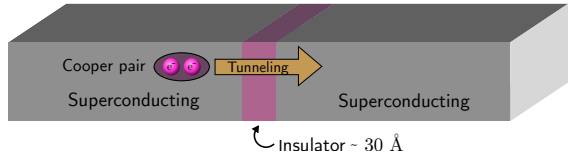

Figure 1.3: *Sketch of a Josephson junction. Two superconducting materials are separated by a thin insulator, with a thickness of the order of* 30 Å*. If a nonsuperconducting metal is used as a separator, it can be several micrometers wide. Cooper pairs can tunnel back and forth between the two superconducting materials.*

law gives us $V_C = -V_L$, assuming no fluctuating external flux. Using Eqs. (1.2a), (1.2b), (1.5), and (1.8) we can set up the equations of motion for the system

$$\ddot{\Phi}(t) = -\frac{1}{LC}\Phi(t), \tag{1.10}$$

where we introduce $\Phi(t) = \Phi_C(t) = -\Phi_L(t)$ to get rid of the subscripts. The system behaves as a simple harmonic oscillator in the flux. This is analogous to a spring, where the flux is the position, and the mass and spring constants are replaced by the capacitance and inverse inductance, respectively.

Josephson junctions

So far, we have considered only components with linear current-voltage relations. For reasons that will become clear when we quantize the lumped circuit, constructing a qubit from only linear components is by no means straightforward. We, therefore, need nonlinear components which come in the form of the Josephson junction. The Josephson junction plays a unique role in superconducting circuits, as it has no simple analog in a nonsuperconducting circuit since it is related to charge quantization effects that occur in superconductors. We start with a short introduction to superconductivity (see Ref. [59] for more details).

When the temperature is decreased, some materials undergo a phase transition where the resistivity drops to zero. With the Meissner effect, i.e., the material perfectly expels all magnetic fields, perfect conduction is the defining property of a superconductor.

The phase transition between the nonsuperconducting phase and the superconducting phase of a material happens because the conduction electrons condense into a so-called BCS ground state, characterized by an amplitude and a phase. *A priori* it might seem impossible for electrons to condense into a single quantum state since the Pauli exclusion principle forbids this. However, as Cooper suggested, some attractive force between the electrons leads to the formation of electron pairs [60], which have integer spin and thus behave like bosons. This makes it possible for these so-called Cooper pairs to condense into a single quantum ground state, and in this state, the solid becomes superconducting.

A Josephson junction consists of two superconducting islands separated by a thin insulator, a nonsuperconducting metal, or a narrow superconducting wire. Cooper pairs can then tunnel through the barrier from one island to the other, a phenomenon known as the Josephson effect [61, 62], see Fig. 1.3. The tunneling rate (current) and the voltage

between the two islands depends on the superconducting phase difference, ϕ, between the islands through [63]

$$I(t) = I_c \sin[\phi(t)], \tag{1.11}$$

$$V(t) = \frac{\hbar}{2e}\dot{\phi}, \tag{1.12}$$

where I_c is the critical current of the junction, which depends on the junction geometry. Equation (1.12) allows us to relate the junction phase difference to the generalized flux through $\Phi = \hbar\phi/2e$. The charge and flux are thus related through

$$\dot{q}(t) = I_c \sin\left(2\pi\frac{\Phi(t)}{\Phi_0}\right), \tag{1.13}$$

where we define the magnetic flux quantum $\Phi_0 = h/2e$. The Josephson junction works as a flux-dependent inductor with inductance given by [47]

$$L(\Phi) = \left(\frac{\partial I}{\partial \Phi}\right)^{-1} = \frac{L_J}{\cos\left(2\pi\frac{\Phi}{\Phi_0}\right)}, \tag{1.14}$$

where we define the Josephson inductance $L_J = \Phi_0/2\pi I_c$, since the inductance is associated with the inertia of the Cooper pairs, it is often referred to as kinetic inductance. See Section 1.10.2 for details on the use of sizeable kinetic inductance. For superconducting qubits, typical values of Josephson inductances are of the order 100 nH. The energy of a Josephson junction is also nonlinear. We have

$$E = \frac{\Phi_0^2}{(2\pi)^2}\frac{1}{L_J}\left[1 - \cos\left(2\pi\frac{\Phi}{\Phi_0}\right)\right], \tag{1.15}$$

where we often neglect the constant term when dealing with the Lagrangian or Hamiltonian, as it is irrelevant for the system's dynamics. We define the factor in front of the bracket to be the Josephson energy of the Josephson junction, $E_J = \Phi_0^2/(2\pi)^2 L_J = \Phi_0 I_c/2\pi$. In this thesis we denote Josephson junctions as a boxed "x" in lumped-circuit diagrams, see Fig. 1.1(a) or Fig. 1.2(c). Sometimes, an "x" without a box is used in the literature.

It is conventional to simplify notation so that charges and fluxes become dimensionless. This is done by using units where

$$\hbar = 2e = 1 \qquad \text{and thus} \qquad \frac{\Phi_0}{2\pi} = 1. \tag{1.16}$$

This means that we eliminate the cumbersome factor of $2\pi/\Phi_0$ in the sinusoidal Josephson junction terms. Note that in this convention, the units of capacitance and inductance become inverse energy. Moreover, with this choice of units, the junction phase differences are equal to the generalized flux $\phi = \Phi$, and the energy of a Josephson junction becomes equal to the critical current, $E_J = I_c$.

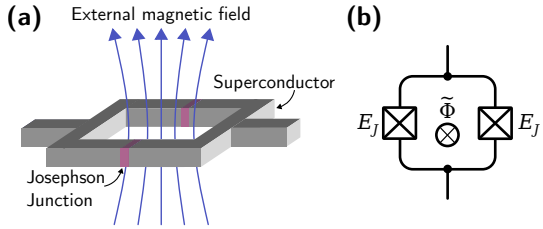

Figure 1.4: *A dc superconducting quantum interference device (dc SQUID).* **(a)** *Implementation of a dc SQUID.* **(b)** *Corresponding circuit diagram.*

dc SQUID

It is often desirable to tune the parameters of the circuit externally. Therefore many circuits employ a direct current superconducting quantum interference device, or dc SQUID, instead of a single Josephson junction. A dc SQUID consists of two Josephson junctions on a ring, with an external magnetic field, $\tilde{\Phi}$, through the ring [64], see Fig. 1.4(a). While this does not change the form of the energy of the Josephson junction, it has the advantage that it makes the front factor in Eq. (1.15) tunable. To see this consider the circuit diagram in Fig. 1.4(b). The energy of this component must be the sum of two Josephson junctions

$$U = -E_J \cos\left(\Phi_L + \frac{\tilde{\Phi}}{2}\right) - E_J \cos\left(\Phi_R + \frac{\tilde{\Phi}}{2}\right), \tag{1.17}$$

where $\Phi_{L/R}$ is the branch flux of the left and right branch, respectively, and we divide the external flux equally between the two arms of the dc SQUID following Kirchhoff's voltage law in Eq. (1.3b). We consider symmetrical junctions here, but it is a neat exercise to extend it to asymmetrical junctions.

Since we are considering the arms of a loop, we can write $\Phi = \Phi_L = -\Phi_R$ in Eq. (1.17). Using the trigonometric identity $2\cos\alpha\cos\beta = \cos(\alpha-\beta) + \cos(\alpha+\beta)$ with $\alpha = \tilde{\Phi}/2$ and $\beta = \Phi$, we can rewrite Eq. (1.17) into the form

$$U = -2E_J \cos\left(\frac{\tilde{\Phi}}{2}\right)\cos\Phi. \tag{1.18}$$

The so-called *fluxoid quantization condition* states that the algebraic sum of branch fluxes of all the inductive elements along the loop plus the externally applied flux must equal an integer number of superconducting flux quanta [55, 65, 66], i.e.,

$$\Phi + \tilde{\Phi} = 2\pi k, \tag{1.19}$$

where k is an integer, together with Kirchhoff's voltage law in Eq. (1.3b) this means that we can remove a degree of freedom. This explains how one goes from two branch fluxes, $\Phi_{L/R}$, to just one branch flux, Φ, since the branch fluxes are the system degrees of freedom. In other words we obtain, an effective Josephson energy of $E_J'(\tilde{\Phi}) = 2E_J|\cos(\tilde{\Phi}/2)|$, where the Josephson energy can be dynamically tuned through the external flux, $\tilde{\Phi}$. This idea is often implemented in superconducting circuits instead of a single Josephson

junction so that the spacing of the energy levels can be tuned dynamically by tuning $\tilde{\Phi}$. However, we usually place a single Josephson junction in a circuit diagram. Due to the sensitivity of the dc SQUID, it has many uses, especially in clinical applications such as magnetoencephalography [67, 68], magnetocardiography, and magnetic resonance imaging (MRI), where they are used for detecting tiny magnetic fields in living organisms [69, 70].

Voltage and current sources

We can treat constant voltage and current sources by representing them as capacitors or inductors. Consider a constant voltage source V. This can be represented by a huge but finite capacitor, in which an initially large charge Q is stored such that $V = Q/C$ in the limit where $C \to \infty$. Similarly, a constant current source can be represented by a huge but finite inductor, in which an initially large flux Φ is stored, such that $I = \Phi/L$ in the limit where $L \to \infty$.

1.2 Equations of motion

In order to describe the dynamics of the lumped-circuit diagrams we presented in the previous section, we now determine the equations of motion for the systems. The equations of motion depend on the circuit components and can be written in terms of the circuit variables using either the voltage and current in Eq. (1.1) or equivalently using the flux and charge in Eq. (1.2). There are several ways of finding the equations of motion, and we start from the most straightforward approach, applying Kirchhoff's laws directly to the circuit. From this starting point, we then progress to the method of nodes and then to the Lagrangian and Hamiltonian.

1.2.1 Applying Kirchhoff's laws directly

The simplest way to find the equations of motion for a given circuit is to apply Kirchhoff's laws. We have already done this for the simple *LC* oscillator example in Fig. 1.2(d), which yielded the harmonic oscillator equation of motion in Eq. (1.10). To get a better feel for this procedure, we will consider a few additional examples.

The next natural step is to exchange the linear inductor in Fig. 1.2(d) with a nonlinear Josephson junction. This yields the circuit in Fig. 1.5(a). From Kirchhoff's current law in Eq. (1.3a) we know that $I_C = I_J$, where I_C and I_J are the currents through the capacitor and Josephson junction, respectively. Kirchhoff's voltage law implies $V_C = -V_J$. Using Eqs. (1.2a), (1.2b), (1.5), and (1.8) we can set up the equations of motion for the system,

$$\ddot{\Phi}(t) = -\frac{I_c}{C}\sin\Phi(t), \tag{1.20}$$

where we introduce $\Phi(t) = \Phi_C(t) = -\Phi_J(t)$. Equation (1.20) is identical to the equation of motion for a simple pendulum, with the critical current, I_c, playing the role of the gravitational constant and the capacitance, C, becoming the mass of the pendulum, similar to the case of the *LC* circuit, see Eq. (1.10), which is the lowest order approximation to

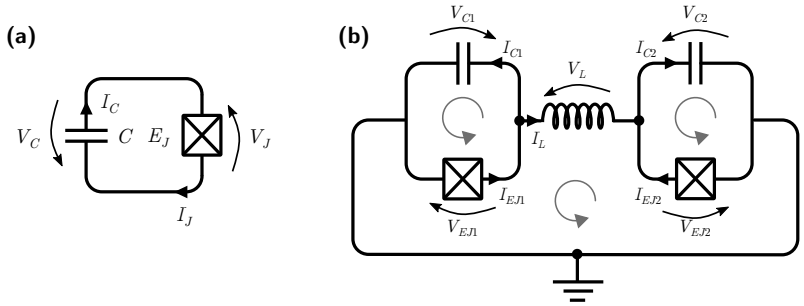

Figure 1.5: (a) *A Josephson junction and capacitor circuit. A capacitor with capacitance C is connected in a closed circuit with a Josephson junction, E_J. The voltage over the two components is V_C and V_J, respectively, while the currents are I_C and I_J, respectively. The resulting equation of motion is a Duffing oscillator.* **(b)** *Example circuit of Fig. 1.1(a) with explicit directions of the voltages and currents shown. All loops are propagated counterclockwise.*

Eq. (1.20). Contrary to Eq. (1.10) this is not linear in Φ, which is an effect of the introduction of the nonlinear Josephson junction.

We now continue to the more complicated example of Fig. 1.1(a). This time Kirchhoff's voltage law gives us three equations, one for each circuit loop. We denote the left capacitor and Josephson junction C_1 and $E_{J,1}$, respectively. Similarly, we have to the right C_2, $E_{J,2}$. The connecting inductor is denoted by L_{12}. Defining the direction of the current and voltages as in Fig. 1.5(b), we find the following equations from Eq. (1.3b)

$$-\Phi_{EJ1} - \Phi_{C1} = 0, \tag{1.21a}$$

$$\Phi_{EJ2} + \Phi_{C2} = 0, \tag{1.21b}$$

$$\Phi_{EJ1} - \Phi_{EJ2} + \Phi_L = \tilde{\Phi}, \tag{1.21c}$$

where $\tilde{\Phi}$ is the external flux in the inductor loop. We propagate all loops counterclockwise, which yields negative signs on the terms in Eq. (1.21) when the voltage of the given branch is in the opposite direction to the loop direction. Note that we can also include external fluxes in the two capacitive loops. However, as we will see in Section 1.2.3, as long as we consider only time-independent fluxes, the external fluxes will only be relevant in purely inductive loops. From Eq. (1.21a) we define $\Phi_1 = \Phi_{EJ1} = -\Phi_{C1}$ and $\Phi_2 = \Phi_{EJ2} = -\Phi_{C2}$. Using this we can also express the flux through the inductor as $\Phi_L = \Phi_2 - \Phi_1 + \tilde{\Phi}$, which significantly reduces the number of variables.

From Kirchhoff's current law, we find the following equations

$$-I_{Cn} + I_{EJn} = \mp I_L, \tag{1.22}$$

for $n = 1, 2$, where the minus is for $n = 1$ and the plus is for $n = 2$. Inserting the current relations for the respective components, we find the following equations of motion

$$C_n \ddot{\Phi}_n = \mp \frac{1}{L_{12}} (\Phi_2 - \Phi_1 + \tilde{\Phi}) - E_{J,n} \sin \Phi_n, \tag{1.23}$$

for $n = 1, 2$.

The end goal of our analysis is to quantize the circuit to treat it quantum mechanically. When doing quantum mechanics, we are usually interested in the Hamiltonian of the system, as it is closely related to the energy spectrum and time evolution of the system. It is possible to infer the system Hamiltonian from the equations of motion. This is usually done by finding a Lagrangian that yields the equation of motion using Lagrange's equations [see Eq. (1.27)] and then performing a Legendre transformation.

While applying Kirchhoff's law directly always yields the correct equations of motion, it quickly becomes cumbersome as the circuits increase in complexity. Therefore, we seek a method for determining the Lagrangian directly, which can be achieved using the method of nodes.

1.2.2 Method of nodes

This section presents the method of nodes that solves most practical problems involving Josephson junctions. The discussion follows the method proposed by Devoret [37, 71].

When determining the Lagrangian of a given circuit, our main obstacle is to remove superfluous degrees of freedom and determine how to include the external fluxes. As we saw above, we can solve these problems by manipulating Kirchhoff's law, and here we present an alternative approach.

We have already defined a node as a point where one or more components connect. We now further define a *ground node* as a node connected to ground. These nodes are inactive since the flux through them is zero, and thus they do not contribute to the dynamics of the system and can thus be ignored. For the remaining nodes, we distinguish between active and passive nodes. An *active node* is defined as a node where at least one capacitor and one inductor (either linear and Josephson junction) meet. A *passive node* is defined as a node where only one type of component meets, either only capacitors or only inductors. It turns out that passive nodes represent superfluous degrees of freedom and therefore only yield constraints on the system's dynamics. This is similar to determining an effective capacitance for a serial or parallel collection of individual capacitances.

Considering the example circuit in Fig. 1.1(a), we can represent the circuit as a set of branches, $\mathcal{B}$, and a set of nodes, $\mathcal{N}$. The set of nodes consists of three nodes; two active nodes and a ground node. The set of branches is equal to the set of components in the circuit, i.e., the example circuit has five branches; two capacitor branches, two Josephson junction branches, and a single linear inductor branch.

We call such a representation consisting of a set of nodes and a set of branches a *network graph* or simply a *graph*. With this notation, we can divide the circuit into subgraphs. There are many possible subgraphs for a given circuit, but we focus on the capacitive subgraph and the inductive subgraph. The *capacitive subgraph* contains only branches of capacitors and the nodes connected to such branches. The *inductive subgraph* contains only branches of inductors and nodes connected to such branches. In the example circuit in Fig. 1.1(a), the two capacitor branches and all three nodes are in the capacitive subgraph, while the inductor branch and the two Josephson junction branches are in the inductive subgraph together with the three nodes. Notice how the nodes can be in both subgraphs at the same time, see Fig. 1.6.

The capacitive subgraph consists only of linear capacitors, and thus we can express the energy of a capacitive branch in terms of the voltages, i.e., the derivative of the flux,

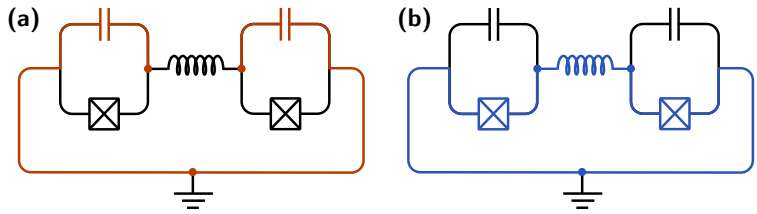

Figure 1.6: *Highlight of* **(a)** *the capacitive subgraph and* **(b)** *the inductive subgraph of the example circuit in Fig. 1.1(a).*

using Eq. (1.7). Doing this, we break the symmetry between charge and flux, and the flux can now be viewed as the "position". With this treatment, the capacitive energy becomes equivalent to the kinetic energy, while the inductive energy becomes equivalent to the potential energy.

This symmetry breaking also explains why passive nodes do not contribute to the system's dynamics. A passive node between two inductors does not have any kinetic energy and can therefore be considered stationary. On the other hand, a node between two capacitors has kinetic energy but no potential energy and can therefore be considered a free particle that does not interact with the rest of the system.

However, any real inductor (both linear and nonlinear) will always introduce some capacitance since a capacitance occurs whenever two conducting materials are in close proximity to each other. Consider the Josephson junction in Fig. 1.3; it quite closely resembles a linear plate capacitor; thus, it is expected that some parasitic capacitance will be present in parallel with the inductor. Nonetheless, we can often make this parasitic capacitance so small that it can be neglected in the lumped-element circuit. One should, however, be aware of these capacitances when designing superconducting circuits.

Spanning tree

We are now ready to consider the most important subgraph of the circuits: the spanning tree. The *spanning tree* is constructed by connecting every node in the circuit to each of the other nodes by only one path. See Definition 3 in Appendix A.1 for a more mathematical definition using graph theory. Note that there are often several choices for the spanning tree. This is not a problem for the analysis and can be seen analogous to the choice of a particular gauge in electromagnetic field theory or a coordinate system in classical mechanics.

Choosing a spanning tree for a given circuit partitions the branches into two sets: The set of branches on the spanning tree, $\mathcal{T}$, and its complementary set, $\bar{\mathcal{T}} = \mathcal{B} \setminus \mathcal{T}$, i.e., the branches *not* on the spanning tree. We call the latter set the set of closure branches because its branches close the spanning tree loop.

We use the spanning tree to determine where to include the external fluxes of the system. Following Kirchhoff's laws, the flux ϕ_n of node n can be written as the sum of incoming and outgoing branch fluxes, with a suitable sign depending on the direction of

Table 1.1: *Energies of different components on either the spanning tree or a closure branch of the circuit. The magnetic flux through the closure branch due to external fields is denoted $\tilde{\Phi}_b$. The time derivative of the magnetic flux is included for linear capacitors on closure branches for completeness. For the rest of this chapter, we assume time-independent external fluxes, i.e., $\dot{\tilde{\Phi}}_b = 0$. We refer to Refs. [72, 73] for a discussion of time-dependent fluxes.*

Element	Spanning tree	Closure branch
Linear capacitor	$\frac{C}{2}(\dot{\phi}_n - \dot{\phi}_{n'})^2$	$\frac{C}{2}(\dot{\phi}_n - \dot{\phi}_{n'} + \dot{\tilde{\Phi}}_b)^2$
Linear inductor	$\frac{1}{2L}(\phi_n - \phi_{n'})^2$	$\frac{1}{2L}(\phi_n - \phi_{n'} + \tilde{\Phi}_b)^2$
Josephson junction	$-E_J \cos(\phi_n - \phi_{n'})$	$-E_J \cos(\phi_n - \phi_{n'} + \tilde{\Phi}_b)$

the flux. With this in mind, we can write the branch fluxes in terms of the node fluxes

$$\Phi_{b\in\mathcal{T}} = \phi_n - \phi_{n'}, \tag{1.24a}$$
$$\Phi_{b\in\bar{\mathcal{T}}} = \phi_n - \phi_{n'} + \tilde{\Phi}, \tag{1.24b}$$

where n and n' are the nodes at the start and end of the given branch, respectively. $\tilde{\Phi}$ is the external flux through the loop closed by the branch. Note that the external flux occurs only if the branch is a closure branch. The fact that external fluxes do not appear in every branch is due to Kirchhoff's law in Eq. (1.3b), which eliminates the external flux on some of the branches. One can therefore choose onto which branches these external fluxes should be included, as long as Eq. (1.3b) is satisfied, which is precisely the choice we make by choosing the spanning tree.

Substituting the node fluxes into the expressions for the energy of the different components, i.e., into Eqs. (1.7), (1.9), and (1.15), we can express the energies as a function of the node fluxes. The results can be seen in Table 1.1.

Note that if the circuit contains only time-independent external fluxes, it is often an advantage to choose a spanning tree containing as few capacitors as possible, such that the capacitors lie on the closure branches. The reason is that a time-independent external flux disappears from capacitive terms since $\dot{\tilde{\Phi}} = 0$. When working with time-independent external fluxes, these are therefore only relevant in purely inductive loops. Time-dependent external fluxes are beyond the scope of this chapter; see Refs. [72, 73] for a general treatment of this case. In Section 3.2 we consider a special case where we employ time-dependent external fluxes.

If we consider the example circuit in Fig. 1.1, we can choose the spanning tree in many different ways. Since we consider only time-independent external fluxes, a particularly nice choice of spanning would be over the two Josephson junction (JJ) branches, which means that any external flux will appear only in the linear inductor term. For this reason, we do not need to worry about any external fluxes through the two capacitive loops.

1.2.3 Lagrangian approach

Having chosen a spanning tree for our circuit, we are now ready to determine its Lagrangian. The Lagrangian is found by subtracting the potential (inductive) energies from the kinetic (capacitive) energies

$$\mathcal{L} = T - U = T_{\text{cap}} - U_{\text{ind}} - U_{\text{JJ}}, \tag{1.25}$$

where T is the kinetic energy and U is the potential energy. The subscripts indicate to which type of element each term refers.

With the definition of the Lagrangian and the energies of Table 1.1, we can write the Lagrangian for the example circuit in Fig. 1.1 as

$$\mathcal{L} = \frac{C_1}{2}\dot{\phi}_1^2 + \frac{C_2}{2}\dot{\phi}_2^2 - \frac{1}{2L_{12}}(\phi_2 - \phi_1 + \tilde{\Phi})^2 + E_{J,1}\cos\phi_1 + E_{J,2}\cos\phi_2, \tag{1.26}$$

where C_n and $E_{J,n}$ are the capacitance and Josephson energy of the capacitor and Josephson junction, the index $n = 1, 2$ corresponds to the left and right side, respectively. The inductance of the inductor is denoted L_{12}. With the Lagrangian, one can obtain the equations of motion from Lagrange's equations

$$\frac{\mathrm{d}}{\mathrm{d}t}\frac{\partial \mathcal{L}}{\partial \dot{\phi}_n} = \frac{\partial \mathcal{L}}{\partial \phi_n}. \tag{1.27}$$

Applying this to the example circuit, we find the equations of motion

$$\ddot{\phi}_n = \mp\frac{1}{L_{12}C_n}(\phi_2 - \phi_1 + \tilde{\Phi}) - \frac{E_{J,n}}{C_n}\sin\phi_n, \tag{1.28}$$

where the minus is for $n = 1$ and the plus is for $n = 2$. This is identical to Eq. (1.23) written up with node fluxes instead of branch fluxes.

Using matrices

Writing the Lagrangian as in Eq. (1.26) can be rather tedious for larger circuits since it includes many sums. We, therefore, seek a more elegant way to write the Lagrangian. This is achieved using matrix notation. First we list all the nodes 1 to N and define a flux column vector $\boldsymbol{\phi}^T = (\phi_1, \ldots, \phi_N)$, where T indicates the transpose of the vector. Note that we do not include the ground node for a grounded circuit since its flux equals zero, and it does not contribute to the true degrees of freedom in any case. We can always choose a ground node in our circuits as one mode will always decouple from the remaining modes for ungrounded circuits, see Section 1.2.6.

We are now ready to set up the system's capacitive matrix $\boldsymbol{C}$. The nondiagonal matrix elements are minus the capacitance, C_{jk}, connecting nodes j and k. The diagonal elements consist of the sum of the non-diagonal values in the corresponding row or column, multiplied by -1, i.e., $C_{jj} = \sum_{k\neq j} C_{jk}$. If a node is connected to ground via a capacitor, this capacitance must also be added to the diagonal element. With this $N \times N$ matrix, we can write the kinetic energy term as

$$T = \frac{1}{2}\dot{\boldsymbol{\phi}}^T \boldsymbol{C}\dot{\boldsymbol{\phi}}. \tag{1.29}$$

In the case of the example circuit in Fig. 1.1, the flux column vector is $\boldsymbol{\phi}^T = (\phi_1, \phi_2)$, and the capacitive matrix becomes

$$\boldsymbol{C} = \begin{bmatrix} C_1 & 0 \\ 0 & C_2 \end{bmatrix}. \tag{1.30}$$

We now consider the contribution from the linear inductors. We set up the inductive matrix $\boldsymbol{L^{-1}}$ in the same way as the capacitive matrix. The nondiagonal elements are $-1/L_{jk}$ if an inductance L_{jk} connects nodes j and k, and zero otherwise, while the diagonal elements consist of the sum of values in the corresponding row or column, multiplied by minus one, $1/L_{jj} = \sum_{k\neq j} 1/L_{jk}$. If a node is connected to the ground via an inductor, this inductance must also be added to the diagonal element. Of course, if no inductor is connecting two nodes, the element should be zero. We must also include the external magnetic flux in this term. Thus the energy due to linear inductors becomes

$$U_{\text{ind}} = \frac{1}{2}\boldsymbol{\phi}^T \boldsymbol{L^{-1}} \boldsymbol{\phi} + \sum_{b\in\bar{\mathcal{T}}} \frac{1}{L_b}(\phi_n - \phi_{n'})\tilde{\Phi}_b, \tag{1.31}$$

where we remove all irrelevant constant terms, the second term sums over all the inductive closure branches of the circuit, where n and n' are the nodes connected by branch b.

If we consider the example circuit again, the inductive matrix is

$$\boldsymbol{L^{-1}} = \begin{bmatrix} 1/L_{12} & -1/L_{12} \\ -1/L_{12} & 1/L_{12} \end{bmatrix}, \tag{1.32}$$

where L_{12} is the inductance of the linear inductor. With this, the inductive energy of the example circuit becomes

$$U_{\text{ind}} = \frac{1}{2}\boldsymbol{\phi}^T \boldsymbol{L^{-1}} \boldsymbol{\phi} + \frac{1}{L_{12}}(\phi_1 - \phi_2)\tilde{\Phi}, \tag{1.33}$$

where $\tilde{\Phi}$ is the external flux through the inductive loop. When there are only a few linear inductors, as in the example circuit, it might be more straightforward to write the energy without the matrix notation. We do not attempt to write the Josephson junction terms using matrix notation as they are nonlinear functions of the node flux variables.

1.2.4 Hamiltonian approach

A simple transformation of the Lagrangian can find the Hamiltonian of the circuit, which is commonly referred to as a Legendre transformation. First, we define the conjugate momentum to each node flux by

$$q_n = \frac{\partial \mathcal{L}}{\partial \dot{\phi}_n}, \tag{1.34}$$

which in vector form becomes $\boldsymbol{q} = \boldsymbol{C}\dot{\boldsymbol{\phi}}$. If the capacitance matrix is invertible, we can express $\dot{\boldsymbol{\phi}}$ as a function of $\boldsymbol{q}$. We denote the conjugate momenta as node charges since they correspond to the algebraic sum of the charges on the capacitances connected to node n.

The Hamiltonian can be expressed in terms of node charges, q_n, for the kinetic energy and node fluxes, ϕ_n, for the potential energy through the Legendre transform

$$\mathcal{H} = \dot{\boldsymbol{\phi}}^T \boldsymbol{q} - \mathcal{L} = \frac{1}{2}\boldsymbol{q}^T \boldsymbol{C}^{-1} \boldsymbol{q} + U(\boldsymbol{\phi}), \tag{1.35}$$

where the potential energy is a nonlinear function of the node fluxes. Note that the functional form of the Hamiltonian may differ depending on the choice of spanning tree. This is because the choice of flux-node coordinates is not unique, much like the electrodynamic potentials, which have a "gauge freedom" in which certain functions can be added to the potentials without any change to the physics, or more concretely; without changes to the electric and magnetic fields [57]. Here a different choice of flux variables would correspond to a change of gauge as well, and a physical quantity like the total energy should not change under such a transformation.

With the Hamiltonian, it is possible to find the equations of motion using Hamilton's equations

$$\dot{\phi}_n = \frac{\partial \mathcal{H}}{\partial q_n}, \qquad \dot{q}_n = -\frac{\partial \mathcal{H}}{\partial \phi_n}, \tag{1.36}$$

which yields results for the equations of motion that are equivalent to Lagrange's equations Eq. (1.27).

1.2.5 Normal modes

Lagrange's equations tell us that for all passive nodes $\dot{q}_n = 0$, since for a passive note we have $\frac{\partial \mathcal{H}}{\partial \phi_n} = 0$. This means that the circuit has, at most, the same number of true degrees of freedom as the number of active nodes except the ground node. The number of true degrees of freedom turn out to be identical to the number of normal modes of the system. If all inductors can be approximated as linear inductors (and external fluxes are ignored), the Lagrangian takes the form

$$\mathcal{L} = \frac{1}{2}\dot{\boldsymbol{\phi}}^T \boldsymbol{C} \dot{\boldsymbol{\phi}} - \frac{1}{2}\boldsymbol{\phi}^T \boldsymbol{L^{-1}} \boldsymbol{\phi}. \tag{1.37}$$

This simple form of the Lagrangian means that the equations of motion become

$$\boldsymbol{C}\ddot{\boldsymbol{\phi}} = -\boldsymbol{L^{-1}}\boldsymbol{\phi}, \tag{1.38}$$

which is essentially Hooke's law in matrix form where the capacitances play the role of the masses and inductances play the role of the spring constants [74]. The normal modes of the entire systems can be found as the eigenvectors of the matrix product $\boldsymbol{\Omega}^2 = \boldsymbol{C}^{-1}\boldsymbol{L^{-1}}$ associated with nonzero eigenvalues. These nonzero eigenvalues correspond to the squared normal mode frequencies of the circuit. Note that $\boldsymbol{C}^{-1}$ and $\boldsymbol{L^{-1}}$ can always be diagonalized simultaneously since they are both positive definite matrices [74]. It can be advantageous to find these eigenmodes and use them to reduce the number of couplings between modes.

1.2.6 Change of basis

Here we present a method for changing into the normal mode basis of a circuit. Given a circuit with N nodes and a matrix product $\boldsymbol{\Omega}^2 = \boldsymbol{C}^{-1}\boldsymbol{L}^{-1}$, let $\boldsymbol{v}_1, \boldsymbol{v}_2, \ldots, \boldsymbol{v}_n$ be the orthonormal eigenvectors of $\boldsymbol{\Omega}^2$, with eigenvalues $\chi_1, \chi_2, \ldots, \chi_n$. Let $\boldsymbol{\phi}$ be the usual vector of the node fluxes of the circuit. We can then introduce the normal modes $\boldsymbol{\psi}$ via

$$\boldsymbol{\phi} = \boldsymbol{\mathcal{V}}\boldsymbol{\psi}, \tag{1.39}$$

where

$$\boldsymbol{\mathcal{V}} = \begin{bmatrix} | & | & & | \\ \boldsymbol{v}_1 & \boldsymbol{v}_2 & \cdots & \boldsymbol{v}_N \\ | & | & & | \end{bmatrix}, \tag{1.40}$$

is a matrix whose columns are the eigenvectors of $\boldsymbol{\Omega}^2$. The kinetic energy term in Eq. (1.29) can now be written

$$T = \frac{1}{2}\dot{\boldsymbol{\psi}}^T \boldsymbol{K} \dot{\boldsymbol{\psi}}, \tag{1.41}$$

where we introduce the capacitance matrix in the transformed coordinates $\boldsymbol{K} = \boldsymbol{\mathcal{V}}^T \boldsymbol{C} \boldsymbol{\mathcal{V}}$.

While we assume the columns of Eq. (1.40) to be the eigenvectors of $\boldsymbol{\Omega}^2$, this is not a requirement, and one can rotate to any frame using an orthonormal basis to construct $\boldsymbol{\mathcal{V}}$. However, only if one uses the eigenvectors of $\boldsymbol{\Omega}^2$ will the transformed capacitance matrix, $\boldsymbol{K}$, be diagonal with entries λ_i. In terms of the canonical momenta $\boldsymbol{p}$ conjugate to $\boldsymbol{\psi}$, the kinetic energy takes the usual form

$$T = \frac{1}{2}\boldsymbol{p}^T \boldsymbol{K}^{-1} \boldsymbol{p}, \tag{1.42}$$

where the inverse of $\boldsymbol{K}$ is trivial to find if it is a diagonal matrix, yielding the entries $1/\lambda_i$. In the above, we have assumed that $\boldsymbol{C}$ is positive definite, which is usually the case. This means that $\lambda_i \neq 0$. We comment on the case where $\boldsymbol{C}$ is not positive definite below.

We must also consider how contributions from the higher-order terms of inductors behave under this coordinate transformation. Even though we have approximated all inductors as linear to find the normal modes, higher-order terms from Josephson junctions still contribute as corrections, often leading to couplings between the modes. Such terms transform the following way

$$\phi_k - \phi_l \to \sum_i \left[(\boldsymbol{v}_i)_k - (\boldsymbol{v}_i)_l\right] \psi_i, \tag{1.43}$$

where $(\boldsymbol{v}_i)_k$ is the kth entry of $\boldsymbol{v}_i$. Considering, for instance, fourth-order terms in ϕ, this can result in both two-body interactions and interactions beyond two-body. These multibody interactions can complicate the equations of motion beyond what the change of basis adds in terms of simplification. Coordinate transformations are, therefore, often most useful in cases where the capacitors are symmetrically distributed, which results in simple normal modes.

The center-of-mass (CM) mode plays a special role in analytical mechanics, as it often decouples from the dynamics of the system. The same is the case for electrical

circuits. The center-of-mass mode corresponds to $\boldsymbol{v}_{\mathrm{CM}} = (1, 1, \ldots, 1)^T/\sqrt{N}$, which yields $\psi_{\mathrm{CM}} = (\phi_1 + \phi_2 + \cdots + \phi_N)/\sqrt{N}$. This mode is always present and it corresponds to charge flowing equally into every node of the circuit from ground and oscillating back and forth between ground and the nodes. Furthermore, since all its entries are identical it always disappears in the linear combination of Eq. (1.43) [$(\boldsymbol{v}_{\mathrm{CM}})_k - (\boldsymbol{v}_{\mathrm{CM}})_l = 0$]. Hence, this mode is completely decoupled from the dynamics.

The decoupling of this mode is related to how we can arbitrarily choose a node in our circuit as the ground node, whose node flux does not enter into our equations, or rather is identically set to zero. For an ungrounded circuit $\boldsymbol{C}$ is no longer positive definite and we have $\lambda_{\mathrm{CM}} = 0$, making $\boldsymbol{K}$ singular. We therefore always assum

1.3 Quantization and effective energies

1.3.1 Operators and commutators

We now quantize the classical Hamiltonian to obtain a quantum-mechanical description of the circuit. This is done through canonical quantization, replacing all the variables and the Hamiltonian with operators

$$\begin{aligned} \phi_n &\to \hat{\phi}_n, \\ q_n &\to \hat{q}_n, \\ \mathcal{H} &\to \hat{\mathcal{H}}, \end{aligned} \tag{1.44}$$

where $\hat{\phi}_n$ is the node flux operator corresponding to position coordinates, $\hat{q}_n$ is the conjugate momentum, and $\hat{\mathcal{H}}$ is the Hamiltonian operator. If the flux operator and the conjugate momentum operator are not constants of motion, they obey the canonical commutator relation

$$[\hat{\phi}_n, \hat{q}_m] = \hat{\phi}_n\hat{q}_m - \hat{q}_m\hat{\phi}_n = i\hbar\delta_{nm}, \tag{1.45}$$

where δ_{nm} is the Kronecker delta. The commutator relation in Eq. (1.45) does not hold if a given node, n, is not a true degree of freedom. This happens if the variable does not appear in $\hat{\mathcal{H}}$, implying that the commutator between the variable and the Hamiltonian will be zero. This means that $\hat{\phi}_n$ or $\hat{q}_n$ will be constants of motion according to Heisenberg's equation of motion. This is, of course, also true for the classical variables as seen in Hamilton's equations in Eq. (1.36).

The commutator relation can be found using the value of the classical Poisson bracket, which determines the value of the corresponding commutator up to a factor of $i\hbar$, as Dirac argued [75]. Using this for the branch flux operators and the charge operators, both defined in Eq. (1.2), we find that the Poisson bracket is

$$\{\Phi_b, Q_b\} = \sum_n \left[\frac{\partial\Phi_b}{\partial\phi_n}\frac{\partial Q_b}{\partial q_n} - \frac{\partial Q_b}{\partial\phi_n}\frac{\partial\Phi_b}{\partial q_n}\right] = \pm 1, \tag{1.46}$$

where the sign is plus for a capacitive branch and minus for an inductive branch. Following Dirac's approach, we arrive at the following commutator relation

$$[\hat{\Phi}_b, \hat{Q}_b] = \pm i\hbar, \tag{1.47}$$

which is equivalent to the commutator in Eq. (1.45). In general, these branch operators are not conjugate in the Hamiltonian. One must still find the true degrees of freedom before quantization is applied.

1.3.2 Effective energies

Consider the generalized momentum $\hat{\boldsymbol{q}} = \boldsymbol{C}\dot{\hat{\boldsymbol{\phi}}}$. The time derivative of the generalized momentum is exactly the current through the capacitors, $\hat{\boldsymbol{I}} = \boldsymbol{C}\ddot{\hat{\boldsymbol{\phi}}}$. Note that in the limiting case of one node, this reduces to the current over a single parallel-plate capacitor, as it should. For this reason, it makes sense to think of the conjugate momentum as the sum of all charges on the capacitors attached to a given node. We therefore define

$$\hat{n}_n = -\frac{\hat{q}_n}{2e} \tag{1.48}$$

as the net number of Cooper pairs stored on the nth node. If we consider the kinetic energy of a circuit, we can write

$$\hat{T} = \frac{1}{2}\hat{\boldsymbol{q}}^T\boldsymbol{C}^{-1}\hat{\boldsymbol{q}} = 4\frac{e^2}{2}\hat{\boldsymbol{n}}^T\boldsymbol{C}^{-1}\hat{\boldsymbol{n}}. \tag{1.49}$$

Now for each diagonal element, we have a contribution of $4E_{C,n}\hat{n}_n^2$, where we define the effective capacitive energy of the nth node as

$$E_{C,n} = \frac{e^2}{2}(\boldsymbol{C}^{-1})_{(n,n)}, \tag{1.50}$$

which is equivalent to the energy required to store a single charge on the capacitor. Note that in our dimensionless notation from Eq. (1.16) we have $\hat{n}_n = -\hat{q}_n$, while the effective energy becomes $E_{C,n} = (\boldsymbol{C}^{-1})_{(n,n)}/8$.

Similarly, we introduce the effective energies of the linear inductances and Josephson junctions, $E_{L,n}$ and $E_{J,n}$, of each node. The effective inductive energy is the diagonal elements of $\boldsymbol{L^{-1}}$, which is equivalent to the sum of the inverse inductances of the inductors connected to the given node. The effective Josephson energy is found as the sum of the Josephson energies of the junctions connected to the given node.

Returning to our example circuit in Fig. 1.1, we can now write it using operators and effective energies. It becomes

$$\hat{\mathcal{H}} = 4\left(E_{C,1}\hat{n}_1^2 + E_{C,2}\hat{n}_2^2\right) + E_{L,12}(\hat{\phi}_1 - \hat{\phi}_2 + \tilde{\Phi})^2 - E_{J,1}\cos\hat{\phi}_1 - E_{J,2}\cos\hat{\phi}_2, \tag{1.51}$$

where the coupling energy of the linear inductor is $E_{L,12} = 1/2L_{12}$. The effective energies of the Josephson junctions are the Josephson energies. Note that since our example does not include any coupling capacitors, we do not obtain any coupling term $(\boldsymbol{C}^{-1})_{(1,2)}\hat{n}_1\hat{n}_2$ since $\boldsymbol{C}$ is diagonal. In reality, this is rarely the case.

1.4 Recasting to interacting harmonic oscillators

We want to consider the low-energy limit of the superconducting circuit since we want to create a qubit using the two lowest-lying states of the nonlinear oscillator quantum system.

This can be done by suppressing the system's kinetic energy, such that the 'position' coordinate will be localized near the minimum of the potential. We consider a single anharmonic oscillator (AHO) as in Fig. 1.5 but with a possible linear inductor in parallel, which means that we can omit subscripts in this section as there is only a single mode. The Hamiltonian we thus consider is

$$\hat{\mathcal{H}}_{\mathrm{AHO}} = 4E_C\hat{n}^2 + E_L\hat{\phi}^2 - E_J\cos\hat{\phi}. \tag{1.52}$$

If the effective capacitive energy, E_C, of the mode is much smaller than the effective Josephson energy, E_J, the flux will be well localized near the bottom of the potential. This is equivalent to a heavy particle moving near its equilibrium position. In this case, we can Taylor expand the potential part of the Hamiltonian up to fourth order in ϕ such that the Josephson-junction term takes the form

$$E_J\cos\phi = E_J - \frac{1}{2}E_J\phi^2 + \frac{1}{24}E_J\phi^4 + O(\phi^6). \tag{1.53}$$

Throwing away the irrelevant constant term, we are left with a Hamiltonian consisting of second- and fourth-order terms. If we require the couplings between different parts of the superconducting circuit to be small, we can treat each mode individually as a harmonic oscillator perturbed by a quartic anharmonicity and possibly some couplings to other modes of the system. For each mode in our system, we have a simple harmonic oscillator (SHO) of the form

$$\hat{\mathcal{H}}_{\mathrm{SHO}} = 4E_C\hat{n}^2 + \left(E_L + \frac{1}{2}E_J\right)\hat{\phi}^2. \tag{1.54}$$

The simple harmonic oscillator is well-understood quantum mechanically, and using the algebraic approach [76] we define the annihilation and creation operators

$$\hat{b} = \frac{1}{\sqrt{2}}\left(\frac{1}{\sqrt{\zeta}}\hat{\phi} - i\sqrt{\zeta}\hat{n}\right), \tag{1.55a}$$

$$\hat{b}^\dagger = \frac{1}{\sqrt{2}}\left(\frac{1}{\sqrt{\zeta}}\hat{\phi} + i\sqrt{\zeta}\hat{n}\right), \tag{1.55b}$$

where we define the impedance

$$\zeta = \sqrt{\frac{4E_C}{E_L + E_J/2}}. \tag{1.56}$$

When restoring dimensions and going away from the dimensionless notation defined in Eq. (1.16) the impedance in Eq. (1.56) must be multiplied with a factor of $R_Q/2\pi$, where $R_Q = h/(2e)^2 \simeq 6.45\,\mathrm{k\Omega}$ is the resistance quantum, which emerges in the quantum Hall effect. The annihilation and creation operators fulfill the usual commutator relation

$$[\hat{b}, \hat{b}^\dagger] = 1. \tag{1.57}$$

Expressing the flux and conjugate momentum operators in terms of the annihilation and creation operators,

$$\hat{\phi} = \sqrt{\frac{\zeta}{2}}(\hat{b} + \hat{b}^\dagger), \tag{1.58a}$$

$$\hat{n} = \frac{i}{\sqrt{2\zeta}}(\hat{b} - \hat{b}^\dagger), \tag{1.58b}$$

Table 1.2: *Overview of the different components and corresponding operators. Subscripts are included where appropriate and refer to different nodes. All constant terms are neglected. The impedance factor can be found in Eq.* (1.56).

Component	Hamiltonian term	Annihilation and creation operators
All terms	$\hat{n}^2 + \hat{\phi}^2$	$4\sqrt{E_C\left(E_L + \frac{1}{2}E_J\right)}\hat{b}^\dagger\hat{b}$
Linear capacitors	$\hat{n}$	$\frac{i}{\sqrt{2\zeta}}(\hat{b} - \hat{b}^\dagger)$
	$\hat{n}^2$	$-\frac{1}{2\zeta}(\hat{b} - \hat{b}^\dagger)^2$
	$\hat{n}_i\hat{n}_j$	$-\frac{1}{2\sqrt{\zeta_i\zeta_j}}(\hat{b}_i - \hat{b}_i^\dagger)(\hat{b}_j - \hat{b}_j^\dagger)$
Linear inductors	$\hat{\phi}$	$\sqrt{\frac{\zeta}{2}}(\hat{b}^\dagger + \hat{b})$
	$\hat{\phi}^2$	$\frac{\zeta}{2}(\hat{b}^\dagger + \hat{b})^2$
	$\hat{\phi}_i\hat{\phi}_j$	$\frac{\sqrt{\zeta_i\zeta_j}}{2}(\hat{b}_i^\dagger + \hat{b}_i)(\hat{b}_j^\dagger + \hat{b}_j)$
Josephson junctions	$\hat{\phi}^4$	$\frac{\zeta^2}{4}(\hat{b}^\dagger + \hat{b})^4$
	$\hat{\phi}^3$	$\frac{\zeta^{3/2}}{2^{3/2}}(\hat{b}^\dagger + \hat{b})^3$
	$\hat{\phi}_i^3\hat{\phi}_j$	$\frac{\zeta_i^{3/2}\zeta_j^{1/2}}{4}(\hat{b}_i^\dagger + \hat{b}_i)^3(\hat{b}_j^\dagger + \hat{b}_j)$
	$\hat{\phi}_i^2\hat{\phi}_j^2$	$\frac{\zeta_i\zeta_j}{4}(\hat{b}_i^\dagger + \hat{b}_i)^2(\hat{b}_j^\dagger + \hat{b}_j)^2$

we can rewrite the oscillator part of the Hamiltonian as

$$\hat{\mathcal{H}}_{\text{SHO}} = 4\sqrt{E_C\left(E_L + \frac{1}{2}E_J\right)}\left(\hat{N} + \frac{1}{2}\right), \tag{1.59}$$

where we introduce the usual number operator $\hat{N} = \hat{b}^\dagger\hat{b}$.

We can rewrite all quadratic and quartic interaction terms using the creation and annihilation operators. The results are in Table 1.2 for the most commonly occurring terms.

Returning to our example circuit in Fig. 1.1, we can write the Hamiltonian in Eq. (1.51) using annihilation and creation operators as

$$\begin{aligned}\hat{\mathcal{H}} = {} & \omega_1\hat{b}_1^\dagger\hat{b}_1 + \omega_2\hat{b}_2^\dagger\hat{b}_2 + \frac{\alpha_1}{12}(\hat{b}_1^\dagger + \hat{b}_1)^4 + \frac{\alpha_2}{12}(\hat{b}_2^\dagger + \hat{b}_2)^4 \\ & + g_{12}(\hat{b}_1^\dagger + \hat{b}_1)(\hat{b}_2^\dagger + \hat{b}_2) + \chi_1(\hat{b}_1 + \hat{b}_1^\dagger) - \chi_2(\hat{b}_2 + \hat{b}_2^\dagger),\end{aligned} \tag{1.60}$$

where we omit all constant terms. We further define

$$\omega_n = 4\sqrt{E_{C,n}\left(E_{L,12} + \frac{1}{2}E_{J,n}\right)}, \tag{1.61a}$$

$$\alpha_n = -\frac{\zeta_n^2}{8}E_{J,n}, \tag{1.61b}$$

$$g_{12} = -\sqrt{\zeta_1\zeta_2}E_{L,12}, \tag{1.61c}$$

$$\chi_n = \sqrt{2\zeta_n}E_{L,12}\tilde{\Phi}, \tag{1.61d}$$

$$\zeta_n = \sqrt{\frac{4E_{C,n}}{E_{L,12} + E_{J,n}/2}}, \tag{1.61e}$$

where we refer to ω_n as the frequency, α_n as the anharmonicity, and g_{12} the oscillator coupling strength. Note that if the effective inductive energy is zero, $E_{L,n} = 0$, then the anharmonicity in Eq. (1.61b) becomes $\alpha_n = -E_{C,n}$, which is often the case.

Note that in the presence of an external flux, one should be careful in identifying the minimum of the potential around which one can then perform the expansion, as in Eq. (1.53).

1.5 Time-averaged dynamics

When analyzing the Hamiltonian of the circuit, it is often advantageous to consider which terms dominate the time evolution and which terms only give rise to minor corrections. The latter can often be neglected without changing the system's overall behavior. It can often be challenging to determine which terms dominate, as different scales influence the system's dynamics. This stems from the fact that the frequencies, ω_n, of the oscillators are usually of the order GHz while the interactions between the different oscillators are usually much smaller, on the order of MHz. We, therefore, employ separation of scales to remove the large energy differences of the modes from the Hamiltonian. This makes it possible to see the details of the interactions. In order to do this, we first introduce the concept of the interaction picture, where the interacting part of the Hamiltonian is in focus. To summarize which terms we consider in the Hamiltonian, we divide the terms into three categories.

- Large trivial terms: Well understood energy difference terms, such as the qubit frequencies, which we remove using separation of scales by transforming into the interaction picture. Usually of the order GHz.
- Smaller but interesting terms: The dominant part of the interesting interaction. Usually of the order MHz
- Small negligible terms: The suppressed part of the interaction, which does not contribute significantly to the time evolution. These can be removed using the rotating-wave approximation (RWA).

Note, however, that the above categorization is only a guide, and one should always consider each term in relation to the concrete system at hand.

1.5.1 Interaction picture

Consider the state $|\psi, t\rangle_S$ at time t. This state satisfies the Schrödinger equation,

$$i\frac{\partial}{\partial t}|\psi, t\rangle_S = \hat{\mathcal{H}}\,|\psi, t\rangle_S\,, \tag{1.62}$$

where $\hat{\mathcal{H}}$ is the Hamiltonian. The subscript S refers to the Schrödinger picture. In the Schrödinger picture operators are time-independent, and states are time-dependent. We wish to change into the interaction picture by splitting the Hamiltonian in a way such that the dynamics are separated from the noninteracting part, $\hat{\mathcal{H}} = \hat{\mathcal{H}}_0 + \hat{\mathcal{H}}_{I,S}$. There are often several ways to split depending on what interaction we want to highlight. This separation comes at the cost that both the operators and states become time-dependent. The advantage of using a specific splitting of the full Hamiltonian is that we can highlight some desired physics while ignoring other parts that are well understood. This is analogous to choosing a reference frame rotating with the Earth when doing classical physics in a reference frame fixed on the surface of the Earth.

States in the interaction picture are defined as

$$|\psi, t\rangle_I = e^{i\hat{\mathcal{H}}_0 t}|\psi, t\rangle_S, \tag{1.63}$$

where the subscript I refers to the interaction picture. The operators in the interaction picture are defined as

$$\hat{\mathcal{O}}_I = e^{i\hat{\mathcal{H}}_0 t}\hat{\mathcal{O}}_S e^{-i\hat{\mathcal{H}}_0 t}, \tag{1.64}$$

where $\hat{\mathcal{O}}_S$ is an operator in the Schrödinger picture.

It is then possible to show that the state satisfies the following Schrödinger equation

$$i\frac{\partial}{\partial t}|\psi, t\rangle_I = \hat{\mathcal{H}}_I|\psi, t\rangle_I, \tag{1.65}$$

where $\hat{\mathcal{H}}_I = e^{i\hat{\mathcal{H}}_0 t}\hat{\mathcal{H}}_{I,S}e^{-i\hat{\mathcal{H}}_0 t}$ is the interaction part of the Hamiltonian in the interaction picture.

In general, one can transform a Hamiltonian to any so-called rotating frame using the transformation rule

$$\hat{\mathcal{H}} \to \hat{\mathcal{H}}_R = \hat{\mathcal{U}}(t)^\dagger \hat{\mathcal{H}}\,\hat{\mathcal{U}}(t) + i\frac{\mathrm{d}\hat{\mathcal{U}}(t)^\dagger}{\mathrm{d}t}\hat{\mathcal{U}}(t), \tag{1.66}$$

where $\hat{\mathcal{U}}(t)$ is a unitary transformation. This transformation rule holds for any unitary transformation and is quite useful to keep in mind. Note that Eq. (1.66) is equivalent to transforming the Hamiltonian into the interaction picture $\hat{\mathcal{H}} \to \hat{\mathcal{H}}_I$ when $\hat{\mathcal{U}}(t) = \exp(-i\hat{\mathcal{H}}_0 t)$, and $\hat{\mathcal{H}}_0$ is the noninteracting part of the Hamiltonian, as the second term removes the noninteracting part of the Hamiltonian.

One can also show that a Heisenberg equation of motion governs the time evolution of the operators in the interaction picture

$$\frac{\mathrm{d}}{\mathrm{d}t}\hat{\mathcal{O}}_I = i[\hat{\mathcal{H}}_0, \hat{\mathcal{O}}_I], \tag{1.67}$$

where we assume no explicit time dependence in $\hat{\mathcal{O}}_S$. Note that this implies that the voltage of the bth branch can be calculated as $\hat{V}_b = i[\hat{\mathcal{H}}, \hat{\Phi}_b]$. For more information about the interaction picture, see, e.g., Ref. [76].

1.5.2 Rotating-wave approximation

Consider now the weakly anharmonic oscillator as seen in Fig. 1.7(c), which has the quantized Hamiltonian

$$\hat{\mathcal{H}} = \omega \hat{b}^\dagger \hat{b} + \frac{\alpha}{12}(\hat{b}^\dagger + \hat{b})^4, \tag{1.68}$$

where we remove all constant terms. The frequency is $\omega = \sqrt{8E_C E_J}$ and the anharmonicity is $\alpha = -E_C$ where E_C and E_J are the effective capacitive energy and Josephson energy, respectively. We choose the first term as the noninteracting Hamiltonian, $\hat{\mathcal{H}}_0 = \omega \hat{b}^\dagger \hat{b}$. We want to figure out how the annihilation and creation operators behave in the interaction picture, i.e., we want to calculate Eq. (1.64) for the annihilation and creation operators. First, we notice that $\hat{\mathcal{H}}_0^n \hat{b}^\dagger = \hat{b}^\dagger (\hat{\mathcal{H}}_0 + \omega)^n$. Using this and expanding the exponential functions, we can prove that

$$e^{i\hat{\mathcal{H}}_0 t} \hat{b}^\dagger e^{-i\hat{\mathcal{H}}_0 t} = \hat{b}^\dagger e^{i\omega t}. \tag{1.69}$$

We find a similar expression for $\hat{b}$, but with a minus in the exponential factor on the right-hand side by taking the complex conjugate.

We now wish to consider how different combinations of the annihilation and creation operators transform in the interaction picture. Starting with the number operator $\hat{N} = \hat{b}^\dagger \hat{b}$, we see the exponential factor from $\hat{b}^\dagger$ cancels the exponential factor from $\hat{b}$, meaning that the number operator is unaffected by the transformation. This is not surprising as the number operator chooses the noninteracting Hamiltonian exactly. However, if we consider terms like $J\hat{b}^\dagger \hat{b}^\dagger$, we find that in the interaction picture, they take the form $J\hat{b}^\dagger \hat{b}^\dagger e^{2i\omega t}$. If ω is sufficiently large compared to the factor, J, in front of the term (which is often the case in superconducting circuit Hamiltonians, where $\omega \sim$ GHz, while other terms are usually of the order $J \sim$ MHz), these terms will oscillate very rapidly on the timescale induced by J. The time average over such terms on a timescale of $\tau \sim 1/J$ is zero, and we can therefore neglect them as they only give rise to minor corrections. This is the rotating-wave approximation which is widely used in atomic physics [77, 78]. The story is similar for $\hat{b}\hat{b}$ terms. All terms that do not conserve the number of excitations (or quanta) of the system, i.e., terms where the number of annihilation operators is not equal to the number of creation operators, will rotate rapidly and can therefore safely be neglected. Note that while these individual terms are nonconserving, they always appear in conjugate pairs in the Hamiltonian such that the full Hamiltonian conserves the excitations, as it should.

It is important to point out that despite the naming, the 'conservation' is not related to a conservation law resulting from symmetry, i.e., like in Noether's theorem. Instead, the statement here means that the excitation conserving terms are much more critical than the nonconserving terms as long as the conditions for using the rotating-wave approximation are satisfied.

Now consider the anharmonicity term of Eq. (1.68). When only including excitation conserving terms and removing irrelevant constants, the anharmonicity term takes the form

$$\frac{\alpha}{12}(\hat{b}^\dagger + \hat{b})^4 = \alpha \left(\frac{1}{2} \hat{b}^\dagger \hat{b}^\dagger \hat{b}\hat{b} + \hat{b}^\dagger \hat{b} \right) + \text{Nonconserving terms}. \tag{1.70}$$

The last term, $\hat{b}^\dagger \hat{b}$, is the number operator, and we can therefore consider it a correction to the frequency, such that the dressed frequency becomes $\tilde{\omega} = \omega + \alpha = \sqrt{8E_C E_J} - E_C$. The

remaining $(\hat{b}^\dagger\hat{b}^\dagger\hat{b}\hat{b})$ term makes the oscillator anharmonic. For this reason, we call α the anharmonicity of the anharmonic oscillator. If we remove terms that do not conserve the number of excitation, the Hamiltonian takes the form (in the Schrödinger picture)

$$\hat{\mathcal{H}} = \tilde{\omega}\hat{b}^\dagger\hat{b} + \frac{\alpha}{2}\hat{b}^\dagger\hat{b}^\dagger\hat{b}\hat{b}. \tag{1.71}$$

Next, consider an interaction term like the one in Eq. (1.60)

$$(\hat{b}_i^\dagger + \hat{b}_i)(\hat{b}_j^\dagger + \hat{b}_j) = \hat{b}_i^\dagger\hat{b}_j + \hat{b}_i\hat{b}_j^\dagger + \hat{b}_i^\dagger\hat{b}_j^\dagger + \hat{b}_i\hat{b}_j. \tag{1.72}$$

Changing into the interaction picture, we realize that the two last terms obtain a phase of $\exp[\pm i(\omega_i + \omega_j)t]$, which can be considered a fast oscillating term if the frequencies $\omega_i + \omega_j$ are much larger than the interaction strength, which is usually the case. We can, therefore, safely neglect these nonconserving terms. The two first terms, on the other hand, obtain a phase of $\exp(\pm i\delta t)$, where $\delta = \omega_i - \omega_j$ is called the detuning of the two oscillators. Therefore, it is tempting to say that these terms only contribute if $\omega_i \approx \omega_j$. This is, however, not the whole story. More precisely, we find that

$$\hat{b}_i^\dagger\hat{b}_j e^{i\delta t} + \hat{b}_i\hat{b}_j^\dagger e^{-i\delta t} = (\hat{b}_i^\dagger\hat{b}_j + \hat{b}_i\hat{b}_j^\dagger)\cos\delta t + i(\hat{b}_i^\dagger\hat{b}_j - \hat{b}_i\hat{b}_j^\dagger)\sin\delta t, \tag{1.73}$$

which can be useful in some situations, e.g., when driving qubits, see Section 1.7. However, as a general rule of thumb, one can neglect these terms unless $\omega_i \simeq \omega_j$, i.e., $\delta = 0$. For a more general discussion on the validity of the time averaging dynamics, see Ref. [79].

If we consider the example circuit in Fig. 1.1, under the assumption that $|\alpha_n| \ll \omega_n$, we can time average its Hamiltonian in Eq. (1.60). We choose the noninteracting Hamiltonian as $\mathcal{H}_0 = \omega_1\hat{b}_1^\dagger\hat{b}_1 + \omega_2\hat{b}_2^\dagger\hat{b}_2$, which means that the interacting part of the Hamiltonian in Eq. (1.60) becomes

$$\begin{aligned}\hat{\mathcal{H}}_I = &\frac{\alpha_1}{2}(\hat{b}_1^\dagger\hat{b}_1^\dagger\hat{b}_1\hat{b}_1 + 2\hat{b}_1^\dagger\hat{b}_1) + \frac{\alpha_2}{2}(\hat{b}_2^\dagger\hat{b}_2^\dagger\hat{b}_2\hat{b}_2 + 2\hat{b}_2^\dagger\hat{b}_2)\\ &+ g_{12}\left(\hat{b}_1^\dagger\hat{b}_2 e^{i\delta t} + \hat{b}_1\hat{b}_2^\dagger e^{-i\delta t} + \hat{b}_1\hat{b}_2 e^{-i(\omega_1+\omega_2)t} + \hat{b}_1^\dagger\hat{b}_2^\dagger e^{i(\omega_1+\omega_2)t}\right)\\ &- \sum_{n=1}^{2}(-1)^n\chi_n(\hat{b}_n e^{-i\omega_n t} + \hat{b}_n^\dagger e^{i\omega_n t}),\end{aligned} \tag{1.74}$$

where we define the detuning $\delta = \omega_1 - \omega_2$. Assuming $\omega_1 \simeq \omega_2$, i.e., $\delta \simeq 0$, and if we further assume that $\omega_n \gg g_{12}$, then the coupling terms $\hat{b}_1\hat{b}_2$ and $\hat{b}_1^\dagger\hat{b}_2^\dagger$ are fast oscillating and can thus be neglected.

We can also write the Hamiltonian in the Schrödinger picture, removing terms that do not conserve excitations. This yields

$$\hat{\mathcal{H}} = \tilde{\omega}_1\hat{b}_1^\dagger\hat{b}_1 + \tilde{\omega}_2\hat{b}_2^\dagger\hat{b}_2 + \frac{\alpha_1}{2}\hat{b}_1^\dagger\hat{b}_1^\dagger\hat{b}_1\hat{b}_1 + \frac{\alpha_2}{2}\hat{b}_2^\dagger\hat{b}_2^\dagger\hat{b}_2\hat{b}_2 + g_{12}(\hat{b}_1^\dagger\hat{b}_2 + \hat{b}_1\hat{b}_2^\dagger), \tag{1.75}$$

where we introduce the revised frequencies $\tilde{\omega}_n = \omega_n + \alpha_n$. Writing the Hamiltonian in this frame without nonconserving terms reveals the effect of the anharmonicity. In Eq. (1.75) we also assume that $\omega_n \gg \chi_n$, meaning that all terms related to the external flux are neglected. However, since χ_n depends on $\tilde{\Phi}$, which can be controlled externally, it is possible to tune χ_n such that the terms involving χ_n are not suppressed. This can drive the modes, i.e., to add excitations to the two degrees of freedom.

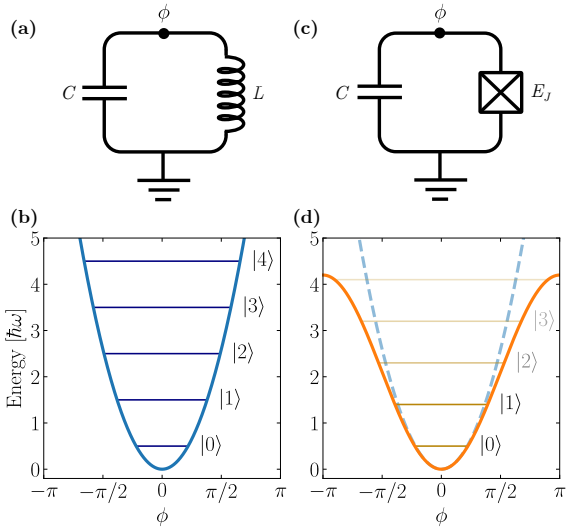

Figure 1.7: (a) *Circuit of an LC oscillator with inductance L and capacitance C. We denote the phase on the superconducting island ϕ, while the ground node has phase zero.* **(b)** *Energy potential of a quantum harmonic oscillator, as can be obtained by an LC-circuit. Here the energy levels are equidistantly spaced $\hbar\omega$ apart, where $\omega = \sqrt{1/LC}$.* **(c)** *Josephson junction qubit circuit, where the linear inductor is replaced by a nonlinear Josephson junction of energy E_J.* **(d)** *The Josephson junction changes the harmonic potential (blue dashed) into a sinusoidal potential (orange solid), yielding non-equidistant energy levels.*

1.6 Truncation

A harmonic oscillator, as one gets from a regular LC-circuit, has a spectrum consisting of an infinite number of equally spaced energy eigenstates [see Fig. 1.7(b)]. This is not desirable, as we wish to consider only the lowest states of the system in order to realize a qubit. However, when we introduce a Josephson junction instead of a linear inductor, we introduce an anharmonicity, compare Fig. 1.7(a) and (c). The anharmonicity stems from the $(\hat{b}^\dagger\hat{b}^\dagger\hat{b}\hat{b})$ terms [see Eq. (1.71)] and can be viewed as perturbations to the harmonic oscillator Hamiltonian if $|\alpha| \ll \omega$. This anharmonicity changes the spacing between the energy levels of the harmonic oscillator, making it an anharmonic oscillator [see Fig. 1.7(d)]. Formally, the anharmonicity is defined as the difference between the first and second energy gap, while we define the relative anharmonicity as the anharmonicity divided by the first energy gap

$$\alpha = E_{12} - E_{01}, \qquad \alpha_r = \frac{\alpha}{E_{01}}. \tag{1.76}$$

Note that this anharmonicity is the same factor in front of the $(\hat{b}^\dagger\hat{b}^\dagger\hat{b}\hat{b})$ terms mentioned in previous sections.

In order to operate only on the two lowest levels of the oscillator, the anharmonicity must be larger than the bandwidth of operations on the qubit. That is, if we want to drive excitation between the two lowest levels of the anharmonic oscillator, the anharmonicity

Table 1.3: *Overview of the different combinations of the annihilation and creation operators and their truncation to two-dimensional Pauli operators. Subscripts are included for the interaction terms and refer to different nodes. All constant terms are ignored.*

Annihilation and creation operators	Pauli operators
$\hat{b}^\dagger - \hat{b}$	$-i\sigma^y$
$\hat{b}^\dagger + \hat{b}$	σ^x
$(\hat{b}^\dagger - \hat{b})^2$	$-\sigma^z$
$(\hat{b}^\dagger + \hat{b})^2$	$-\sigma^z$
$(\hat{b}^\dagger + \hat{b})^3$	$3\sigma^x$
$(\hat{b}^\dagger + \hat{b})^4$	$-6\sigma^z$
$(\hat{b}_i^\dagger - \hat{b}_i)(\hat{b}_j^\dagger - \hat{b}_j)$	$-\sigma_i^y\sigma_j^y$
$(\hat{b}_i^\dagger + \hat{b}_i)(\hat{b}_j^\dagger + \hat{b}_j)$	$\sigma_i^x\sigma_j^x$
$(\hat{b}_i^\dagger + \hat{b}_i)^3(\hat{b}_j^\dagger + \hat{b}_j)$	$3\sigma_i^x\sigma_j^x$
$(\hat{b}_i^\dagger + \hat{b}_i)^2(\hat{b}_j^\dagger + \hat{b}_j)^2$	$\sigma_i^z\sigma_j^z - 2\sigma_i^z - 2\sigma_j^z$

must be larger than the amplitude of the driving field (also known as the Rabi frequency, see Section 1.7). If the anharmonicity is smaller than the amplitude of the driving field, we cannot distinguish between the energy gaps of the oscillator, and we end up driving multiple transitions in the spectrum instead of just the lowest one.

Considering this, we find that as a rule-of-thumb, the relative anharmonicity should be at least a couple of percent for the system to make an effective qubit. In actual numbers, this converts to an anharmonicity around 100-300 MHz for a qubit frequency around 3-6 GHz [55, 80]. It does not matter whether the anharmonicity is positive or negative. For transmon-type qubits, it will be negative, while it can be either positive or negative for flux-type qubits. The relative anharmonicity is proportional to $\sqrt{E_J/E_C}$, which means that this ratio must be of a certain size for the anharmonicity to have an effect. This is in contrast to what was discussed at the beginning of Section 1.4, where we argued that we required this ratio to be as low as possible to allow for the expansion of cosines. Thus we need to find a suitable regime for the ratio, E_J/E_C. This regime is usually called the transmon regime around 50-100.

The following section assumes that we have a sufficiently large anharmonicity to truncate the system into a two-level system. However, nothing is stopping us from keeping more levels, as we do in Section 1.6.2.

As an alternative to the methods for truncation presented in this thesis, black-box quantization can help determine the effective low-energy spectrum of a weakly anharmonic Hamiltonian [81–83]. This approach is instrumental when dealing with impedances in the circuit but is beyond the scope of this thesis.

1.6.1 Two-level model (qubit)

In a two-level system, which is equivalent to a qubit, we can represent the state of the system with two-dimensional vectors

$$|0\rangle \sim \begin{bmatrix} 1 \\ 0 \end{bmatrix}, \qquad |1\rangle \sim \begin{bmatrix} 0 \\ 1 \end{bmatrix}. \tag{1.77}$$

In this reduced Hilbert space, all operators can be expressed by the Pauli matrices,

$$\sigma^x = \begin{bmatrix} 0 & 1 \\ 1 & 0 \end{bmatrix}, \quad \sigma^y = \begin{bmatrix} 0 & -i \\ i & 0 \end{bmatrix}, \quad \sigma^z = \begin{bmatrix} 1 & 0 \\ 0 & -1 \end{bmatrix}, \tag{1.78}$$

and the identity, since these four matrices span all 2×2 Hermitian matrices. If we view the unitary operations as rotations in the Hilbert space, we can parameterize the superposition of the two states using a complex phase, ϕ, and a mixing angle, θ

$$|\psi\rangle = \alpha\,|0\rangle + \beta\,|1\rangle = \cos\left(\frac{\theta}{2}\right)|0\rangle + e^{i\phi}\sin\left(\frac{\theta}{2}\right)|1\rangle, \tag{1.79}$$

where $0 \leq \theta \leq \pi$ and $0 \leq \phi < 2\pi$ and $|\alpha|^2 + |\beta|^2 = 1$. With this, we can illustrate the qubit as a unit vector on the Bloch sphere, see Fig. 1.8. It is conventional to let the north pole represent the $|0\rangle$ state, while the south pole represents the $|1\rangle$ state. These lie on the z axis, called the longitudinal axis, representing the quantization axis for the states in the qubit. The x and y axes are called the transverse axes.

Solving the Schrödinger equation in Eq. (1.62) for the state in Eq. (1.79) shows that it precesses around the z axis at the qubit frequency. However, changing into a frame rotating with the frequency of the qubit, following the approach in Section 1.5.1 makes the Bloch vector stationary.

Unitary operations can be seen as rotations on the Bloch sphere, and the Pauli matrices are thus the generators of rotations. Linear operators will then be represented by 2×2 matrices as

$$M_2[\hat{O}] = \begin{bmatrix} \langle 0|\hat{O}|0\rangle & \langle 0|\hat{O}|1\rangle \\ \langle 1|\hat{O}|0\rangle & \langle 1|\hat{O}|1\rangle \end{bmatrix}. \tag{1.80}$$

In general we denote the $n \times n$ matrix representation of an operator $\hat{O}$ with $M_n[\hat{O}]$.

In order to apply this mapping to the Hamiltonian, we must map each operator in each term. As an example, we truncate the $(\hat{b}^\dagger + \hat{b})^3$ term from Table 1.3:

$$\begin{aligned}
(\hat{b}^\dagger + \hat{b})^3|0\rangle &= (\hat{b}^\dagger + \hat{b})^2|1\rangle \\
&= (\hat{b}^\dagger + \hat{b})\left(\sqrt{2}|2\rangle + |0\rangle\right) \\
&= \sqrt{6}|3\rangle + 3|1\rangle, \\
(\hat{b}^\dagger + \hat{b})^3|1\rangle &= (\hat{b}^\dagger + \hat{b})^2\left(\sqrt{2}|2\rangle + |0\rangle\right) \\
&= (\hat{b}^\dagger + \hat{b})\left(\sqrt{6}|3\rangle + 3|1\rangle\right) \\
&= \sqrt{24}|4\rangle + 6\sqrt{2}|2\rangle + 3|0\rangle.
\end{aligned}$$

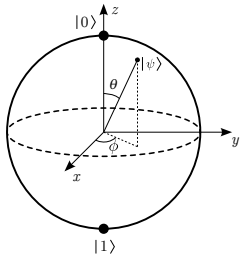

Figure 1.8: *The Bloch sphere. Each point on the Bloch sphere corresponds to a quantum state, and rotations around the sphere correspond to transformations of the state.*

Using the orthonormality of the states, we obtain the representation of the operator

$$M_2[(\hat{b}^\dagger + \hat{b})^3] = \begin{bmatrix} \langle 0|(\hat{b}^\dagger + \hat{b})^3|0\rangle & \langle 0|(\hat{b}^\dagger + \hat{b})^3|1\rangle \\ \langle 1|(\hat{b}^\dagger + \hat{b})^3|0\rangle & \langle 1|(\hat{b}^\dagger + \hat{b})^3|1\rangle \end{bmatrix} = \begin{bmatrix} 0 & 3 \\ 3 & 0 \end{bmatrix} = 3\sigma^x.$$

Truncation of the remaining terms is presented in Table 1.3.

If we consider the example circuit in Fig. 1.1 after we remove nonconserving terms as in Eq. (1.75) and assume an anharmonicity large enough for truncation to a two-level system, we obtain the following Hamiltonian:

$$\hat{\mathcal{H}} = -\frac{\tilde{\omega}_1}{2}\sigma_1^z - \frac{\tilde{\omega}_2}{2}\sigma_2^z + g_{12}(\sigma_1^+\sigma_2^- + \sigma_1^-\sigma_2^+), \tag{1.81}$$

where we define $\sigma_n^\pm = (\sigma_n^x \mp i\sigma_n^y)/2$. This Hamiltonian represents two qubits that can interact by swapping excitation between them, i.e., interacting via a swap coupling.

1.6.2 Three-level model (qutrit)

It can be desirable to truncate to the three lowest levels of the anharmonic oscillator, i.e., the three lowest states of Fig. 1.7(d). This can, e.g., be useful if one wants to study qutrit systems [43, 84, 85], or the leakage from the qubit states to higher states [**III**, 86]. In this case, the operators will be represented as 3×3 matrices. The matrix representation of the annihilation and creation operators become

$$M_3[\hat{b}^\dagger] = \begin{bmatrix} 0 & 0 & 0 \\ 1 & 0 & 0 \\ 0 & \sqrt{2} & 0 \end{bmatrix}, \quad M_3[\hat{b}] = \begin{bmatrix} 0 & 1 & 0 \\ 0 & 0 & \sqrt{2} \\ 0 & 0 & 0 \end{bmatrix}, \tag{1.82a}$$

while the number operator is

$$M_3[\hat{b}^\dagger\hat{b}] = \begin{bmatrix} 0 & 0 & 0 \\ 0 & 1 & 0 \\ 0 & 0 & 2 \end{bmatrix}, \tag{1.82b}$$

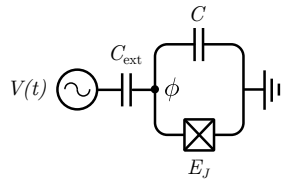

Figure 1.9: *Circuit diagram of a single transmonlike superconducting qubit capacitively coupled to a microwave drive line.*

and powers of $\hat{b}^\dagger + \hat{b}$ become

$$M_3[(\hat{b}^\dagger + \hat{b})^2] = \begin{bmatrix} 1 & 0 & \sqrt{2} \\ 0 & 3 & 0 \\ \sqrt{2} & 0 & 5 \end{bmatrix}, \tag{1.82c}$$

$$M_3[(\hat{b}^\dagger + \hat{b})^3] = \begin{bmatrix} 0 & 3 & 0 \\ 3 & 0 & 6\sqrt{2} \\ 0 & 6\sqrt{2} & 0 \end{bmatrix}, \tag{1.82d}$$

$$M_3[(\hat{b}^\dagger + \hat{b})^4] = \begin{bmatrix} 3 & 0 & 6\sqrt{2} \\ 0 & 15 & 0 \\ 6\sqrt{2} & 0 & 39 \end{bmatrix}. \tag{1.82e}$$

From Eq. (1.82e) it is clear to see the varying size of the anharmonicity, as the differences $15 - 3 = 12$ and $39 - 15 = 24$ between the levels changes. This pattern continues for higher levels and means that we can distinguish between all the levels in principle.

As we are dealing with 3×3 matrices, we can no longer use the Pauli spin-1/2 matrices as a basis for the operators. In this case, one can use the Gell-Mann matrices as a basis. However, often it is more convenient to leave the annihilation and creation operators as above. Three levels do not limit us, and it is possible to truncate the system to an arbitrary number of levels, thus creating a so-called qudit.

1.7 Microwave driving

Single-qubit rotations in superconducting circuits can be achieved by capacitive microwave driving. This section goes through the steps of analyzing a microwave-controlled transmonlike qubit and then generalizing to a d-level qudit. To this end, we consider the superconducting qubit seen in Fig. 1.9, which is capacitively coupled to a microwave source. Using the approach presented in Section 1.2.2, the Lagrangian of this circuit becomes

$$\mathcal{L} = \frac{C}{2}\dot{\phi}^2 + E_J \cos\phi + \frac{C_{\text{ext}}}{2}\left(V(t) - \dot{\phi}\right)^2, \tag{1.83}$$

where ϕ is the node flux. Expanding the last term, we obtain

$$\mathcal{L} = \mathcal{L}_0 + \frac{C_{\text{ext}}}{2}\left(V(t)^2 + \dot{\phi}^2 - 2V(t)\dot{\phi}\right), \tag{1.84}$$

where $\mathcal{L}_0$ is the static part of the Lagrangian, i.e., the two first terms of Eq. (1.83). The first term in the parenthesis is an irrelevant offset term, the second term is a change of the capacitance of the node, and the last term is our driving term. We throw away the offset term and rewrite

$$\mathcal{L} = \frac{C + C_{\text{ext}}}{2}\dot{\phi}^2 + E_J \cos\phi - C_{\text{ext}} V(t)\dot{\phi}. \tag{1.85}$$

The conjugate momentum of the node flux, ϕ, is then

$$q = (C + C_{\text{ext}})\dot{\phi} - C_{\text{ext}} V(t). \tag{1.86}$$

Doing the usual Legendre transformation, our Hamiltonian takes the form

$$\mathcal{H} = \underbrace{\frac{1}{2}\frac{1}{C + C_{\text{ext}}}q^2 - E_J \cos\phi}_{\mathcal{H}_{\text{AHO}}} + \underbrace{\frac{C_{\text{ext}}}{C + C_{\text{ext}}}V(t)q}_{\mathcal{H}_{\text{ext}}}, \tag{1.87}$$

where we denote the anharmonic oscillator part of the Hamiltonian $\mathcal{H}_{\text{AHO}}$ and the external driving part $\mathcal{H}_{\text{ext}}$. We are now ready to perform the quantization, and the driving part becomes

$$\hat{\mathcal{H}}_{\text{ext}} = \frac{i}{\sqrt{2\zeta}}\frac{C_{\text{ext}}}{C + C_{\text{ext}}}V(t)(\hat{b}^\dagger - \hat{b}). \tag{1.88}$$

Assuming a large enough anharmonicity, we can truncate the Hamiltonian into the two lowest levels

$$\hat{\mathcal{H}} = -\frac{1}{2}\omega\sigma^z + \Omega V(t)\sigma^y, \tag{1.89}$$

where ω is the qubit frequency and $\Omega = C_{\text{ext}}/[\sqrt{2\zeta}(C + C_{\text{ext}})]$ is the Rabi frequency of the transition between the ground state and the excited state. Note that the size of the Rabi frequency is limited by the size of the anharmonicity, as discussed in Section 1.6. The name Rabi frequency may confuse first as it is not the frequency of the driving microwave but rather the amplitude. However, the Rabi frequency is named so since it is equal to the frequency of oscillation between the two states in a qubit when the driving frequency, ω_{ext}, is equal to the qubit frequency, ω, i.e., when we drive the qubit 'on resonance' [78].

We now change into a frame rotating with the frequency of the qubit, also known as the interaction frame as discussed in Section 1.5. In particular we use $\mathcal{H}_0 = -\omega\sigma_z/2$ for the transformation in Eq. (1.66). In this frame, the Hamiltonian becomes

$$\hat{\mathcal{H}}_R = \Omega V(t)\left(\cos(\omega t)\sigma^y - \sin(\omega t)\sigma^x\right), \tag{1.90}$$

which is equivalent to the external driving part of the Hamiltonian in the interaction picture, i.e., $\mathcal{H}_R = \mathcal{H}^I_{\text{ext}}$. We assume that the driving voltage is sinusoidal

$$\begin{aligned} V(t) &= V_0\eta(t)\sin(\omega_{\text{ext}}t + \varphi) \\ &= V_0\eta(t)\left[\cos(\varphi)\sin(\omega_{\text{ext}}t) + \sin(\varphi)\cos(\omega_{\text{ext}}t)\right], \end{aligned} \tag{1.91}$$

where V_0 is the amplitude of the voltage, $\eta(t)$ is a dimensionless envelope function, ω_{ext} is the external driving frequency, and φ is the phase of the driving. One usually defines the in-phase component $I = \cos(\varphi)$ and the out-of-phase component $Q = \sin(\varphi)$ [55].

Inserting the voltage in Eq. (1.91) into the Hamiltonian in Eq. (1.90) and rewriting we obtain

$$\hat{\mathcal{H}}_R = \frac{1}{2}\Omega V_0 \eta(t)\big\{ -[Q\sin(\delta t) + I\cos(\delta t)]\,\sigma^x + [Q\cos(\delta t) - I\sin(\delta t)]\,\sigma^y\big\}, \tag{1.92}$$

where $\delta = \omega - \omega_{\text{ext}}$ is the difference between the qubit frequency and the driving frequency and we neglect fast oscillating terms, i.e., terms with $\omega + \omega_{\text{ext}}$, following the rotating-wave approximation. This Hamiltonian can be written very simple in matrix form

$$\hat{\mathcal{H}}_R = -\frac{1}{2}\Omega V_0 \eta(t) \begin{bmatrix} 0 & e^{-i(\delta t-\varphi)} \\ e^{i(\delta t-\varphi)} & 0 \end{bmatrix}. \tag{1.93}$$

From this, we conclude that if we apply a pulse at the qubit frequency, i.e., $\omega_{\text{ext}} = \omega$, we can rotate the state of the qubit around the Bloch sphere in Fig. 1.8. By setting $\varphi = 0$, i.e., using only the I component, we rotate about the x axis. By setting $\varphi = \pi/2$, i.e., using only the Q component, we rotate about the y axis.

1.7.1 Single-qubit gates

One of the objectives of using superconducting circuits is to be able to perform high-quality gate operations on qubit degrees of freedom [87]. Microwave driving of the qubits can be used to perform single-qubit rotation gates. To see how this works, we consider the unitary time-evolution operator of the driving Hamiltonian. At qubit frequency, i.e., $\delta = 0$, it takes the form

$$\begin{aligned} \hat{\mathcal{U}}(t) &= \exp\left[-i\int_0^t \hat{\mathcal{H}}_R(t')\,\mathrm{d}t'\right] \\ &= \exp\left[\frac{i}{2}\Theta(t)(I\sigma^x - Q\sigma^y)\right], \end{aligned} \tag{1.94}$$

where we take the Pauli operators outside the integral as there is no time dependence other than on the envelope $\eta(t)$, note that this holds only for $\delta = 0$, as here the Hamiltonian commutes with itself at different times. For nonzero δ, one needs to solve the full Dyson's series in principle [76]. Equation (1.94) is known as Rabi driving and can be used for engineering efficient single-qubit gate operations. The angle of rotation is defined as

$$\Theta(t) = \Omega V_0 \int_0^t \eta(t')\,\mathrm{d}t', \tag{1.95}$$

which depends on the circuit's macroscopic design parameters, via the coupling Ω, the envelope of the pulse, $\eta(t)$, and the amplitude of the pulse, V_0. The latter two can be controlled using arbitrary wave generators (AWGs). If one wishes to implement a π pulse, one must adjust these parameters such that $\Theta(\tau) = \pi$, where τ is the driving pulse length.

Consider a π pulse. For the in-phase case, i.e., $\varphi = 0$, the time-evolution operator takes the form

$$\hat{\mathcal{U}}_{\text{X}}(\tau) = \exp\left[\frac{i}{2}\pi\sigma^x\right] = \begin{bmatrix} 0 & 1 \\ 1 & 0 \end{bmatrix}, \tag{1.96}$$

which is a Pauli-X gate, also known as a NOT-gate, which maps $|0\rangle$ to $|1\rangle$ and vice versa [88–90], see Chapter 2 for an example of how to create a controlled version of such a gate.

This corresponds to a rotation by π radians around the x axis of the Bloch sphere. By changing the value of $\Theta(\tau)$, it is possible to change the rotation angle. Had we instead considered the out-of-phase case, i.e., $\varphi = \pi/2$ then we would have obtained a Pauli-Y gate which maps $|0\rangle$ to $i|1\rangle$ and $|1\rangle$ to $-i|0\rangle$, corresponding to a rotation around the y axis of the Bloch sphere.

A Pauli-Z gate can be implemented in one of three ways:

- By detuning the qubit frequency with respect to the driving field for some finite amount of time. This introduces an amplified phase error, which can be modeled as effective qubit rotations around the z axis [91].
- Driving with an off-resonance microwave pulse. This introduces a temporary Stark shift, which causes a phase change, corresponding to a rotation around the z axis.
- Virtual Z gates where a composition of X and Y gates rotates the qubit state around the x and y axes, which is equivalent to a rotation around the z axis [92]. This can be achieved very effectively simply by adjusting the phases of subsequent microwave gates [93].

Finally, we note that the Hadamard gate can be performed as a combination of two rotations: a π rotation around the z axis and a $\pi/2$ rotation around the y axis.

1.7.2 Generalization to qudit driving

Now let us generalize the discussion to a d-dimensional qudit. Quantizing and truncating the anharmonic oscillator part of the Hamiltonian in Eq. (1.87) to d levels, the qudit Hamiltonian becomes

$$\hat{\mathcal{H}}_{\text{osc}} = \sum_{n=0}^{d-1} \omega_n |n\rangle\langle n| , \tag{1.97}$$

where ω_n is the energy of qudit state $|n\rangle$. This is a rewriting of the $\omega \hat{b}^\dagger \hat{b}$ term and the anharmonicity term, where the anharmonicity has been absorbed into the set of ω_n. Starting from Eq. (1.88) and for simplicity setting the phase in Eq. (1.91) to $\pi/2$ such that $V(t) = V_0 \cos(\omega_{\text{ext}} t)$, we can move to the rotating frame as was also done above for the qubit using Eq. (1.66). We choose the frame rotating with the external driving frequency

$$\mathcal{H}_0 = \sum_{n=0}^{d-1} n\, \omega_{\text{ext}} |n\rangle\langle n| , \tag{1.98}$$

which is contrary to for the qubit, where we rotated into a frame equal to the qubit frequency. We see that for a qubit ($d = 2$) we get $\mathcal{H}_0 = -\omega_{\text{ext}} \sigma_z/2$ up to a global constant, which we could have also chosen to use above, instead of the qubit frame.

Applying Eq. (1.66) to the qudit Hamiltonian in Eq. (1.97), we get

$$\hat{\mathcal{H}}_{\text{osc},R} = \sum_{n=0}^{d-1} (\omega_n - n\omega_{\text{ext}}) |n\rangle\langle n| . \tag{1.99}$$

The same transformation is performed on $\mathcal{H}_{\text{ext}}$ by using the standard expansion of the bosonic operators. By expanding the cosine in the voltage drive using Euler's formula, the total Hamiltonian in the rotating frame can be found. It becomes

$$\hat{\mathcal{H}}_R = \sum_{n=0}^{d-1} \delta_n |n\rangle\langle n| + i\Omega_n \left(|n+1\rangle\langle n| - |n\rangle\langle n+1|\right), \tag{1.100}$$

where $\delta_n = \omega_n - n\omega_{\text{ext}}$ is the detuning of the nth state relative to the ground state driven by the external field and

$$\Omega_n = \sqrt{n+1}\Omega = \sqrt{n+1}\frac{C_{\text{ext}}}{C+C_{\text{ext}}}\frac{V_0}{\sqrt{2\zeta}} \tag{1.101}$$

is the Rabi frequency of the nth transition. Thus, we achieve great control over this specific qudit transition by using a single drive. Transitions between neighboring qudit states can be performed simultaneously using a multimode driving field. Note that the i in the second term of Eq. (1.100) comes from the choice of $\varphi = \pi/2$, which can, of course, be changed if desired.

The external field enables transitions between two states in the qudit if the effective detuning, $\Delta_{n,n+1}$, is small compared to the size of the Rabi frequency, Ω_n. The effective detuning between the nth and $(n+1)$th states is the difference between the detuning of the two states:

$$\Delta_{n,n+1} = \delta_{n+1} - \delta_n = \omega_{n+1} - \omega_n - \omega_{\text{ext}}, \tag{1.102}$$

from which we see that the frequency of the external field, ω_{ext}, has to match the energy difference between the two states, $\omega_{n+1} - \omega_n$, for the driving to be efficient.

As mentioned in Section 1.6, leakage to other states when driving between two states depends on the size of the anharmonicity. This can be understood from Eq. (1.102). For a small anharmonicity, $\Delta_{n,n+1}$ is approximately the same for all n since ω_n will be approximately the same for all n; thus, it becomes difficult to single out the desired transition we want to drive since the driving frequency, ω_{ext}, will overlap with multiple transition frequencies. Luckily, tailored control pulse methods such as derivative removal by adiabatic gate (DRAG) and its improvements [90, 94] can reduce this leakage significantly, which allows for relative anharmonicities of just a couple of percent. The topic of tailored control pulses is beyond the scope of this discussion, and we refer to the cited works.

1.8 Coupling of modes

In our central example of Fig. 1.1, we considered direct inductive coupling. While this coupling is relatively straightforward theoretically, it is not easy to implement experimentally. We, therefore, now consider more straightforward ways to couple qubits. By coupling qubits, we also open up the possibility of implementing two-qubit gates. Examples of more sophisticated approaches to coupling qubits are discussed in Section 1.10.3.

1.8.1 Capacitive coupling

The simplest form of coupling, both experimentally and theoretically, is arguably capacitive coupling. Consider two transmonlike qubits coupled by a single capacitor with

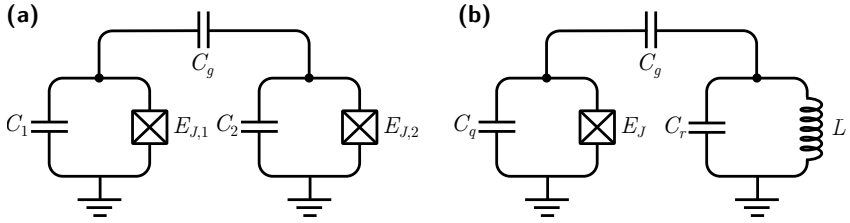

Figure 1.10: (a) *Two transmonlike qubits coupled by a single capacitor with capacitance C_g, resulting in a static coupling between the modes.* **(b)** *A transmonlike qubit coupled to a linear resonator via a capacitor of capacitance C_g.*

capacitance C_g, as seen in Fig. 1.10(a). Note the similarities between this coupling and the circuit in Fig. 1.1. As we see, the resulting Hamiltonian of Fig. 1.10(a) is close to the Hamiltonian in Eq. (1.75). However, capacitive coupling is much simpler to achieve experimentally.

The Hamiltonian is easily found following the approach in Section 1.2.2

$$\mathcal{H} = \frac{1}{2}\boldsymbol{q}^T\boldsymbol{C}^{-1}\boldsymbol{q} - E_{J,1}\cos\phi_1 - E_{J,2}\cos\phi_2, \tag{1.103}$$

where $\boldsymbol{q} = (q_1, q_2)^T$ is the vector of conjugate momentum and the capacitance matrix is

$$\boldsymbol{C} = \begin{bmatrix} C_1 + C_g & -C_g \\ -C_g & C_2 + C_g \end{bmatrix}, \tag{1.104}$$

which is invertible

$$\boldsymbol{C}^{-1} = \frac{1}{C_\Sigma}\begin{bmatrix} C_2 + C_g & C_g \\ C_g & C_1 + C_g \end{bmatrix} \simeq \begin{bmatrix} \frac{1}{C_1} & \frac{C_g}{C_1 C_2} \\ \frac{C_g}{C_1 C_2} & \frac{1}{C_2} \end{bmatrix}, \tag{1.105}$$

where $C_\Sigma = \det(C) = C_1C_2 + C_1C_g + C_2C_g$. In the approximation of the second step above, we assume that the shunting capacitances are larger than the coupling capacitance, $C_n \gg C_g$, as is usually the case. After rewriting to interacting harmonic oscillators, the diagonal elements of $\boldsymbol{C}^{-1}$ contribute to the respective modes with the frequencies

$$\omega_n = \sqrt{E_{C,n}E_{J,n}} + \alpha_n, \tag{1.106}$$

where the effective capacitive energy is $E_{C,n} = (C_n + C_g)/C_\Sigma$ and the anharmonicity is $\alpha_n = -E_{C,n}$. The off-diagonal elements on the other hand contribute to the interaction. The interaction term of the Hamiltonian is

$$\mathcal{H}_{\text{int}} = \frac{C_g}{C_\Sigma} q_1 q_2. \tag{1.107}$$

Quantizing the Hamiltonian and changing into annihilation and creation operators the interaction part takes the form

$$\mathcal{H}_{\text{int}} = g_{12}\left(\hat{b}_1^\dagger \hat{b}_2 + \hat{b}_2 \hat{b}_1^\dagger\right), \tag{1.108}$$

where we remove terms that do not conserve the total number of excitations by using the RWA. The coupling strength is

$$g_{12} = \frac{C_g}{2C_\Sigma\sqrt{\zeta_1\zeta_2}}, \tag{1.109}$$

where ζ_n is the impedance in Eq. (1.56). Note the similarity with Eq. (1.61c) if one defines $E_{C,12} = C_g/2C_\Sigma$. This is called a transverse coupling since the interaction Hamiltonian only has nonzero matrix elements in off-diagonal entries. This is contrary to the longitudinal coupling discussed in Section 1.8.4.

1.8.2 Two-qubit gates

As with the single-qubit gates in Section 1.7.1, we can calculate the time-evolution operator, as in Eq. (1.94) of the interacting Hamiltonian in order to determine the gate operation. However, contrary to microwave driving, we cannot directly turn the interaction on and off. Luckily there are several approaches to this problem, the simplest being tuning the two qubits in and out of resonance such that the interaction terms time average to zero due to the RWA discussed in Section 1.5. Examples of more complex and tunable coupling schemes are discussed Section 1.10.3.

Consider the interaction part of the Hamiltonian in Eq. (1.108); we calculate the time-evolution operator of the two-level truncation of this

$$\begin{aligned}\hat{\mathcal{U}}(t) &= \exp\left[i\int_0^t \eta(t')\hat{\mathcal{H}}_{\text{int}}\mathrm{d}t'\right] = \exp\left[i\Theta(t)(\sigma_1^+\sigma_2^- + \sigma_1^-\sigma_2^+)\right] \\ &= \begin{bmatrix} 1 & 0 & 0 & 0 \\ 0 & \cos\Theta(t) & -i\sin\Theta(t) & 0 \\ 0 & -i\sin\Theta(t) & \cos\Theta(t) & 0 \\ 0 & 0 & 0 & 1 \end{bmatrix},\end{aligned} \tag{1.110}$$

where $\eta(t)$ is the envelope constructed to correspond to tuning the two qubits in and out of resonance, and we assume that this is the only part of the integral with time dependence. We also assume that the Hamiltonian commutes with itself at different times. The coupling angle is given as

$$\Theta(t) = g\int_0^t \eta(t')\mathrm{d}t', \tag{1.111}$$

which depends on the coupling strength, g, and the envelope $\eta(t)$. By setting $\Theta(\tau) = \pi/2$ we obtain the iSWAP gate from Eq. (1.110) and taking $\Theta(\tau) = \pi/4$ we find the $\sqrt{i\text{SWAP}}$ gate.

Note that a similar procedure to the iSWAP gate can be used to create a CZ gate [95].

1.8.3 Linear resonators: control and measurement

So far, we have considered how to engineer anharmonic oscillators and truncate them into qubits and how to drive the qubits. However, for a qubit to be useful, we must also be able to control it and perform measurements on it [96]. These two things can be accomplished by coupling the qubit to a linear resonator, which is a simple harmonic oscillator [97].

Consider, therefore, the circuit presented in Fig. 1.10(b) consisting of a transmonlike qubit capacitively coupled to an LC oscillator or linear resonator. This circuit is similar to the example circuit presented in Fig. 1.10(a) and the analysis up until truncation is identical with $1 \to q, 2 \to r$, and only one anharmonicity meaning that we must change $-E_{J,2}\cos\phi_2$ to $\phi_r^2/2L$ in Eq. (1.103). Thus, we can truncate only the mode with the anharmonicity, which results in the following Hamiltonian

$$\hat{\mathcal{H}}_{\text{JC}} = \omega_r \hat{b}^\dagger \hat{b} + \frac{1}{2}\omega_q \sigma^z + g\left(\sigma^+ \hat{b} + \sigma^- \hat{b}^\dagger\right), \tag{1.112}$$

where $\hat{b}^\dagger$ and $\hat{b}$ are the creation and annihilation operators for the linear resonator, σ^z is the z Pauli operator of the qubit, and $\sigma^\pm$ represents the process of exciting and de-exciting the qubit. The qubit frequency is given as in Eq. (1.106), the resonator frequency is given by

$$\omega_r = \sqrt{E_{C,r}/L}, \tag{1.113}$$

and the coupling strength is given as in Eq. (1.109)

The Hamiltonian in Eq. (1.112) is known as the Jaynes-Cummings (JC) Hamiltonian, which was initially used in quantum optics to describe a two-level atom in a cavity [98–100]. Since then, the model has found application in many areas of physics, including superconducting electronic circuits, where a qubit is typically coupled to a transmission line resonator [101–109]. Because the Jaynes-Cummings Hamiltonian comes from quantum optics and cavity quantum electrodynamics (cavity QED), coupling between superconducting circuits and linear resonators is often denoted circuit QED.

Consider the limit where the qubit frequency is far detuned from the resonator frequency compared to the coupling rate and resonator linewidth $\kappa = \omega_r/Q$, where Q is the quality factor of the resonator, i.e., $\Delta = |\omega_r - \omega_q| \gg g, \kappa$. This is known as the dispersive limit since there is no direct exchange of energy between the two systems, i.e., only dispersive interactions between the resonator and the qubit occur. Using second-order perturbation theory, we see that the qubit and the resonator change each other's frequencies [110–112].

In the dispersive regime the Jaynes-Cummings Hamiltonian can be approximately diagonalized using the unitary transformation $e^{\hat{S}}$ where $\hat{S} = \lambda(\sigma^+ \hat{b} - \sigma^- \hat{b}^\dagger)$ and $\lambda = g/\Delta$ is a small parameter. This transformation is called a Schrieffer-Wolff transformation [113]. Using the Baker-Campbell-Hausdorff formula [76] to second order in λ we find the Hamiltonian in the dispersive regime becomes

$$\hat{\mathcal{H}}_{\text{disp}} = e^{\hat{S}}\hat{\mathcal{H}}_{\text{JC}}e^{-\hat{S}} = (\omega_r + \chi\sigma^z)\hat{b}^\dagger\hat{b} + \frac{1}{2}\tilde{\omega}_q\sigma^z, \tag{1.114}$$

where we define $\chi = g^2/\Delta$ as the qubit dependent frequency shift or dispersive shift. The qubit frequency is Lamb shifted to $\tilde{\omega}_q = \omega_q + \chi$, induced by the vacuum fluctuations in the resonator. Note that Eq. (1.114) is derived for a two-level atom/qubit. Taking the second excited state into account modifies the expression for the shift into

$$\chi = -\frac{g_{01}^2}{\Delta}\left(\frac{1}{1+\Delta/\alpha}\right), \tag{1.115}$$

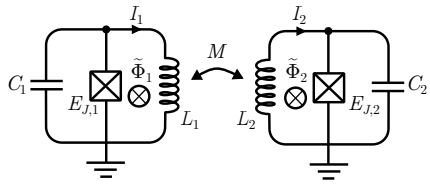

Figure 1.11: *Mutual inductive coupling between two modes.*

where g_{01} is the coupling rate between the 0 and 1 state of the qubit and α is the anharmonicity of the qubit, Eq. (1.76).

One can interpret the dispersive qubit-resonator interaction in two ways. Either as a shift of the qubit frequency by a quantity proportional to the photon population of the resonator $2\chi\langle\hat{b}^\dagger\hat{b}\rangle$ or as a qubit-dependent pull of the resonator frequency, $\omega_r \to \omega_r \pm \chi$.

In the first interpretation, the bare qubit frequency is modified by a Lamb shift and an additional amount proportional to the number of photons populating the resonator. This is known as the ac Stark shift. It has the consequence that fluctuations in the photon number of the resonator induce small shifts in the qubit frequency, which brings it slightly out of its rotating frame and causes dephasing [114–120]. Therefore, in an experiment, it is vital to reduce photon-number fluctuations of the resonator, e.g., by keeping the process properly thermalized.

In the second interpretation, the resonator frequency depends on the qubit's state. This means that it is possible to make a quantum nondemolition (QND) measurement of the qubit by shinning microwaves into the resonator at a frequency close to ω_r and then measuring the transmitted signal using standard homodyne techniques [121]. However, the approximation in Eq. (1.114) is only valid in the small-photon limit, i.e., when the resonator photon number, $\hat{N} = \hat{b}^\dagger\hat{b}$ is less than the critical photon number $N_c = \Delta^2/4g^2$. This sets an upper limit to the resonator power as a probe while maintaining the conditions for a QND measurement. However, this is not the whole story; Ref. [108] has shown that level crossings with other states of the qubit-resonator system induce state transitions which the Jaynes-Cummings model can explain. This is beyond the scope of our discussion, and we refer to the cited work for more information.

In the other limit, when the detuning between the qubit and the resonator frequency is small compared to the coupling rate, i.e., $\Delta \ll g$, we obtain a hybridization of the energy levels of the two systems. This opens up for a Rabi mode splitting, where each transition between the qubit and the resonator splits into two states with distance $\sqrt{N}g/\pi$ where N denotes the resonator mode, i.e., the photon number. Thus excitation is coherently swapped between the two systems. While this cannot be used to perform measurements on the qubit, it can be used to mediate couplings between two qubits by coupling another qubit to the resonator [122, 123]. We do not dive deeper into the details of measurements and couplings to linear resonators. For an experimental-minded review, see, e.g., Ref. [55].

1.8.4 Inductive coupling

So far, we have considered only direct inductance to coupling two qubits. This section considers the mutual inductance of two modes to couple the modes. Consider, therefore, the two circuits in Fig. 1.11, consisting of a Josephson junction, a capacitor, and a linear inductor. Such circuits are known as rf SQUIDs [124]. Each of the circuits has the following Hamiltonian

$$\hat{\mathcal{H}}_j = 4E_{C,j}\hat{n}_j^2 + \frac{1}{2L_j}\hat{\phi}_j^2 - E_{J,j}\cos(\hat{\phi}_j + \tilde{\Phi}_j). \tag{1.116}$$

If two such circuits are brought into proximity of each other, they will share a mutual inductance, yielding an interaction Hamiltonian

$$\hat{\mathcal{H}}_{\text{int}} = M_{12}\hat{I}_1\hat{I}_2 = M_{12}I_{c1}\sin(\hat{\phi}_1 + \tilde{\Phi}_j)I_{2c}\sin(\hat{\phi}_2 + \tilde{\Phi}_j), \tag{1.117}$$

where $\hat{I}_j$ is the current operator of the Josephson junction, see Eq. (1.11). The mutual inductance M_{12} between the two circuits depends on the relative geometrical placement of the circuits. This can be increased, e.g., by overlapping the circuits [125] or by letting them share the same wire or Josephson-junction inductor [126–129].

Consider now the case of no external flux, i.e., $\tilde{\Phi} = 0$. If we expand the potential to fourth-order, the interaction Hamiltonian takes the form

$$\hat{\mathcal{H}} = M_{12}\left[\hat{\phi}_1\hat{\phi}_2 - \frac{1}{36}(\hat{\phi}_1\hat{\phi}_2^3 + \hat{\phi}_1^3\hat{\phi}_2)\right]. \tag{1.118}$$

Truncating into a two-level model using Tables 1.2 and 1.3 we find that the coupling becomes transverse

$$\hat{\mathcal{H}}_{\text{int}} = g_x\sigma_1^x\sigma_2^x, \tag{1.119}$$

where the coupling constant is

$$g_x = \frac{1}{2}M_{12}\sqrt{\zeta_1\zeta_2}\left[1 - \frac{1}{24}(\zeta_1 + \zeta_2)\right], \tag{1.120}$$

with impedances given by Eq. (1.56).

Consider now an external flux of $\tilde{\Phi} = \pi/2$. In this case, the sine terms obtain a phase, effectively changing the terms into cosines. Expanding these to second-order yields

$$\hat{\mathcal{H}}_{\text{int}} = \frac{M_{12}}{4}\left[-(\hat{\phi}_1^2 + \hat{\phi}_2^2) + \frac{1}{144}(\hat{\phi}_1^4 + \hat{\phi}_2^4) + \hat{\phi}_1^2\hat{\phi}_2^2\right], \tag{1.121}$$

where we recognize the two first terms as corrections to the qubit frequencies, the following two terms as corrections to the anharmonicities, and finally, the last term is the interaction term. Considering only the last term and truncating into a two-level model we find (see Tables 1.2 and 1.3)

$$\hat{\mathcal{H}}'_{\text{int}} = g_z(\sigma_1^z\sigma_2^z - 2\sigma_1^z - 2\sigma_2^z). \tag{1.122}$$

The first term is a longitudinal coupling between the two qubits with coupling constant

$$g_z = \frac{1}{16}M_{12}\zeta_1\zeta_2. \tag{1.123}$$

It is called longitudinal because all off-diagonal matrix elements are zero, contrary to transverse coupling. Longitudinal coupling can be used to create entanglement without exchanging energy between the modes by enabling a so-called phase gate [55, 122, 130]. From the last two terms in Eq. (1.122), we see that we obtain further corrections to the qubit frequencies.

1.9 Noise and decoherence

So far, we have considered only closed quantum systems, i.e., systems without interaction with the environment. This is usually a good approximation as we are dealing with cryogenic and thus isolated superconducting circuits. However, even in the best experimental setups, random and uncontrollable processes in the environment surrounding the system do occur. These are sources of noise and lead to decoherence of the quantum system. It is, therefore, necessary to develop a formalism to treat this theoretically as well. We assume that the Hamiltonian of the system and the environment is separable and has the form

$$\hat{\mathcal{H}} = \hat{\mathcal{H}}_{\text{sys}} + \hat{\mathcal{H}}_{\text{env}} + \nu \hat{S} \cdot \hat{\lambda}, \tag{1.124}$$

where $\hat{\mathcal{H}}_{\text{sys}}$ is the Hamiltonian of the system, $\hat{\mathcal{H}}_{\text{env}}$ is the Hamiltonian of the environment. The interaction strength between the system and the environment is given by ν. In contrast, $\hat{S}$ is an operator within the system Hamiltonian $\hat{\mathcal{H}}_{\text{sys}}$ and $\hat{\lambda}$ represents the noisy environment which produces fluctuations $\delta\lambda$.

The treatment of open quantum systems is a whole subject on its own, and a complete treatment is beyond the scope of this thesis. We, therefore, present only a method for modeling noise in qubit systems. For a more extensive treatment of open quantum systems, see, e.g., Ref. [131], and for an introduction on how to treat noise in an experiment see, e.g., Ref. [55].

1.9.1 Bloch-Redfield model

Consider an arbitrary state on the Bloch sphere as in Eq. (1.79). The density matrix for such a pure state is [87]

$$\rho = |\psi\rangle\langle\psi| = \frac{1}{2}(I + \boldsymbol{a} \cdot \boldsymbol{\sigma}) = \begin{bmatrix} |\alpha|^2 & \alpha\beta^* \\ \alpha^*\beta & |\beta|^2 \end{bmatrix}, \tag{1.125}$$

where I is the identity matrix, $\boldsymbol{a}$ is the Bloch vector, and $\boldsymbol{\sigma} = (\sigma^x, \sigma^y, \sigma^z)$ is the vector of Pauli spin matrices. If ρ represents a pure state, ψ, then $\operatorname{tr}\rho^2 = 1$ and the Block vector becomes a unit vector, $\boldsymbol{a} = (\sin\theta\cos\phi, \sin\theta\sin\phi, \cos\theta)$, where θ and ϕ are the angles of the Bloch vector. If, on the other hand, $|\boldsymbol{a}| < 1$ the density matrix ρ represents a mixed state with $\operatorname{tr}\rho^2 < 1$. In this case the Bloch vector terminates at points inside the unit sphere.

In the Bloch-Redfield formulation of two-level systems, sources of noise are weakly coupled to the system with short correlation times compared to the system dynamics [131–134]. The noise in this formulation is determined by the longitudinal relaxation rate and the transverse relaxation rate.

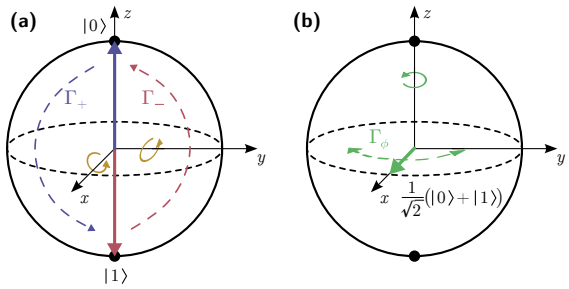

Figure 1.12: *Bloch-sphere representation of noise.* **(a)** ***Longitudinal relaxation*** *is the result of energy exchange between the qubit and the environment. Transverse noise couples to the qubit and drives a rotation (transition) around an axis in the x-y plane. Longitudinal relaxation is driven by energy emission to the environment, Γ_- and absorption of energy from the environment, Γ_+. For a typical superconducting qubit, the temperature is much lower than the qubit's frequency, $k_B T \ll \hbar\omega$, which suppresses the absorption rate, such that $\Gamma_1 \simeq \Gamma_-$.* **(b)** ***Pure dephasing*** *is the result of longitudinal noise that drives a rotation around the z axis. Due to stochastic frequency fluctuations, a Bloch vector will diffuse both clockwise and counterclockwise around the z axis parallel to the equator.*

Longitudinal relaxation

The longitudinal relaxation rate, $\Gamma_1 = 1/T_1$, describes depolarization along the qubit quantization axis, often referred to as "energy decay" or "energy relaxation", which is why it is often referred to as the relaxation time. Longitudinal relaxation is caused by transverse noise, via the x or y axis on the Bloch sphere, see Fig. 1.12(a). Depolarization of the superconducting circuit occurs due to the exchange of energy with the environment, leading both to excitation and relaxation of the qubits, meaning that one can write

$$\Gamma_1 = \Gamma_+ + \Gamma_-. \tag{1.126}$$

Due to Boltzmann statistics and the fact that superconducting qubits are operated at low temperatures ($T \lesssim 20\,\text{mK}$) and with a qubit frequency in the GHz regime, the qubits generally lose energy to the environment, meaning that the excitation rate Γ_+ is suppressed exponentially as

$$\frac{\Gamma_+}{\Gamma_-} = e^{-\beta\omega}, \tag{1.127}$$

where $\beta = 1/k_B T$ is the inverse of the Boltzmann constant multiplied with the temperature. Note, however, that empirically we often see a stray population of the excited state much higher than expected from this theory. From Maxwell-Boltzmann statistics, we would expect a thermal population of the excited state of $P_{|1\rangle} \sim 10^{-5}\%$, but the measured excited-state population is often orders of magnitudes higher at around 1% [135].

The longitudinal relaxation rate can be determined using Fermi's golden rule

$$\Gamma_1 = \frac{1}{\hbar^2} |\langle 0|\hat{S}|1\rangle|^2 S_\lambda(\omega_q), \tag{1.128}$$

where $\hat{S}$ is the transverse coupling of the qubit to the environment, i.e., a coupling of the

type σ^x or σ^y. The qubit frequency is denoted ω_q. The noise power spectral density

$$S_\lambda(\omega) = \int_{\infty}^{-\infty} \mathrm{d}t \langle \hat{\lambda}(t)\hat{\lambda}(0)\rangle e^{-i\omega t}, \tag{1.129}$$

characterizes the frequency distribution of the noise power for a stationary noise process $\hat{\lambda}$. Note that the Wiener-Khintchine theorem states that $S_\lambda(\omega)$ is the Fourier transform of the autocorrelation function $c_\lambda(t) = \langle \hat{\lambda}(t)\hat{\lambda}(0)\rangle$ of the noise source λ [136, 137].

The longitudinal relaxation rate can be measured by preparing the qubit in state $|1\rangle$ (e.g., using a π pulse as in Section 1.7) and then making multiple measurements of the qubit excited-state population at a set of subsequent times [55].

Transverse relaxation

The transverse relaxation time

$$\Gamma_2 = \frac{1}{T_2} = \frac{\Gamma_1}{2} + \Gamma_\phi \tag{1.130}$$

describes the loss of coherence of a superposition. As seen in Eq. (1.130), it is caused both by transverse noise, which leads to energy (longitudinal) relaxation of the excited-state component of the superposition state and by longitudinal noise, which causes fluctuations of the qubit frequency and leads to pure dephasing, see Section 1.9.1 below. Note that the sum in Eq. (1.130) is only valid for weak noise that also is only correlated at short times [138].

We introduce transverse relaxation as it is a measurable quantity, contrary to pure dephasing, which can only be inferred using Eq. (1.130). Transverse relaxation can be measured using Ramsey interferometry [55, 139]. In Ramsey interferometry, a $\pi/2$ pulse rotates the Bloch vector from $|0\rangle$ to the equator of the Bloch sphere. If we know the qubit frequency perfectly, it should remain stationary at the equator, and if we apply another $\pi/2$ pulse at some time later, we should measure $|1\rangle$. However, if our knowledge of the qubit frequency and our assumed frame does not match the qubit's actual rotation frame, then the state will not remain stationary at the equator of the Bloch sphere after the first $\pi/2$ pulse is applied. Instead, it will precess around the equator at a frequency equal to the difference between the assumed frame and the actual qubit frequency. This means that if we perform two $\pi/2$ pulses with variable delay in between, we should observe oscillations in the measured state of the qubit. In reality, one often chooses a frame that is intentionally detuned from the qubit frequency so that these oscillations are observed even for the perfectly calibrated qubit. This means that an error in qubit frequency will result in a difference from the expected oscillation frequency [140]. For simple Markovian noise, these oscillations are exponentially damped with characteristic time T_2 [55].

Pure dephasing

The pure dephasing rate Γ_ϕ describes depolarization in the x-y plane of the Bloch sphere. It is referred to as "pure dephasing" to distinguish it from other phase-breaking processes such as energy excitation or relaxation. Pure dephasing is caused by longitudinal noise that couples to the qubit via the z axis. This longitudinal noise causes the qubit frequency,

ω, to fluctuate such that it is no longer equal to the interaction frame frequency, causing the Bloch vector to precess forward or backward in the interacting frame as seen in Fig. 1.12(b).

To lowest order, the pure dephasing rate is orthogonal to the difference between the two diagonal matrix elements [48, 131]

$$\Gamma_\phi = \frac{1}{\hbar^2}\left(|\langle 0|\hat{S}|0\rangle - \langle 1|\hat{S}|1\rangle|^2\right) S_\lambda(0), \tag{1.131}$$

where $\hat{S}$ is the longitudinal coupling of the qubit to the environment, i.e., a coupling of the type σ^z. This means that pure dephasing disappears if $\langle 0|\hat{\mathcal{H}}_{\text{env}}|0\rangle = \langle 1|\hat{\mathcal{H}}_{\text{env}}|1\rangle$. For superconducting circuits, this can often be realized by tuning the system to the so-called "sweet spot" using external flux biasing. This means that the transverse relaxation becomes approximately half the longitudinal relaxation rate as in Eq. (1.130). Thus decreasing the longitudinal relaxation rate becomes the main focus when developing qubits to increase the lifetime. However, in reality, pure dephasing will never disappear entirely due to effects beyond the linear theory, such as higher-order corrections, other noise sources, or nonmarkovian effects. Nevertheless, these effects are small at the "sweet spot", and therefore relaxation noise will often be the dominant source of noise.

Note that pure dephasing is, in principle, reversible as there is no energy exchange with the environment, which means that it can be undone without destroying any quantum information [141]. It is also worth noting that qubit dephasing is subject to broadband noise since noise at any frequency can modify the qubit frequency and cause dephasing.

The impact of noise alters the density matrix of Eq. (1.125) giving us the Bloch-Redfield density matrix [142]

$$\rho_{\text{BR}} = \begin{bmatrix} 1 + (|\alpha|^2 - 1)e^{-\Gamma_1 t} & \alpha\beta^* e^{-i\delta t} e^{-\Gamma_2 t} \\ \alpha^*\beta e^{-i\delta t} e^{-\Gamma_2 t} & |\beta|^2 e^{-\Gamma_1 t} \end{bmatrix}. \tag{1.132}$$

Note that the longitudinal relaxation rate influences the diagonal, while the transverse influences only the off diagonal. We also include the phase difference $\delta = \omega_q - \omega_{\text{ext}}$ between the qubit frequency, ω_q, and the rotating frame frequency, ω_{ext}, which is needed in order to perform Ramsey interferometry.

1.9.2 Master equation

As we are interested in the effect of noise on the dynamics of the system, we consider a so-called *master equation* for the system. A master equation describes the time evolution of a system (in our case, an electrical circuit) where we model the system as an ensemble of states described by a density matrix ρ, and where we can determine the transition between the states by a transition matrix [131].

From the time-dependent Schrödinger equation in Eq. (1.62), we can derive a master equation for the closed system called the Liouville-von Neumann equation

$$\dot{\rho}(t) = -i[\hat{\mathcal{H}}, \rho(t)], \tag{1.133}$$

where $\hat{\mathcal{H}}$ is the Hamiltonian of the system, and ρ is the density matrix in Eq. (1.125). Note how it resembles Heisenberg's equations of motion in Eq. (1.67), but with a different sign

since the density matrix is a dynamical variable, i.e., it is an operator in contrast to a quantum state or wave function.

As we are interested in the effect of noise, we must add other terms to the Liouville-von Neumann equation. For a system that is weakly coupled to the environment, the evolution is described by the Lindblad master equation [48, 131, 143]

$$\dot{\rho}(t) = -i[\hat{\mathcal{H}}, \rho(t)] + \sum_i \Gamma_i \left(\hat{L}_i \rho \hat{L}_i^\dagger - \frac{1}{2}\{\hat{L}_i \hat{L}_i^\dagger, \rho\} \right), \tag{1.134}$$

where $\{\cdot,\cdot\}$ is the anticommutator, and $\hat{L}_i$ are the so-called jump operators representing the interaction between the system and the environment.

For the case of a two-level model with both longitudinal and transverse relaxation weakly coupled to the environment, the Lindblad master equation takes the form

$$\begin{aligned} \dot{\rho}(t) = &-i[\hat{\mathcal{H}}, \rho(t)] \\ &+ \Gamma_- \left(\sigma_- \rho \sigma_+ - \frac{1}{2}\{\hat{\sigma}_- \hat{\sigma}_+, \rho\} \right) \\ &+ \Gamma_+ \left(\sigma_+ \rho \sigma_- - \frac{1}{2}\{\hat{\sigma}_+ \hat{\sigma}_-, \rho\} \right) \\ &+ \Gamma_\phi \left(\sigma_z \rho \sigma_z - \rho \right), \end{aligned} \tag{1.135}$$

where the decoherence rates, Γ_i, can be found in Eqs. (1.126) and (1.130). Equation (1.134) can be used to simulate a system including noise and is usually solved numerically using, e.g., QuTiP [144].

1.10 Examples

This section presents some examples of more or less well-known superconducting qubits. We start from some simple, early single-qubit designs, then move to the transmon and flux qubit, and finally, we discuss couplings between qubits. In Fig. 1.13 we present an overview of the qubits discussed in the examples.

There are four fundamental types of qubits: Phase qubits, charge qubits, flux qubits, and quasicharge qubits. These qubits can be ordered in pairs according to the behavior of quantum fluctuation in the Cooper pair condensate. Charge qubits with single-charge tunneling are dual to flux qubits with single-flux tunneling, while phase qubits with phase oscillation are dual to the quasicharge qubits with quasicharge oscillations. These fundamental qubits can be seen in Fig. 1.13.

The most straightforward realization of a superconducting qubit is a phase qubit. It is a current-biased Josephson junction, which essentially is just a Josephson junction with a current applied across it. It operates in the so-called phase regime where $E_C \ll E_J$. In this regime, the Josephson tunneling dominates over the charging of the capacitor, making the anharmonicity relatively small. This can be interpreted as a low kinetic (capacitive) energy compared to the potential (inductive) energy. The bias current introduces the anharmonicity, and adjusting the bias current closer to the critical current of the Josephson junction increases the anharmonicity. The fact that one can tune the anharmonicity

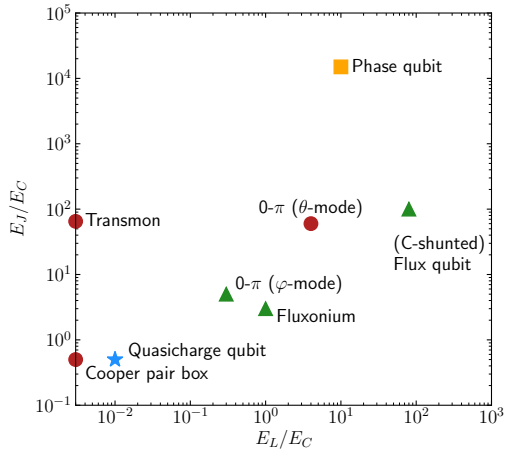

Figure 1.13: *Parameter space of the "qubit zoo." The qubits are plotted according to their effective Josephson energy, E_J, and inductive energy, E_L, both normalized by their effective capacitive energy, E_C. The marker indicates the type of qubits, with a yellow square indicating the phase qubit, red dots indicating charge qubits, green triangles indicating flux qubits, and a blue star for the quasicharge qubit. Note that the placement of the qubits is only approximate as the effective energies are not definitive. Note that the 0-π qubit is plotted for each mode; the φ mode works similar to a fluxonium qubit, and the θ mode works similarly to the transmon qubit.*

dynamically is a strength of this qubit. However, the phase qubit has a relatively large decoherence noise, and we do not further detail the phase qubit as it is rarely used in modern circuit designs. For more details, see Refs. [71, 145].

1.10.1 Charge qubits

Central types of qubits are the so-called charge qubits. These have their name from the fact that the basis states of the qubit are charge eigenstates, meaning that they are only dependent on the number of excess Cooper pairs in a disconnected superconducting island and primarily independent of the node fluxes. We start from the single Cooper pair box and move on to the transmon qubit based on the Cooper pair box.

Single Cooper pair box

In 1997 the first charge qubit, known as the single Cooper pair box (SCPB), was invented [146–148]. As with the phase qubit, it is not used in modern qubit implementations due to bad coherence times. However, we detail this qubit as it forms the basis for the renowned transmon qubit and is a nice example of how to analyze a circuit.

The SCPB consists of a Josephson junction, with energy E_J, and a capacitor with capacitance C_g in series, yielding a superconducting island in between them. A parasitic capacitance C_J is included in the Josephson junction. This is a lumped-circuit element representation of the natural capacitance that the junction will have by way of construction. The circuit is biased with a gate voltage V_g over the capacitor, making it possible to transfer

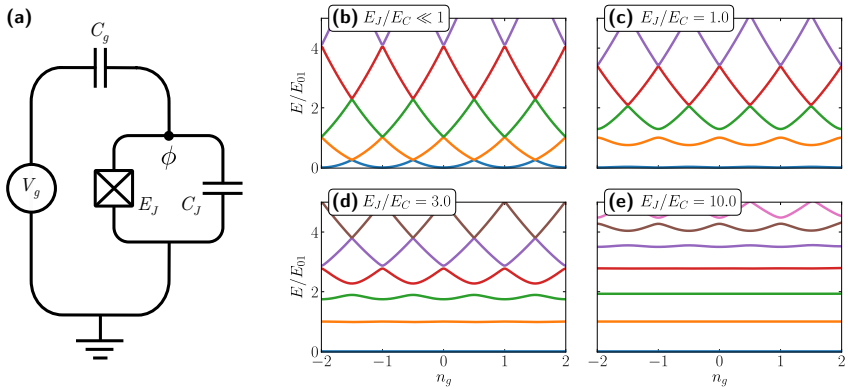

Figure 1.14: (a) *Circuit diagram of the single Cooper pair box, consisting of a Josephson junction, with energy E_J and parasitic capacitance C_J, in series with a gate capacitor with capacitance C_g. The gate voltage is denoted V_g, and the system is connected to ground in the right corner. A dot denotes the only active node.* **(b)-(e)** *The energies of the lowest-lying states of the single Cooper pair box and transmon qubit as a function of the bias charge n_g. The difference between the two lowest bands is approximately equal to E_J at the avoided crossing.*

electrons from the reservoir to the superconducting island via the gate capacitance C_g. The circuit is connected to ground, and thus there is only one active node with flux ϕ through it. The corresponding circuit diagram can be seen in Fig. 1.14(a).

We follow the method presented in Section 1.2.2. In order to write the Lagrangian, we must consider the fixed gate voltage. We model this as an external node with a well defined flux $\phi_V = V_g t$, meaning $\dot{\phi}_V = V_g$. Setting $\phi^T = (\phi, \phi_V)$ we write the Lagrangian

$$\mathcal{L} = \frac{1}{2}\dot{\phi}^T \boldsymbol{C}\dot{\phi} + E_J \cos\phi, \tag{1.136}$$

where the capacitance matrix is

$$\boldsymbol{C} = \begin{bmatrix} C_J + C_g & -C_g \\ -C_g & C_g \end{bmatrix}. \tag{1.137}$$

Since we know that $\dot{\phi}_V = V_g$ is a classical externally controlled variable, it should not be quantized. Therefore, we only calculate one conjugate momentum

$$q = (C_g + C_j)\dot{\phi} - C_g V_g. \tag{1.138}$$

Solving for $\dot{\phi}$ we perform a Legendre transformation and find the Hamiltonian

$$\mathcal{H} = \frac{1}{2(C_g + C_J)}(q + C_g V_g)^2 - \frac{C_g V_g^2}{2} - E_J \cos\phi. \tag{1.139}$$

We now change into conventional notation and define the effective capacitive energy

$$E_C = \frac{e^2}{2(C_g + C_J)}, \tag{1.140}$$

which means that we can write the Hamiltonian as

$$\hat{\mathcal{H}} = 4E_C(\hat{n} - n_g)^2 - E_J \cos\hat{\phi}, \tag{1.141}$$

where we quantize the dynamic variables and remove constant terms. We further define the offset charge $n_g = C_g V_g / 2e$.

We can now discuss the operational regime of the Cooper pair box. When the Josephson energy is much smaller than the capacitive energy ($E_J/E_C \ll 1$), the energy spectrum of the system becomes a set of parabolas when plotted against n_g, one for each eigenvalue of $\hat{n}$. The parabolas cross at $n_g = n + 1/2$, where $n \in \mathbb{Z}$, see Fig. 1.14(b). If we consider the eigenstates of $\hat{n}$ we find that the states $|n\rangle$ and $|n+1\rangle$ are degenerate at $n_g = n + 1/2$. These states are essentially charge states of the capacitor. In this picture, the Hamiltonian of the capacitor becomes

$$\hat{\mathcal{H}}_C = 4E_C \sum_{n=-\infty}^{\infty} (n - n_g)^2 \, |n\rangle\langle n| \,, \tag{1.142}$$

which in matrix representation is just a diagonal matrix with $(n - n_g)^2$ on the diagonal.

Introducing the Josephson junction lifts the degeneracy and introduces an avoided crossing at $n_g = n + 1/2$. The matrix representation becomes a tridiagonal matrix with $E_J/2$ on the diagonals below and above the main diagonal, consisting of the capacitor entries discussed above.

To show this, we must relate the phase states of the Josephson junction $|\phi\rangle$ to the charge states $|n\rangle$. This can be done through a Fourier transform (this treatment is analogous to the treatment of a one-dimensional solid, see, e.g., Ref. [76])

$$|\phi\rangle = \frac{1}{\sqrt{2\pi}} \sum_{n=-\infty}^{\infty} e^{-in\phi} \, |n\rangle \,. \tag{1.143}$$

Note that, since n is a discrete variable, the phase must be 2π periodic. This is in agreement with the fact that we consider ϕ as the phase of the Josephson junction. The commutator between the two corresponding operators is

$$[\hat{\phi}, \hat{n}] \sim i, \tag{1.144}$$

where the '$\sim$' indicates that this is only true up to the association $\phi \sim \phi + 2\pi$. Since the phase is continuous, the inverse transformation of Eq. (1.143) is

$$|n\rangle = \frac{1}{\sqrt{2\pi}} \int_0^{2\pi} \mathrm{d}\phi \, e^{i\phi n} \, |\phi\rangle \,. \tag{1.145}$$

Now writing the last term of Eq. (1.141) as the sum of exponentials and inserting the

identity relation, we find

$$\begin{aligned}\hat{\mathcal{H}}_J &= -E_J \cos\hat{\phi} \\ &= -\frac{E_J}{2}\int_0^{2\pi} \mathrm{d}\phi\, |\phi\rangle\langle\phi| \left(e^{i\phi} + e^{-i\phi}\right) \\ &= -\frac{E_J}{4\pi}\iint_0^{2\pi} \mathrm{d}\phi\, \mathrm{d}\phi' \sum_{n=-\infty}^{\infty} |\phi\rangle\langle\phi'| \left(e^{-in\phi} e^{i(n+1)\phi'} + e^{in\phi'} e^{-i(n+1)\phi}\right) \\ &= -\frac{E_J}{2}\sum_{n=-\infty}^{\infty} \left(|n\rangle\langle n+1| + |n+1\rangle\langle n|\right),\end{aligned}$$

where we apply both Eqs. (1.143) and (1.145) in the second to last step and use the definition of the delta function as an integral in the last step.

Solving the full system, $\hat{\mathcal{H}} = \hat{\mathcal{H}}_C + \hat{\mathcal{H}}_J$, using either Mathieu functions [149] or numerically, yields the avoided crossings seen in Fig. 1.14(c). The distance between these avoided crossings is approximately equal to the Josephson-junction energy E_J for the lowest states in the spectrum. To realize a qubit, we set n_g equal to some half-integer, which yields two states close to each other but with a large gap to higher states [150]. That way, we obtain a significant anharmonicity, see Fig. 1.14(c) where the distance between the green and the yellow lines is significantly different from the distance between the blue and yellow line at, e.g., $n_g = 1/2$.

The SCPB is, however, quite sensitive to small fluctuations of the gate voltage V_g, since this changes n_g and the energy dispersion is steep around the working point $n_g = n + 1/2$, as seen in Fig. 1.14(c) for $E_J/E_C = 1.0$. This means that the qubit works only in this sweet spot as it is otherwise susceptible to charge noise. This reduces the decoherence time of the system. The transmon qubit attempts to fix this problem.

Transmon qubit

The transmission-line shunted plasma oscillation qubit, or transmon qubit for short, was proposed in 2007 as an attempt to increase the coherence time in charge qubits [80, 151]. It exploits the fact that the charge dispersion reduces exponentially in E_J/E_C, while the anharmonicity decreases only algebraically in E_J/E_C following a power law. The setup resembles that of the single Cooper pair box, the difference being a large shunting capacitance, C_B, between the two superconducting islands, followed by a similar increase in the gate capacitance C_g. The circuit diagram is seen in Fig. 1.15.

Capacitors in parallel add to one effective capacitor; hence the effective capacitance can be seen as the sum of the capacitance of the three capacitors $C_\Sigma = C_J + C_B + C_g$. With this elementary knowledge, the Hamiltonian of the transmon becomes identical to that of the single Copper pair box from Eq. (1.141) with the exception that

$$E_C = \frac{e^2}{2(C_J + C_B + C_g)}, \tag{1.146}$$

where we change the effective capacitance in Eq. (1.140). This gives much more freedom in choosing the ratio E_J/E_C, and we can thus solve the Hamiltonian for the energy dispersion for larger E_J/E_C. The result is seen in Fig. 1.14(d) and (e).

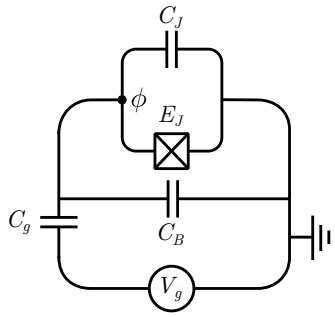

Figure 1.15: *Circuit diagram of the transmon qubit consisting of a Josephson junction with energy E_J and parasitic capacitance C_J in series with a capacitor, C_g. A large capacitance, C_B, shunts the system. The gate voltage is denoted V_g, and the system is connected to ground in the right corner. There is only one active node. The diagram should be compared to Fig. 1.14(a).*

From these results, we observe that the energy dispersion becomes flatter for larger ratios of E_J/E_C, which means that the qubit becomes increasingly insensitive to charge noise. An utterly flat dispersion would lead to no charge noise sensitivity at all. However, we also notice that the anharmonicity decreases for larger ratios. This is a result of the before-mentioned fact that the charge dispersion decreases exponentially in E_J/E_C while the anharmonicity has a slower rate of change given by a power law. Therefore we cannot just increase the shunting capacitance until all charge noise disappears as we still need a working qubit. We are thus left with some effective values for the transmon, which are usually somewhere in the range $E_J/E_C \in [50, 100]$.

Even though the transmon has a ratio E_J/E_C close to that of the phase regime ($E_C \ll E_J$), it is still classified as a charge qubit due to the structural similarity to the single Cooper pair box qubit and the fact that the eigenstates still have reasonably well-defined charge [80]. Due to that and the fact that capacitors in parallel add, we often just put a Josephson junction and a parasitic capacitance in place of the transmon in larger circuits for simplicity. We further notice that if the ratio E_J/E_C is very large, the bias voltage becomes irrelevant and can be omitted as well.

When implementing the transmon qubit on an actual chip, various architectures are used, including the Xmon, which is developed for nearest-neighbor capacitive coupling of qubits [31, 152–155], the three-dimensional (3D) transmon where the Josephson junction is coupled to a three-dimensional cavity [156], or the gatemon which is based on a semiconductor nanowire and controlled by an electrostatic gate [157, 158]. In general, there are many shapes of the transmon, and these can often be tailor-made to the specific experiment, see, e.g., Ref. [159]. Typical for these different architectures is that they can be treated theoretically equivalently to the basic transmon setup discussed above. Therefore, they are often referred to as transmonlike qubits when the architecture is irrelevant from a theoretical point of view.

Recently a dual to the transmon qubit called a quasicharge qubit, or blochnium, has been proposed, where a large shunting inductance replaces the shunting capacitance. This large inductance makes the qubit robust against flux noise, which could open up for

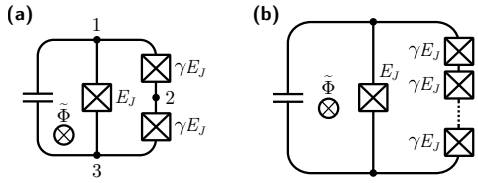

Figure 1.16: *Circuit diagrams of different flux qubits.* **(a)** *C-shunted flux qubit. Two Josephson junctions in series are placed in parallel with a third Josephson junction. Both the parasitic and shunting capacitances are included in the capacitance.* **(b)** *Fluxonium qubit. An array of N Josephson junctions are placed in parallel with another Josephson junction, effectively creating an inductor in parallel with the Josephson junction.*

exploring high-impedance circuits [160].

1.10.2 Flux qubits

Flux qubits are generally implemented in a looped superconducting circuit interrupted by one or more Josephson junctions. A current is induced in these circuits because fluxoid quantization means that only an integer number of magnetic flux quanta is allowed to penetrate the loop. As a response to the external flux, currents flow in superconducting materials to enhance or diminish the total flux such that an integer number of flux quanta is achieved in total.

A superposition of clockwise and counterclockwise currents is obtained by setting the external magnetic field at half a magnetic flux quantum. Changing to node flux space, this superposition of currents can be seen as a superposition of the ground states in a double-well potential. In the double-well potential, small tunneling occurs between the two sides of the well, which couples the two wave functions, making an avoided crossing, and thus a closely spaced two-level system with a considerable gap to the remaining states. We now elaborate on some concrete realizations of these general ideas.

C-shunted flux qubit

The C-shunted flux qubit (CSFQ) idea is the same as for the transmon. However, here the capacitive shunting is over a flux qubit, sometimes called a persistent-current qubit (PCQ) [161, 162]. As with the transmon qubit, the capacitive shunting improves the coherence of the qubit [30, 163]. We, therefore, consider the flux qubit without going into details of the shunting, see Section 1.10.1. The coherence of the flux qubit can further be improved by placing it in a 3D [164], or coplanar [165] resonator.

The flux qubit consists of two Josephson junctions in series, with energy γE_J, which are then placed in parallel with a third Josephson junction, with Josephson energy E_J. Here γ is the ratio of the geometrical size of the Josephson junctions. To a good approximation, all capacitances (both parasitic and shunting) can be collected into one, as seen in Fig. 1.16(a), when assuming $\gamma > 1$. When this is the case, the node between the two Josephson junctions becomes a passive node.

Using the same trigonometric tricks as for the dc SQUID (see Section 1.1.2), we can

write the potential energy of the three Josephson junctions as

$$U = -E_J \left[2\gamma \cos\left(\frac{\psi_+}{2} - \psi_2 \right) \cos\frac{\psi_-}{2} + \cos(\psi_- + \tilde{\Phi}) \right]. \tag{1.147}$$

Here we introduce the change of coordinates $\psi_\pm = \phi_1 \pm \phi_3$ and $\psi_2 = \phi_2$ where $n = 2$ is the middle coordinate in between the two Josephson junctions. This coordinate transformation turns out to diagonalize the capacitance matrix and leave only ψ_- with a nonzero eigenvalue. Thus, the two remaining node fluxes are superfluous, and from the constraints obtained from the Euler-Lagrange equations, we find that $\psi_2 = \psi_+/2$, which yields the potential energy

$$U = -E_J \left[2\gamma \cos\frac{\psi_-}{2} + \cos(\psi_- + \tilde{\Phi}) \right]. \tag{1.148}$$

This no longer has the usual sinusoidal form, and its final form depends on the external flux $\tilde{\Phi}$ and the junction ratio γ. The most common configuration for an external flux is $\tilde{\Phi} = (1 + 2l)\Phi_0/2$, where $l \in \mathbb{Z}$. These points are often called the flux degeneracy points and correspond to one-half of the superconducting flux quantum threading the qubit loop. In this configuration, the qubit frequency is most robust against flux noise, leaving the qubit with optimal coherence times.

As mentioned above, we assume $\gamma > 1$, which eliminates one degree of freedom. This can be seen as an approximation in which a particle starts in two dimensions but is forced to move along just one dimension and is sometimes called the quasi-one-dimensional (1D) approximation. This approximation fails if $\gamma < 1$. If $1 < \gamma < 2$, the potential takes the form of a double-well, which has been investigated as the PCQ [161, 162]. If $\gamma > 2$, the potential becomes a single well, very similar to the transmon qubit, which is why the CSFQ has been investigated in this regime [30, 163]. In both cases, if the anharmonicity is sufficiently large, the quantized potential can be truncated to the lower level

Fluxonium

The fluxonium qubit is the natural extension of the flux qubit. Instead of two Josephson junctions in parallel with another Josephson junction, the fluxonium features an array of up to $N = 100$ Josephson junctions [166–168], sometimes referred to as a *superinductance* [169, 170]. The circuit diagram can be seen in Fig. 1.16(b). Using the same quasi-1D approximation as in Section 1.10.2 repeatedly, we arrive at a potential

$$U = -E_J \left[N\gamma \cos\frac{\psi}{N} + \cos(\psi + \tilde{\Phi}) \right], \tag{1.149}$$

where ψ is the sum of all node fluxes in between the array of Josephson junctions on the left side of Fig. 1.16(b). When the number of Josephson junctions N becomes large, the argument in the first cosine, ψ/N becomes small such that the cosine can be approximated by a second-order approximation which yields

$$U = \frac{1}{2} E_L \psi^2 - E_J \cos(\psi + \tilde{\Phi}), \tag{1.150}$$

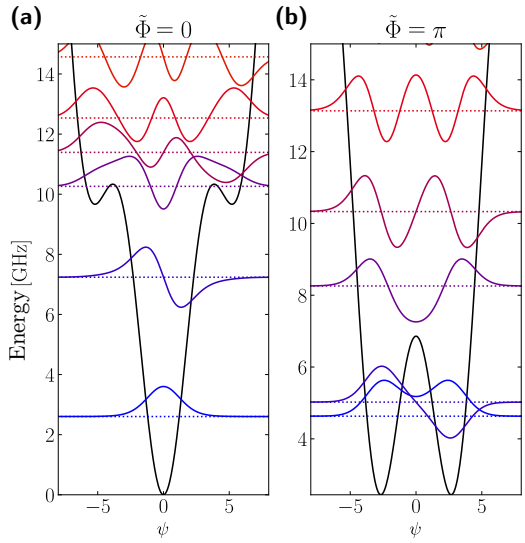

Figure 1.17: *Spectrum of the fluxonium qubit at the two different flux-biasing points. For this plot the parameters are set to* $E_C/h = 1\,\text{GHz}$, $E_J/h = 3.43\,\text{GHz}$ *and* $E_L/h = 0.58\,\text{GHz}$.

where $E_L = E_J\gamma/N$ is the resulting superinductance of the array of Josephson junctions. This has the same effective form as a rf SQUID [124]. However, the superinductance of the fluxonium qubit is much larger than the geometric inductance of the rf SQUID. This is because the superinductance is produced by the kinetic inductance of the array of Josephson junctions. It is therefore not limited, contrary to the geometrical inductance where the loop impedance cannot exceed αR_Q. Here α is the fine-structure constant and R_Q is the resistance quantum [169]. Recent implementations of superinductors are based on nanowires of disordered granular aluminum or Nb alloys [171–174].

When the external flux bias is $\tilde{\Phi} = 0$ the potential has minimum at $\psi = 0$. For small fluctuations of ψ, the potential is approximately harmonic and the lowest-lying states are close to simple harmonic oscillator states. At higher energies, the anharmonic cosine term of the potential comes into play as seen in Fig. 1.17(a). This ensures the anharmonicity necessary for using the two lowest-lying states as the qubit subspace. However, the fluxonium qubit is most often operated at $\tilde{\Phi} = \pi$, similarly to the flux qubit. In this regime, the potential exhibits a double-well structure, and it is possible to achieve a much larger anharmonicity than in the $\tilde{\Phi} = 0$ case, see Fig. 1.17(b).

In experiments, fluxonium qubits have reached impressive lifetimes of 100-400 µs [167, 168], while recent experiments yields lifetimes in the 1-ms regime [175]. This is done while maintaining a large anharmonicity suitable for fast gate operations. It puts fluxonium among the top qubit candidates for near future quantum-computing applications. In addition, the success of the fluxonium qubit proves that long coherence times can be achieved even in a more complicated system with a large number of spurious modes [176]. This should encourage quantum engineers to further explore circuit design utilizing large

superinductance.

A circuit element related to the fluxonium and the flux qubit is the superconducting nonlinear asymmetric inductive element (SNAIL), which has the same architecture as the fluxonium qubit in Fig. 1.16(b) but fewer Josephson junctions in the array than the fluxonium, i.e., $N \geq 2$ but less than for the fluxonium. For some particular choices of γ and $\tilde{\Phi}$ it is possible to cancel any fourth-order term, ϕ^4 while keeping a substantial cubic term, ϕ^3 [177]. This can be used for amplifying three-wave-mixing [178, 179].

0-π qubit

A new type of qubit is the 0-π qubit. It has been proposed more recently than the above qubits, but it shows promising tendencies in topological protection from noise [180–186].

The 0-π qubit consists of four nodes that are all connected by two large superinductors, two Josephson junctions, and two large shunting capacitors, as shown in Fig. 1.18(a). We denote the shunting capacitors as C, the superinductors as L, and the Josephson junctions as E_J and assume they have parasitic capacitances of C_J. The superinductors are usually made as an array of Josephson junctions (see Section 1.10.2). However, here we draw them as regular inductors, which is their effective form. An external flux, $\tilde{\Phi}$, goes through the qubit. It is advantageous to choose the spanning tree such that only the Josephson junctions lie in the set of closure branches.

The node fluxes of the circuit are denoted $(\phi_1, \phi_2, \phi_3, \phi_4)$, and the normal modes of the circuit can be written using the transformation

$$\begin{bmatrix} \varphi \\ \theta \\ \zeta \\ \Sigma \end{bmatrix} = \frac{1}{2} \begin{bmatrix} -1 & 1 & -1 & 1 \\ -1 & 1 & 1 & -1 \\ 1 & 1 & -1 & -1 \\ 1 & 1 & 1 & 1 \end{bmatrix} \begin{bmatrix} \phi_1 \\ \phi_2 \\ \phi_3 \\ \phi_4 \end{bmatrix}. \tag{1.151}$$

Here Σ is the CM coordinate, which has no influence on the dynamics of the system and can be discarded. This basis transformation diagonalizes the capacitance matrix $\boldsymbol{C} = 2\,\mathrm{diag}(C_J, C_J + C, C)$. The Hamiltonian then takes the form

$$\begin{aligned} \mathcal{H} = {} & 4E_{C\varphi} n_\varphi^2 + 4E_{C\theta} n_\theta^2 + 4E_{C\zeta} n_\zeta^2 + \frac{E_L}{2}(\varphi^2 + \zeta^2) \\ & - E_J \left[\cos(\theta + \varphi) + \cos(\theta - \varphi - \tilde{\Phi})\right], \end{aligned} \tag{1.152}$$

where $n_\varphi, n_\zeta, n_\theta$ are the canonical momenta, $E_{C\varphi}^{-1} = 16C_J$, $E_{C\theta}^{-1} = 16(C + C_J)$ and $E_{C\zeta}^{-1} = 16C$ are the charging energies of each mode, while $E_L = 2/L$ is the effective inductive energy. Note that the ζ mode completely decouples from the rest of the system and can thus be ignored. By transforming the θ variable $\theta \to \theta + \frac{\tilde{\Phi}}{2}$ we can rewrite the Hamiltonian into the simpler form

$$\mathcal{H} = 4E_{C\varphi} n_\varphi^2 + 4E_{C\theta} n_\theta^2 - 2E_J \cos\theta \cos\left(\varphi + \frac{\tilde{\Phi}}{2}\right) + \frac{E_L}{2}\varphi^2. \tag{1.153}$$

The circuit is engineered so $C \gg C_J$, and we can think of the system as a heavy particle moving along the θ axis and a lighter particle moving along the φ axis. In the basis of the

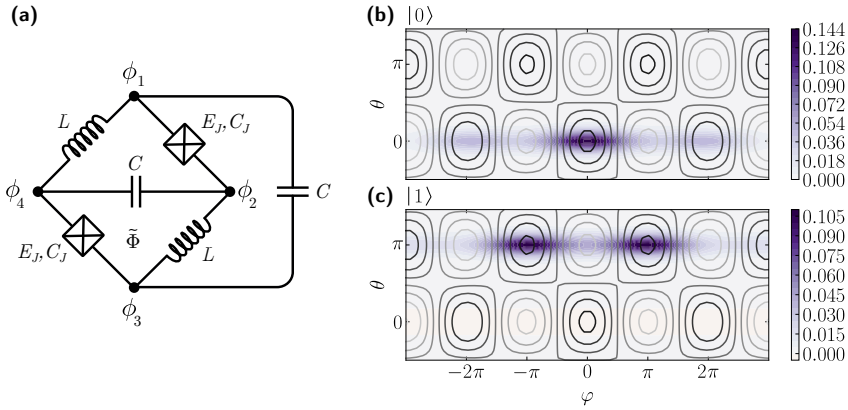

Figure 1.18: (a) *Circuit diagram of the 0-π qubit. Four nodes are connected to each other by two large superinductors (drawn here as regular inductors) L, two Josephson junctions E_J with parasitic capacitance C_J, and two shunting capacitors C.* **(b)-(c)** *Wave functions of* **(b)** *the ground state and* **(c)** *first excited state for the 0-π qubit. The contour lines indicate the qubit potential. For this plot the parameters are set to $E_{C,\theta} = 0.1$, $E_{C,\varphi} = 10$, $E_J = 10$ and $E_L = 1$. In the figure $\tilde{\Phi} = 0$. Changing the external flux would translate the potential along the θ axis.*

computational states $|0\rangle$ and $|1\rangle$, which are chosen as the ground and first excited state, respectively, the θ variable is well localized around either 0 or π, as shown in Fig. 1.18(b) and (c). This is the reason for the naming of the qubit. Setting $\theta = 0$ or π in Eq. (1.153) the potential along the φ axis becomes similar to the fluxonium biased by a flux of 0 or π. As a result the two states have vanishing matrix elements $\langle 0| \theta^n |1\rangle$, $\langle 0| \varphi^n |1\rangle \simeq 0$. This makes the qubit highly resistant to noise-induced relaxation.

In recent experiments [185] with the 0-π qubit, relaxation times above 1 ms have been achieved, making it an exciting candidate for future research. As with fluxonium, the 0-π qubit proves that it is not only the most simple qubits, such as the charge and flux qubit families, that can achieve long coherence times. Researchers should make a note of this when developing new circuit designs to tap into the potential that more complicated components, such as the superinductances used in fluxonium and the 0-π qubit, bring to the table.

1.10.3 Tunable couplers

In Section 1.8 we have presented some simple static couplings of qubits. Here we present some tunable couplers from the literature. By tunable, we mean couplers where the interaction strength can be changed *in situ*, without changing the circuit layout. We consider both capacitive and inductive coupling. The list of couplers presented here is, of course, not exhaustive as there are other types of couplers in the literature, see, e.g., Refs. [187, 188] or Chapter 3.

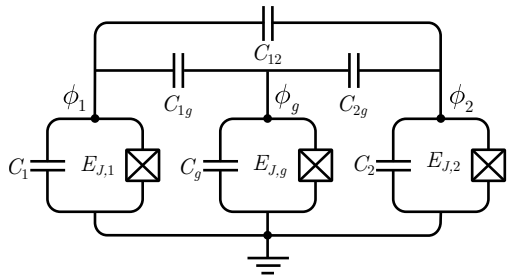

Figure 1.19: *Circuit diagram implementing a tunable capacitive coupler. Two transmonlike qubits are connected via another tunable transmonlike qubit and directly to each other.*

Tunable capacitive coupler

Here we present a tunable capacitive coupling between two modes [189–192]. Consider the circuit in Fig. 1.19 where two transmonlike qubits, subscript 1 and 2, are connected capacitively to each other and a mediating transmonlike qubit, subscript g. If we require the Josephson junctions of the qubits to be dc SQUIDs, we can tune the frequency of the qubits. Writing down the Hamiltonian of this circuit following the approach in Section 1.2.2 is straightforward

$$\mathcal{H} = \frac{1}{2}\boldsymbol{q}^T\boldsymbol{C}^{-1}\boldsymbol{q} - \sum_j E_{J,j}\cos\phi_j, \tag{1.154}$$

where the sum is over all three modes, i.e., $1, 2, g$. The capacitance matrix is

$$\boldsymbol{C} = \begin{bmatrix} C_1 + C_{1g} + C_{12} & -C_{1g} & -C_{12} \\ -C_{1g} & C_g + C_{1g} + C_{2g} & -C_{2g} \\ -C_{12} & -C_{2g} & C_2 + C_{2g} + C_{12} \end{bmatrix}, \tag{1.155}$$

which is invertible. We leave this inversion to the reader and note that assuming the qubit-coupler capacitances are smaller than the mode capacitances but more significant than the qubit-qubit capacitance, i.e., $C_n \gg C_{ng} \gg C_{12}$, it can be simplified significantly, see, e.g., Ref. [190]. The diagonal terms of $\boldsymbol{C}^{-1}$ contribute to the frequencies of the modes, while the three off-diagonal terms contribute to the coupling. Quantizing the Hamiltonian, the interacting part takes the form

$$\hat{\mathcal{H}}_{\text{int}} = \sum_{i>j} (\boldsymbol{C}^{-1})_{(i,j)} \hat{n}_i \hat{n}_j, \tag{1.156}$$

where $\hat{n}_i$ is the Cooper pair number operator of the ith mode, and $i, j \in \{1, 2, g\}$. Mapping to annihilation and creation operators connected to the harmonic degrees of freedom yields

$$\hat{\mathcal{H}}_{\text{int}} = \sum_{i>j} g_{ij} \left(\hat{b}_i^\dagger \hat{b}_j + \hat{b}_i \hat{b}_j^\dagger - \hat{b}_i^\dagger \hat{b}_j^\dagger - \hat{b}_i \hat{b}_j \right), \tag{1.157}$$

where the coupling strength is given as

$$g_{ij} = (\boldsymbol{C}^{-1})_{(i,j)} \frac{1}{2\sqrt{\zeta_i \zeta_j}}, \tag{1.158}$$

and the impedances are given in Eq. (1.56). Note that we have to keep the nonconserving terms in Eq. (1.157) as these can be significant in the dispersive regime, i.e., when the coupler frequency is larger than the difference in qubit frequencies; $|\Delta_j| = |\omega_j - \omega_g| \gg g$.

To see this, we perform a Schrieffer-Wolff transformation similar to the one performed in Section 1.8.3. However, this time we have three modes and include the nonconserving terms. We thus take

$$\hat{S} = \sum_{j=1,2} \left[\frac{g_{jg}}{\Delta_j} (\hat{b}_g^\dagger \hat{b}_j - \hat{b}_g \hat{b}_j^\dagger) - \frac{g_{jg}}{\Sigma_j} (\hat{b}_g^\dagger \hat{b}_j^\dagger - \hat{b}_g \hat{b}_j) \right], \tag{1.159}$$

where $\Sigma_j = \omega_j + \omega_g$. Assuming a small anharmonicity $\alpha_j \ll \Delta_j$, we can expand the transformation to second order (note that g_{12} is considered a second-order small quantity on its own). We find the full Hamiltonian to be

$$\hat{\mathcal{H}}_{\text{disp}} = e^{\hat{S}} \hat{\mathcal{H}} e^{-\hat{S}} = \sum_{j=1,2} \left[\tilde{\omega}_j \hat{b}_j^\dagger \hat{b}_j + \frac{\alpha_j}{2} \hat{b}_j^\dagger \hat{b}_j^\dagger \hat{b}_j \hat{b}_j \right] + \tilde{g}_{12} (\hat{b}_1^\dagger \hat{b}_2 + \hat{b}_1 \hat{b}_2^\dagger), \tag{1.160}$$

where

$$\tilde{\omega}_j = \omega_j + g_{jg}^2 \left(\frac{1}{\Delta_j} - \frac{1}{\Sigma_j} \right), \tag{1.161}$$

$$\tilde{g}_{12} = g_{12} + \frac{g_{1g} g_{2g}}{2} \left(\frac{1}{\Delta_1} + \frac{1}{\Delta_2} - \frac{1}{\Sigma_1} - \frac{1}{\Sigma_2} \right). \tag{1.162}$$

In the dispersive regime $|\Delta_j| \simeq |\Sigma_j|$ the nonconserving terms contribute to the coupling. The total effective coupling $\tilde{g}_{12}$ depends on g_{jg} as well as Δ_j and Σ_j, all of which depend on the coupler frequency ω_g, which can be tuned. Thus $\tilde{g}_{12}$ is tunable as it is implicitly a function of ω_g.

Note that instead of the tunable transmon coupler, one could also have employed a tunable harmonic oscillator or cavity for coupling the two qubits as used in Section 1.8.3. The analysis is essentially the same.

Delft coupler

The Delft coupler [193] introduces tunable nonlinear couplings between two qubits in a center-of-mass basis. As with the above coupler, it is based on capacitors. The following example is a simplification of the Supplementary Material of Ref. [193].

Consider the circuit diagram in Fig. 1.20. Following the approach in Section 1.2.2, we find the following capacitance matrix

$$\boldsymbol{C} = \begin{bmatrix} C + C_g & -C & 0 & 0 \\ -C & C + C_g + C_c & -C_c & 0 \\ 0 & -C_c & C + C_g + C_c & -C \\ 0 & 0 & -C & C + C_g \end{bmatrix}, \tag{1.163}$$

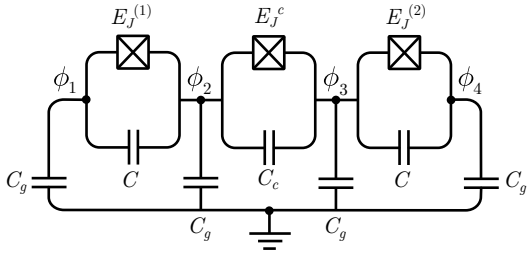

Figure 1.20: *Circuit diagram of the Delft coupler. Two transmonlike qubits (1 and 2) coupled via another transmonlike coupler (c).*

where we define the flux vector as $\boldsymbol{\phi} = (\phi_1, \phi_2, \phi_3, \phi_4)^T$. This yields the following circuit Lagrangian

$$\mathcal{L} = \frac{1}{2}\dot{\boldsymbol{\phi}}^T \boldsymbol{C}\dot{\boldsymbol{\phi}} + E_J^{(1)}\cos(\phi_1 - \phi_2) + E_J^c \cos(\phi_2 - \phi_3) + E_J^{(2)}\cos(\phi_3 - \phi_4). \tag{1.164}$$

We now change into a CM basis (see Section 1.2.5) of the capacitive subsystem using the following transformations

$$\psi_{\text{CM}} = \frac{1}{2}(\phi_1 + \phi_2 + \phi_3 + \phi_4), \tag{1.165a}$$

$$\psi_1 = \frac{1}{\sqrt{2}}(\phi_1 - \phi_2), \tag{1.165b}$$

$$\psi_2 = \frac{1}{\sqrt{2}}(\phi_4 - \phi_3), \tag{1.165c}$$

$$\psi_S = \frac{1}{2}(\phi_1 + \phi_2 - \phi_3 - \phi_4). \tag{1.165d}$$

This decouples the center-of-mass coordinate, ψ_{CM}, from the remaining coordinates (note that this is due to the identical grounding capacitances C_g) as the transformed capacitance matrix takes the form

$$\boldsymbol{K} = \frac{1}{2}\begin{bmatrix} 2C_g & 0 & 0 & 0 \\ 0 & 4C + 2C_g + C_c & -C_c & -\sqrt{2}C_c \\ 0 & -C_c & 4C + 2C_g + C_c & \sqrt{2}C_c \\ 0 & -\sqrt{2}C_c & \sqrt{2}C_c & 2C_g + 2C_c \end{bmatrix}, \tag{1.166}$$

where we choose the basis such that $\boldsymbol{\psi} = (\psi_{\text{CM}}, \psi_1, \psi_2, \psi_S)^T$. Doing a Legendre transformation and quantizing, we find the Hamiltonian

$$\hat{\mathcal{H}} = \frac{1}{2}\hat{\boldsymbol{p}}^T \boldsymbol{K}^{-1}\hat{\boldsymbol{p}} - E_J^{(1)}\cos(\sqrt{2}\hat{\psi}_1) - E_J^{(2)}\cos(\sqrt{2}\hat{\psi}_2) - E_J^c \cos\left(\frac{\hat{\psi}_1 - \hat{\psi}_2}{\sqrt{2}} - \hat{\psi}_S\right), \tag{1.167}$$

where $\hat{\boldsymbol{p}}$ is the vector of conjugate momentum of the $\hat{\boldsymbol{\psi}}$ vector. Expanding the cosines and changing into annihilation and creation operators [Eq. (1.58)], the noninteracting part of the Hamiltonian takes the form

$$\hat{\mathcal{H}}_0 = \sum_{i=\{S,1,2\}} \left[\omega \hat{b}_i^\dagger \hat{b}_i + \frac{\alpha}{2}\hat{b}_i^\dagger \hat{b}_i^\dagger \hat{b}_i \hat{b}_i\right], \tag{1.168}$$

where we define $\omega = 4\sqrt{E_C E_J} + \alpha$ and $\alpha = -\zeta^2(E_J + 3E_J^{(1)})/8$, with the effective capacitive energies being the usual $E_C^{(i)} = (\boldsymbol{K}^{-1})_{(i,i)}/8$, which turn out to be the same for the 1 and 2 mode. Thus, we denote it $E_C = E_C^{(1)} = E_C^{(2)}$. We also define the effective Josephson energy $E_J = E_J^{(1)} + E_J^c/4$ and assume that the 1 and 2 modes are resonant, i.e., $E_J^{(1)} = E_J^{(2)}$. Lastly, we define the impedance as given in Eq. (1.56). We do not include the center-of-mass coordinate as it does not influence the system's dynamics. Note how the 1 and 2 modes are affected by their "own" Josephson junction and the coupling Josephson junction.

Assuming that the so-called sloshing mode, ψ_S, is detuned from the remaining two modes, we can remove couplings to it, using the rotating-wave approximation from Section 1.5. After this approximation, the interaction part of the Hamiltonian takes the form

$$\hat{\mathcal{H}}_I = J\hat{b}_1\hat{b}_2^\dagger + \frac{V}{2}\hat{b}_1^\dagger\hat{b}_1\hat{b}_2^\dagger\hat{b}_2 + \frac{V}{4}\hat{b}_1^\dagger\hat{b}_1^\dagger\hat{b}_2\hat{b}_2 + \frac{V}{2}(\hat{b}_1\hat{n}_1\hat{b}_2^\dagger + \hat{b}_2\hat{n}_2\hat{b}_1^\dagger) + \text{H.c.}, \tag{1.169}$$

where we use the assumption that the 1 and 2 modes are resonant. The swapping coupling strength is given by

$$J = \frac{1}{2\zeta}(\boldsymbol{K}^{-1})_{(1,2)} - \frac{\zeta E_J^c}{4} - \frac{V}{2}, \tag{1.170}$$

where the nonlinear coupling factor is given as

$$V = -\frac{E_J^c\zeta^2}{16}. \tag{1.171}$$

The first nonlinear term in Eq. (1.169) is sometimes called the cross-Kerr coupling term with coupling strength $V/2$, while the second nonlinear term tunnels a pair of excitations from one mode to the other with coupling strength $V/4$. Therefore this term does not contribute to the Hamiltonian if truncated to a two-level model, but it may result in corrections to the model. Thus truncating to a two-level model, the Hamiltonian becomes

$$\hat{\mathcal{H}} = \hat{\mathcal{H}}_0 + J(\sigma_1^+\sigma_2^- + \sigma_1^-\sigma_2^+) + \frac{V}{4}\sigma_1^z\sigma_2^z, \tag{1.172}$$

where we have both transverse ($\sigma^+\sigma^- + \sigma^-\sigma^+$) and longitudinal coupling ($\sigma_z\sigma_z$) between the 1 and 2 modes. Both J and V depend on the Josephson energy of the coupler, which can be tuned using the external flux, thus making the coupling tunable.

Gmon coupler

The gmon coupler introduces tunable swapping couplings between two transmonlike qubits by exploiting mutual inductance [189, 194–196].

Consider the circuit diagram in Fig. 1.21 of the gmon. A Josephson junction in parallel with a capacitor and in series with a linear inductor is coupled to a similar setup via another Josephson junction. An external flux through the coupling loop makes it possible to tune the inductance of the coupling Josephson junction, such that $L_{\text{eff}} = L_g/\cos\delta$

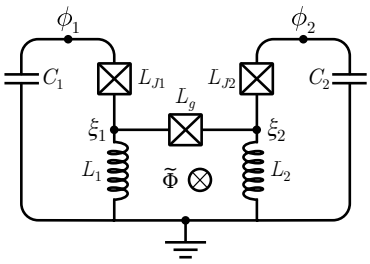

Figure 1.21: *Circuit diagram of the gmon coupler. Two Josephson junctions, L_{Ji}, in parallel with a capacitor, C_i, and in series with a linear inductor, L_i, are coupled via a Josephson junction, L_g. The inductors lead to mutual inductance between the two loops, and an external flux through the middle loop allows for tuning off the coupling.*

[see Eq. (1.15)]. Here we define the dc phase difference across the Josephson junction, $\delta = \tilde{\Phi} + \bar{\xi}_2 - \bar{\xi}_1$, where the bar indicates the equilibrium position of the coordinates.

The ξ coordinates are passive nodes as they are only coupled to inductors and not any capacitors. We can therefore remove the ξ coordinates from the Hamiltonian. To do this, we must first determine the voltage of the ϕ coordinates. This can be done using Kirchhoff's voltage law, Eq. (1.3b), which yields

$$V_i = (L_{Ji} + L_i)\dot{I}_i \pm M(\dot{I}_2 - \dot{I}_1), \tag{1.173}$$

where M is the mutual inductance between the right and left loop and we have plus for $i = 1$ and minus for $i = 2$. In order to simplify this expression we define $L_{qi} = L_{Ji} + L_i - M$, which is the inductance in the ith loop.

To determine the mutual inductance M, we consider a current I_1 in the left qubit. A small fraction of this current flows through the coupler Josephson junction. This fraction is

$$I_g = \frac{L_1}{L_1 + L_2 + L_{\text{eff}}} I_1, \tag{1.174}$$

where we use the effective inductance in place of L_g. This current generates a flux in the right qubit $\phi_2 = L_2 I_g$. This means that we can express the mutual inductance as

$$M = \frac{\phi_2}{I_1} = \frac{L_1 L_2}{L_1 + L_2 + L_{\text{eff}}}. \tag{1.175}$$

With the mutual inductance determined, we are ready to find the Hamiltonian of the circuit in Fig. 1.21. It is as follows:

$$\mathcal{H} = \sum_{i=1,2} \left[\frac{q_i^2}{2C_i} + \frac{\xi_i^2}{2L_i} - \frac{1}{L_{Ji}} \cos(\phi_i - \xi_i) - \frac{1}{L_g} \cos(\xi_1 - \xi_2 + \tilde{\Phi}) \right], \tag{1.176}$$

where q_i is the conjugate momentum of the ith flux. Since the ξ coordinates are passive nodes, we want to remove them from the Hamiltonian. We do this by minimizing ξ_i for a fixed ϕ_i. This is equivalent to solving Lagrange's equations, Eq. (1.27), for ξ_i. This is

straightforward but cumbersome work as we end up with transcendental equations for ξ_i. We, therefore, skip straight to the resulting Hamiltonian. Details can be found in Ref. [195]. The Hamiltonian in the harmonic and weak coupling limit, $L_q \gg M$, becomes

$$\mathcal{H} = \sum_{i=1,2} \left[\frac{q_i^2}{2C_i} + \frac{\phi_i^2}{2L_{qi}} \right] + \Gamma \phi_1 \phi_2, \tag{1.177}$$

where we do not include the anharmonic corrections, see Ref. [195]. The coupling is given as

$$\Gamma = -\frac{M}{L_{q1}L_{q2}} = -\frac{L_1 L_2}{(L_1 + L_{j1})(L_2 + L_{J2})(L_{\text{eff}} + L_1 + L_2)}, \tag{1.178}$$

and changing into annihilation and creation operators yields a coupling strength of

$$g = \frac{1}{2}\Gamma\sqrt{\zeta_1 \zeta_2}, \tag{1.179}$$

where the impedances are found in Eq. (1.56). This coupling strength is tunable via the parameter L_{eff}.

1.11 Summary and outlook

In this chapter, we have presented various methods used when analyzing superconducting electrical circuits. We have summarized the methods in Fig. 1.22.

An analysis usually starts by determining over which components possible external flux should be added, either using Kirchhoff's law directly, as in Section 1.2.1 or via constructing a spanning tree as described in Section 1.2.2. The Lagrangian can then be constructed by determining the capacitor (kinetic) energy and subtracting the inductive (potential) energy as in Section 1.2.3. The Hamiltonian is found using a Legendre transformation in Section 1.2.4. One can then optionally change basis, e.g., into normal modes as in Sections 1.2.5 and 1.2.6. The Hamiltonian can then be quantized using the canonical quantization in Section 1.3.1. Asserting that the system is only weakly anharmonic, it can be rewritten into interacting harmonic oscillators perturbed by the anharmonicity following the approach in Section 1.4. After changing to annihilation and creation operators, the rotating-wave approximation can be applied if needed as in Section 1.5. If the anharmonicity is large, the system can be truncated into qubits or qudits using either the methods in Section 1.6. Note that this final truncation of the Hilbert space is not strictly necessary to perform computations using the superconducting circuit as other approaches work with the entire Hilbert space of the oscillators. These approaches are beyond the scope of this chapter, and more information can be found in Refs. [197–209].

Besides the essential steps mentioned above, we have also discussed control of the modes via microwave driving in Section 1.7 and used to perform single-qubit gates. Simple coupling of modes is discussed in Section 1.8, and this enables the implementation of two-qubit gates. We also discussed coupling to linear resonators and inductive coupling via mutual inductance in the same section. Finally, we have discussed how to include noise when calculating the dynamics of the system using the Bloch-Redfield model and master equation in Section 1.9. We have illustrated the methods with concrete examples

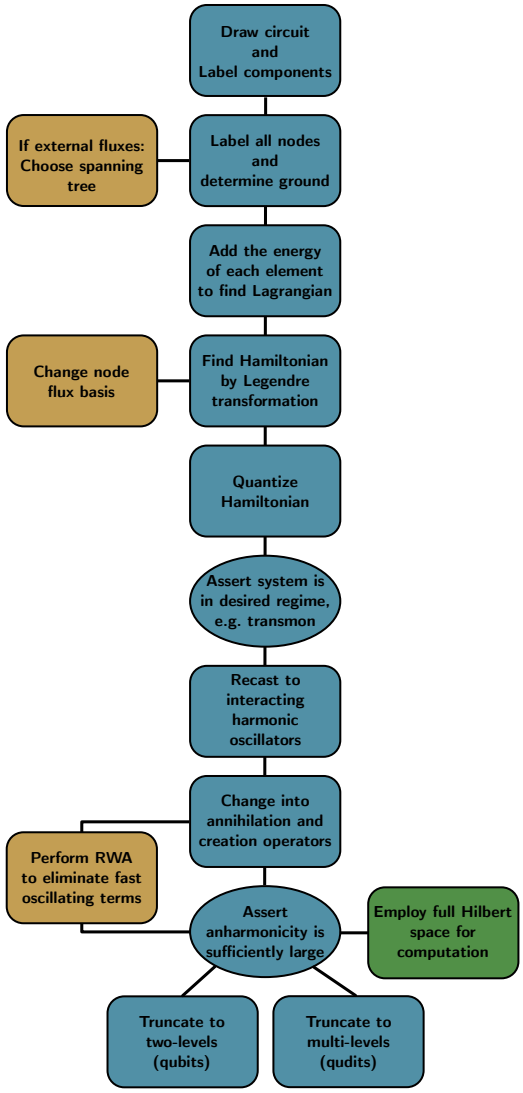

Figure 1.22: *Overview of the methods presented in this chapter. Blue blocks indicate the essential methods, while yellow blocks indicate optional steps. Green boxes are beyond the scope of this chapter. Round blocks are assertions that must be satisfied before advancing in the flowchart.*

throughout the chapter, and finally, in Section 1.10 we discussed several key examples of contemporary qubit designs and some couplers that allow the qubits to interact.

The methods presented here are by no means exhaustive regarding circuit analysis. Classical electrical circuit analysis has been performed for decades by both physicists and engineers, and much more information on this subject can be found in the existing literature. Therefore, the methods presented here should not be seen as a limit to what can be done with superconducting circuits but merely as a starting point for researchers new to the field of superconducting electrical circuit analysis.

In the following three chapters of this thesis, we will consider controlled gates which can be implemented in superconducting circuits and analyzed using the methods presented in this chapter. Therefore, these three gates can be seen as an example of what this chapter's methods can be used.

PART II

Three Little Controlled Gates in Superconducting Circuits

CHAPTER 2

The n-bit iToffoli gate

The inspiration for the n-bit iToffoli gate is a circuit I worked on during my master's thesis; however, it was not until much later, during my PhD studies, that I realized it could be engineered into a controlled gate. Apparently, we were not the only people working on this, since when we put the preliminary paper on arXiv, a research group from the University of Amsterdam contacted us, and we ended up collaborating with them, making Ref. [V], on which this chapter is based. Text and figures have been edited to fit into the thesis.

The n-bit Toffoli gates are a family of reversible logic gates, where each gate has n control bits and one bit, which is inverted if the control bits are in the right state. The n-bit Toffoli gates, and especially the two-bit Toffoli gate, also known as *the* Toffoli gate [210], are of great interest in the field of quantum information [87]. The two-bit Toffoli gate, on its own, is universal in classical computing, and together with the Hadamard gate, it constitutes a universal set of quantum gates [87]. The n-bit Toffoli gates are further important since they play a pivotal role in schemes for quantum error correction [211, 212], in fault-tolerant quantum computing [213, 214], and in Shor's algorithm [215].

While high-fidelity quantum gates on one or two qubits have been reported [216–220], proper implementations of multiqubit gates such as the Toffoli gate remain challenging. In a conventional circuit decomposition, where the Toffoli gate is performed as a sequence of one- and two-qubit gates, it is known that at least five two-qubit operations are needed to obtain a two-bit Toffoli gate. For larger n, these numbers grow steeply: The n-bit Toffoli can be implemented with a circuit of depth $O(\log(n))$, requiring $O(n)$ ancilla bits. If no ancillae may be used, the number of controlled-NOT (CNOT) gates is lower bounded at $2n$, although the best-known implementations require a quadratic number of CNOT gates [221].

Circumventing this decomposition has also attracted significant attention. Reference [222] considers a shorter circuit for the two-bit Toffoli gate by requiring one qutrit and Refs. [85, 223, 224] implement a similar scheme, employing superconducting transmon qubits or atoms in coupled cavities. Other proposals rely on the properties of resonant driving, such as the two-bit Toffoli gate using a modified Jaynes-Cummings model [225] or other multiqubit gates in integrable spin chains [226, 227]. References [228–230] describe

a Toffoli gate for general n by exploiting the Rydberg blockade, and Ref. [231] proposes the same gate using trapped ions. Another proposal for the two-bit Toffoli gate using the Rydberg atom is based on Stark-tuned three-body Förster resonances [232]. A recent result in Ref. [233] addresses a driven two-bit Toffoli gate for silicon spin qubits.

This chapter presents a simple single-step implementation of the n-bit Toffoli gate for an arbitrary n. We require a strong, Ising-type coupling between a "target" qubit and n "control" qubits, and then apply a driving field to invert the target qubit selectively. This results in an operation we call *i*Toffoli, which can be straightforwardly mapped into a conventional Toffoli gate by demoting a single qubit to an ancilla. Surprisingly, we find that the gate time and error do not increase with n in theory, which beats previously known results. We critically note that our assumptions may break down at larger system sizes: We require interactions between n qubits and a single target, where the interaction strength should not decrease with n. Moreover, the required driving frequency scales with the number of qubits. Still, the protocol could significantly enhance the capabilities of specific near-term quantum computers [234], and we perform a detailed study of its performance on superconducting circuits. Our simulations find that when decoherence is neglected, the fidelity is approximately constant above 0.995, and when decoherence is included, the *i*Toffoli attains fidelities above 0.98 with up to five control qubits, for gate times of 50 ns. A similar driving approach allows a "fanout" gate, where a CNOT gate takes place between a single control and n target qubits. We discuss its application in error correction, where qubits can be encoded in fewer steps.

The n-bit *i*Toffoli gate is closely related to previous work on multiqubit gates that exploit the Rydberg blockade interaction, especially Ref. [228]. In contrast to such prior art, we do not assume a perfect blockade interaction but consider an Ising model with finite interaction strength, allowing a rigorous analysis of gate times and errors. Moreover, our broader perspective results in the same operation in fewer steps without restricting the study to a single platform.

This chapter is organized as follows: In Section 2.1 we present a simple Hamiltonian and show how it yields an n-bit Toffoli gate. As an example, we consider the $n = 1$ case, which turns out to be identical to the universal Barenco gate. We then discuss the effectiveness of the gate, exploring the important $n = 2$ case as an example in Section 2.1.3. In Section 2.2 we explain how to use the same ideas to implement a CNOT gate on several qubits at the same time. We further, in Section 2.3, present possible implementations of the gates using superconducting circuits. In Section 2.4 we combine the gates and show how to create a more efficient quantum error correction by simulating the three-qubit bit-flip correcting code and the Steane seven-qubit code using our single step gates. In Section 2.5 we provide a summary and outlook.

2.1 Implementation of selective inversion

Consider $n + 1$ qubits each with frequency ω_j. All of the qubits are connected with Ising coupling with strength J_{jk} as described by the Ising Hamiltonian

$$\hat{\mathcal{H}}_{\text{Ising}} = \frac{1}{2} \sum_{j<k=0}^{n} J_{jk} \sigma_j^z \sigma_k^z, \tag{2.1}$$

while the non-interacting part of the Hamiltonian is given as

$$\hat{\mathcal{H}}_0 = -\frac{1}{2}\sum_{j=0}^{n}\omega_j\sigma_j^z, \tag{2.2}$$

where $\sigma^{x,y,z}$ denote the Pauli operators. We denote the quantum states in the computational basis by $|x_0, \boldsymbol{x}\rangle$, where $x_0 \in \{0,1\}$ represents states of the zeroth qubit, which we will call the target qubit, and $\boldsymbol{x} \in \{0,1\}^n$ denotes the string of the state of the remaining qubits, which we call control qubits. These states are eigenstates of $\mathcal{H}_0 + \mathcal{H}_{\text{Ising}}$, whose energies we denote by $E_{x_0,\boldsymbol{x}}$. We drive the zeroth qubit with a field of the form

$$\hat{\mathcal{H}}_{\text{drive}} = \alpha_0(t)\sigma_0^x + \beta_0(t)\sigma_0^y. \tag{2.3}$$

When the driving is included in the Hamiltonian, the Hilbert space decomposes into conserved subspaces, one for each $\boldsymbol{x}$. Each of these subspaces is spanned by $|0,\boldsymbol{x}\rangle$ and $|1,\boldsymbol{x}\rangle$. We define the energy gap between such two states due to the Ising interaction, as

$$\Delta_{\boldsymbol{x}} = E_{0,\boldsymbol{x}} - E_{1,\boldsymbol{x}} + \omega_0 = \sum_{j=1}^{n} J_{j0}(-1)^{\boldsymbol{x}_j}, \tag{2.4}$$

where $\boldsymbol{x}_j$ denotes the jth entry in the string of control qubit states. Similarly, we define the mean energy as $\bar{E}_{\boldsymbol{x}} = (E_{0,\boldsymbol{x}} + E_{1,\boldsymbol{x}})/2$. The Hamiltonian of a given subspace is then

$$\hat{\mathcal{H}}_{\boldsymbol{x}} = \frac{1}{2}(\Delta_{\boldsymbol{x}} - \omega_0)\sigma^z + \alpha(t)\sigma^x + \beta_0(t)\sigma^y + \bar{E}_{\boldsymbol{x}}\mathbb{1}_2. \tag{2.5}$$

Here $\mathbb{1}_2$ denotes the two-dimensional identity matrix.

We now consider the driving fields. In general different combinations of the driving fields, $\alpha_j(t)$ and $\beta_j(t)$ will lead to the same result, and here we consider a balanced two quadrature driving

$$\begin{aligned}\alpha_0(t) &= \Omega\cos\left[(\Delta_0 - \omega_0)t + \theta\right],\\ \beta_0(t) &= \Omega\sin\left[(\Delta_0 - \omega_0)t + \theta\right],\end{aligned} \tag{2.6}$$

where Δ_0 is the driving frequency of qubit 0, Ω is the Rabi frequency, and θ is the driving phase. We now transform into the rotating frame using the transformation

$$\hat{\mathcal{U}}_{\text{int}}(t) = \exp\left(i\left[\hat{\mathcal{H}}_0 + \frac{1}{2}\Delta_0\sigma_0^z + \sum_{\boldsymbol{x}\in\{0,1\}^n}\bar{E}_{\boldsymbol{x}}\,|\boldsymbol{x}\rangle\langle\boldsymbol{x}|\right]t\right). \tag{2.7}$$

In this frame, for each subspace labeled by $\boldsymbol{x}$, the Hamiltonian takes the form,

$$\hat{\mathcal{H}}_{\boldsymbol{x},I} = \delta_{\boldsymbol{x}}\sigma_0^z + \Omega(\sigma_0^x\cos\theta + \sigma_0^y\sin\theta), \tag{2.8}$$

where $\delta_{\boldsymbol{x}} = (\Delta_{\boldsymbol{x}} - \Delta_0)/2$ defines the detuning. With the now time-independent Hamiltonian we can calculate the time evolution operator for all two-dimensional subspaces

$$\hat{\mathcal{U}}(t) = \bigoplus_{\boldsymbol{x}\in\{0,1\}^n}\left(\mathbb{1}_2\cos v_{\boldsymbol{x}}t - i\frac{\boldsymbol{\sigma}\cdot\boldsymbol{v}_{\boldsymbol{x}}}{v_{\boldsymbol{x}}}\sin v_{\boldsymbol{x}}t\right), \tag{2.9}$$

where $\boldsymbol{\sigma} = (\sigma^x, \sigma^y, \sigma^z)$, and

$$\boldsymbol{v}_{\boldsymbol{x}} = \begin{bmatrix} \Omega\cos\theta \\ \Omega\sin\theta \\ \delta_{\boldsymbol{x}} \end{bmatrix}, \tag{2.10}$$

with $v_{\boldsymbol{x}} = |\boldsymbol{v}_{\boldsymbol{x}}|$ being the length of the vector.

It follows from Eq. (2.9) that we have obtained selective state inversion. In order to see this, we consider the case where the driving frequency is resonant with an energy gap of a single subspace $\boldsymbol{x}'$, i.e., $\Delta_0 = \Delta_{\boldsymbol{x}'}$, in which case we obtain a rotation around a vector in the x-y plane, leading to a perfect inversion at times $T = (2m+1)\pi/2\Omega$ for $m \in \mathbb{Z}$, where the time-evolution operator of that subspace takes the form

$$\hat{\mathcal{U}}_{\boldsymbol{x}'}(t = T) = \pm i\left(\sigma^x\cos\theta + \sigma^y\sin\theta\right). \tag{2.11}$$

The remaining off-resonant subspaces, i.e., assuming $|\Omega| \ll |\Delta_0 - \Delta_{\boldsymbol{x}}|$, evolve approximately as if no driving takes place:

$$\hat{\mathcal{U}}_{\boldsymbol{x}}(t = T) \approx \exp(-i\delta_{\boldsymbol{x}}\sigma^z t). \tag{2.12}$$

Thus we conclude that if we set $\Delta_0 = \Delta_{\boldsymbol{x}'}$, we obtain an inversion of the resonant subspaces, while the off-resonant subspaces are not inverted.

Note that we do not require the J_{jk}s to be equal, but we do require them to be larger than the Rabi frequency, i.e., $J_{jk} \gg \Omega$, to satisfy the off-resonance condition. We further note that if instead of the two quadratures in Eq. (2.6), we had used one quadrature driving, i.e., $\beta(t) = 0$, we would have had two driving fields of opposite sign:

$$\alpha(t) = 2\Omega\left(e^{i(\Delta_0-\omega_0)t} + e^{-i(\Delta_0-\omega_0)t}\right). \tag{2.13}$$

When $\omega_0 = 0$, there would be two resonant subspaces in which the zeroth qubit is inverted. This problem is fixed by demanding a relatively large frequency of the zeroth qubit, $\omega_0 \gg \Omega$. Moreover, in the case $\beta = 0$ the above results are then no longer exact, but remain valid if the rotating-wave approximation ($\Delta_{\boldsymbol{x}}, \Delta_0 \gg \Omega$) applies.

2.1.1 The Barenco gates

There is no two-qubit gate in classical reversible computing that is both universal and reversible. However, in quantum computing, any entangling two-qubit gate is universal when assisted by one-qubit gates [235, 236]. Some two-qubit gates are even universal on their own. The first two-qubit gates, which were shown to be universal, were the family of Barenco gates [237], and it turns out that our implementation above yields exactly such gates for $n = 1$. Therefore, and for the sake of an example, we discuss the $n = 1$ more in-depth.

Consider the Hamiltonian $\hat{\mathcal{H}} = \hat{\mathcal{H}}_0 + \hat{\mathcal{H}}_{\text{Ising}} + \hat{\mathcal{H}}_{\text{drive}}$ for $n = 1$. In this case the Hamiltonian splits up into two subspaces: $\{|00\rangle, |10\rangle\}$ and $\{|01\rangle, |11\rangle\}$. We now transform into the interacting picture using the transformation

$$\hat{\mathcal{U}}_{\text{int}} = \exp\left[\hat{\mathcal{H}}_0 - \delta_1\sigma_1^z + \frac{1}{2}\delta_1\mathbb{1}_4 + \Delta_0\sigma_0^z\sigma_1^z\right], \tag{2.14}$$

where δ_1 is some detuning from the frequency of the control qubit. Now, if we require the driving to be on resonance with the target qubit, i.e., $\Delta_0 = -J_{10}$ then the interacting Hamiltonian takes the form

$$\hat{\mathcal{H}}_I = \delta_1(|01\rangle\langle 01| + |11\rangle\langle 11|) + \Omega(\sigma^+ e^{-i\theta} + \sigma^- e^{i\theta}). \tag{2.15}$$

Exponentiating this to get the time evolution operator we obtain

$$\hat{\mathcal{U}}(t) = \begin{bmatrix} 1 & 0 & 0 & 0 \\ 0 & 1 & 0 & 0 \\ 0 & 0 & e^{i\delta_1 t}\cos\Omega t & -ie^{i(\delta_1 t-\theta)}\sin\Omega t \\ 0 & 0 & -ie^{i(\delta_1 t+\theta)}\sin\Omega t & e^{i\delta_1 t}\cos\Omega t \end{bmatrix}, \tag{2.16}$$

which is identical to the family of Barenco gates.

As the Barenco gates are closely related to the Deutsch gate, this begs the question whether our implementation yields a Deutsch gate for $n = 2$. However, this turns out not to be the case; there is a phase of i to differ.

2.1.2 The $(n-1)$-bit Toffoli gate

To form an approximate Toffoli gate with n control qubits, we choose the driving frequency Δ_0 to be such that the zeroth qubit flips if and only if all control qubits are in the state $|1\rangle$, i.e., $\Delta_0 = \Delta_{11\ldots1}$. Equations (2.11) and (2.12) suggest that we have indeed obtained the aimed operation. However, moving back from the rotating frame to the laboratory frame using $\hat{\mathcal{U}}_{\boldsymbol{x},\text{lab}} = \hat{\mathcal{U}}^\dagger_{\text{int}}(t)\hat{\mathcal{U}}_{\boldsymbol{x}}$ [see Eq. (2.7)], we encounter two discrepancies:

(i) The additional phases $\exp(-iE_{x_0,\boldsymbol{x}}T)$ accumulated on each computational basis state due to $\hat{\mathcal{H}}_{\text{Ising}}$.

(ii) The additional phase $-i$ in the resonant subspace $\boldsymbol{x} = 1\ldots1$. (note that this is *not* a global phase).

Note that such phases in the laboratory frame become relevant when subsequent non-commuting operations are performed.

The 2^{n+1} different energies $E_{x_0,\boldsymbol{x}}$ can in general be hard to compute for a large system. Undoing them may be even harder. However, one can conceive various specific configurations where resetting the phases is possible. In particular, whenever the Ising couplings J_{jk} are symmetric under permutations on the control qubits, then the evolution depends only on the Hamming weight (the number of qubits in state $|1\rangle$) of the control qubits, which we define as $q = |\boldsymbol{x}|_H$. In such cases, only $n+1$ subspaces are unique, and hence only $n+1$ relative phases have to be considered. Various techniques can then be used to undo these dynamic phases. One example is to choose a total gate time T such that all phases $E_{x_0,\boldsymbol{x}}T$ become a multiple of 2π. For example, when all J_{jk} are integer multiples of some energy scale J, then the values of $E_{x_0,\boldsymbol{x}}$ are also integer multiples of $2J$ such that a total driving time $T = 2k\pi/J$ ($k \in \mathbb{N}$) gets rid of unwanted phases. Note that random experimental imperfections in J_{jk} may still cause the fidelity of such phase recurrences to be affected. A different strategy is to invert the sign of all J_{jk} halfway through the protocol [227]. This undoes the accumulated phases, although care has to be taken to change the

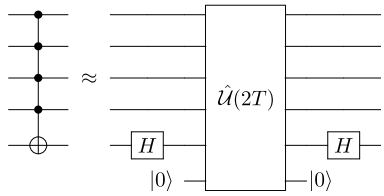

Figure 2.1: *Circuit that turns two applications of the iToffoli (here indicated as the result of our protocol, with total time $2T = \pi/\Omega$ and arbitrary θ) into a conventional Toffoli gate, at the cost of a single ancilla. The Hs denote Hadamard gates.*

phase θ of the resonant driving fields such that the previously caused rotation on the zeroth qubit is not counteracted.

Assuming that we removed the phases due to $\hat{\mathcal{H}}_{\text{Ising}}$, e.g., by transforming into the frame rotating with $\hat{\mathcal{H}}_{\text{Ising}}$, we turn to removing the phase $-i$. This phase results from evolution by a Hamiltonian with trace 0, which generates unitaries with determinant 1. We will refer to the operation that acts as $-i\sigma^x$ on the target, if and only if all controls are in the state $|1\rangle$. To turn this into a conventional Toffoli gate, we propose the circuit in Fig. 2.1, which employs a single ancilla qubit and requires a Hadamard gate before and after our gate. Applying the resonant operation twice leads to a phase -1 in the resonant subspace. This is similar to a multiple-controlled Z gate except that the sign is applied both when the target is in state $|0\rangle$ and when it is in state $|1\rangle$. Hence, we obtain a multiple-controlled Z gate which applies a sign -1 to the control qubits if and only if all these qubits are in the state $|1\rangle$. The state of the target is unimportant, and we may just as well initialize it to $|0\rangle$ before the protocol. Finally, the controlled Z gate is mapped to a controlled X gate by using two Hadamard gates; these can be applied to any control qubit, which then takes the role of target of the resultant $(n-1)$-bit Toffoli gate.

2.1.3 Simulation of the two-bit *i*Toffoli gate with decoherence

To illuminate the system's performance in a practical setting, we simulate our protocol for the *i*Toffoli gate under realistic decoherence for $n = 2$. We characterize the performance of the gate by calculating the average process fidelity, which is defined as [238, 239]:

$$\bar{F} = \int d\psi \langle\psi|\hat{\mathcal{U}}_{\text{target}}^{\dagger}\mathcal{E}(\psi)\hat{\mathcal{U}}_{\text{target}}|\psi\rangle, \tag{2.17}$$

where integration is performed over the subspace of all possible initial states, $\hat{\mathcal{U}}_{\text{target}}$ is the target gate, and $\mathcal{E}$ is the quantum map realized by our system. We simulate the system using the Lindblad master equation (see Section 1.9) and the interaction Hamiltonian of Eq. (2.8) using the QuTiP Python toolbox [240]. The result is then transformed into the frame rotating with the diagonal of the Hamiltonian, and then the average process fidelity is calculated using the simplified formula found be Ref. [241]

$$\bar{F}(t) = \frac{1}{5} + \frac{1}{80}\sum_{j=1}^{16} \text{Tr}\left(\hat{\mathcal{U}}_{\text{target}} U_j^{\dagger} \hat{\mathcal{U}}_{\text{target}}^{\dagger} \mathcal{E}_t(\hat{\mathcal{U}}_j)\right), \tag{2.18}$$

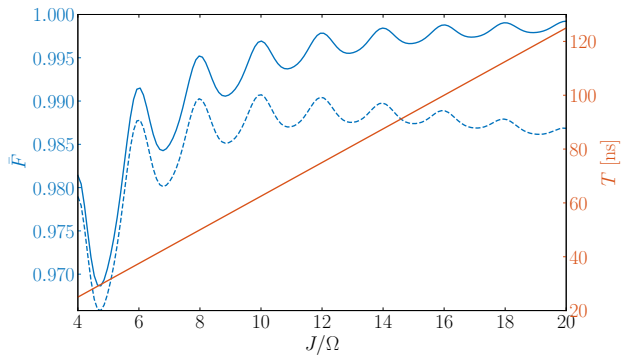

Figure 2.2: *Simulation of the two-bit iToffoli gate for different values of the driving J. The straight red line indicates the gate time T on the right y axis, while the blue lines indicate the average fidelity, at the gate time, on the left y axis. The dashed blue line is the average fidelity with a decoherence time of $T_1 = T_2 = 30\,\mu s$, while the solid line is without decoherence.*

which evaluates how well a quantum map, $\mathcal{E}_t$, approximates the target gate, $\hat{\mathcal{U}}_{\text{target}}$, over a uniform distribution of input quantum states, $\hat{\mathcal{U}}_j$. The target operator is the time evolution operator in Eq. (2.9).

We choose parameters that lie in a realistic range for a superconducting circuit experiment for all simulations. However, our simulation is done for the general Hamiltonian and thus valid for any implementation with identical parameters. In particular we have $J_{0k}/2\pi = J/2\pi = 40\,\text{MHz}$ and all other couplings are zero, while we change the Rabi frequency $\Omega/2\pi$ from 2 to 10 MHz. The average fidelity of the simulation can be seen in Fig. 2.2 together with the gate time. The figure shows the average fidelity both without any decoherence and with decoherence times of $T_1 = T_2 = 30\,\mu s$ [53], where T_1 indicates the relaxation time and T_2 indicates the dephasing time. Without any decoherence, we find that the average fidelity increases asymptotically towards unity as the driving decreases, with the only expense being an increase in gate time. Since decoherence increases over time, a longer gate time means lower fidelity, which we observe when including decoherence in the simulations. In this case we find that the fidelity peaks just above 0.99 at $J/\Omega = 8$, which yields a gate time of $T = 62.5\,\text{ns}$. This fidelity is higher than any previously measured Toffoli gate fidelities [232, 242]. However, we note that the fidelity is dependent on the parameters J and Ω, and thus changing these will change the fidelity. The oscillation of the average fidelity is due to a minor mismatch in the phase of the evolved state compared to the desired gate, which disappears when $J/\Omega \in 2\mathbb{Z}$.

As an indication of the fidelity of a conventional Toffoli gate, we simulate the same protocol for time $2T$ (see Fig. 2.1), resulting in still above 0.98 fidelity. An additional two Hadamard gates should still be applied, but we remain agnostic to the errors these would introduce.

We investigate the peak fidelity of the n-bit iToffoli gate as a function of the number of control qubits. This is done by simulating the gate for different n but with $J/\Omega = 8$

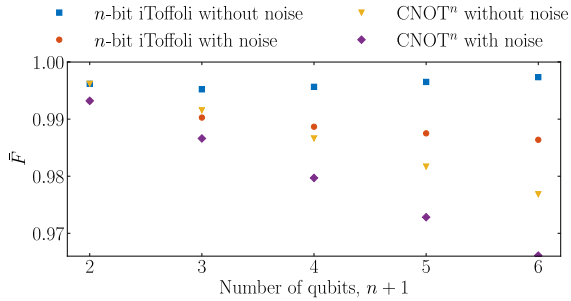

Figure 2.3: *Average fidelity as a function of the number of qubits for the n-bit iToffoli gate and the* CNOT^n *gate. Simulations done with noise have a decoherence time of* $T_1 = T_2 = 30\,\mu s$. *All simulations are done with* $J/\Omega = 8$, *i.e., peak fidelity (cf. Fig. 2.2). Note that the one-bit iToffoli and* CNOT^1 *are the same gate, which is an example of a Barenco gate.*

in all cases. The result is shown in Fig. 2.3. We find that when we omit the decoherence of the qubits, the average fidelity [found using Eq. (2.18)] increases when there are more than two control qubits, and we stay above 0.995 fidelity for all cases. When decoherence is included, the fidelity decreases as the number of qubits increases, as one would expect. Thus we conclude that the major contribution to errors in the scheme is the decoherence of the qubits.

2.2 A single control, multiple inversion gate

Multiple applications of a controlled-NOT gate on several different qubits, with the same qubit controlling all the gates, are essential in many aspects of quantum information, particularly in error correction such as Shor's code [87]. We, therefore, present a scheme for implementing inverting multiple qubits with the same control qubit in a single step. We will refer to this scheme as a CNOT^n-gate, but it is also often known as a fan-out gate.

Starting with $n+1$ qubits, we employ the same overall Hamiltonian as in Section 2.1, $\hat{\mathcal{H}} = \hat{\mathcal{H}}_0 + \hat{\mathcal{H}}_{\text{Ising}} + \hat{\mathcal{H}}_{\text{drive}}$, where $\hat{\mathcal{H}}_0$ and $\hat{\mathcal{H}}_{\text{Ising}}$ are given in Eqs. (2.1) and (2.2), respectively, while we require $J_{jk} = 0$ for $k > 0$. The driving Hamiltonian is now given as

$$\hat{\mathcal{H}}_{\text{drive}} = \sum_{j=1}^{n} \left[\alpha_j(t)\sigma_j^x + \beta_j(t)\sigma_j^y \right]. \tag{2.19}$$

where the driving fields are given as in Eq. (2.6). This is essentially identically to the system in Section 2.1; however, now with driving on what was before denoted the control qubits. We, therefore, denote our quantum states in the same way as before, $|x_0, \boldsymbol{x}\rangle$; however, now we are interested in flipping the qubits in the state $\boldsymbol{x}$ conditional on the state of the zeroth qubit x_0. This means that the Hilbert space only decomposes into two conserved subspaces, one spanned by $\{|0, \boldsymbol{x}\rangle\}$, and one spanned by $\{|1, \boldsymbol{x}\rangle\}$. We now transform into

a rotating frame using the transformation

$$\hat{\mathcal{U}}_{\text{int}}(t) = \exp\left(i \left[\hat{\mathcal{H}}_0 + \frac{1}{2} \sum_{j=1}^{n} J_{j0} \sigma_j^z \sigma_0^z \right] t \right). \tag{2.20}$$

In this frame the Hamiltonian takes the form

$$\hat{\mathcal{H}}_I = \sum_{j=1}^{n} \Omega \left\{ \sigma_j^x \cos\left[(\Delta_j - J_{j0}\sigma_0^z)t + \theta_j \right] + \sigma_j^y \sin\left[(\Delta_j - J_{j0}\sigma_0^z)t + \theta_j \right] \right\}, \tag{2.21}$$

from which we see that we obtain selective inversion of the n qubits, at time $T = (2m + 1)\pi/2\Omega$, if we require $\Delta_j = -J_{j0}$. The time evolution operator takes the form

$$\hat{\mathcal{U}}(t = T) = |0\rangle\langle 0|_0 \bigotimes_{j=1}^{n} \hat{I}_j + (-i)^n |1\rangle\langle 1|_0 \bigotimes_{j=1}^{n} \left(\sigma_j^x \cos\theta_j + \sigma_j^y \sin\theta_j \right), \tag{2.22}$$

where $\hat{I}_j$ is the identity of the jth qubit and $|0\rangle\langle 0|_0$ and $|1\rangle\langle 1|_0$ operate only on the zeroth qubit. We find that the phase $(-i)^n$ on the inverting part of the operator is now dependent on the number of target qubits. In this case, it is canceled by a single-qubit phase gate of the form $\text{diag}(1, i^n)$ on the control qubit. Note that in the case of an even number of qubits, the phase is either ± 1, which can be taken care of by choosing suitable phases θ_j, in which case the single-qubit phase gate is unnecessary.

Since the only difference between the Hamiltonian of the CNOT^n gate and the n-bit Toffoli gate in Section 2.1 is which qubits are being driven, a numerical simulation of the CNOT^n gate as a function of the ratio J/Ω yields an average fidelity comparable to the one for the n-bit iToffoli gate in Fig. 2.2. However, the CNOT^n gate has a slightly lower fidelity since more qubits are now inverted. The peak average fidelity can be seen in Fig. 2.3, where the average fidelity decreases as a function of the number of qubits. This behavior is expected since the CNOT^n gate does not approximate the identity better for larger n. Note that the one-bit iToffoli gate is the same as the CNOT gate, which is why the average fidelities are identical in this case. This is also the fidelity one gets when simulating the Barenco gate in Section 2.1.1.

2.3 Superconducting circuit implementation

The ideas presented here are applicable in various quantum information technologies, e.g., ultracold atoms of the Rydberg type, which natively feature a strong Ising-type interaction [243] or trapped ions which are very well suited to simulate the Ising model with all-to-all connectivity [244].

Notwithstanding, we focus on implementing the gates using superconducting circuits, which is the technology in focus in this thesis. Such an implementation would require quite large longitudinal ZZ couplings, in the sense that they must dominate over the transversal XX couplings. For superconducting circuits, this regime is within experimental reach according to Ref. [193].

We propose to implement the n-bit Toffoli gate and the CNOT^n gate by connecting n transmon qubits via Josephson junctions (with as small a parasitic capacitance as possible)

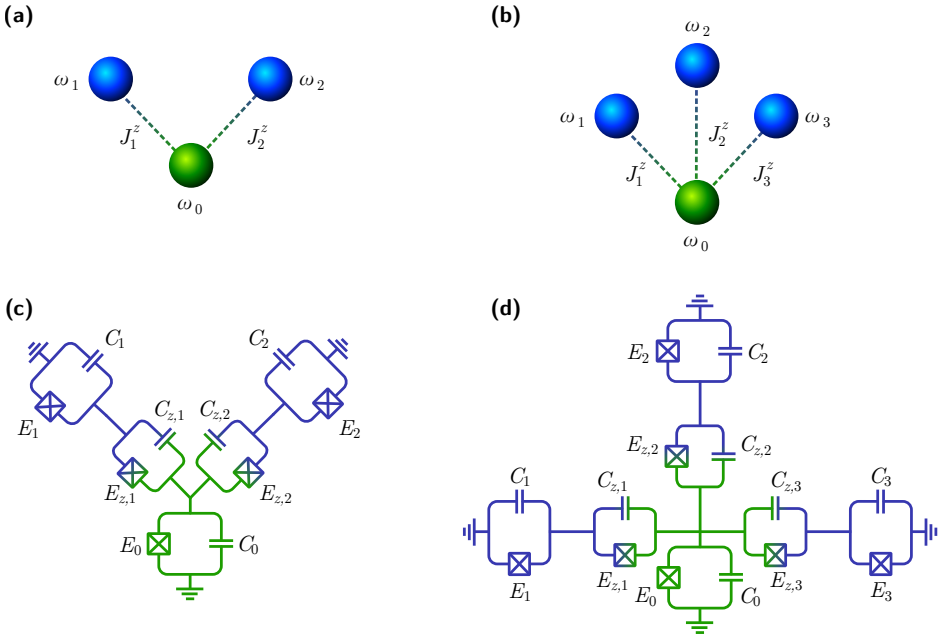

Figure 2.4: *Schematics of* **(a)** *the two-bit and* **(b)** *the three-bit iToffoli gates with the green spheres (ω_0) representing the target qubit and the blue spheres representing the control qubits. Also shown are* **(c)** *and* **(d)** *the superconducting circuits yielding the models in* **(a)** *and* **(b)**, *respectively. The different parts of the system are colored according to their role, as per* **(a)** *and* **(b)**.

to another transmon qubit, which we call the zeroth transmon, in correspondence with the naming of the qubits in Section 2.1. This can be seen for $n = 2$ and 3 in Fig. 2.4. Following the approach presented in Section 1.2.3 we obtain the Lagrangian for the circuit

$$\mathcal{L} = 2\sum_{i=0}^{n} C_i \dot{\phi}_i^2 + 2\sum_{i=1}^{n} C_{z,i}\left(\dot{\phi}_i - \dot{\phi}_0\right)^2 + \sum_{i=0}^{n} E_i \cos\phi_i + \sum_{i=1}^{n} E_{z,i}\cos(\phi_0 - \phi_i), \tag{2.23}$$

where $\hat{\phi}_i$ are the node fluxes across the Josephson junctions of the respective qubits. The first two terms come from the capacitors and are interpreted as kinetic terms, and the remaining terms come from the Josephson junctions and are interpreted as potential terms. The n indicates the number of blue transmon qubits on the circuit diagram, i.e., in Fig. 2.4(c) $n = 2$.

The Lagrangian can be rewritten into the Hamiltonian doing the Legendre transformation in Section 1.2.4

$$\mathcal{H} = \frac{1}{2}\boldsymbol{q}^T\boldsymbol{C}^{-1}\boldsymbol{q} - \sum_{i=0}^{n} E_i \cos\phi_i - \sum_{i=1}^{n} E_{z,i}\cos(\phi_0 - \phi_i), \tag{2.24}$$

where the capacitance matrix in the two-bit case [Fig. 2.4(c)] is

$$\boldsymbol{C} = \begin{bmatrix} C_0 + C_{z,1} + C_{z,2} & -C_{z,1} & -C_{z,2} \\ -C_{z,1} & C_1 + C_{z,1} & 0 \\ -C_{z,2} & 0 & C_2 + C_{z,2} \end{bmatrix}, \tag{2.25}$$

while in the three-bit case [Fig. 2.4(d)] it becomes

$$\boldsymbol{C} = \begin{bmatrix} C_0 + C_{z,1} + C_{z,2} + C_{z,3} & -C_{z,1} & -C_{z,2} & -C_{z,3} \\ -C_{z,1} & C_1 + C_{z,1} & 0 & 0 \\ -C_{z,2} & 0 & C_2 + C_{z,2} & 0 \\ -C_{z,3} & 0 & 0 & C_3 + C_{z,3} \end{bmatrix}, \tag{2.26}$$

and so on for higher n. The typical transmon has a charging energy much smaller than the junction energy, and therefore the phase is well localized near the bottom of the potential. We can therefore expand the potential part of the Hamiltonian to fourth order

$$U(\phi) = \sum_{i=0}^{n} E_i \left[\frac{1}{2}\phi_i^2 - \frac{1}{24}\phi_i^4 \right] + \sum_{i=1}^{n} E_{z,i} \left[\frac{1}{2}\left(\phi_i - \phi_0\right)^2 - \frac{1}{24}\left(\phi_i - \phi_0\right)^4 \right].$$

By collecting terms we write the full Hamiltonian as

$$\begin{aligned} \mathcal{H} = &\sum_{i=0}^{n} \left[\frac{1}{2}E_i^C q_i^2 + \frac{1}{2}E_i^J \phi_i^2 - \frac{1}{24}E_i^J \phi_i^4 \right] + \sum_{i=1}^{n} (\boldsymbol{C}^{-1})_{(i,0)} q_i q_0 \\ &+ \sum_{i>j=1}^{n} (\boldsymbol{C}^{-1})_{(i,j)} q_i q_j + \sum_{i=1}^{n} E_{z,i} \left[-\frac{1}{4}\phi_i^2 \phi_0^2 - \phi_i \phi_0 + \frac{1}{6}\left(\phi_i^3 \phi_0 + \phi_i \phi_0^3 \right) \right], \end{aligned}$$

where the effective energy of the capacitances is $E_i^C = (\boldsymbol{C}^{-1})_{(i,i)}/8$. Note that there is a capacitive coupling between all of the qubits regardless of whether there is a capacitor between them. The effective Josephson energies are

$$E_i^J = E_i + E_{z,i} \quad \text{for } i \neq 0, \tag{2.27a}$$

$$E_0^J = E_0 + \sum_{i=1}^{n} E_{z,i}. \tag{2.27b}$$

We can now quantize the Hamiltonian following the approach in Section 1.3.1 and then change into annihilation and creation operators, and if the anharmonicities $\alpha_i = E_i^C/2$ of the qubits are sufficiently large, we can justify projecting the Hamiltonian in the lowest two eigenstates of each qubit (Section 1.6.1)

$$\begin{aligned} \hat{\mathcal{H}} = &-\frac{1}{2}\sum_{i=0}^{n} \omega_i \sigma_i^z + \frac{1}{2}\sum_{n=1}^{n} J_i^z \sigma_i^z \sigma_0^z + \frac{1}{2}\sum_{i=1}^{n} J_i^x \left(\sigma_i^+ \sigma_0^- + \sigma_i^- \sigma_0^+ \right) \\ &+ \frac{1}{2}\sum_{i\neq j=1}^{n} J_{ij}^x \left(\sigma_i^+ \sigma_j^- + \sigma_i^- \sigma_j^+ \right), \end{aligned} \tag{2.28}$$

where we neglect terms that do not conserve number excitation. We note that the first term is the desired non-interacting Hamiltonian, and the second term is the desired Ising

coupling term. The qubit frequencies and the coupling strengths are given as

$$\omega_i = \sqrt{8E_i^C E_i^J} + \frac{1}{2}E_i^C + \frac{1}{6}E_{z,i}\zeta_i\zeta_0 \quad \text{for } i \neq 0, \tag{2.29a}$$

$$\omega_0 = \sqrt{8E_0^C E_0^J} + \frac{1}{2}E_0^C + \frac{1}{6}\sum_{i=1}^{n} E_{z,i}\zeta_i\zeta_0, \tag{2.29b}$$

$$J_i^z = -\frac{1}{12}E_{z,i}\zeta_i\zeta_0, \tag{2.29c}$$

$$J_i^x = \frac{(\boldsymbol{C}^{-1})_{(i,0)}}{\sqrt{\zeta_i\zeta_0}} - E_{z,i}\sqrt{\zeta_i\zeta_0} + \frac{1}{4}E_{z,i}(\zeta_i + \zeta_0)\sqrt{\zeta_i\zeta_0}, \tag{2.29d}$$

$$J_{ij}^x = \frac{(\boldsymbol{C}^{-1})_{(i,j)}}{\sqrt{\zeta_i\zeta_j}}, \tag{2.29e}$$

where the impedance is given as in Eq. (1.56).

If we operate in the weak-coupling regime for the transversal couplings $C_{z,i} \ll C_0, C_i$, for all i, the detuning $\delta_{i0} = \omega_i - \omega_0$, of the zeroth qubit compared to all other qubits, becomes much larger than the transverse couplings in Eq. (2.29d). We can then ignore the first-order excitation swaps between these qubits using the rotating wave approximation. In this case, the Hamiltonian takes the form

$$\hat{\mathcal{H}} = \hat{\mathcal{H}}_0 + \frac{1}{2}\sum_{n=1}^{n} J_i^z \sigma_i^z \sigma_0^z + \frac{1}{2}\sum_{i\neq j=1}^{n} J_{ij}^x \left(\sigma_i^+\sigma_j^- + \sigma_i^-\sigma_j^+\right). \tag{2.30}$$

The last term represents the cross-couplings between the ith and jth qubit for $i, j = 1, 2, \ldots, n$. We get rid of this term as we are in the weak-coupling limit, $C_{z,i} \ll C_i$, which makes the Hamiltonian take the desired form.

Finally, we can engineer the driving term $\hat{\mathcal{H}}_{\text{drive}}$ using the microwave approach presented in Section 1.7. In Appendix B we present realistic parameters for the circuit model which realizes the desired iToffoli gate.

2.4 Applications within quantum error correction

In this section, we discuss how to use the results in this chapter to create an efficient error correction code. We consider the three-qubit bit-flip code [87] and the Steane seven-qubit code [245, 246]. We focus on bit flip rather than phase errors in the three-qubit code since the decay time for relaxation is usually half the decay time for dephasing in the case of transmons [151, 247]. One can, however, easily change the code into correcting phase errors by applying Hadamard gates around the source of error [87]. This could be useful in an implementation of a 0-π qubit, which has a long relaxation time but a rather short dephasing time [182, 183, 248]. The three-qubit code has previously been implemented using superconducting circuits to a fidelity of 0.85 [223] and with trapped ions to a fidelity of approximately 0.98 [249]. The Steane seven-qubit code has been implemented with a state fidelity between 0.85 and 0.95 using trapped ions [250].

In the following, all simulations are done without worrying about the phase generated by the inverting, i.e., it is done with the iToffoli gate, as it is irrelevant for the

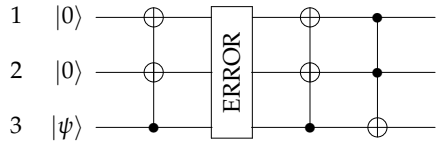

Figure 2.5: *Effective three-qubit error correction code using two* CNOT^2 *gates and a Toffoli gate. We label the top qubit 1, the middle qubit 2, and the lowest qubit 3. Note that the figure is shown with regular Toffoli gates, while our simulation is done with the iToffoli gates; however, it does not change the result.*

encoding. The error correction codes are simulated using the Lindblad master equation using the QuTiP toolbox [240]. All Ising couplings are assumed to be $J/2\pi = 40\,\mathrm{MHz}$.

2.4.1 Three-qubit bit flip code

The original three-qubit bit-flip code works by first applying two CNOT gates before the error source, and then two CNOT gates are followed by a single two-bit Toffoli gate. This means a total of five steps. However, using our results, the code can be performed in merely three steps: apply a single CNOT^2 gate before the source of error, a single CNOT^2 gate after the error, and finally a single n-bit Toffoli gate. A quantum circuit of the error-correcting code can be seen in Fig. 2.5.

The first two qubits are initiated in the state $|0\rangle$, while the third qubit is initiated in the normalized state

$$|\psi\rangle = \alpha\,|0\rangle + \beta\,|1\rangle\,. \tag{2.31}$$

The system is then operated as a CNOT^2 gate by driving the first two qubits with an Rabi frequency of $\Omega = J/8$ for one period, i.e., $T = 50\,\mathrm{ns}$. After this, a bit-flip error might occur. This is followed by another driving of the two first qubits for one period. Finally, the last qubit is driven for one period. All this is done in 150 ns. By averaging over the Bloch sphere for the input state $|\psi\rangle$ in Eq. (2.31) we find the average fidelity of the code. In Fig. 2.6 we present the average fidelities for the three-qubit error correction code for a single bit flip on the different bits. The simulation shows that the error is corrected with a fidelity above 0.99.

2.4.2 Steane code

The Steane code is a bit more intricate than the three-qubit code because it encodes seven qubits. This is two more than the minimum number of qubits needed for protection against both bit-flip and phase errors [87], but it is the simplest Calderbank-Shor-Steane (CSS) code (stabilizers built from only either Z or X rotations) that protects against both bit-flip and phase errors. The encoding scheme for the Steane code can be seen in Fig. 2.7.

As the encoding scheme only uses CNOT^2 and CNOT^3 gates, it is necessary to be able to perform gate operations on some of the seven qubits but not all. This can be achieved *in situ* in superconducting circuits by varying the magnetic flux through the Josephson junctions, which connects qubits that are desired unconnected. An overview of how to connect the seven qubits in the four steps of the encoding can be seen in Fig. 2.8.

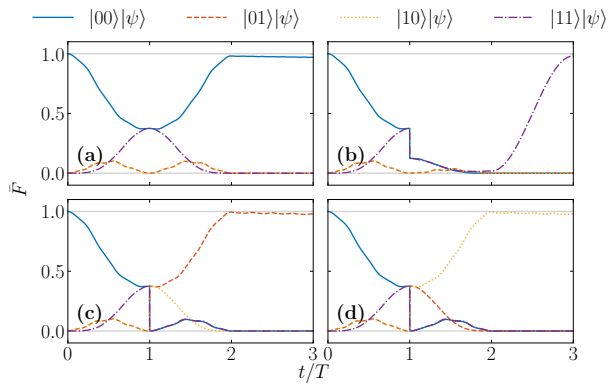

Figure 2.6: *Average fidelity [Eq. (2.18)] of different states found by simulating the quantum error correction code shown in Fig. 2.5 using the gates developed in the previous sections:* **(a)** *no error,* **(b)** *error on the first qubit,* **(c)** *error on the second qubit,* **(d)** *error on the third qubit.*

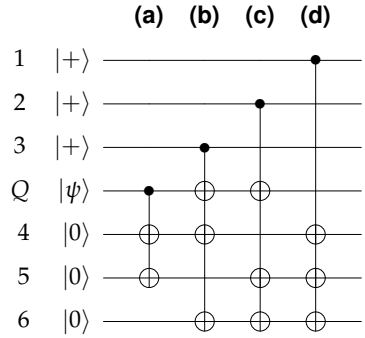

Figure 2.7: *Encoding scheme for the Steane code. Qubit Q is initially in state $|\psi\rangle$, and the circuit encodes it into a seven-qubit state using one* CNOT^2 *gate and three* CNOT^3 *gates. The first three qubits are prepared in the state $|+\rangle = (|0\rangle + |1\rangle)/\sqrt{2}$, while the last three qubits are prepared in the state $|0\rangle$.*

Using the regular CNOT gate, the Steane encoding takes 11 steps, while with CNOT^n gates, it can be done in just four steps.

Seven qubits are initialized, three in the state $|+\rangle = (|0\rangle + |1\rangle)/\sqrt{2}$ and three in the state $|0\rangle$, while the last qubit is prepared in the state of Eq. (2.31). The driving of the target qubits is the same for all steps, yielding a total time of $4T$ for the encoding. We average over the Bloch sphere for the input state $|\psi\rangle$ in order to find the average fidelity. The fidelity is found by taking the overlap between the seven-qubit output state and the state $\alpha\,|0\rangle_L + \beta\,|1\rangle_L$, where the expressions for the two states $|0\rangle_L$ and $|1\rangle_L$ are the appropriate encoding states for the Steane code when the encoding is done with *i*Toffoli gates. We absorb the additional phases i^n that come with our driven protocol into the definitions of $|0\rangle_L$ and $|1\rangle_L$. These additional phases do not change the error-correcting

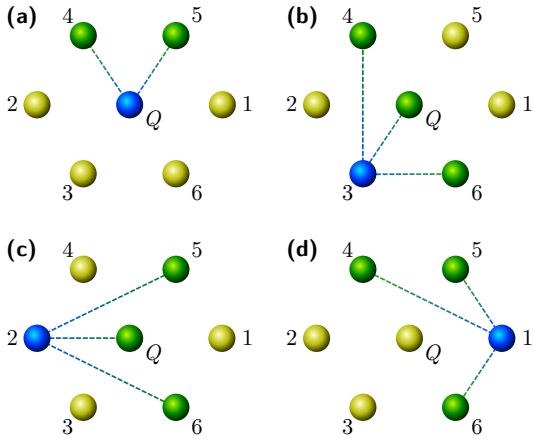

Figure 2.8: *The four steps realizing the Steane code using* CNOT^n *gates. Green spheres (spheres with one connection) represent target qubits, i.e., qubits on which the* NOT *operation is performed, blue spheres (spheres with multiple connections) are control qubits, and the yellow spheres (unconnected spheres) represents idle qubits. The four steps* **(a)**-**(d)** *corresponds to the four gates in Fig. 2.7.*

properties of the code; see the appendix of [**V**].

The results of the simulation can be seen in Fig. 2.9. The result is similar to the one presented in Fig. 2.2, however, with longer gate times and lower fidelities. When not considering decoherence, the lower fidelity is also a result of the fact that we need four gates, and thus the infidelities of all gates accumulate. The fidelity peaks below 0.9 when including decoherence in the simulation, which is lower than before because more qubits are subjected to decoherence. The longer gate time is a result of the fact that we are now dealing with four gates, compared to one in Fig. 2.2. However, this is still a relatively short time compared to if we had only used two-qubit gates, which would increase the gate time by almost a factor of 3.

2.5 Summary and outlook

In this chapter, we proposed a simple single-step implementation of n-bit Toffoli gates, CNOT^n-gates, and the Barenco gate and showed that these exhibit a high fidelity, with the leading cause of error being the qubits' decoherence. These gates can easily be transformed into C^nZ or CZ^n gates by applying Hadamard gates on the target qubits. While the difficulty of implementing our gates does increase with n, we believe that our gates can provide many advantages to certain types of quantum computers, especially compared to rather deep equivalent circuits built from one- and two-qubit gates. As an example of an implementation of the gates for quantum information processing, we discussed superconducting circuit design of the gates, though the idea is not limited to this quantum information scheme. We showed that the gates could easily be concatenated into error correction codes by simulating the protocol. The gates proposed in this chapter are not limited to the three-qubit error-correcting code or the Steane code, and they can

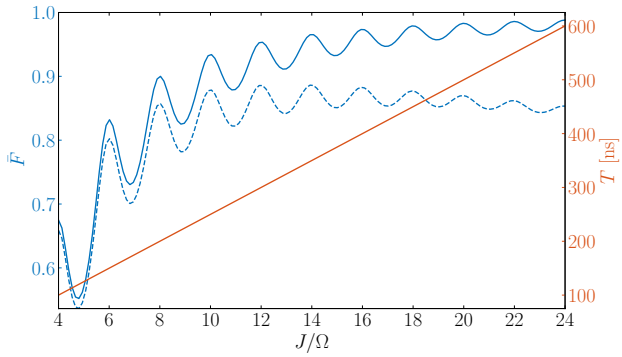

Figure 2.9: *Simulation of the Steane encoding scheme seen in Fig. 2.7, using* CNOT^n *gates. The simulation is done for* $J/2\pi = 40\,\text{MHz}$. *The straight red line indicates the gate time T on the right y axis, while the blue lines indicate the average fidelity, at the gate time, on the left y axis. The dashed blue line is the average fidelity with a decoherence time of* $T_1 = T_2 = 30\,\mu\text{s}$, *while the solid line is without decoherence.*

be applied to numerous other codes making them more effective. These results could enhance the performance of near-term quantum computing experiments on algorithms that require many Toffoli gates or same-control CNOT gates.

Multiqubit Toffoli gates is an active research field, and several papers have been published since the work in this chapter was done. This includes multiqubit gates in Rydberg atoms [251–256], trapped ions [257, 258], and superconducting circuits [251, 255, 258, 259]. Multiqubit gates can also be useful in quantum algorithms for solving differential equations [260] and string matching [261], as well as other error mitigation schemes [262] than those discussed in this chapter and quantum-inspired algorithms [263].

References [264, 265] have explored how to improve the method presented in this chapter for trapped ions, and recently a paper was put on arXiv proposing a single-shot method for executing an *i*Toffoli gate, inspired by the approach in this chapter [266].

CHAPTER 3

The Controlled *i*SWAP Gate

*Following the work on the iToffoli gate of the previous chapter, I realized that one could probably use the same idea of detuning in and out of resonance to create a controlled swap gate. This idea led to the controlled i*SWAP *gate of Ref.* ***[VI]*** *on which this chapter is based. Text and figures have been edited to fit into the thesis.*

Previously we discussed controlled NOT gates such as the CNOT and the Toffoli gate. In particular, we showed how to implement an n-bit *i*Toffoli in the previous chapter. Equivalent (in the sense that they both constitute a universal set of gates together with the set of one-qubit operations) to the CNOT gate is the *i*SWAP gate which we denote $\hat{S} = |00\rangle\langle 00| \pm i(|10\rangle\langle 01| + |01\rangle\langle 10|) + |11\rangle\langle 11|$. The *i*SWAP gate is a perfect entangling version of the SWAP gate, which is why it is equivalent to the CNOT gate. However, the *i*SWAP gate has the advantage over the CNOT gate that it occurs naturally in systems with XY interaction or Heisenberg models, such as solid-state systems [267, 268], superconducting circuits [269], and in cavity mediated between spin qubits and superconducting qubits [19, 110, 270]. Other implementations of the *i*SWAP gate include linear optics [271, 272] and nuclear spin using qudits [273].

Despite several attemps of implementing the *i*SWAP gate [187, 274, 275], the Fredkin gate [43, 276–283], and other controlled-swapping gates [**III**, 44, 86], no one have embarked in the implementation of a *controlled i*SWAP gate, to the best of our knowledge. Recently a deterministic Fredkin and exponential SWAP gate was implemented using three-dimensional, fixed frequency superconducting microwave cavities [201, 284].

This chapter presents a simple implementation of a multiqubit controlled *i*SWAP gate which we call C^n*i*SWAP, where the n indicates the number of control qubits. This is essentially an *i*Fredkin gate for a single control qubit, i.e., a Fredkin gate with a phase of i on the swapping part. The implementation is based on using the control qubits to tune the target qubits in and out of resonance by following the approach presented in Chapter 2 and can be realized using different schemes for quantum information processing. We include circuit design for implementating of the *i*SWAP gate in superconducting circuits as well as for the C^2*i*SWAP gate in the appendix. The gate requires a single flux pulse to operate, and the gate time is thus independent of the number of control qubits. When

neglecting the decoherence of the qubits, we find a fidelity above 0.998 for one control qubit. When including decoherence of the qubits, the fidelity stays above 0.99 for up to four control qubits.

Being able to exponentiate quantum gates can be helpful in different quantum information schemes such as in continuous variable (CV) systems [208], where exponentiated gates, such as $\exp(i\theta\hat{X})$, can be used to operate on the systems [209, 285]. Another scheme that might benefit from being able to exponentiate non-Hermitian quantum gates is quantum random walks [286], where non-unitary operations are needed for, e.g., graph coloring [287, 288]. We, therefore, present a quantum circuit for probabilistic exponentiating of non-Hermitian operators, based on the method by [289] which works for exponentiating Hermitian operators. Our method is exact for a cyclic operator, i.e., operators fulfilling $\hat{T}^n = \mathbb{1}$, while it is approximate for all other non-Hermitian operators.

This chapter is organized as follows: In Section 3.1 we present a simple Hamiltonian and show how it yields an C^n*i*SWAP gate. We discuss the effectiveness of the gate exploring the single-qubit controlled *i*SWAP gate as an example in Section 3.1.1. We further, in Section 3.2, present an implementation using superconducting circuits of the C^n*i*SWAP gate and discuss how to expand it to more controls. In Section 3.3 we show how to expand the implementation of the controlled *i*SWAP gate into controlling swapping of an array of qubits. In Section 3.2.1 we discuss a realistic implementation of the gate, including fabrication errors and decoherence noise. In Section 3.4 we present a quantum circuit for probabilistic exponentiating cyclic quantum gates and discuss its range of validity. In Section 3.5 we provide a summary and outlook for future work.

3.1 Implementation of the controlled *i*SWAP gate

Consider $n+2$ qubits each with frequency ω_i. The first n qubits are connected to one of the two last qubits by Ising couplings J_i^z, where i refers to the first n qubits. The last two qubits are further connected by a transversal coupling J^x. We denote the last two qubits as target qubit $T1$ and $T2$. The Hamiltonian for the system is

$$\hat{\mathcal{H}} = \hat{\mathcal{H}}_0 - \frac{\Delta}{2}\sigma_{\mathrm{T1}}^z + \sum_{i=1}^{n} \frac{J_i^z}{2}\sigma_{\mathrm{T1}}^z\sigma_i^z + \frac{J^x}{2}(\sigma_{\mathrm{T1}}^x\sigma_{\mathrm{T2}}^x + \sigma_{\mathrm{T1}}^y\sigma_{\mathrm{T2}}^y), \tag{3.1}$$

where $\sigma^{x,y,z}$ denotes the Pauli matrices, and the non-interacting part of the Hamiltonian is given as

$$\hat{\mathcal{H}}_0 = -\sum_{i=1}^{n} \frac{\omega_i}{2}\sigma_i^z - \frac{\omega_{\mathrm{T2}}}{2}\left(\sigma_{\mathrm{T1}}^z + \sigma_{\mathrm{T2}}^z\right), \tag{3.2}$$

and $\Delta = \omega_{\mathrm{T1}} - \omega_{\mathrm{T2}}$ is the detuning of the two target qubits. Changing to the interaction picture using the transformation $\hat{\mathcal{U}}_{\mathrm{int}}(t) = \exp(i\hat{\mathcal{H}}_0 t)$, the Hamiltonian takes the form

$$\hat{\mathcal{H}}_I = -\frac{\Delta}{2}\sigma_{\mathrm{T1}}^z + \sum_{i=1}^{n} \frac{J_i^z}{2}\sigma_{\mathrm{T1}}^z\sigma_i^z + J^x(\sigma_{\mathrm{T1}}^+\sigma_{\mathrm{T2}}^- + \sigma_{\mathrm{T2}}^+\sigma_{\mathrm{T1}}^-). \tag{3.3}$$

In order to realize the behavior of the controlled *i*SWAP gate, we must require the detuning to be

$$\Delta = -\sum_{i=1}^{n} J_i^z, \tag{3.4}$$

and $J_i^z \gg J^x$ for all i. Thus the energy shift due to the first n qubits must be large enough to bring the last two qubits in and out of resonance, making the first n qubits the control qubits and the last two the swapping qubits.

Changing into the frame rotating with the diagonal part of the Hamiltonian, we obtain

$$\hat{\mathcal{H}}_{\text{rot}} = J^x \left[\sigma_{\text{T1}}^+ \sigma_{\text{T2}}^- e^{i \sum_{i=1}^n J_i^z (1+\sigma_i^z) t} + \text{H.c.} \right]. \tag{3.5}$$

With the condition that $J^z \gg J^x$ both terms of $\hat{\mathcal{H}}_{\text{rot}}$ will rotate rapidly, and can thus be neglected using the rotating wave approximation, *unless all* of the control qubits are in the state $|1\rangle$. This means that the Hamiltonian effectively becomes

$$\hat{\mathcal{H}}_{\text{rot}} = J^x \, |\tilde{1}\rangle\langle\tilde{1}|_C \otimes \left[\sigma_{\text{T1}}^+ \sigma_{\text{T2}}^- + \sigma_{\text{T2}}^+ \sigma_{\text{T1}}^- \right], \tag{3.6}$$

where subscript C denotes the state of the control qubits, i.e. the first n qubits, and T denotes the state of the target qubit, i.e., qubit $T1$ and $T2$. The state $|\tilde{1}\rangle_C = |11\ldots1\rangle_C$ denotes the state where all control qubits are in the state $|1\rangle$.

We can calculate the time evolution operator by taking the matrix exponential, $\hat{\mathcal{U}}(t) = \exp(i\hat{\mathcal{H}}_{\text{rot}} t)$, which yields

$$\hat{\mathcal{U}}(t) = \hat{\tilde{I}}_C \otimes \hat{I}_T + |\tilde{1}\rangle\langle\tilde{1}|_C \otimes \begin{pmatrix} 1 & 0 & 0 & 0 \\ 0 & \cos(Jt) & -i\sin(Jt) & 0 \\ 0 & -i\sin(Jt) & \cos(Jt) & 0 \\ 0 & 0 & 0 & 1 \end{pmatrix}, \tag{3.7}$$

where $\tilde{I}_C$ denotes the reduced identity of the control qubits where the states $|\tilde{1}\rangle\langle\tilde{1}|_C$ have been removed. The identity of the target qubits is denoted $\hat{I}_T$.

From Eq. (3.7) we see that for times $T = (2m+1)\pi/2J^x$, $m \in \mathbb{Z}$ the time evolution operator takes the form of a controlled *i*SWAP gate.

$$\hat{\mathcal{U}}(t = T) = \hat{\tilde{I}}_C \otimes \hat{I}_T + |\tilde{1}\rangle\langle\tilde{1}|_C \otimes \hat{S}_T, \tag{3.8}$$

where $\hat{S}_T$ is the two-qubit *i*SWAP gate on the target qubits, swapping the target qubit with a phase of $\pm i$. The phase on the target qubit depends on the sign of $\mp|J^x|$. For completeness we note that for times $T' = (2m+1)\pi/4J^x$ we obtain the controlled-$\sqrt{i\text{SWAP}}$ gate [55]. Note that once time has passed, the desired gate has been performed, interactions must be turned off. Thus the gate depends on control over the exchange interaction. This can be achieved differently depending on which scheme is used to implement the gate. In Section 3.2 we present an implementation of the gate in superconducting circuits, where we also discuss how to control the exchange interaction.

3.1.1 Example: The single controlled *i*SWAP gate

In order to illuminate the performance of the system worked as a C^n*i*SWAP gate, we explore the example of the single controlled *i*SWAP gate. We chose this example since not only is it the simplest non-trivial example, it is also closely related to the Fredkin gate. A schematic presentation of the model yielding the C*i*SWAP gate can be seen in Fig. 3.3(a), which corresponds to Eq. (3.1) with $n = 1$.

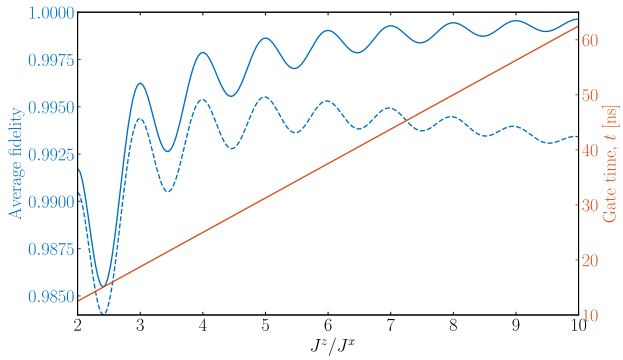

Figure 3.1: *Simulation of the controlled i*SWAP *gate for different coupling values J^x. The blue lines indicate the average fidelity at the gate time (left y axis), while the straight red line indicates the gate time T (right y axis). The dashed blue line is the average fidelity with a decoherence time of $T_1 = T_2 = 30\,\mu s$, while the solid is without decoherence.*

We characterize the performance of the gate by calculating the average process fidelity, Eq. (2.18), with the target gate being Eq. (3.8). We simulate the system similarly to in Section 2.1.3 using the Lindblad Master equation and the interaction Hamiltonian of Eq. (3.3) using the QuTiP Python toolbox [240]. The result is then transformed into the frame rotating with the diagonal of the Hamiltonian, and then the average fidelity is calculated.

For all simulations, we have $J^z/2\pi = 50\,\text{MHz}$, while we change the transversal coupling, $J^x/2\pi$, from 5 to 25 MHz. The average fidelity of the simulation can be seen in Fig. 3.1 together with the gate time. The figure shows both the average fidelity without any decoherence and with a decoherence time of $T_1 = T_2 = 30\,\mu s$ [53]. We model decoherence as relaxation and phase errors; we do not include excitation by thermal photon, as it contributes very little to the decoherence [135]. Without any decoherence, we find that the average fidelity increases asymptotically towards unity as the driving decreases, with the only expense being an increase in gate time. Since decoherence increases over time, a longer gate time means lower fidelity, which we observe when including decoherence in the simulations. In this case we find that the fidelity peaks at ~ 0.995 around $J^z/J^x \sim 4$, which yields a gate time of $T \sim 25\,\text{ns}$. However, we note that the fidelity is dependent on the parameters J^x and J^z; thus, changing these will change the fidelity. We also see that for just $J^z = 2J^x$ we obtain an average fidelity above 0.99 for a gate time $T \sim 15\,\text{ns}$. The oscillation of the average fidelity is due to a minor mismatch in the phase of the evolved state compared to the desired matrix in Eq. (3.7), which disappears when $J^z/J \in \mathbb{Z}$.

We simulate the C^n*i*SWAP gate for different n in the optimal ratio between couplings, $J^z/J^x \sim 4$. The result of this simulation is seen in Fig. 3.2. We observe that the fidelity stays above 0.998 for up to $n = 4$ control qubits when decoherence is not included. This is because, for larger n, the gate resembles the identity more. This is because the identity operation is applied to the control qubits, meaning that for a large number of control qubits, the gate will perform the identity on the control qubits, and the swapping

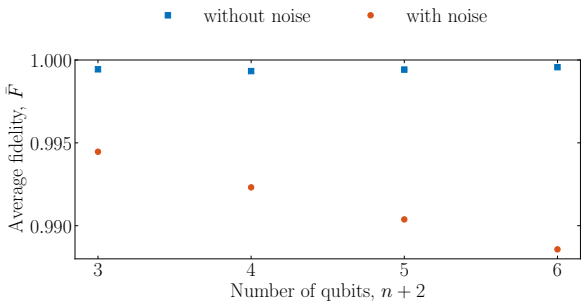

Figure 3.2: *Average fidelity as a function of the number of qubits in the* C$^n i$SWAP *gate. The blue square markers indicate the simulation without decoherence, while the round red markers indicate the simulation done with a decoherence time of* $T_1 = T_2 = 30\,\mu$s. *All simulations are done with* $J^z/J = 5$, *i.e., peak fidelity cf. Fig. 3.1.*

operation will only be performed on the target qubits. When decoherence is included, the average fidelity decreases for larger n as it should; however, we still find a fidelity above 0.99 for up to 4 controls.

3.2 Superconducting circuit implementation

A possible implementation of the CiSWAP gate using superconducting circuits can be seen in Fig. 3.3(c). The circuit consists of three fixed-frequency transmon qubits, where two of them are connected through a tunable bus qubit, following the approach by Ref. [187], and the third qubit is connected to the other two by Josephson junctions, with as small a parasitic capacitance as possible. In our analysis, we connect a number, n, of fixed frequency qubits to the target qubits. It is irrelevant to which target qubit these control qubits are connected. The control qubits can be connected to either (or both) target qubits, but for simplicity, we connect all control qubits to target qubit 1.

Following the approach presented in Section 1.2.3, we obtain the Lagrangian for the C$^n i$SWAP circuit

$$\begin{aligned}\mathcal{L} =& 2 \sum_{\substack{i=\mathrm{T1,T2,}\\ \mathrm{TB,TB',1,...}}}^{n} \left[C_i \dot{\phi}_i^2 + E_i \cos\phi_i\right] + 2C_x \left(\dot{\phi}_{\mathrm{T1}} - \dot{\phi}_{\mathrm{TB}}\right)^2 + 2C_x \left(\dot{\phi}_{\mathrm{T2}} - \dot{\phi}_{\mathrm{TB'}}\right)^2 \\ &+ 2\sum_{i=1}^{n} C_{z,i} \left(\dot{\phi}_i - \dot{\phi}_{\mathrm{T1}}\right)^2 + \sum_{i=1}^{n} E_{z,i} \cos(\phi_{\mathrm{T1}} - \phi_i) + E_{\mathrm{TB}}(\tilde{\Phi}) \cos\phi_{\mathrm{TB}},\end{aligned} \tag{3.9}$$

where the first summation is understood as the summation over T1, T2, TB, TB′, $1, 2, \ldots, n$. We denote ϕ_{T1} and ϕ_{T2} as the node fluxes of the target qubits [green islands in Fig. 3.3(c) and (d)], ϕ_{TB} and $\phi_{\mathrm{TB'}}$ are the node fluxes of the tunable bus [red islands in Fig. 3.3(c) and (d)], and ϕ_i are the node fluxes of the control qubits [blue islands in Fig. 3.3(c) and (d)]. $\tilde{\Phi}$ is the external magnetic flux through the tunable bus in units of $\Phi_0/2\pi$, where Φ_0 is the flux quantum. We have also used the fact that the tunable bus is essentially a

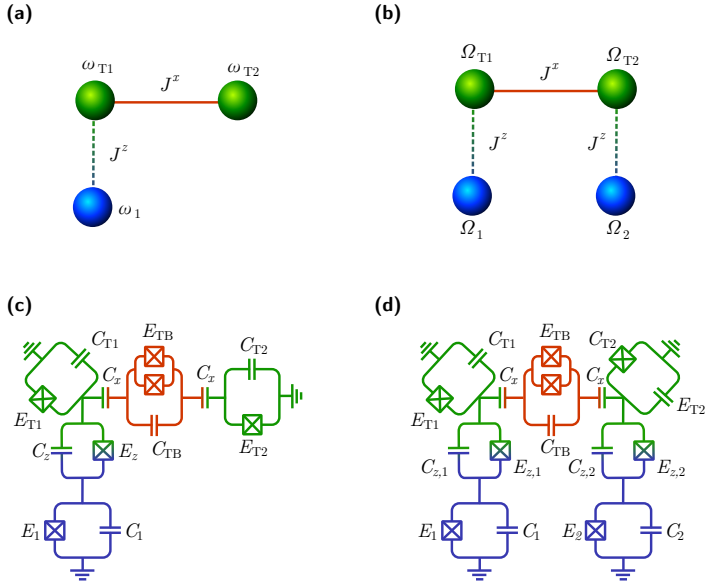

Figure 3.3: *Schematics of* **(a)** *the* C*i*SWAP *gate and* **(b)** *the* C^2*i*SWAP *gate in superconducting circuits with the green spheres (subscript T1 and T2) representing the target qubits and the blue spheres (subscript 1 and 2) representing the control qubits. The red lines indicates an interaction which can be turn on and off.Also shown are* **(c)** *and* **(d)** *the superconducting circuits yielding the models in* **(a)** *and* **(b)**, *respectively. The different parts of the system are colored according to their role, as per* **(a)** *and* **(b)**.

dc SQUID, see Section 1.1.2, in order to write the tunable Josephson energy of the bus as $E_{TB}(\tilde{\Phi}) = 2E_{TB}\cos(\tilde{\Phi}/2)$. In doing so we have used Kirchhoff's voltage law, Eq. (1.3b) which states that $\phi_{TB'} = \tilde{\Phi} - \phi_{TB}$. Using this we rewrite the Lagrangian into

$$\begin{aligned}\mathcal{L} =& 2\sum_{\substack{i=\mathrm{T1,T2,}\\ \mathrm{TB,1,...}}}^{n}\left[C_i\dot{\phi}_i^2 + E_i\cos\phi_i\right] + 2C_x\left[\dot{\phi}_{T1}^2 + \dot{\phi}_{T2}^2 + 2\dot{\phi}_{TB}^2 + 2\dot{\phi}_{TB}\left(\dot{\phi}_{T2} - \dot{\phi}_{T1}\right)\right] \\ &+ 4C_{TB}\dot{\phi}_{TB}^2 + 2\sum_{i=1}^{n} C_{z,i}\left(\dot{\phi}_i - \dot{\phi}_{T1}\right)^2 + \sum_{i=1}^{n} E_{z,i}\cos(\phi_{T1} - \phi_i) + 2E_{TB}(\tilde{\Phi})\cos\phi_{TB},\end{aligned} \tag{3.10}$$

where we have ignored all terms concerning $\dot{\tilde{\Phi}}$ since these all contribute with irrelevant constant terms.

The terms coming from the capacitors are interpreted as kinetic terms, while the remaining terms come from the Josephson junctions and are interpreted as potential terms. The n indicates the number of blue islands on the circuit diagram, i.e., for the C*i*SWAP in Fig. 3.3(c) $n = 1$. Considering the case of a single control qubit and arranging the node

fluxes in a vector as $\phi^T = (\phi_1, \phi_{\mathrm{T1}}, \phi_{\mathrm{TB}}, \phi_{\mathrm{T2}})$, the capacitance matrix becomes

$$\boldsymbol{C} = \begin{bmatrix} C_1 + C_{z,1} & -C_{z,1} & 0 & 0 \\ -C_{z,1} & C_{\mathrm{T1}} + C_{z,1} + 2C_x & -C_x & 0 \\ 0 & -C_x & 4C_{\mathrm{TB}} + 2C_x & -C_x \\ 0 & 0 & -C_x & C_{\mathrm{T2}} + 2C_x \end{bmatrix}. \tag{3.11}$$

For two control qubits [see Fig. 3.3(d) for circuit diagram of this gate] the capacitance matrix takes the form

$$\boldsymbol{C} = \begin{bmatrix} C_1 + C_{z,1} & 0 & -C_{z,1} & 0 & 0 \\ 0 & C_2 + C_{z,2} & -C_{z,2} & 0 & 0 \\ -C_{z,1} & -C_{z,2} & C_{\mathrm{T1}} + C_{z,1} + 2C_x & -C_x & 0 \\ 0 & 0 & -C_x & 4C_{\mathrm{TB}} + 2C_x & -C_x \\ 0 & 0 & 0 & -C_x & C_{\mathrm{T2}} + 2C_x \end{bmatrix}. \tag{3.12}$$

and so on for higher n. With this, we can do a Legendre transform as in Section 1.2.4 and write the Hamiltonian as

$$\mathcal{H} = \frac{1}{2}\hat{\boldsymbol{q}}^T \boldsymbol{C}^{-1} \hat{\boldsymbol{q}} + U(\phi), \tag{3.13}$$

where $\boldsymbol{q}^T = (q_1, q_{\mathrm{T1}}, q_{\mathrm{TB}}, q_{\mathrm{T2}})$ is the conjugate momentum and $U(\phi)$ is the potential energy coming from the Josephson junctions.

The typical transmon has a charging energy much smaller than the junction energy, and therefore the phase is well localized near the bottom of the potential. We can therefore expand the potential part of the Hamiltonian to fourth order

$$\begin{aligned} U(\phi) = &\sum_{\substack{i=\mathrm{T1,T2,} \\ \mathrm{TB},1,\ldots}}^{n} E_i \left[\frac{1}{2}\phi_i^2 - \frac{1}{24}\phi_i^4\right] + \sum_{i=1}^{n} E_{z,i} \left[\frac{1}{2}\left(\phi_i - \phi_{\mathrm{T1}}\right)^2 - \frac{1}{24}\left(\phi_i - \phi_{\mathrm{T1}}\right)^4\right] \\ &+ 2E_{\mathrm{TB}}(\tilde{\Phi}) \left[\frac{1}{2}\phi_{\mathrm{TB}}^2 - \frac{1}{24}\phi_{\mathrm{TB}}^4\right]. \end{aligned}$$

By collecting terms we can write the full Hamiltonian as

$$\begin{aligned} \mathcal{H} = &\sum_{\substack{i=\mathrm{T1,T2,} \\ \mathrm{TB},1,\ldots}}^{n} \left[\frac{1}{2}E_i^C q_i^2 + \frac{1}{2}E_i^J \phi_i^2 - \frac{1}{24}E_i^J \phi_i^4\right] + \frac{1}{2} \sum_{\substack{i \neq j= \\ T1,T2,TB,1}}^{n} \left(K^{-1}\right)_{(i,j)} q_i q_j \\ &+ \sum_{i=1}^{n} E_{z,i} \left[-\frac{1}{4}\phi_i^2 \phi_{\mathrm{T1}}^2 - \phi_i \phi_{\mathrm{T1}} + \frac{1}{6}\left(\phi_i^3 \phi_{\mathrm{T1}} + \phi_i \phi_{\mathrm{T1}}^3\right)\right] \\ &+ \frac{1}{2}E_{\mathrm{TB}}^C q_{\mathrm{TB}}^2 + \frac{1}{2}E_{\mathrm{TB}}(\tilde{\Phi})\phi_{\mathrm{TB}}^2 - \frac{1}{24}E_{\mathrm{TB}}(\tilde{\Phi})\phi_{\mathrm{TB}}^4, \end{aligned}$$

where the effective energy of the capacitances is $E_i^C = \left(\boldsymbol{C}^{-1}\right)_{(i,i)}/8$. The second summation is understood as the sum over i and $j = \mathrm{T1}, \mathrm{T2}, \mathrm{TB}, 1, \ldots, n$, where i and j is never equal. Note that there is a capacitive coupling between all of the qubits regardless of

whether there actually is a capacitor between them. The effective Josephson energies are

$$E_i^J = E_i + 2E_{z,i}, \tag{3.14a}$$
$$E_{\mathrm{T1}}^J = E_{\mathrm{T1}} + \sum_{i=1}^{n} E_{z,i}, \tag{3.14b}$$
$$E_{\mathrm{T2}}^J = E_{\mathrm{T2}}, \tag{3.14c}$$
$$E_{\mathrm{TB}}^J = E_{\mathrm{TB}}(\Phi). \tag{3.14d}$$

We are now ready to do the canonical quantization and transform it into annihilation and creation operators as in Sections 1.3.1 and 1.4. If we operate the circuit in the weak coupling regime $E_{z,i} \ll E_j$ and $C_{z,i} \ll C_j$ for all i and j we can view the system as $n+2$ harmonic oscillators perturbed by their interactions. If we also assume that the modes of oscillator $T1$ and $T2$ are close to resonant, we can treat their detuning as part of the perturbation. The total Hamiltonian is the sum of the harmonic oscillator Hamiltonian $\hat{H}_0$ and a perturbation $\hat{V}$. If we introduce the number operator $\hat{N} = \hat{b}^\dagger \hat{b}$ and swap operator $\hat{X}_{ij} = \hat{b}_j \hat{b}_i^\dagger + \hat{b}_j^\dagger \hat{b}_i$, we can write the two parts of the Hamiltonian as

$$\hat{\mathcal{H}}_0 = \sum_{i=1}^{n} \omega_i \hat{N}_i + \omega_{\mathrm{T2}}(\hat{N}_{\mathrm{T1}} + \hat{N}_{\mathrm{T2}}) + \omega_{\mathrm{TB}} \hat{N}_{\mathrm{TB}}, \tag{3.15a}$$
$$\begin{aligned}\hat{V} =& \delta \hat{N}_{\mathrm{T1}} - \frac{1}{2} \sum_{i=T1,T2,TB,1}^{n} E_i^C \hat{N}_i(\hat{N}_i - 1) + \sum_{i=1}^{n} g_{iT1}^z \hat{N}_i \hat{N}_{\mathrm{T1}} + \sum_{\substack{i \neq j = \\ T1,T2,TB,1}}^{n} g_{ij}^x \hat{X}_{ij} \\ &+ \sum_{i=1}^{n} g_{iT1}^{xz} \left[\zeta_i \left(\hat{X}_{iT1} \hat{N}_i + \hat{N}_i \hat{X}_{iT1} \right) + \zeta_{\mathrm{T1}} \left(\hat{X}_{iT1} \hat{N}_{\mathrm{T1}} + \hat{N}_{\mathrm{T1}} \hat{X}_{iT1} \right) \right],\end{aligned} \tag{3.15b}$$

where the qubit frequencies are then given as

$$\omega_i = \sqrt{8 E_i^J E_i^C} - \frac{1}{12} E_{z,i} \zeta_i \zeta_{\mathrm{T1}} \qquad \text{for } i = 1, 2, \ldots n, \tag{3.16a}$$
$$\omega_{\mathrm{T1}} = \sqrt{8 E_{\mathrm{T1}}^J E_{\mathrm{T1}}^C} - \frac{1}{12} E_{z,i} \zeta_{\mathrm{T1}} \sum_{i=1}^{n} \zeta_i, \tag{3.16b}$$
$$\omega_{\mathrm{T2}} = \sqrt{8 E_{\mathrm{T2}}^J E_{\mathrm{T2}}^C}, \tag{3.16c}$$
$$\omega_{\mathrm{TB}} = \sqrt{8 E_{\mathrm{TB}}^J E_{\mathrm{TB}}^C}, \tag{3.16d}$$
$$\delta = \frac{1}{2} \left(\omega_{\mathrm{T1}} - \omega_{\mathrm{T2}} \right), \tag{3.16e}$$

and the coupling strengths are given as

$$g^z_{i\mathrm{T1}} = -\frac{1}{4}E_{z,i}\zeta_i\zeta_{\mathrm{T1}}, \qquad \text{for } i = 1,2,\ldots,n, \tag{3.17a}$$

$$g^{xz}_{i\mathrm{T1}} = -\frac{1}{16}E_{z,i}\sqrt{\zeta_i\zeta_{\mathrm{T1}}}, \qquad \text{for } i = 1,2,\ldots,n, \tag{3.17b}$$

$$g^x_{ij} = -\frac{1}{2}\frac{(\boldsymbol{C}^{-1})_{(i,j)}}{\sqrt{\zeta_i\zeta_j}}, \qquad \text{for } j,i = 1,2,\ldots,n, \tag{3.17c}$$

$$g^x_{\mathrm{T}j\mathrm{TB}} = -\frac{1}{2}\frac{(\boldsymbol{C}^{-1})_{(Tj,TB)}}{\sqrt{\zeta_{\mathrm{T}j}\zeta_{\mathrm{TB}}}}, \qquad \text{for } j = 1,2, \tag{3.17d}$$

$$g^x_{i\mathrm{T1}} = -\frac{1}{2}\frac{(\boldsymbol{C}^{-1})_{(i,\mathrm{T1})}}{\sqrt{\zeta_i\zeta_{\mathrm{T1}}}} - \frac{1}{2}E_{z,i}\sqrt{\zeta_i\zeta_{\mathrm{T1}}} + \frac{1}{16}E_{z,i}(\zeta_i+\zeta_{\mathrm{T1}})\sqrt{\zeta_i\zeta_{\mathrm{T1}}}, \qquad \text{for } i = 1,2,\ldots,n, \tag{3.17e}$$

where the impedance is given as in Eq. (1.56).

If we only consider the two lowest-lying states of each oscillator, the uncoupled Hamiltonian has a degenerate spectrum with 2^{n+2} states. If we require the detunings $\Delta_{ij} = \omega_i - \omega_j$ between each of the control qubits to be much larger than the transversal couplings in Eq. (3.17c), we can ignore the first order excitations swaps between the control qubits. If we further require that the control qubits are detuned from the target qubits in such a way that $\Delta_{iTj} = \omega_i - \omega_{\mathrm{T}j}$ is much larger than the transversal coupling in Eq. (3.17e) we can also neglect first order excitation swaps between the target qubits and the control qubits. This leaves only one transversal coupling in Eq. (3.17d).

If the anharmonicity is sufficiently larger than the transversal coupling between the target qubits, we can justify projecting the final effective Hamiltonian into the two lowest states of each qubit. This projection is made using degenerate second-order perturbation theory. In this case, each degenerate subspace is well described by an effective interaction

$$\hat{P}\hat{V}_{\mathrm{eff}}\hat{P} = \hat{P}\hat{V}\hat{P} + \hat{P}\hat{V}\hat{Q}\frac{1}{E_D - \hat{Q}\hat{\mathcal{H}}_0\hat{Q}}\hat{Q}\hat{V}\hat{P}, \tag{3.18}$$

where $\hat{P}$ projects onto the degenerate subspace consisting of the 2^{n+2} lowest-lying states and $\hat{Q} = 1 - \hat{P}$ projects onto the orthogonal complement. Doing so yields an effective interaction between the qubits given by

$$\hat{V}_{\mathrm{eff}} = -\frac{\Delta_{\mathrm{T1}}}{2}\sigma^z_{\mathrm{T1}} + \sum_{i=1}^{n}\frac{J^z_i}{2}\sigma^z_{\mathrm{T1}}\sigma^z_i + \sum_{j=1}^{2} g^x_{\mathrm{T}j\mathrm{TB}}\left(\sigma^+_{\mathrm{T}j}\sigma^-_{\mathrm{TB}} + \sigma^-_{\mathrm{T}j}\sigma^+_{\mathrm{TB}}\right). \tag{3.19}$$

The detuning of the target qubit can then be calculated and the second-order matrix elements are

$$\Delta_{\mathrm{T1}} = -\delta + \sum_{i=1}^{n}\left[\frac{g^z_{i\mathrm{T1}}}{2} - \frac{g^x_{i\mathrm{T1}} - g^{xz}_{i\mathrm{T1}}(\zeta_i + 2\zeta_{\mathrm{T1}})}{\Delta_{i\mathrm{T}}}\right], \tag{3.20}$$

where $\Delta_{i\mathrm{T}} = \omega_i - \omega_{\mathrm{T2}}$ is the detuning of the target qubits with respect to the ith control qubit. The longitudinal coupling between the target qubits and the control qubits are

$$J^z_i = \frac{g^z_{i\mathrm{T1}}}{2} + \frac{g^{xz}_{i\mathrm{T1}}(\zeta_i - 2\zeta_{\mathrm{T}j})}{\Delta_{i\mathrm{T}}}. \tag{3.21}$$

The purpose of this longitudinal coupling is to tune the target qubits in and out of resonance, depending on the state of the control qubits. We thus require this coupling to be significantly larger than the coupling between the target qubits and the tunable bus, $g^x_{\mathrm{T}j\mathrm{TB}}$.

Time-dependent external fluxes

We now wish to perform the same trick as Ref. [187] in order to gain control over the transversal couplings to the target qubits. We there consider the dispersive regime, where $|g^x_{\mathrm{T}j\mathrm{TB}}/(\omega_{\mathrm{T}j}-\omega_{\mathrm{TB}})| \ll 1$. In this regime, we can adiabatically eliminate the tunable bus, which yields the following terms in the Hamiltonian

$$\hat{\mathcal{H}}_0 = \sum_{i=1}^{n} \frac{\omega_i}{2}\sigma_i^z + \frac{\tilde{\omega}_{\mathrm{T2}}}{2}(\sigma_{\mathrm{T1}}^z + \sigma_{\mathrm{T2}}^z), \tag{3.22a}$$

$$\hat{V}_{\mathrm{eff}} = -\frac{\tilde{\Delta}_{\mathrm{T1}}}{2}\sigma_{\mathrm{T1}}^z + \sum_{i=1}^{n}\frac{J_i^z}{2}\sigma_{\mathrm{T1}}^z\sigma_i^z + \tilde{J}^x\left(\sigma_{\mathrm{T1}}^+\sigma_{\mathrm{T2}}^- + \sigma_{\mathrm{T1}}^-\sigma_{\mathrm{T2}}^+\right), \tag{3.22b}$$

where the dressed qubit frequency and dressed detuning is

$$\tilde{\omega}_{\mathrm{T}j} = \omega_{\mathrm{T}j} + \frac{(g^x_{\mathrm{T}j\mathrm{TB}})^2}{\omega_{\mathrm{T}j}-\omega_{\mathrm{TB}}}, \tag{3.23a}$$

$$\tilde{J}^x = \frac{g^x_{\mathrm{T1TB}}g^x_{\mathrm{T2TB}}}{2}\left(\frac{1}{\omega_{\mathrm{T1}}-\omega_{\mathrm{TB}}} + \frac{1}{\omega_{\mathrm{T2}}-\omega_{\mathrm{TB}}}\right). \tag{3.23b}$$

In order to interact the qubits via the tunable bus coupler we apply a sinusoidal fast-flux bias modulation of amplitude, χ, such that the flux applied to the tunable bus becomes $\tilde{\Phi}(t) = \Theta + \chi\cos(\omega_{\tilde{\Phi}}t)$. By expanding the dressed qubit frequency $\tilde{\omega}_{\mathrm{T}j}$ in the parameter $\chi\cos(\omega_{\tilde{\Phi}}t)$, where $\chi \ll 1$, we obtain

$$\begin{aligned}\tilde{\omega}_{\mathrm{T}j}(\tilde{\Phi}(t)) &\simeq \tilde{\omega}_{\mathrm{T}j}(\Theta) + \left.\frac{\partial\tilde{\omega}_{\mathrm{T}j}}{\partial\tilde{\Phi}}\right|_{\tilde{\Phi}\to\Theta}\chi\cos(\omega_{\tilde{\Phi}}t) + \frac{1}{2}\left.\frac{\partial^2\tilde{\omega}_{\mathrm{T}j}}{\partial\tilde{\Phi}^2}\right|_{\tilde{\Phi}\to\Theta}(\chi\cos(\omega_{\tilde{\Phi}}t))^2 \\ &= \left[\tilde{\omega}_{\mathrm{T}j}(\Theta) - \frac{\chi^2}{4}\left.\frac{\partial^2\tilde{\omega}_{\mathrm{T}j}}{\partial\tilde{\Phi}^2}\right|_{\tilde{\Phi}\to\Theta}\right] + \left.\frac{\partial\tilde{\omega}_{\mathrm{T}j}}{\partial\tilde{\Phi}}\right|_{\tilde{\Phi}\to\Theta}\chi\cos(\omega_{\tilde{\Phi}}t) \\ &\quad + \frac{\chi^2}{4}\left.\frac{\partial^2\tilde{\omega}_{\mathrm{T}j}}{\partial\tilde{\Phi}^2}\right|_{\tilde{\Phi}\to\Theta}\cos(2\omega_{\tilde{\Phi}}t).\end{aligned} \tag{3.24}$$

There is a similar expansion for the coupling J^x. In a frame rotating at the qubit frequencies for $\chi = 0$, oscillating σ^z terms and dc exchange coupling terms time average to zero. This means that the time-averaged qubit frequencies and couplings become

$$\bar{\omega}_{\mathrm{T}j}(\tilde{\Phi}(t)) = \tilde{\omega}_{\mathrm{T}j}(\Theta) - \frac{\chi^2}{4}\left.\frac{\partial^2\tilde{\omega}_{\mathrm{T}j}}{\partial\tilde{\Phi}^2}\right|_{\tilde{\Phi}\to\Theta}, \tag{3.25a}$$

$$\bar{J}^x(\tilde{\Phi}(t),t) = \left.\frac{\partial\tilde{J}^x}{\partial\tilde{\Phi}}\right|_{\tilde{\Phi}\to\Theta}\chi\cos(\omega_{\tilde{\Phi}}t) + \frac{\chi^2}{4}\left.\frac{\partial^2\tilde{J}^x}{\partial\tilde{\Phi}^2}\right|_{\tilde{\Phi}\to\Theta}\cos(2\omega_{\tilde{\Phi}}t). \tag{3.25b}$$

Because there is a drive-induced qubit shift, all N qubits will acquire a phase during the flux modulation pulse. This phase may be compensated after applying single-qubit Z gates. In a frame rotating with $\hat{\mathcal{H}}_0$ (including the drive-induced shift), the Hamiltonian is

$$\hat{\mathcal{H}} = -\frac{\bar{\Delta}_{\mathrm{T1}}}{2}\sigma_{\mathrm{T1}}^z + \sum_{i=1}^{n}\frac{J_i^z}{2}\sigma_{\mathrm{T1}}^z\sigma_i^z + \bar{J}^x(\tilde{\Phi}(t),t)\left(\sigma_{\mathrm{T1}}^+\sigma_{\mathrm{T2}}^- + \sigma_{\mathrm{T1}}^-\sigma_{\mathrm{T2}}^+\right). \tag{3.26}$$

Now in order to fix the oscillation of the exchange coupling and create the controlled iSWAP gate we require the flux frequency to be resonant with the phase when the target qubits are in the $|1\rangle$ state, i.e.,

$$\omega_{\tilde{\Phi}} = \bar{\Delta}_{\mathrm{T1}} + \sum_{i=1}^{n} J_i^z. \tag{3.27}$$

In a frame rotating with the diagonal terms, the Hamiltonian takes the form

$$\begin{aligned}\hat{\mathcal{H}} =& \bar{J}^x(\tilde{\Phi}(t),t)e^{i(\bar{\Delta}_{\mathrm{T1}}-\sum_{i=1}^{n}J_i^z\sigma_i^z)t}\left(\sigma_{\mathrm{T1}}^+\sigma_{\mathrm{T2}}^- + \sigma_{\mathrm{T1}}^-\sigma_{\mathrm{T2}}^+\right)\\ =& \chi\left.\frac{\partial\tilde{J}^x}{\partial\tilde{\Phi}}\right|_{\tilde{\Phi}\to\Theta}|\tilde{1}\rangle\langle\tilde{1}|_C \otimes \left(\sigma_{\mathrm{T1}}^+\sigma_{\mathrm{T2}}^- + \sigma_{\mathrm{T1}}^-\sigma_{\mathrm{T2}}^+\right),\end{aligned} \tag{3.28}$$

where we have used the rotating wave approximation to remove all fast-rotating terms, i.e., all terms other than the term where all control qubits are in the state $|1\rangle$. Thus the condition in the original implementation, Eq. (3.4) is now replaced by the more easily obtainable expression in Eq. (3.27). This also means that the gate time becomes $T = (2m+1)\pi/J^x$ due to the cosine function. Nevertheless, the result is the same, and we obtain a controlled iSWAP gate.

Note that there is also a resonant coupling at $2\omega_{\tilde{\Phi}} = \bar{\Delta}_{\mathrm{T1}} + \sum_{i=1}^{n} J_i^z$, in which case the exchange coupling is via the second order terms in Eq. (3.25b). This could be used to lower the coupling in order to satisfy the requirement $J^x \ll J^z$.

An alternative approach to implementing such a tunable exchange coupling is to use the gmon-based design mentioned in Section 1.10.3.

3.2.1 Simulations

In order to show that the superconducting circuit model presented in the previous section does indeed give the desired result, we find realistic parameters for the circuit presented in Fig. 3.3 and their corresponding gate parameters. These parameters can be found in Tables C.1 to C.3 in Appendix C for $\Phi = 0$. In Fig. 3.4 we present typical parameters relevant for the gate implementation, i.e., derivatives of J^x and $\tilde{\omega}$ as a function of the external flux, Φ. In a realistic implementation, the circuit parameter is not perfect compared to the ones found in our simulations. Therefore we simulate with errors. We assume a fabrication error of up to 10% of 95% of the simulations. We then Monte Carlo simulates the circuit to find the error on the gate parameters. These errors are presented as the dashed lines in Fig. 3.4. While these errors might seem large, they are not a problem for the gate, as the gate operation is mainly dependent on Eq. (3.27), which can be achieved only with control over just the external flux.

Using the gate parameters found in Table C.2 and Fig. 3.4 we simulate the gate using an external DC flux of $\Phi = 0.100\Phi_0$ and a modulation of $\chi = 0.100\Phi_0$. The external

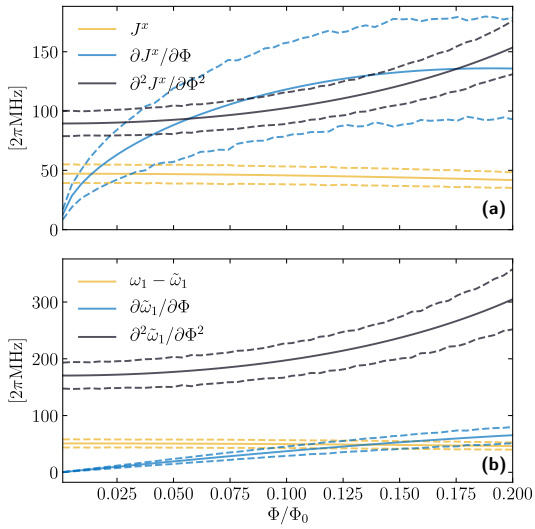

Figure 3.4: *Typical derivatives of the gate parameters* **(a)** J^x *and* **(b)** $\tilde{\omega}$*. The dashed lines indicates the error on the parameters, found using Monte Carlo simulations. In particular the parameters comes from column 2 in Table C.2.*

flux frequency is determined from Eq. (3.27); however, we include an error corresponding to a standard deviation of $1\mathrm{MHz}/2\pi$ in our simulation. In Ref. [187] they have an error of $0.1\mathrm{MHz}/2\pi$. The result of these Monte Carlo simulations can be seen in Fig. 3.5 where we have plotted the average fidelity of a subset of the simulations as a function of time. From the distribution of fidelities, we see that 60% of the simulations end up with a fidelity above 0.99, while 90% of the simulations are above 0.98 when simulating without decoherence noise. In contrast, the fidelity is smaller when decoherence noise is included in the simulations.

We conclude that even when including significant errors in the fabrication of the circuit, the gate still yields a high fidelity with the perfect C*i*SWAP gate.

3.3 Controlled swapping arrays

Suppose we have multiple qubits, which we want to swap in a controlled way, i.e., first swapping two qubits, then swapping two other qubits, and so on. This might be useful in a range of quantum algorithms.

This section discusses how to expand the idea of the C*i*SWAP gate previous section into a system where we can swap qubits in an array arbitrarily. We will discuss this for the case of an array of first three qubits and then briefly for four qubits, but the ideas will be easily expandable to more qubits.

In an attempt to create such a system, we connect all qubits which we wish to swap to each other with transversal coupling, J^x. Each of these n qubits are detuned from

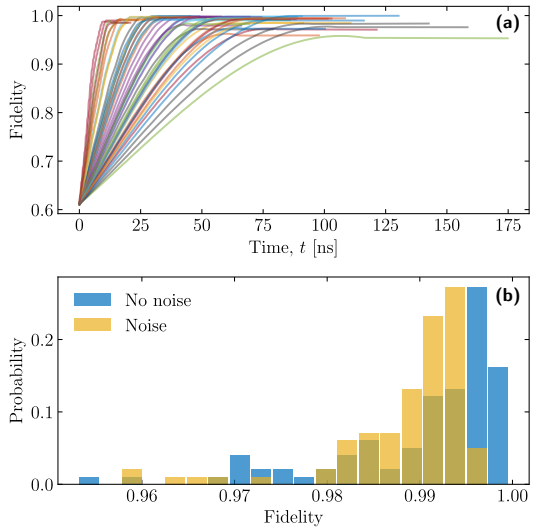

Figure 3.5: (a) *Average fidelity of the Monte Carlo simulation of the gate as a function of time. All shown simulations are without noise* **(b)** *Distribution of fidelities of the simulations at the gate time. The noise is the same as in Section 3.1.1.*

the average frequency of the qubits, such that $\Delta_i \neq \Delta_j$ for $i \neq j = 1, 2, \ldots, n$. Following the idea of Fig. 3.3 we add a control qubit for each target qubit and couple it with Ising couplings, J_i^z, to each qubit. A schematic representation of the model for $n = 3$ can be seen in Fig. 3.6(a). The Hamiltonian for such a system becomes

$$\hat{\mathcal{H}} = -\sum_{i=1}^{n}\left[\frac{\omega + \Delta_i}{2}\sigma_{\mathrm{T}i}^z + \frac{\omega_{\mathrm{C}i}}{2}\sigma_{\mathrm{C}i}^z\right] + \sum_{i=1}^{n}\frac{J_i^z}{2}\sigma_{\mathrm{T}i}^z\sigma_{\mathrm{C}i}^z + \frac{1}{4}\sum_{j\neq i=1}^{n} J^x\sigma_{\mathrm{T}i}^x\sigma_{Tj}^x. \tag{3.29}$$

where ω is the average over all the target qubits frequency, Δ_i is the detuning of the ith target qubit from the average frequency of the target qubits, and the subscript Ti indicates the ith target qubit, while the subscript Ci indicates the ith control qubit.

If we require that the Ising couplings have the strengths $J_i^z = -\Delta_i$, and require that $J_i^z \gg J^x$ for all i, then at times $T = (2m+1)\pi/(2J^x)$, $m \in \mathbb{Z}$ the time evolution operator for the $n = 3$ case takes the form

$$\begin{aligned}\hat{\mathcal{U}}(T) =& \hat{\tilde{I}}_C \otimes \hat{I}_T + |110\rangle\langle 110|_C \otimes \hat{S}_{12} + |011\rangle\langle 011|_C \otimes \hat{S}_{23} + |101\rangle\langle 101|_C \otimes \hat{S}_{13} \\ &+ |111\rangle\langle 111|_C \otimes \hat{S}_{123}.\end{aligned} \tag{3.30}$$

where $\hat{\tilde{I}}_C$ denotes the reduced identity of the control qubits where the states $|100\rangle\langle 100|_C$, $|010\rangle\langle 010|_C$, and $|001\rangle\langle 001|_C$ have been removed. The identity of the three target qubits is denoted $\hat{I}_T$, and $\hat{S}_{ij}$ is the two-qubit iSWAP gate which swaps the state of the qubits i and j. The quantum circuit of the model can be seen in Fig. 3.6(c).

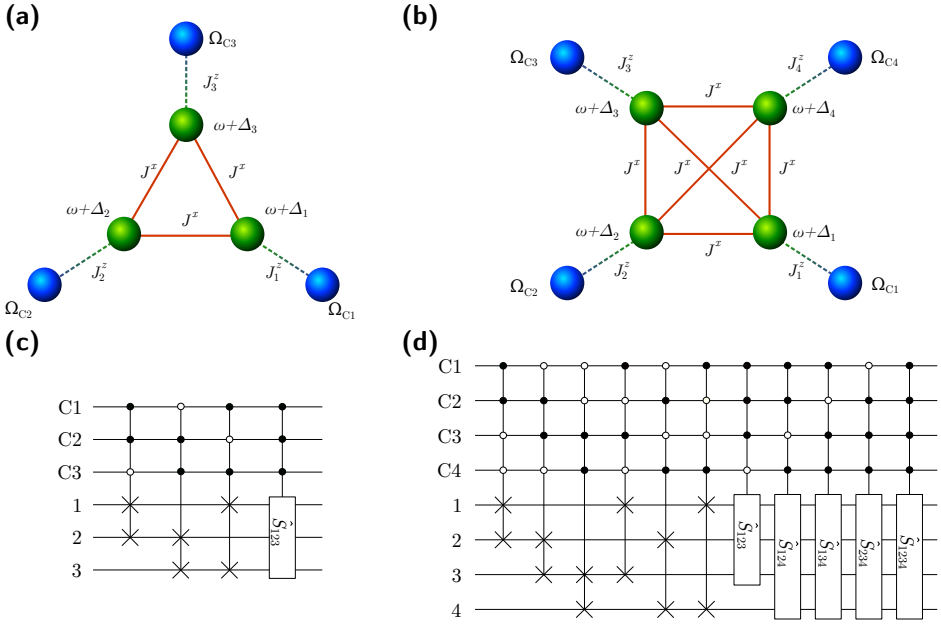

Figure 3.6: *Schematic representation of the model leading to controlled swapping between* **(a)** *three qubits and* **(b)** *four qubits. The green spheres (subscripts 1, 2, 3, and 4) represent the swapping qubits, while the blue spheres (subscripts C1, C2, C3, and C4) represent the ancilla qubits, which controls the swapping.* **(c)** *and* **(d)** *quantum circuit representations of the models in* **(a)** *and* **(b)**, *respectively, for times* $T = (2m+1)\pi/(2J^x)$, $m \in \mathbb{Z}$. *The top three or four ancilla qubits control the swapping and corresponds to the blue spheres, while the lower three or four qubits correspond to the green spheres. The filled circles indicate that the ancilla qubits must be the state* $|1\rangle$ *for the swap to be activated, while the non-filled circles indicate that the ancilla qubits must be in the state* $|0\rangle$*; for the three-qubit case, this corresponds to the time evolution operators in Eq.* (3.30).

From the time evolution operator in Eq. (3.30) we see that we have complete control over which qubits we wish to swap, depending on the three ancilla qubits, i.e., if we wish to swap qubits Ci and Cj to be in the $|1\rangle$ state and remaining control qubits to be in the state $|0\rangle$, in which case with the $\pm i$SWAP-operators $\hat{S}_{ij}$ swaps the state of the two qubits i and j. We note that we also obtain a three-way swapping operator when all control qubits are in the $|1\rangle$ state. In its matrix representation, the three-way swap-operator is an 8×8 matrix and takes the form

$$\hat{S}_{123} = \begin{pmatrix} 1 & 0 & 0 & 0 \\ 0 & \hat{S}_1 & 0 & 0 \\ 0 & 0 & \hat{S}_2 & 0 \\ 0 & 0 & 0 & 1 \end{pmatrix}, \tag{3.31}$$

where the two operators $\hat{S}_1$ and $\hat{S}_2$ are 3×3 matrices and operate on the three-dimensional subspaces of one and two excitation number of the target subspace, respectively. In their

matrix representation, these take the same form

$$\hat{S}_{1,2} = \frac{1}{3} e^{iJ^x t/2} \begin{pmatrix} 3\cos\left(\frac{3J^x t}{2}\right) - i\sin\left(\frac{3J^x t}{2}\right) & 2i\sin\left(\frac{3J^x t}{2}\right) & 2i\sin\left(\frac{3J^x t}{2}\right) \\ 2i\sin\left(\frac{3J^x t}{2}\right) & 3\cos\left(\frac{3J^x t}{2}\right) - i\sin\left(\frac{3J^x t}{2}\right) & 2i\sin\left(\frac{3J^x t}{2}\right) \\ 2i\sin\left(\frac{3J^x t}{2}\right) & 2i\sin\left(\frac{3J^x t}{2}\right) & 3\cos\left(\frac{3J^x t}{2}\right) - i\sin\left(\frac{3J^x t}{2}\right) \end{pmatrix}, \quad (3.32)$$

which can be used to entangle all three qubits. We consider the particular case of $T' = m\pi/3J^x$, $m \in \mathbb{Z}$, for which the operator takes the form

$$\hat{S}_{1,2} = \frac{1}{3} i e^{i\pi/6} \begin{pmatrix} -1 & 2 & 2 \\ 2 & -1 & 2 \\ 2 & 2 & -1 \end{pmatrix}. \quad (3.33)$$

This operator can be used to create a state belonging to the same non-biseparable classes of three-qubit states as the W state [290]. Note that this simultaneous three-way swapping can be used to create multiqubit gates that are faster than the usual two-qubit gates [291].

In Fig. 3.6(b), we show the model for a four qubit swapping array with all-to-all couplings corresponding to Hamiltonian in Eq. (3.29) with $n = 4$. In Fig. 3.6(d), we present the corresponding gates of the model coming from making the time evolution operator from the Hamiltonian. As above, we obtain fully controllable two-qubit swapping between all four qubits. We further obtain four three-qubit entangling gates, similar to the one in Eq. (3.32) and one single four-qubit entangling gate.

In order to test the viability of our analysis we simulate the Hamiltonian in Eq. (3.29) using the PYTHON toolbox QUTIP using the same approach as in Section 3.1.1. Using parameters $J_i^z/(2\pi) \in \{-20, 20, 60\}$MHz and $J^x = \min_i |J_i^z|/5$ we find a fidelity of 0.993 at time $T = \pi/(2J^x) = 62.5$ ns without including decoherence, and a fidelity of 0.98 when including a decoherence time of $T_1 = T_2 = 30\,\mu$s.

3.4 Probabilistic exponentiating of cyclic non-Hermitian quantum gates

This section presents an exact probabilistic method for exponentiating cyclic non-Hermitian gates using an explicit quantum circuit. While our method is exact for cyclic operators, it is approximate for non-cyclic operators. The C*i*SWAP gate presented in this paper is, in fact, a cyclic non-Hermitian gate. Note that exponentiating non-Hermitian gates leads to non-unitary gates.

Unitary Hermitian gates can be exponentiated using the method developed by Marvian and Lloyd [289]. Albeit they only present their method for the controlled-SWAP gate, it works for all unitary Hermitian gates. Here we extend their method in order to exponentiate non-Hermitian gates. Our method is exact for a gate, $\hat{T}$, for which $\hat{T}^n = \mathbb{1}$ for $n \in \mathbb{Z}$ and approximately correct if this is not the case. We call gates where $\hat{T}^n = \mathbb{1}$ for cyclic gates with cyclic order n. For $n > 2$, all cyclic gates become non-Hermitian, since all eigenvalues of Hermitian matrices must be real and a diagonal matrix, $\hat{D}$, fulfilling the Spectral theorem such that $\hat{T} = \hat{U}\hat{D}\hat{U}^{-1}$, where $\hat{U}$ is a unitary, must then fulfill $\hat{D}^n = \mathbb{1}$.

Our result becomes interesting as soon as one wants to exponentiate any phase gate, with a phase other than -1, in which case the gate becomes non-Hermitian. This

Table 3.1: *Common non-Hermitian quantum gates and their cyclic order n. We assume φ to be π divided by an integer. The controlled version of the gates mentioned in this table is non-Hermitian with the same cyclic order.*

Gate		n
Phase shift	R_φ	π/φ
Square root of not	$\sqrt{\text{NOT}}$	4
Imaginary swap	*i*SWAP	4
Square root of swap	$\sqrt{\text{SWAP}}$	4
Ising XX coupling	XX_0 or XX_π	8
Ising YY coupling	YY_φ	$2\pi/\varphi$
Ising ZZ coupling	ZZ_φ	$2\pi/\varphi$
Deutch	D_φ	$2\pi/\varphi$

means that the result of such exponentiating will be non-unitary for $n > 2$. In Table 3.1 we mention a few often used non-Hermitian gates and their cyclic order. We note that to use our method, we must perform a controlled version of the gate we wish to exponentiate, i.e., if we wish to exponentiate an *i*SWAP, we would need a controlled *i*SWAP, as discussed above.

Suppose we have a controlled cyclic gate $\hat{T}$ working on an arbitrary number of qubits. In order to create a circuit for exponentiating such an operator, we must first Taylor expand the exponential

$$\begin{aligned} e^{i\theta\hat{T}} &= \sum_{j=0}^{\infty} \frac{1}{(nj)!}(i\theta)^{nj}\mathbb{1} + \sum_{j=0}^{\infty} \frac{1}{(nj+1)!}(i\theta)^{nj+1}\hat{T} + \cdots \\ &\quad + \sum_{j=0}^{\infty} \frac{1}{((n+1)j-1)!}(i\theta)^{((n+1)j-1)}\hat{T}^{j-1} \\ &= \sum_{k=0}^{n-1}\sum_{j=0}^{\infty} \frac{1}{(nj+k)!}(i\theta)^{nj+k}\hat{T}^k. \end{aligned}$$

In total, this yields n Taylor terms, meaning that our quantum circuit would need $n-1$ ancilla qubits to perform the controls. We then apply the controlled gate $n-1$ times, each time controlled by a different ancilla qubit. The quantum circuit can be seen in Fig. 3.7.

We now prepare the ancilla qubits in the state

$$|\tilde{\varphi}\rangle = N\sum_{k=0}^{n-1}\sum_{j=0}^{\infty} \frac{1}{(nj+k)!}(i\theta)^{nj+k}\left|\tilde{k}\right\rangle, \tag{3.34}$$

where N is a normalization which depends on θ, and the state $\left|\tilde{k}\right\rangle$ indicates a state with k excitations, i.e. we have $\left|\tilde{0}\right\rangle = |00\cdots00\rangle$, and $\left|\tilde{1}\right\rangle = |10\cdots00\rangle$, $\left|\tilde{1}\right\rangle = |01\cdots00\rangle$, or $\left|\tilde{1}\right\rangle = |00\cdots01\rangle$, etc.

Let $|\gamma\rangle$ be the initial state of the target qubits. If we act with the $n-1$ controlled-$\hat{T}$ gates on the initial state $|\tilde{\varphi}\rangle|\gamma\rangle$, as in Fig. 3.7 we arrive at the state

$$|\tilde{\varphi}\rangle|\gamma\rangle \to N\sum_{k=0}^{n-1}\sum_{j=0}^{\infty} \frac{1}{(nj+k)!}(i\theta)^{nj+k}\hat{T}^k\left|\tilde{k}\right\rangle|\gamma\rangle.$$

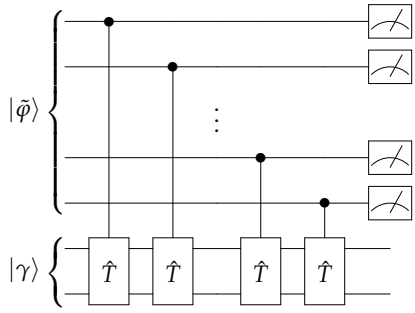

Figure 3.7: *Quantum circuit used to exponentiate a matrix $\hat{T}$ for which $\hat{T}^n = \mathbb{1}$. On top we have $n-1$ ancilla qubits which are prepared in the state $|\tilde{\varphi}\rangle$. Each acts as a conditional for a $\hat{T}$ operation, and finally, they are all measured in the $\{|\pm\rangle\}$-basis. Note that the $\hat{T}$ operation does not have to be a two-qubit operation; it can operate on m qubits.*

If we measure the $n-1$ ancillae in the $\{|\pm\rangle\} = \{(|0\rangle + |1\rangle)/\sqrt{2}\}$ basis, there is a probability of around $1/2^{n-1}$ that we measure $|+\rangle$ in all of the ancillae, if we require θ to be small. This means that the total state becomes

$$|+\cdots+\rangle\, N \sum_{k=0}^{n-1} \sum_{j=0}^{\infty} \frac{1}{(nj+k)!} (i\theta)^{nj+k} \hat{T}^k |\gamma\rangle = |+\cdots+\rangle\, N e^{i\theta\hat{T}} |\gamma\rangle\,,$$

which is the desired result. If this state is not measured, the experiment must be repeated until the desired result is obtained.

We note that if the gate is not cyclic, our method works approximately as long as θ is small, in which case the first terms of the Taylor expansion will dominate. This means that we can choose the number of terms we want in our Taylor expansion as the number of ancillae we include in our quantum circuit.

3.4.1 Example

For an example of the Hermitian $n = 2$ case, see Ref. [289]. Here we consider the case $n = 4$. This could, for example, be a C*i*SWAP. The exponential in this case becomes

$$\begin{aligned} e^{i\theta\hat{T}} =& \frac{1}{2}\Big[(\cos\theta + \cosh\theta)\mathbb{1} + i(\sin\theta + \sinh\theta)\hat{T} \\ &+ (\cos\theta - \cosh\theta)\hat{T}^2 + i(\sin\theta - \sinh\theta)\hat{T}^3\Big]. \end{aligned} \tag{3.35}$$

Remember that the operator in the exponent is *not* Hermitian, and thus we are *not* dealing with a unitary. This means that if θ becomes large, then the hyperbolic functions will blow up. Therefore we keep θ small. Notwithstanding, we prepare three ancillae in the state

$$\begin{aligned} |\tilde{\varphi}\rangle =& \frac{K}{2}\big[(\cos\theta + \cosh\theta)\,|\tilde{0}\rangle + i(\sin\theta + \sinh\theta)\,|\tilde{1}\rangle \\ &+ (\cos\theta - \cosh\theta)\,|\tilde{2}\rangle + i(\sin\theta - \sinh\theta)\,|\tilde{3}\rangle\,\big] \\ =& A\,|000\rangle + B\,|001\rangle + C\,|011\rangle + D\,|111\rangle\,. \end{aligned} \tag{3.36}$$

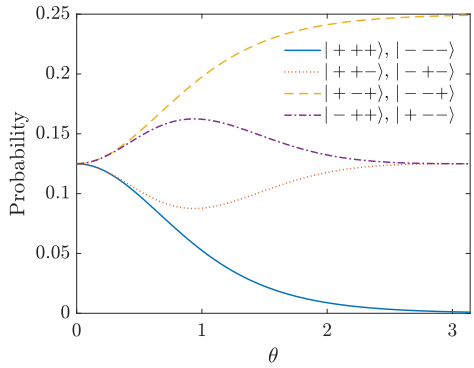

Figure 3.8: *Probability of measuring each of the states in Eq.* (3.37).

All normalization is included in K. Note that we could have chosen other states such as $|100\rangle$ and $|101\rangle$ in the second and third term of $|\tilde{\varphi}\rangle$ as well, as this choice can be made without loss of generality.

Now performing the three controlled T-gates on the qubits, we arrive at the state

$$\begin{aligned}|\tilde{\varphi}\rangle\,|\gamma\rangle \rightarrow \frac{K}{2}\big[&(\cos\theta+\cosh\theta)\,|\tilde{0}\rangle + i(\sin\theta+\sinh\theta)\,|\tilde{1}\rangle\,\hat{T}\\ &+(\cos\theta-\cosh\theta)\,|\tilde{2}\rangle\,\hat{T}^2 + i(\sin\theta-\sinh\theta)\,|\tilde{3}\rangle\,\hat{T}^3\big]\,|\gamma\rangle\,.\end{aligned}$$

By measuring in the $\{|\pm\rangle\}$-basis there is a probability that we will measure the state $|+++\rangle$ which means that we have achieved matrix exponentiation by arriving at the state $|+++\rangle\, Ke^{i\theta\hat{T}}\,|\gamma\rangle$.

3.4.2 Measuring probabillity

In order to investigate the probability of measuring the correct state, we consider the state $|\tilde{\varphi}\rangle$ in Eq. (3.36). In the $\{|\pm\rangle\}$-basis, it takes the form

$$\begin{aligned}|\tilde{\varphi}\rangle = &[A+B+C+D]\,|+++\rangle\\ &+[A-B-C-D]\,|++-\rangle\\ &+[A+B-C-D]\,|+-+\rangle\\ &+[A+B+C-D]\,|-++\rangle\\ &+[A-B+C+D]\,|+--\rangle\\ &+[A-B-C+D]\,|-+-\rangle\\ &+[A+B-C+D]\,|--+\rangle\\ &+[A-B+C-D]\,|---\rangle\,,\end{aligned} \tag{3.37}$$

We wish to measure a state with a coefficient $A+B+C+D$, and thus we want to measure the state $|+++\rangle$. Note that if we chose our $|\tilde{k}\rangle$ states as superpositions, such as $|\tilde{1}\rangle =$

$a|001\rangle + b|010\rangle + c|100\rangle$, then there is no state in the $\{|\pm\rangle\}$-basis with a coefficient $A + B + C + D$, since the normalization then require the B and C coefficients to be normalized by the superposition coefficients a, b, and c, which means that we get an imbalance between the B and C coefficients and the A and D coefficients.

We plot the probabilities of measuring the eight states as a function of θ to see how they behave. The result is seen in Fig. 3.8. Unfortunately, we observe that the probability of measuring the state $|+++\rangle$ decreases exponentially with θ. This supports our previous understanding that we should keep θ small.

3.5 Summary and Outlook

We have proposed a simple implementation of a controlled *i*SWAP-gate and shown that this exhibits a high fidelity. We have discussed an implementation of our gates using superconducting circuits and simulated the gate, including possible fabrication errors and decoherence noise. Even when including these, we still find a reasonably high fidelity. The general implementation presented in Section 3.1 is, however, not limited to superconducting circuits. While the difficulty of implementing our gates increases with the number of controls, we believe that our gates will be superior in certain types of quantum computations, especially compared to equivalent circuits built from one- and two-qubit gates, which often become quite deep. Our controlled *i*SWAP can easily be extended to swapping between more qubits, such that it is possible to control swapping between three, four, and so on qubits. We also propose a quantum circuit for probabilistic exponentiating non-Hermitian quantum gates, which are exact for cyclic gates and approximately exact given small parameters for all other non-Hermitian gates. These results could enhance the performance of near-term quantum computing experiments on algorithms that require multiqubit swapping gates and exponentiating of gates.

CHAPTER 4

The Linear Controlled Swapping Gate

*This chapter is based on Ref. [**III**]; however, we do not include the circuit analysis, as it was part of my master's thesis, but we do present the circuit diagram. This is also why it is included last of the controlled gates even though it was published before the two other gates. Text and figures have also been edited to fit into the thesis.*

We discussed controlled versions of the CNOT and *i*SWAP gates in the two previous chapters. This chapter presents yet another controlled gate that occurs natively in superconducting circuits based on a linear Heisenberg model. In particular, we investigate what kind of quantum mechanical two-qubit gates a linear chain of qubits implements. We further mention a way of implementing such a chain using superconducting qubits. We show that such a chain swaps the end qubits' states and obtains a phase, with an average fidelity of around 0.99. The swapping operation is controlled on the middle qubits, acting as ancilla qubits. Altogether, this implements a conditional two-qubit swapping gate.

This chapter is organized as follows: In Section 4.1.1 we introduce the Hamiltonian of the system and the requirements to it. This is followed by Section 4.1.2 where we present the swapping gate which the Hamiltonian implements and perform a numerical investigation of the average fidelity of the gate when varying the parameters of the system. Then, in Section 4.2, we present a superconducting circuit that implements the desired Hamiltonian in the case of four qubits. Finally, in Section 4.3 we present a summary and outlook of the chapter.

4.1 The system

Using a linear Heisenberg model, we can implement a two-qubit swapping gate. The Heisenberg model consists of several connected qubits. We start by presenting the Hamiltonian of the system and then explain how it yields the gate.

4.1.1 The Hamiltonian

We consider a linear Heisenberg chain consisting of N qubits. In the Schrödinger picture, the linear Heisenberg model takes the form

$$\hat{\mathcal{H}} = -\frac{1}{2}\sum_{j=1}^{N}\omega_j\sigma_j^z + \sum_{j=1}^{N-1}\left[J_j^x(\sigma_j^x\sigma_{j+1}^x + \sigma_j^y\sigma_{j+1}^y) + J_j^z\sigma_j^z\sigma_{j+1}^z\right],$$

where $\sigma_j^{x,y,z}$ are the Pauli matrices, ω_j denotes the frequency of qubit j, and the $J_j^{x,z}$'s denotes the coupling between the jth and $(j+1)$th qubits. This means that we consider only nearest neighbor XXZ interactions.

Following Ref. [292] we assume a spatially symmetric spin chain, meaning that $\omega_j = \omega_{N+1-j}$ and $J_j^{x,z} = J_{N-j}^{x,z}$. In order to study the role of the interactions, we transform into the interaction picture choosing the non-interacting Hamiltonian as

$$\hat{\mathcal{H}}_0 = -\frac{1}{2}\omega_1\sum_{j=1}^{N}\sigma_j^z, \tag{4.1}$$

which yields the interaction Hamiltonian

$$\hat{\mathcal{H}}_I = -\frac{1}{2}\sum_{j=2}^{N-1}\delta_j\sigma_j^z + \sum_{j=1}^{N-1}\left[J_j^x(\sigma_j^x\sigma_{j+1}^x + \sigma_j^y\sigma_{j+1}^y) + J_j^z\sigma_j^z\sigma_{j+1}^z\right],$$

where the detuning is $\delta_j = \omega_j - \omega_1$ and we have used the rotating wave approximation to neglect interaction terms, see Section 1.5. This is justified under the assumption that $\omega_1 \gg J_j$, which we assume for the rest of this chapter.

Although the result of Ref. [292] is valid for any $N \geq 4$, we will now focus on the case of $N = 4$. This is partly because it simplifies the arguments while the ideas remain intact and partly because a physical implementation, discussed in **[III]**, is more easily done with fewer qubits. With only four qubits, we are left with just one detuning; why we drop the subscript, $\delta \equiv \delta_2$, and four interaction terms, $J_{1,2}^{x,z}$. The last requirements for the gate relates these parameters; the first is $\delta = \delta_\pm \equiv 2(J_2^z \pm J_2^x)$, in accordance with Ref. [292], while the second requirement is $J_1 \equiv J_1^x = J_1^z$. For a derivation of these requirements, see Ref. [292]. A schematic model of the system is seen in Fig. 4.1(a).

4.1.2 The two-qubit swapping gate

The above Hamiltonian, with $N = 4$, implements a two-qubit swapping gate, where the first and the last qubits are the swapped qubits, while the middle ancilla qubits control the state of the gate. We thus have a multiqubit controlled gate, where the combined state of the control qubits determine the state of the gate, effectively working as a single control qubit [293–295]. The control qubits then constitutes a switch which can either be in an "open" state, which, in the case of four qubits, i.e., two control qubits, is $|0\rangle_C \equiv |00\rangle_C$, or a "closed" state, which, in this case is the Bell states $|1^\pm\rangle_C = (|10\rangle_C \pm |01\rangle_C)/\sqrt{2}$, depending on the choice of $\delta_\pm$. Note that the subscript C denotes the $(N-2)$-qubit state of the control qubits, while we use T for the target, i.e., first and last, qubits. In the

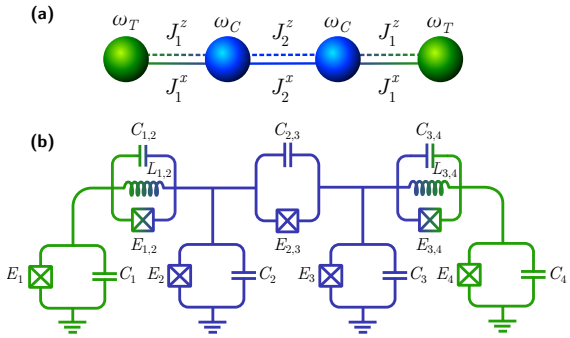

Figure 4.1: (a) *The desired qubit model as seen in Eq.* (4.2). **(b)** *The lumped circuit model for the super conducting circuit used to implement the above system. The crossed boxes represent Josephson junctions, the parallel lines are capacitors, and the bent lines are linear inductors.*

computational basis of the target qubits, $\{|00\rangle_T, |01\rangle_T, |10\rangle_T, |11\rangle_T\}$, the open gate can be expressed as

$$\hat{\mathcal{U}}_{\text{open}} = \begin{pmatrix} 1 & 0 & 0 & 0 \\ 0 & 0 & \mp 1 & 0 \\ 0 & \mp 1 & 0 & 0 \\ 0 & 0 & 0 & i \end{pmatrix}, \tag{4.2}$$

where the choice of $\delta_\pm$ dictates the phase on the swap. The closed state of the gate is simply the identity $U_{\text{closed}} = \mathbb{1}_4$. The open gate will entangle the input and output qubits. This can be quantified using the entanglement power [296], which in our case is $1/9$.

We characterize the performance of the gate by calculating the average process fidelity, Eq. (2.18), with the target gate being $\hat{\mathcal{U}}_{\text{open}}$ and $\hat{\mathcal{U}}_{\text{closed}}$. We simulate the system similarly to in Sections 2.1.3 and 3.1.1 using the Lindblad Master equation and the interaction Hamiltonian of Eq. (4.2) using the QuTiP Python toolbox [240]. The result is then transformed into the frame rotating with the diagonal of the Hamiltonian, and then the average fidelity is calculated.

Given a set of model parameters, the average fidelity can be calculated as a function of time for both sets of gate configurations. In the case of the open gate, i.e., configuration $|0\rangle_C$, the average fidelity rises from some initial value to a maximum (unity for the perfect gate) at the gate time, which we denote t_g. Analytically, we expect this to be [292]

$$t_g = \frac{\pi}{|2J_1|}; \tag{4.3}$$

however, for the simulations, we find the best gate time numerically. In the case of the closed gate, i.e., the configuration $|1\rangle_C$, the average fidelity is initially unity and deviates only from this value due to leakage to the control qubits or as a result of decoherence noise.

In order to investigate the sensitivity of the parameter space, we vary the parameters J_1, J_2, and δ and show the gate time and average fidelities at the gate time in Fig. 4.2. The figure shows both the average fidelity without any decoherence and with a decoherence time of $T_1 = T_2 = 100\,\mu\text{s}$ [297]. In Figs. 4.2(a) and (d), we vary the coupling of the

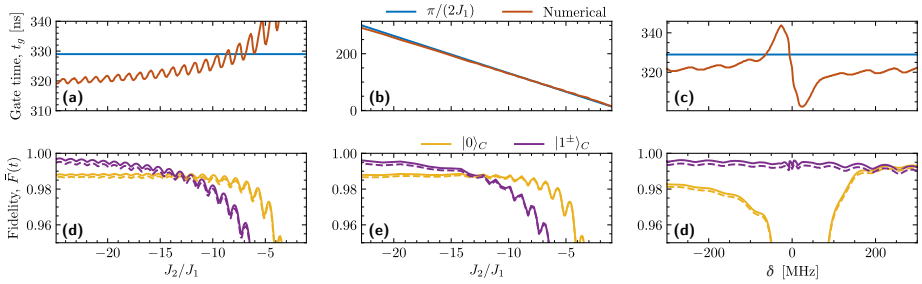

Figure 4.2: (a)-(c) *Gate time as a function of the model parameters J_2, $1/J_1$, and δ. The blue lines indicate the analytical result of Eq.* (4.3) *and the red lines indicate the point of maximum average fidelity.* **(d)-(e)** *Average fidelities at the numerical gate time as a function of the model parameters J_2, $1/J_1$, and δ, both with (dashed lines) and without (solid lines) decoherence noise. The yellow lines indicate the fidelity when the gate is in the open configuration, while the purple line indicates that it is in the closed configuration.*

control qubits, $J_2 \equiv J_2^x = J_2^z$, in the configuration $\left|1^+\right\rangle_C$, while keeping the remaining coupling constants at $J_1 = 30\,\text{MHz}$. Setting $J_2^x = J_2^z$ is merely done for the simplicity of the numerical investigation and is not a requirement, as we will exploit later. From this simulation, we observe that the optimal numerical gate time is about 5% faster than the analytical, and for large J_2/J_1, we observe almost unity average fidelity for the closed configuration of the gate, and between 0.98 and 0.99 for the open configuration. In Figs. 4.2(b) and (e), we vary the coupling between the target qubits and the control qubits, i.e., J_1, while keeping the coupling between the control qubits constant at $J_2 = 750\,\text{MHz}$, in the configuration $\left|1^+\right\rangle_C$. Again, we observe a slightly shorter numerical gate time and fidelities of close to unity and just between 0.98 and 0.99 for the closed and open configuration, respectively. In Figs. 4.2(c) and (f), we vary J_2^x and keeping $J_2^z = 600\,\text{MHz}$ in the case of the gate being in the configuration $\left|1^-\right\rangle_C$ to effectively vary Δ around zero. We observe that the gate completely fails around zero, as it should, but we also conclude that we achieve a larger average fidelity (just above 0.99) for a positive detuning, i.e., $J_2^z > J_2^x$, rather than a negative detuning. However, for the case of $\left|1^+\right\rangle_C$, we find that the average fidelity is slightly larger when $J_2^z < J_2^x$. The simulations also find that a different sign on the couplings J_1 and J_2 yields a slightly larger average fidelity.

The simulations mentioned above beg the question of why the average gate fidelities do not approach unity, even when the requirements mentioned in Section 4.1.1 are fulfilled. The answer to this question is found together with the answer as to why the numerical gate time is shorter than the analytical gate time in Eq. (4.3). It all comes down to the fact that even though the state $|1\rangle\,|0\rangle_C\,|1\rangle$ is indeed an eigenstate of the Hamiltonian, it is also degenerate with the states $|1\rangle\,\left|1^{\mp}\right\rangle_C\,|0\rangle$ and $|0\rangle\,\left|1^{\mp}\right\rangle_C\,|1\rangle$ depending on the choice of $\delta_{\pm}$ (note that these states are not the same as the configurations of the closed gate). This means that the system will oscillate between these three states, like how the open gate oscillates between states with a single excitation. However, the time scale of this oscillation is less than for the single excitation, with an oscillation time around 90% of the analytical gate time. This means that sometimes between $0.9t_g$ and t_g, we will observe maximum average fidelity, less unity, depending on the system's configuration.

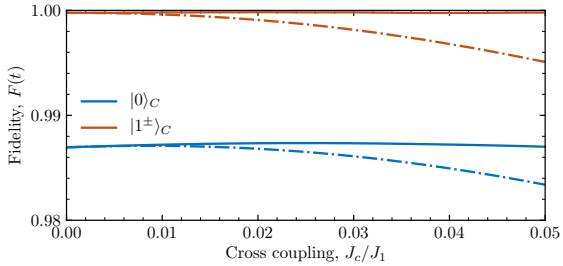

Figure 4.3: *Average fidelities of the control qubits in both states for increasing coupling strength beyond nearest-neighbor coupling, J_c. The solid lines are with next-to-nearest couplings included, and the dash-dotted lines are with up to next-to-next-to-nearest neighbor coupling.*

This does, however, not mean that it is impossible to achieve perfect transfer for some states in a well-configured system. Namely, as long as not *both* the input and output qubit are in a superposition state, the state is transferred perfectly when disregarding decoherence noise.

Note that the resonance of the eigenstates mentioned above is the same resonance that makes the gate work to begin with, in that case it is the states $|1\rangle\,|0\rangle_C\,|0\rangle$, $|0\rangle\,|0\rangle_C\,|1\rangle$, and $|0\rangle\,|1^{\mp}\rangle_C\,|0\rangle$ that are in resonance.

4.2 Superconducting circuit implementation

A possible superconducting circuit implementing the desired gate for $N = 4$ can be seen in Fig. 4.1(b). It consists of four transmon qubits connected through a Josephson junction and the two end qubit connected to the middle ones via an inductor, while the middle two are connected through a capacitor of arbitrary size. The capacitive coupling between the to end qubits should be as small as possible to avoid coupling beyond nearest-neighbor coupling. It is essential to minimize capacitive couplings between every other pair of qubits when the circuit is scaled up to larger N. When this is the case, the capacitance matrix becomes approximately block diagonal, and its inverse becomes block-diagonal, which means that unwanted cross-talk beyond the nearest neighbor is suppressed. When the capacitance between every other pair of qubits is not minimized, the capacitance matrix becomes tridiagonal, and its inverse will feature components leading to coupling beyond nearest-neighbor coupling. In reality, there will always be a parasitic capacitance between two nodes connected through a Josephson junction; however, not including these are equivalent to assuming $C_i \gg C_{i,i+1}$, where C_i is the shunting capacitance of the ith qubit and $C_{i,i+1}$ is the parasitic capacitance between the ith and $(i+1)$th node. A detailed analysis of the circuit can be found in **[III]**.

In order to quantify the effect of coupling beyond nearest-neighbor coupling, we simulate the gate, including next-to-nearest couplings and next-to-next-to-nearest couplings. We calculate the average fidelity, for the two states of the control qubits, as a function of increasing cross-talk, and the result can be seen in Fig. 4.3.

From the simulation, we see that next-to-nearest couplings have no effect on the gate when it is in its closed configurations $|1^{\pm}\rangle_C$, and have only little effect when it is in its open configuration $|0\rangle_C$. The average fidelity increases a tiny amount until the next-to-nearest neighbor coupling is $\sim 3\%$ of the nearest neighbor coupling between the target qubits and the control qubits. This is consistent with the result of Ref. [298]. On the other hand, next-to-next-to-nearest couplings have a much more significant influence on the system when the coupling strength is above 2% of the target-control coupling, and we conclude that the gate fidelity decreases as the square of the next-to-next-to-nearest coupling strength. This is expected since the next-to-next-to-nearest coupling is a direct coupling of the input and output qubits.

4.3 Summary and Outlook

This chapter investigates how a linear chain of qubits can be configured into operating as a controlled two-qubit swapping gate. In particular, we have focused on the case of four qubits and shown that it can create a swapping gate with a fidelity around 0.99, even when including realistic decoherence noise. We have also presented a superconducting circuit design that could be used to implement the gate.

PART **III**

Hybrid Quantum-Classical Algorithms

CHAPTER 5

Parameterized Quantum Circuits

*At some point during my PhD studies, my focus shifted from superconducting circuits to quantum algorithms, more specifically hybrid quantum-classical algorithms. This shift came naturally since such algorithms are the ones that are applied to emerging quantum chips based on superconducting circuits. In other words, my focus went from "how do one build a quantum chip?" to "given such a quantum chip, what can we do with it?". This chapter is based on Ref. [**VII**]. Text and figures have been edited to fit the thesis, and the section on photonic circuits has been omitted as it is outside the scope of this thesis.*

Until now, we have primarily been focusing on building qubits and performing gate-operations on them using superconducting circuits. However, producing such quantum chips is not all there is to quantum technology. We must also figure out which algorithms we should apply to such quantum chips. Ideally, we would like to apply some great algorithm to a large-scale, fault-tolerant, universal quantum computer, but although we are closer to this significant milestone than ever before, it may take years before we achieve this. Current quantum technology supports only a couple of tens of qubits and a few hundred gate operations before the noise becomes too overwhelming. Nonetheless, there is a growing consensus that these Noisy Intermediate-Scale Quantum (NISQ) devices may find a practical application in the near future or at least a lot sooner than large-scale, fault-tolerant universal quantum computing [234].

A strategy for optimizing the use of noisy quantum hardware is to divide the computational tasks between classical and quantum resources. Hybrid quantum-classical (HQC) algorithms are such schemes. Examples of HQC algorithms are the quantum approximate optimization algorithm (QAOA) [299–301], the quantum autoencoder (QAE) [302], the quantum variational error corrector (QVECTOR) [303], classification via near term quantum neural networks (QNN) [304–307], quantum generative adversarial networks (QuGAN) [308–311], and the variational quantum eigensolver (VQE) [312–319]. All these algorithms have in common that they share a quantum subroutine for producing parameterized trial states, where the parameters can be tuned to optimize a function value. Thus the performance of these algorithms depends on the configuration of the parameterized quantum circuit (PQC). This has led to several studies of circuit properties,

and capabilities [320–324]. In this chapter, we discuss PQCs and characterize their power by their entangling capability and so-called expressibility, introduced recently by Sukin Sim *et al.* [320]. In particular, we focus on the effect of single-qubit rotations and investigate whether it is possible to saturate the expressibility and entangling capability when gradually increasing the number of single-qubit rotations.

While single-qubit rotations are often cheap to implement in quantum circuits, they sum up many variational parameters for classical optimization. If some of these variational parameters are redundant, the result of an HQC algorithm should not suffer by removing them from the classical optimization. In addition, the presence of redundant parameters slows down the optimizer and may get it stuck in a local minimum, preventing the HQC algorithm from converging to the global minimum. With the current few-qubit HQC experiments, this has posed no problem, but for future applications to large systems beyond classical numerical methods, the number of variational parameters in the classical part of the HQC algorithm may become a limiting factor. Therefore, we investigate how many rotations are necessary to run these algorithms without compromising the results. We do this by considering the expressibility and entangling capability [320], and investigate whether they saturate before we reach the maximum amount of single-qubit rotations. To verify that these metrics capture the capability of an actual HQC algorithm, we also simulate a VQE for the same number of single-qubit rotations. We discuss these results in Section 6.1 where we go into detail concerning the variational quantum eigensolver. In Section 5.1 we present PQCs and introduce the two metrics we investigate. In Section 5.2 we present our results of the metrics and consider how the expressibility and entangling capability are affected when the number of qubits in the PQC is increased up to ten qubits, where previous investigations have only considered four qubits [320]. In particular, in Section 5.3 we consider how different entangling gates perform when the number of qubits is increased. In Section 5.4 we present a summary and outlook for future work.

5.1 Theory behind PQCs

A parameterized quantum circuit (PQC) is essentially just a circuit consisting of N interconnected qubits, which we can operate on with quantum-logic gates, often just called gates. Some of these gates should be parameterized, e.g., in the rotation angle of a single-qubit rotation gate (see Section 1.7.1 for how to do this with superconducting circuits). We represent a PQC by a parameter-dependent unitary matrix, $\hat{\mathcal{U}}(\boldsymbol{\theta})$, that is used to map an initial state of N qubits, often $|0\ldots0\rangle$, to some other state $\hat{\mathcal{U}}(\boldsymbol{\theta})\,|0\ldots0\rangle$, which is typically used to approximate the ground state of some predefined Hamiltonian $\hat{\mathcal{H}}$.

Parameterized quantum circuits can take many forms, but the order and type of gates are usually fixed before the experiment starts, and only the gate parameters are optimized during the algorithm. Often PQCs are built using a layered structure where each layer consists of some parameterized single-qubit rotations followed by a set of unparameterized entangling gates. In Fig. 5.1 we present an example of such a PQC, which consists of N qubits and L layers. A predefined number of single-qubit rotations are performed in each layer, followed by an entangling operation, V. Generally, it takes three rotations to map an arbitrary qubit state to another state. We, therefore, include

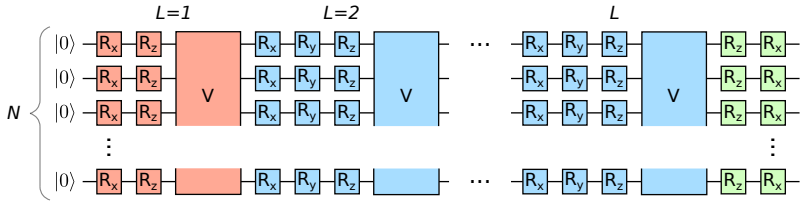

Figure 5.1: *Possible implementation of a parameterized quantum circuit (PQC). Single-qubit rotations are denoted R_x, R_y, and R_z, while the multiqubit block indicates entangling gates spanning multiple qubits. The first layer (red) consists of two single-qubit rotations on each qubit and an entangling gate, V. The bulk layers (blue) each consists of three single-qubit rotations on each qubit and an entangling gate. The circuit ends with two single-qubit rotations on each qubit.*

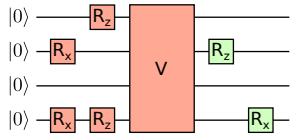

Figure 5.2: *Example circuit with $N = 4$ qubits, $L = 1$ layer, and $m = 6$ randomly configured single-qubit rotations.*

three rotations on each qubit in each layer. However, if we assume that the qubit starts in the $|0\rangle$-state, then we can map it to any other state using just two rotation gates. We can therefore eliminate a gate in the first layer (red part of Fig. 5.1) without losing any expressibility of the circuit. In many quantum algorithms, one measure each qubit in the z basis, which by the same reasoning as for the first qubits makes final z rotations irrelevant, meaning that we can remove a gate from the last part of the circuit (red part of Fig. 5.1). Note that this part is not considered a part of any layer and that the number of layers is equal to the number of V operations. For now, we assume that the entangling gates, V, have no variational parameters, meaning that the total number of parameters is equal to the number of single-qubit rotations,

$$M = N(3L + 1). \tag{5.1}$$

For an HQC problem of fixed V, L, and N, we wish to investigate the quality of the PQC as a function of the number of single-qubit rotations, $m \in [0, M]$. However, as this will leave 2^M possible PQCs for each VQE problem, we select the PQC realizations randomly. For a given number of variational parameters, m, we pick a random circuit configuration with m single-qubit rotations. This is equivalent to fixing $M - m$ rotation angles in Fig. 5.1 to zero. An example circuit with $L = 1$, $N = 4$ and $m = 6$ is shown in Fig. 5.2. Producing many randomly chosen circuit configurations with m rotations allows us to collect statistics about circuits with a certain "rotations filling degree".

5.1.1 Expressibility

We wish to measure how well a given PQC performs in an HQC algorithm, such as VQE. One way to do this is to simulate a VQE algorithm for a specific system. However, we

would like to characterize the PQC more generally, independent of the specific VQE problem. One way to do this is to calculate the expressibility (and entangling capability as presented in Section 5.1.2) [320]. The expressibility measures how close the PQC comes to uniformly map the initial state, $|0\dots0\rangle$, to the entire Hilbert space. This mapping is done by comparing the probability distribution of the PQC with the probability of a uniform distribution in Hilbert space, i.e., an ensemble of Haar random states. Loosely, one may think of the expressibility as how many final states the PQC can reach.

It is important to note that the expressibility and entangling capability are not perfect metrics for the suitability of a PQC in an HQC [324]. Some chemistry and condensed matter Hamiltonians contain specific symmetries, which can be solved accurately by a PQC respecting these symmetries, which is rated poorly by the expressibility and entangling capability metrics.

We calculate the expressibility following the approach in Ref. [320]:

1. Pick the gate operation, V, qubit number, N, and the number of layers, L.
2. For a given number of rotations, m, pick a random PQC resulting in a parameterized unitary, $\hat{\mathcal{U}}(\boldsymbol{\theta})$.
3. Calculate the expressibility of the circuit:
   a) Uniformly sample $1000(N+1)$ sets of parameter vectors, $\boldsymbol{\theta}_1, \boldsymbol{\theta}_2$.
   b) Compute the overlap fidelity of the final states,
   $$F = |\langle 0\dots0|\hat{\mathcal{U}}^\dagger(\boldsymbol{\theta}_2)\hat{\mathcal{U}}(\boldsymbol{\theta}_1)|0\dots0\rangle|^2. \tag{5.2}$$
   c) Create a histogram over the fidelities, in order to estimate the probability distribution, $P(F)$, of the fidelities found in the previous step. Not that this estimation will depend on the number of bins in the histogram, n_{bins}. For the sake of consistency we set $n_{\text{bins}} = 75$ as in Ref. [320].
   d) Compare $P(F)$ with the probability distribution achieved from an ensemble of Haar random states, $P_{\text{Haar}}(F) = (2^N-1)(1-F)^{2^N-2}$, using the same number of bins as in the previous step. We do this by computing the Kullback-Liebler divergence
   $$\begin{aligned}\text{Expr} =& D_{KL}(P(F)||P_{\text{Haar}}(F)) \\ =& \sum_F P(F)\ln\left(\frac{P(F)}{P_{\text{Haar}}(F)}\right),\end{aligned} \tag{5.3}$$
   where the sum is taken over the bins. This measure is known as the expressibility of a PQC.
4. Calculate the relative expressibility
   $$\mathcal{E} = -\ln\left[\frac{\text{Expr}}{\text{Expr(Idle circuit)}}\right]. \tag{5.4}$$

Note that $\text{Expr} = 0$ for the most expressible circuit that reaches all final states uniformly, $P(F) = P_{\text{Haar}}(F)$. On the other hand, the least expressible circuit (the idle circuit with

no gates) has Expr(Idle circuit) $= (2^N - 1)\ln(n_{\text{bins}}) > 0$. The above also illustrates the dependence on the chosen number of histogram bins. We, therefore, normalize our results with the expressibility of the idle circuit. To better resolve the most expressible circuits (Expr ~ 0), we take the logarithm and multiply by minus one in order to make the result positive. We call this relative expressibility; see Equation 5.4.

We note that instead of calculating the expressibility via the Haar measure, we could also have used other metrics, such as the qBAS score, where the probability distribution $P(F)$ is compared to the bars and stripes data set [325]. Had we instead tried to maximize the expressibility, this could be considered training the circuit for approximating a given probability distribution. This unsupervised machine learning task is also known as generative modeling. Such a training model is an example of data-driven quantum circuit learning [325].

5.1.2 Entangling capability

It is expected that HQC algorithms may have an advantage over similar classical algorithms in the future since entanglement occurs naturally in the quantum mechanical part of the HQC algorithm. Therefore we also wish to measure how well quantum circuits can produce entangled states. Reference [320] proposes to use the entangling capability and defines it as the average Meyer-Wallach entanglement measure [326]

$$Q(|\psi\rangle) = \frac{4}{n}\sum_{j=1}^{n} D(\iota_j(0)\,|\psi\rangle\,, \iota_j(1)\,|\psi\rangle), \tag{5.5}$$

where the generalized distance, D, is

$$D(|u\rangle\,, |v\rangle) = \frac{1}{2}\sum_{i,j} |u_i v_j - u_j v_i|^2, \tag{5.6}$$

and the linear mapping $\iota_j(b)$ removes the jth qubit in the computational basis

$$\iota_j(b)\,|b_1 \dots b_n\rangle = \delta_{bb_j}\,|b_1 \dots \hat{b}_j \dots b_n\rangle\,, \tag{5.7}$$

where $b_j \in \{0, 1\}$ and the "hat" denotes the absence of the jth qubit. The average of Q is then taken over a uniformly sampled set of parameters $\boldsymbol{\theta}$. We denote the entangling capability $\mathcal{C}$. The entangling capability lies between zero and one, zero being a non-entangling circuit and one representing a maximally entangling circuit. We wish to investigate whether the entangling capability saturates around the same amount of single-qubit rotations where the expressibility saturates.

5.2 Reducing the amount of single-qubit rotations

We consider the following protocol: For each fixed number of rotations, m, we sample 100 random circuits and calculate their relative expressibility and entangling capability[1].

[1]Some of the numerical results presented here were obtained at the Centre for Scientific Computing, Aarhus `http://phys.au.dk/forskning/cscaa/`.

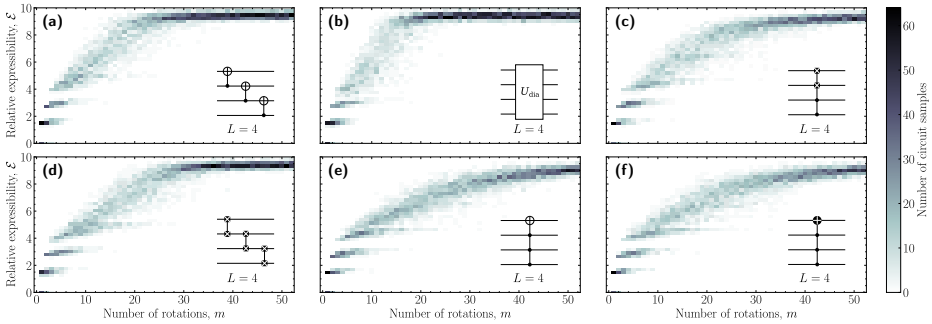

Figure 5.3: *Relative expressibility of different circuits with $N = 4$ qubits and $L = 4$ layers as a function of the number of rotations. The inset in the right upper corner of each plot shows the entangling gate, V, used in each layer.* ***(a)*** *Three* CNOTs, ***(b)*** *diamond gate,* ***(c)*** C^2iSWAP, ***(d)*** *three* iSWAPs, ***(e)*** C^3NOT, ***(f)*** *3-bit iToffoli gate.*

The PQC is considered saturated if the relative expressibility and entangling capability converge after a given number of single-qubit rotations. The two metrics do not necessarily converge at the same number of single-qubit rotations, but, as we will see, this usually happens around the same point. One could argue that this is expected since we are only adding single-qubit gates, and thus we are not adding any entangling gates to the circuit. Therefore, a PQC that is saturated in the relative expressibility should be capable of applying the maximal entangling capability of the given V-gate.

In Fig. 5.3 we have plotted a two-dimensional histogram of the relative expressibility as a function of the number of rotations, m, in the circuit. The calculations are performed with $N = 4$ qubits in $L = 4$ layers, allowing for a maximum of $M = 52$ single-qubit rotations according to Eq. (5.1). The calculation for different entangling operations, V, displayed as the inset in each subplot. We present two-dimensional histograms of the entangling capabilities in Fig. 5.4, for the same cases. For results concerning less layers ($L = 1, 2, 3$) and/or more qubits ($N = 6, 8$) see the supplementary material of the original paper **[VII]**.

Before discussing the details of each of the different V-gates, we first consider some general features of the results. First of all, if no V-gates are present, all product states can be represented using only three single-qubit rotations on each qubit. In the case of $N = 4$ qubits, this implies that 12 single-qubit rotations are sufficient, which yields a relative expressibility of $\mathcal{E} = 5.8$ and, of course, zero entangling capability. All non-entangling circuits yield this maximum relative expressibility and zero entangling capability.

Most of the plots show a "stripe" pattern, which is especially pronounced for low relative expressibility or entangling capability. These stripes occur when the single-qubit rotations are placed on the same qubits. For $N = 4$, we observe up to four stripes, the lowest stripe when all rotations are placed on one qubit, the second-lowest when all rotations are placed on two qubits, and so forth.

The final point is that a circuit that has converged in relative expressibility and entangling capability is not necessarily capable of finding any arbitrary state in the selected Hilbert space. The fact that we achieve convergence means that this particular choice

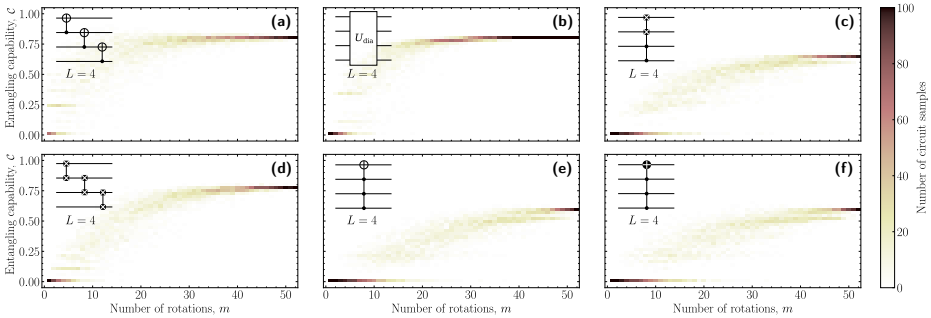

Figure 5.4: *Entangling capability of different circuits with $N = 4$ qubits and $L = 4$ layers as a function of the number of rotations. The inset in the right upper corner of each plot shows the entangling gate, V, used in each layer.* ***(a)*** *Three* CNOTs, ***(b)*** *diamond gate,* ***(c)*** C^2iSWAP, ***(d)*** *three* iSWAPs, ***(e)*** C^3NOT, ***(f)*** *3-bit iToffoli gate.*

of PQC has reached its limit. This limit is seen by considering the minimum required parameters to specify an arbitrary N-dimensional state, which is $2(2^N) - 2$ parameters. Here the factor 2^N comes from the number of amplitudes of each basis state, the factor of two arises because the amplitudes are complex, and the subtraction of two parameters is due to global phase and normalization conditions. Thus for the $N = 4$ case, the minimum parameter count is 30. This means that if a PQC saturates below $m = 30$, it cannot reach arbitrary states in the Hilbert space.

$V =$ CNOTs

One of the most frequently used two-qubit entangling gates is the CNOT gate. We, therefore, consider the case where V is a CNOT between each consecutive pair of qubits. See Fig. 5.3(a) for the case of four qubits and four layers. The relative expressibility converges towards $\mathcal{E} = 10$ within 30 single-qubit rotations. The story is similar for fewer layers; the relative expressibility is converged at $m = 30$ single-qubit rotations. The above implies that we do not saturate the relative expressibility for one and two layers, as we have less than 30 rotations in both cases. However, more than three layers of CNOTs and 30 single-qubit rotations seem to be a waste of resources, as the relative expressibility does not increase further. However, this does not mean that this PQC configuration is optimal, as we will see when discussing the diamond gate. From Fig. 5.4(a), we observe that the entangling capability saturates around 0.8 at approximately 30 single-qubit rotations.

For $N = 6$ qubits (see original paper **[VII]**), we observe the same tendencies; however, the relative expressibility converges towards $\mathcal{E} = 9$. This convergence happens at around 40 single-qubit rotations, obtained for just two layers, significantly fewer than the minimum parameter count: 126 for six qubits.

Turning towards the case of eight qubits, we again observe a saturation of the relative expressibility and entangling capability (see original paper **[VII]**). Convergence is reached after approximately 30 single-qubit rotations at a relative expressibility $\mathcal{E} = 7.5$, which is lower than for both four and six qubits and the same as for having no entangling

V gate. This fact is due to the number of bins used in the definition of the relative expressibility; see Section 5.3 for further discussion.

$V =$ iSWAPs

An entangling version of the SWAP gate is the *i*SWAP gate. The *i*SWAP gate has an entangling power equivalent to the CNOT gate and occurs naturally in systems with XY-interaction or Heisenberg models, such as superconducting circuits [269] as mentioned in Section 1.8.2, and in cavity mediated interaction between spin qubits and superconducting qubits [19, 110, 270]. In Fig. 5.3(d), we present the relative expressibility where the V gate is an *i*SWAP gate between each qubit. The relative expressibility of this configuration goes towards the same as for the CNOT; however, it converges a bit slower. For four qubits, the difference is about five rotations. However, it is more pronounced for six qubits with a difference of around 20 single-qubit rotations. The behavior for eight qubits and the *i*SWAP gates is the same as for the CNOT gate.

The entangling capability in Fig. 5.4(d) saturates a bit below 0.8, and the saturation point is later than for the CNOT gates as for the relative expressibility. Overall, the *i*SWAP gate performs worse than the CNOT gate.

$V =$ DIAMOND

An example of an entangling four-qubit gate is the diamond gate [327], which is an entangling swapping gate with two control qubits, where the two control qubits must be in an entangled state to control the swapping operation. The diamond gate is difficult to synthesize into one- and two-qubit gates. A decomposition into standard gates requires 21 gates, while it can be done with purely CNOT gates and single-qubit gates using 42 and 49 gates, respectively. It does, however, naturally occur in superconducting circuit schemes for quantum information processing. See Ref. [327] or the supporting material of Ref. **[VII]** for more details.

In Fig. 5.3(b) we present the relative expressibility for circuits with four qubits, four layers and $V = U_{\text{dia}}$, where U_{dia} is the diamond gate. We see that the relative expressibility converges rapidly towards $\mathcal{E} = 10$, which it reaches within 20 single-qubit rotations, which is less than for both the CNOT and *i*SWAP gates in subfigures (a) and (d) and less than the minimum number of parameters. We, therefore, conclude that even though the PQC has saturated, it is incapable of reaching any arbitrary state in the Hilbert space. This also means that other circuits that have saturated at the same relative expressibility must also be incapable. In the case of the entangling capability [Fig. 5.4(b)], we also find saturation at around 20 single-qubit rotations.

We observe the same behavior for six qubits: When the diamond gate is used as an entangling gate, convergence is reached faster than when CNOT or *i*SWAP gates are used. For eight qubits, the performance of the diamond gate is reduced to the same level as the two other gates. We also see that the stripe patterns are less pronounced in the case of the diamond gate. This is because the gate is highly entangling, mixing the qubits and thus blurring out the stripes.

$V =$ MULTIQUBIT GATES

In order to investigate whether the diamond gate performs well simply because it is a multiqubit gate, we consider a few other multiqubit gates. In Chapters 2 and 3 we discussed different multi-qubit gates, more specifically the C^{n}NOT, the n-bit iToffoli, and the C$^n i$SWAP gate. We, therefore, consider these three gates as our entangling gates one at a time. The result using these gates can be seen in subfigures (c), (e), and (f) of Fig. 5.3 for $N = 4$.

Common for all three gates is that they converge towards the same relative expressibility as the other entangling gates, namely $\mathcal{E} = 10$ for four qubits. However, they are much more dependent on the number of rotations, as the convergence point is only reached for the maximum amount of rotations. The main difference between the three gates is that the double controlled iSWAP in Fig. 5.3(c) converges a bit faster than the multiple controlled NOT gates. However, this difference cannot be seen for six or more qubits, where all three multiqubit gates converge at the same rate. Thus, the double controlled iSWAP converges faster because it has twice as many target qubits compared to the multiple controlled NOT gates, which is less significant for more qubits. An interesting thing to notice is the fact that the diamond gate seems to converge much faster than the double controlled iSWAP gate (compare subfigures (b) to (c)) although both gates are swapping gates with two controls. This difference is probably because the controlling part of the diamond gate requires a superposition state to activate the swap, compared to the multiple controlled iSWAP gate, which does not require a superposition.

In terms of entangling capability, multiple control gates perform only at an average level with a maximal entangling capability of 0.5, see Fig. 5.4(c), (e), and (f). As for the relative expressibility, we need the maximum number of rotations for the entangling capabilities to reach their maximum. We also observe that the three multiqubit gates barely outperform the non-entangling gates for six qubits. This is because most of the qubits become control qubits when the number of qubits increases, and this means that the multiqubit gates will act trivially on more states as the number of qubits increases. We conclude that the entangling capability and relative expressibility saturates for approximately the same number of qubit rotations as the VQE simulation saturates. In the following section, we consider the entangling capability and the relative expressibility as the number of qubits increases, but only for the case of a fully saturated PQC.

Table 5.1 presents a comparison of the different V-gates used in the analysis. The comparison is made after the saturation point is reached for the diamond gate with two layers and 25 single-qubit rotations for both four and six qubits. We do not compare the eight qubit case as the expressibility is the same for all V-gates. See Section 5.3 for a discussion of why this is the case. We note that other entangling gates may outperform the gates we have considered here.

5.3 Increasing the number of qubits

In the light of the fact that all PQCs consisting of eight qubits seem to converge approximately towards the same relative expressibility, we investigate the relative expressibility as a function of the number of qubits. We, therefore, plot the relative expressibility for

Table 5.1: *Comparison of relative expressibility and entangling capability for the different multiqubit V-gates. The comparison is made after the saturation point of the diamond gate is reached with $L = 2$ layers and $m = 25$ rotations. Expressibility and entangling capabilities are taken as averages over the sample size. We compare both four and six qubits, but not eight qubits, since the expressibility is the same for all V-gates due to our choice of bins.*

	$N = 4$		$N = 6$	
V-gate	$\mathcal{E}$	$\mathcal{C}$	$\mathcal{E}$	$\mathcal{C}$
None	5.8	0	6.6	0
CNOT	8.7	0.68	7.9	0.70
*i*SWAP	8.3	0.61	7.2	0.42
DIAMOND	9.4	0.79	8.4	0.76
MULTIQUBIT	7.3	0.35	6.7	0.05

different V gates in the top part of Fig. 5.5 where we depict up to three layers. In order to ensure that the relative expressibility has converged, we use the maximum number of rotations, i.e., M rotations. We use a selection of the same gates discussed in the previous section: The identity, CNOTs, *i*SWAPs, diamond gates, and the multiqubit controlled NOT gates.

For less than eight qubits, we observe that the relative expressibility is quite scattered in Fig. 5.5, with the entangling gates yielding the best relative expressibility and the identity gate yielding the worst relative expressibility. However, as the number of qubits increases, the relative expressibility seems to converge towards $\mathcal{E} = 6.5$ for all cases. This convergence is because when the number of qubits increases, the Haar measure peaks at low fidelity, meaning that the lowest bins dominate in calculating the relative expressibility. When the number of qubits becomes sufficiently large, only the lowest bin becomes relevant when calculating the relative expressibility. Therefore, one should consider increasing the number of bins if one wishes to investigate the relative expressibility for more qubits. However, to compare the relative expressibility for circuits with different numbers of qubits, one should have the same number of bins, which is why we have chosen 75 bins for all calculations. This also means that even though the relative expressibility seems to converge towards a lower value for larger N, it does not necessarily mean these PQCs are worse than similar PQC for lower N. It is simply a result of the way relative expressibility is defined. Therefore, one should be cautious when comparing PQCs across a different number of qubits.

Contrary to the relative expressibility, the entangling capability is not dependent on the number of qubits, and we do not expect it to converge towards a specific value for all cases. The entangling capability is plotted in the bottom part of Fig. 5.5. Without any entangling gates, the entangling capability is, of course, zero. When introducing the CNOT gates, we obtain an asymptotically increasing entangling capability. Not surprisingly, more layers increase the entangling capability of the CNOT gates. We observe that for up to three layers, there is a slow convergence towards one, i.e., 0.7 for one layer, 0.92 for two layers, and 0.95 for three layers.

The entangling capability of *i*SWAP gates between each qubit is constant for a single layer around 0.3, which is significantly lower than for the CNOT gates, despite both having the maximum entangling power [328]. Increasing the number of layers dramatically

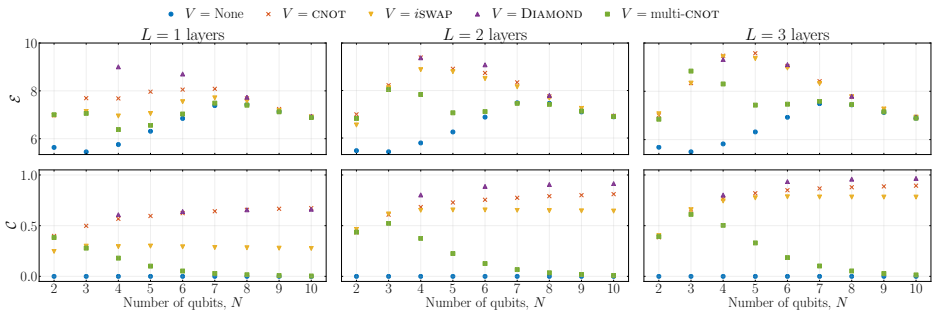

Figure 5.5: Top: *Relative expressibility and* bottom: *entangling capability for different choices of V gate as a function of the number of qubits. In order to ensure convergence, all circuits are simulated with the maximum number of rotations, i.e., M rotations.*

increases the entangling capability of the circuit; however, it remains inferior to a circuit with CNOT gates for the same amount of layers. Turning to the diamond gate, we observe that for one layer, its entangling capability is approximately equal to that of the CNOT gates, though it does seem to increase a bit slower. For two layers, it outperforms the CNOT gates for three layers, and for three layers of the diamond gate, it looks like the entangling capability converges towards unity. Contrary to the other entangling gates, the entangling capability of the multiqubit controlled NOT gate converges towards zero as the number of qubits increases. Since for a large number of control qubits, the multiqubit gate resembles the identity gate quite well, as it acts trivially on most of the qubits in the system.

5.4 Summary and outlook

We have investigated the relative expressibility and entangling capability for PQCs for a varying number of single-qubit rotations. We found that the relative expressibility and entangling capability can be saturated using fewer single-qubit rotations than the maximum possible amount supported by the circuit. This could significantly decrease the classical computational complexity of many hybrid quantum-classical algorithms. We also find that it is subordinate where these single-qubit rotations are placed in the circuit when the number of rotations is large. When the number of rotations is small, one must spread the rotations evenly among the qubits, such that no qubit becomes saturated with rotations to obtain an advantage. We note that even though this saturation point is reached, it does not mean that the given PQC is capable of finding any arbitrary state in the Hilbert space, and it implies that the given PQC has reached the limit of its capability.

Once the saturation point is achieved, the only remaining component to change in a given PQC is each layer's type of multiqubit gate. We find that highly entangling multiqubit gates, such as the CNOT gate or the diamond gate [327] reaches the saturation point of the relative expressibility, $\mathcal{E}$, and entangling capability, $\mathcal{C}$, with less single-qubit rotations compared to less entangling gates.

We assess that an efficient PQC can be created by employing highly entangling gates such as the diamond gate or the CNOT in each layer for three layers and then doing five to ten single-qubit rotations on each qubit. The placement of the single-qubit rotations can be randomized. Of course, a high relative expressibility and entangling capability are not enough to prove that PQCs are beneficial for all HQC algorithms. The next step would then be to investigate the PQCs mentioned in this paper in an actual HQC setting, which, coincidentally, is the objective of the next chapter.

CHAPTER 6

Variational Quantum Eigensolver

*In this chapter, I will present the Variational Quantum Eigensolver algorithm that I have used during my PhD studies. I have mainly been focusing on solving simple molecules and Heisenberg chains. Most of the results in this chapter are unpublished, but the results regarding the number of single-qubit rotations (Section 6.4 and Fig. 6.2) have been published in Ref. [**VII**].*

Variational Quantum Eigensolver (VQE) is an algorithm used for finding an approximate ground state energy of a given Hamiltonian. It was initially proposed in 2014 as an alternative to the quantum phase estimation algorithm, and the quantum mechanical part was based on photonic quantum processors [312]. Since then, several other research groups have adapted this algorithm [313, 314, 316–319]. Most relevant to this thesis, a VQE algorithm was implemented on a superconducting chip in 2017 [315]. Below we present the VQE algorithm and its extensions and simulations of the algorithm solving molecules along with Heisenberg spin chains.

6.1 The algorithm

The Variational Quantum Eigensolver (VQE) is based on the variation principle, which gives an upper bound for the ground state energy, E_0, of some given Hamiltonian, $\hat{\mathcal{H}}$. In general, it states that given any normalized state, $|\psi\rangle$, we have the following

$$E_0 \leq \langle\psi|\hat{\mathcal{H}}|\psi\rangle\,. \tag{6.1}$$

In other words, the expectation value of the Hamiltonian will always be larger or equal to the actual ground state energy, no matter what trail state we choose. The equal sign is only valid for the case where we chose the ground state as our trial state. Now say that we can parameterize our trail states in a way such that $|\psi(\boldsymbol{\theta})\rangle$ depends on a set of parameters $\boldsymbol{\theta}$. In that case, we can minimize the expectation value of the Hamiltonian in order to approximate the ground state energy. The remaining question is, how do we choose our trial states?

The idea behind the VQE is that a quantum circuit might be better at choosing trial states than a classical computer. Therefore, computing the trail states is done on a

quantum processor while calculating expectation values, and minimizing the energy is done on a classical computer. This is the core idea of HQC algorithms; computational tasks are divided between a quantum resource and a classical computer to complement the strengths of each process.

To summarize, a Variational Quantum Eigensolver must perform the following steps:

1. Chose a parameterized quantum circuit (PQC), e.g., the one in Fig. 5.1. We denote this circuit $\hat{\mathcal{U}}(\boldsymbol{\theta})$, and it is often called the circuit ansatz.

2. Minimize the energy given by

$$E(\boldsymbol{\theta}) = \langle\psi(\boldsymbol{\theta})|\hat{\mathcal{H}}|\psi(\boldsymbol{\theta})\rangle = \langle 0\ldots 0|\hat{\mathcal{U}}(\boldsymbol{\theta})^{\dagger}\hat{\mathcal{H}}\hat{\mathcal{U}}(\boldsymbol{\theta})|0\ldots 0\rangle\,, \tag{6.2}$$

   using a classical optimization algorithm.

3. The resulting energy $E(\boldsymbol{\theta})$ and state $|\psi(\boldsymbol{\theta})\rangle$ should be compared to the classically found results.

There are several ways of choosing a circuit ansatz before performing VQE calculation. Some construct their ansatz depending on the quantum hardware, i.e., the choice and order of the gates depend on which gates are possible to perform on a quantum chip [315]. Others start from a unitary coupled-cluster ansatz where the PQC is built such that it has properties similar to the ones seen in classical unitary coupled-cluster calculations [313, 329]. Finally, there have been researchers trying to use machine learning to figure out the optimal circuit ansatz [330]. We will only concern ourselves with circuits similar to the ones discussed in Chapter 5, i.e., single-qubit rotation gates layered with entangling gates.

6.2 VQE beyond the ground state

Even though the Variational Quantum Eigensolver was built to find ground states, there are several ways to expand this method to find excited state [331–335]. Here we discuss some of these approaches:

VQE for excited states

The first expansion of the VQE method we consider uses overlap estimation to find subsequent states that are orthogonal to previous found states [334]. Suppose we have minimized the energy of some Hamiltonian as Eq. (6.2) leading to an approximate ground state $|\psi(\boldsymbol{\theta}_0)\rangle$. Now we perform the VQE algorithm all over again, however this time we include a penalty term based on the overlap between the ground state and the new state, $|\psi(\boldsymbol{\theta}_1)\rangle$, i.e., $\langle\psi(\boldsymbol{\theta}_0)|\psi(\boldsymbol{\theta}_1)\rangle$. This penalty ensures that the next state we find is orthogonal to the first state, as required quantum mechanically. Continuing this scheme, we can find the kth excited state by minimizing

$$F(\boldsymbol{\theta_k}) = \langle\psi(\boldsymbol{\theta}_k)|\hat{\mathcal{H}}|\psi(\boldsymbol{\theta}_k)\rangle + \sum_{i=0}^{k-1}\eta_i\,\langle\psi(\boldsymbol{\theta}_i)|\psi(\boldsymbol{\theta}_k)\rangle\,, \tag{6.3}$$

where η_i is some constant that determines the size of the penalty, which must be chosen larger than the energy gap between the two relevant states. Although this method can be used to find any excited state in the Hilbert space spanned by the qubits of the ansatz, it does require knowledge of all lower-lying states, which means that an iterative procedure is required to find the kth excited state. Besides the linear scaling of the computation time, this method also introduces the problem of determining η_i without prior knowledge of the energy levels. Another problem with this method is that the crossing of states is impossible to detect, as the method just finds the next lowest state.

Constrained VQE

Similar to the approach for the excited states, one can also penalize the VQE algorithm using other metrics [333]. Given an operator $\hat{\mathcal{O}}$ (this could be spin, $\hat{\mathcal{S}}^2$, electron number, $\hat{\mathcal{N}}$, etc.) and its desired mean value, $\mathcal{O}$, we now optimize the cost function

$$F(\boldsymbol{\theta}) = \langle\psi(\boldsymbol{\theta})|\hat{\mathcal{H}}|\psi(\boldsymbol{\theta})\rangle + \eta\left[\langle\psi(\boldsymbol{\theta})|\hat{\mathcal{O}}|\psi(\boldsymbol{\theta})\rangle - \mathcal{O}\right]^2, \tag{6.4}$$

where η is again some number whose size depends on the spacing of the energy levels. Note that the constraint in Eq. (6.4) is relatively standard within constrained numerical optimization [336], and one can, of course, add several different constraints at the same time.

Subspace-Search Variational Quantum Eigensolver

The final example of an expansion of the original VQE we consider the subspace-search Variational Quantum Eigensolver (SSVQE) [335]. This method can find up to the kth excited state using just a single optimization procedure. The idea behind the procedure is that instead of using a single input state as $|0\rangle = |0\ldots0\rangle$ we chose a set of orthogonal states, $\{|\varphi\rangle_j\}_{j=0}^k$, meaning that $\langle\varphi_i|\varphi_j\rangle = \delta_{ij}$, and then minimize a cost function consisting of the sum of matrix elements given by these states. In other words, we minimize the following function

$$F(\boldsymbol{\theta}) = \sum_{j=0}^{k} \eta_i \langle\varphi_j|\hat{\mathcal{U}}(\boldsymbol{\theta})^\dagger\hat{\mathcal{H}}\hat{\mathcal{U}}(\boldsymbol{\theta})|\varphi_j\rangle, \tag{6.5}$$

where η_i is some weight between 0 and 1 satisfying $\eta_i > \eta_j$ when $i < j$, which chooses which state becomes the excited states. When optimized this cost function maps the $|\varphi_j\rangle$ to the jth excited state for each $j \in \{0, 1, \ldots, k\}$. While this procedure only requires one optimization step, the overall time required for optimization may increase.

In an actual VQE implementation, one can create a set of orthogonal states by applying a Pauli-X to a different set of qubits all initiated in the state $|0\rangle$. For example applying a Pauli-X gate to the first qubit yields $X_1|0\ldots00\rangle = |0\ldots01\rangle$, which is orthogonal to the original state.

6.3 Simulating molecules with VQE

We showed, in Chapter 5, how the expressibility and entanglement capability of a PQC depended on the number of single-qubit rotations when the circuit layout was as in Fig. 5.1.

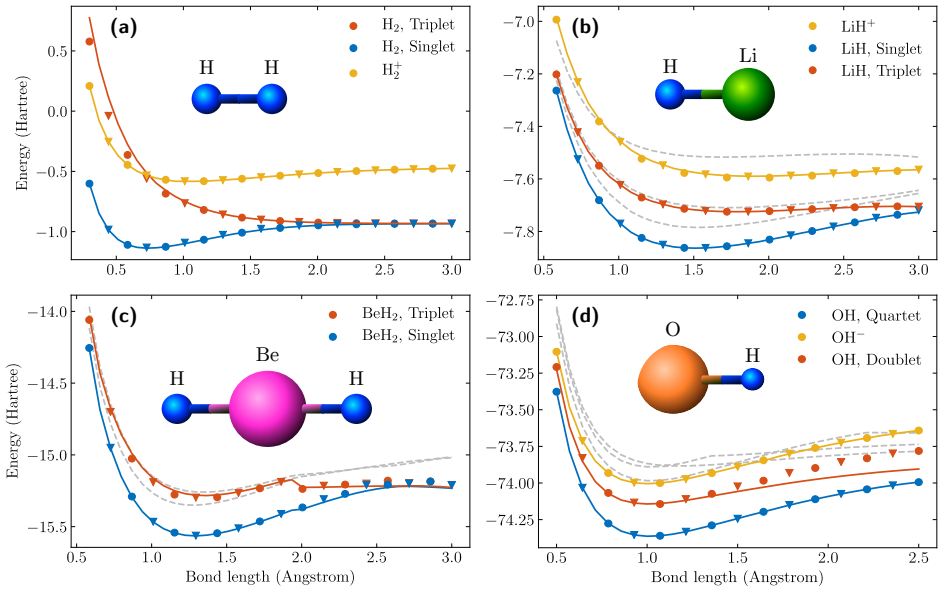

Figure 6.1: *Lowest lying states of small molecules. Lines indicates classical eigenvalue calculation of the qubit Hamiltonian. Dots indicates VQE results using a two layers of diamond gates, while triangles represents VQE results using* CNOT *gates. The gary dashed lines represent low lying states not found by the VQE.* **(a)** *H_2,* **(b)** *LiH,* **(c)** *BeH_2, and* **(d)** *OH.*

We will now verify these results by applying the VQE algorithm to the same circuits.

To apply the VQE, we must choose a Hamiltonian to which we can apply it. Often used in VQE algorithms are the Hamiltonians of small molecules, especially H_2, LiH, and BeH_2 [315, 333, 334]. These molecules are often chosen since their active space can be effectively represented by 2, 4, and 6 qubits. In order to apply the VQE to molecular problems, the Hamiltonians must be encoded onto qubits. When starting from fermionic Hamiltonian in second quantization, this can be done using either a Bravyi-Kitaev [337] or Jordan-Wigner [338] transformation. Following such a transformation, a Hamiltonian for, e.g., four qubits take the form

$$\hat{\mathcal{H}} = \sum_{\substack{\alpha,\beta,\gamma,\delta \\ \in x,y,z,I}} h_{\alpha\beta\gamma\delta}\sigma_1^\alpha\sigma_2^\beta\sigma_3^\gamma\sigma_4^\delta, \tag{6.6}$$

where $\sigma_i^{x,y,z}$ are the Pauli operators and σ_i^I is the identity on qubit $i = 1,2,3,4$. The coefficients $h_{\alpha\beta\gamma\delta}$ are given by one- and two-body integrals of the molecule and do generally depend on the molecular basis. We find the fermionic Hamiltonian using the Python-based Simulations of Chemistry Framework (PySCF) [339]. The matrix elements are calculated in the STO-3G basis, and we map the Hamiltonian to a qubit Hamiltonian using OpenFermion [340]. This procedure can, in principle, be applied to all molecules for all geometries; however, we restrict ourselves to small molecules with less than ten qubits to avoid diverging computation times. The fact that the above procedure produces

Table 6.1: *Molecular properties of the ground state of the molecules considered in Fig. 6.1. The multiplicity is given as $2\mathcal{S}+1$, where $\mathcal{S}$ is the spin of the state, and it is equal to the degeneracy of the state. All equilibrium bond lengths have been obtained from [341], while the active space configurations have been determined theoretically and confirmed to be realistically numerically.*

	H_2	LiH	BeH_2	OH
Multiplicity	1	1	1	2
Charge	0	0	0	0
Equilibrium bond length [Å]	0.7414	1.595	1.326	0.964
Initial active space orbital	0	1	1	1
Final active space orbital	2	3	4	5
Qubit active space	4	4	6	8

diverging computation times for larger molecules is one of the motivations for developing a more efficient quantum algorithm. We consider the molecules H_2, LiH, BeH_2, and OH. The chemical properties of the molecules can be seen in Table 6.1.

In this section, we simulate a VQE algorithm[1] using the PYTHON package QUTIP to create parameterized quantum circuits, which we then use to calculate the expectation value of the qubit Hamiltonian. The expectation value is minimized using BFGS optimization. We consider two-layer circuits, fully saturated with single-qubit rotations, as in Fig. 5.1, with either CNOT or diamond gates as the entangling gates, V, with a layout identical to the one discussed Section 5.2. We simulate all four molecules for different interatomic distances around their equilibrium length. The results is seen in Fig. 6.1. We use the constrained VQE algorithm to find low-lying excited states of the molecules. Using the penalty for the spin operator $\hat{\mathcal{S}}$ we find states with single and triplet multiplicity (defined as $2\mathcal{S}+1$) for H_2, LiH, and BeH_2 and doublet and quartet states for OH. We also consider a penalty term for the number of electrons, $\hat{\mathcal{N}}$, in order to find ions for LiH, BeH_2, and OH.

From Fig. 6.1 we see that the ground state is accurately found for all four molecules. The excited states are also accurately found for H_2 and LiH. For LiH, we note that there are several excited states the VQE simulation does not find. Had we used a VQE with an overlap penalty, we would probably have found these states; however, then there is no way of determining, e.g., the multiplicity of the molecule. For BeH_2, there is a kink around 2 Å; this is due to some symmetry discrepancy in the chemical PYSCF calculations. Nevertheless, the VQE simulation finds these states as well. The doublet state is not found accurately for an increasing bond length for the OH molecule, and this could probably be managed by increasing the number of layers in the PQC.

6.4 Single-qubit rotations in VQE

Having shown that the VQE simulation accurately reproduces the potential energy surfaces of small molecules using PQCs saturated with single-qubit rotations, we consider removing single-qubit rotations as in Chapter 5. In other words, we want to perform the

[1]Some of the numerical results presented here were obtained at the Centre for Scientific Computing, Aarhus `http://phys.au.dk/forskning/cscaa/`.

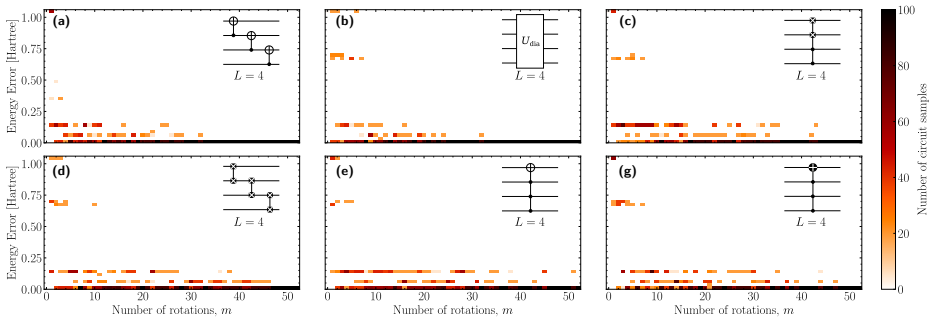

Figure 6.2: *Energy error of the ground state LiH found using VQE of different circuits with $N = 4$ qubits and $L = 4$ layers as a function of the number of rotations. The energy found using VQE is compared to a FCI calculation, which yields the energy error. The inset in the right upper corner of each plot shows the entangling gate, V, used in each layer.* ***(a)*** *Three* CNOTs, ***(b)*** *diamond gate,* ***(c)*** C^2*i*SWAP, ***(d)*** *three* *i*SWAPs, ***(e)*** C^3NOT, ***(f)*** *3-bit iToffoli gate.*

VQE simulation using the PQC with a fixed number of rotations, m, that are smaller or equal to M of Eq. (5.1). As in Section 5.2 we sample 100 random circuits for each m and then we perform a VQE simulation for each circuit. We simulate LiH, BeH_2, and OH for $N = 4, 6, 8$ qubits, respectively.

In Fig. 6.2 we plot the energy error (compared to a classical eigenvalue calculation) for the LiH calculations with four layers. For results concerning less layers ($L = 1, 2, 3$) and/or more qubits ($N = 6, 8$) see the supplementary material of the original paper **[VII]**. We perform the simulation for the same types of gates as in Section 5.2. In Fig. 6.2(a), we see that the energy error saturates at less than 0.05 Hartree around 30 single-qubit rotations when the entangling gates are CNOT gates. This is entirely consistent with the saturation points found in Figs. 5.3 and 5.4(a), which also saturates around the same point. For the case of BeH_2 and OH ($N = 6, 8$ respectively), we also observe saturation before reaching the maximum number of rotations. For the *i*SWAP gate in Fig. 6.2(d), we observe a slower convergence, which is not reached before 45 rotations. This is consistent with the previous results for expressibility and entangling capabilities in Figs. 5.3 and 5.4(d), which are also reached slower than for the CNOT gates.

On the other hand, for the diamond gate in Fig. 6.2(b), we find a faster convergence than for both the CNOT and *i*SWAP gates. Again, this is consistent with previous expressibility and entangling capability, which converged faster than for the two other gates. Finally, for the multiqubit gates in subfigures (c), (e), and (g), we also observe the same tendencies as in the calculations of expressibility and entangling capability, namely that the saturation point is reached close to the maximum number of single-qubit rotations. In conclusion, we find that the VQE simulations agree very well with the results found in Section 5.2.

6.5 Entangling gates in VQE

Until now, we have only considered unparameterized entangling gates, i.e., entangling gates that cannot be optimized during the VQE. This is also the standard approach in the literature where only the single-qubit gates are optimized while the entangling gates are fixed. However, some references point in the direction that removing entangling gates, similarly, as we did for the rotational gates in Section 5.2, can improve VQE performance for low-entangled ground states [259].

One can think of a fixed entangling gate and no entangling gate as the two extremes of parameterization. However, there is no reason to consider only these two extremes since, in experimental implementations of entangling gates, they are often controlled by tuning of the gate, e.g., as in superconducting circuits where magnetic fluxes can be used to tune qubits in and out of resonance, see Sections 1.8.2 and 1.10.3. In other words, most experimental implementations already accommodate parameterized entangling gates, where the parameter is given by the time the qubits are in resonance, as seen in Eqs. (1.110) and (1.111), which implements a parameterized iSWAP gate.

We, therefore, consider whether parameterized entangling gates improve the performance of VQEs. In particular, we consider three different parameterized entangling gates: the CNOT(Θ), iSWAP(Θ), and the CZ(Θ) gates, which are defined in the following way

$$\text{CNOT}(\Theta) = \begin{bmatrix} 1 & 0 & 0 & 0 \\ 0 & 1 & 0 & 0 \\ 0 & 0 & \cos(\Theta/2) & -ie^{i\Theta/2}\sin(\Theta/2) \\ 0 & 0 & -ie^{i\Theta/2}\sin(\Theta/2) & \cos(\Theta/2) \end{bmatrix}, \tag{6.7a}$$

$$i\text{SWAP}(\Theta) = \begin{bmatrix} 1 & 0 & 0 & 0 \\ 0 & \cos(\Theta/2) & -i\sin(\Theta/2) & 0 \\ 0 & -i\sin(\Theta/2) & \cos(\Theta/2) & 0 \\ 0 & 0 & 0 & 1 \end{bmatrix}, \tag{6.7b}$$

$$\text{CZ}(\Theta) = \begin{bmatrix} 1 & 0 & 0 & 0 \\ 0 & 1 & 0 & 0 \\ 0 & 0 & 1 & 0 \\ 0 & 0 & 0 & e^{i\Theta} \end{bmatrix}, \tag{6.7c}$$

where we denote Θ the coupling angle. We consider these three gates since these are the parameterized versions of the most commonly used entangling gates. Further, the iSWAP(Θ) and CZ(Θ) gates are easily implemented in superconducting circuits using capacitive coupling, see Section 1.8.2, and the CNOT(Θ) gate can be implemented in superconducting circuits using the approach in Chapter 2.

When investigating the performance of the parameterized entangling gates, we consider a VQE simulation and not the expressibility and entangling power as discussed in Chapter 5. Trivially expressibility must increase when including more parameters, as a more significant portion of the Hilbert space is available. On the other hand, the entangling capability does not increase when parameterizing the three entangling gates since these are already maximally entangled in their fixed version when $\Theta = \pi$. In Fig. 6.3

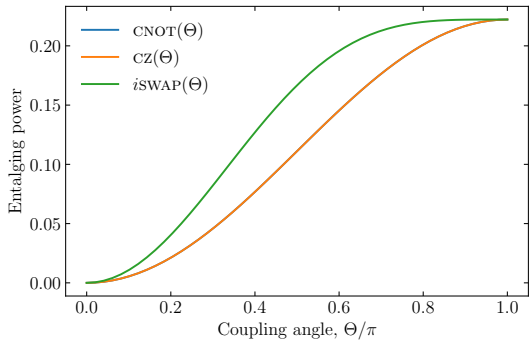

Figure 6.3: *Entangling power [328] of the three parameterized entangling gates in Eq.* (6.7)*. Note that the entangling power of the* CNOT(Θ) *and* CZ(Θ) *gates lie on top of each other.*

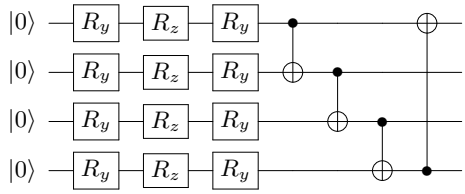

Figure 6.4: *Example of one layer of the circuit ansatz used in Section 6.5 for four qubits. First, an Euler rotation is performed on each qubit, followed by a nearest-neighbor coupling of all the qubits using the given entangling gate. Here it is shown using* CNOT *gates.*

we show the entangling power [328] of the three parameterized entangling gates as a function of their coupling angle.

In this section we consider a simulation of SSVQE implemented using TensorFlow Quantum [342]. TensorFlow Quantum is an open-source Python library for prototyping hybrid quantum-classical models, based on the classical machine learning library TensorFlow used for deep learning models. In this sense, TensorFlow Quantum is built such that PQCs are considered layers similar to how one would consider layers in a classical neural network. We will not go into details of how TensorFlow Quantum work but refer to the original white paper [342].

We consider PQCs similar to the ones we have previously considered; however, this time, we only consider full layers, i.e., blue layers in Fig. 5.1. We consider Euler rotations, i.e., *y*-*z*-*y* rotations instead. Since we only consider two-qubit entangling gates, we chose a nearest-neighbor coupling scheme with periodic boundary conditions. See Fig. 6.4 for an example of the circuit ansatz.

Besides some of the molecular Hamiltonians we considered in Section 6.3 we will also consider a one-dimensional Heisenberg model with periodic boundary conditions,

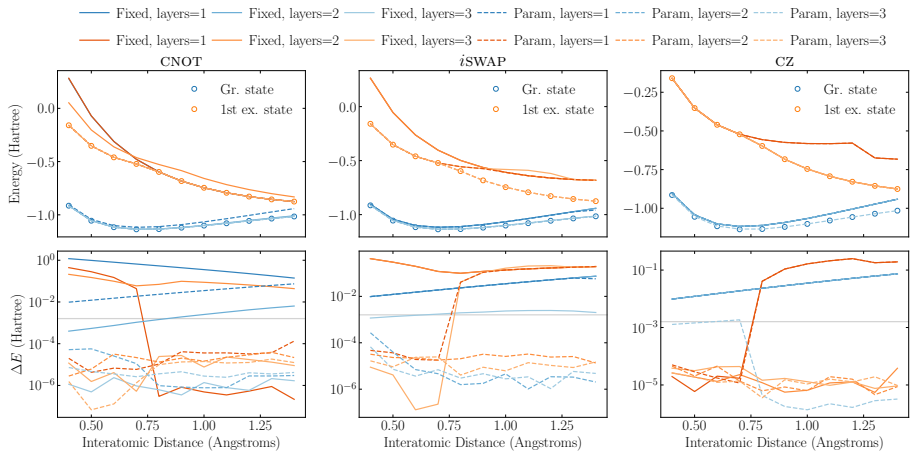

Figure 6.5: *Potential energy surfaces for H_2 calculated using SSVQE for the two lowest states. The title of each column indicates which entangling gate is used in the calculation, either fixed (solid line) or parameterized (dashed lines). In the top row, we show the calculated energy, and in the bottom row, we show the energy difference, ΔE, between the classical and VQE calculations. Lighter colors indicate that more layers are used in the simulation. The gray line indicates chemical accuracy at* 0.0016 *Hartree. The results shown here are the best out of 100 samples.*

i.e.,

$$\hat{\mathcal{H}} = \sum_{i=1}^{N} \left(B\sigma_i^z + J_x \sigma_i^x \sigma_{i+1}^x + J_y \sigma_i^y \sigma_{i+1}^y + J_z \sigma_i^z \sigma_{i+1}^z \right), \tag{6.8}$$

where the subscripts are modulo N. We consider both the XXX model with $J = J_x = J_y = J_z$ and the pure swap model with $J = J_x = J_y$ and $J_z = 0$. We also consider a transverse-field Ising model

$$\hat{\mathcal{H}} = \sum_{i=1}^{N} \left(B\sigma_i^x + J_z \sigma_i^z \sigma_{i+1}^z \right). \tag{6.9}$$

As with the molecular Hamiltonians, we consider a range of configurations; more specifically, we consider $J/B \in [0, 2]$ varied in steps of 0.1. We perform all VQE calculations 100 times, and since we are doing variational simulations, we pick the calculation resulting in the lowest energies

In Fig. 6.5 we show the results for the two lowest states of H_2, plotting results for up to three layers for both fixed and parameterized entangling gates. Starting with the CNOT gate, we see that the parameterized gates outperform the fixed gates for one and two layers, while the performance is somewhat identical for three layers. We note that we achieve chemical accuracy using only two layers for the parameterized gate, compared to three for the fixed gates. Note the sharp drop in ΔE for the fixed gate for one layer around 0.75 Å; this happens since here we have a crossing of states, where the H_2^+ state crosses the triplet state of H_2 (see Fig. 6.1). The SSVQE cannot distinguish between these states and find the lowest. However, the one-layer fixed gate only finds the second-lowest to

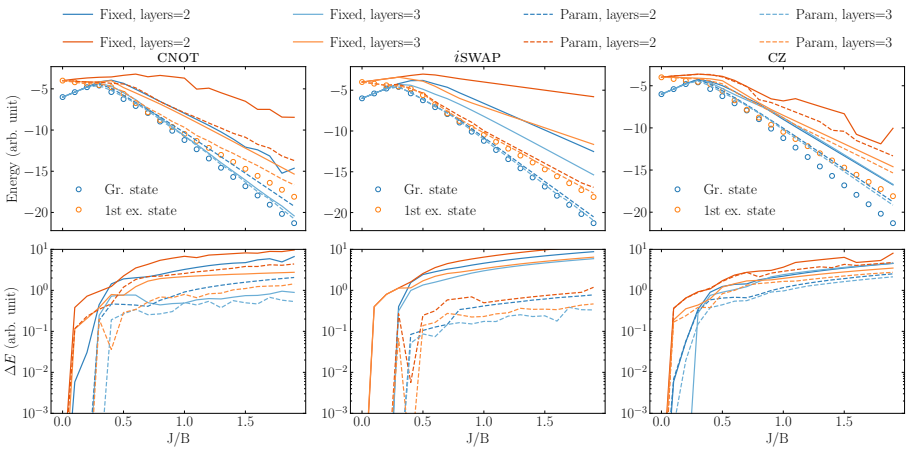

Figure 6.6: *Potential energy surfaces for the Heisenberg model in Eq.* (6.8) *with six qubits calculated using SSVQE for the two lowest states. The title of each column indicates which entangling gate is used in the calculation, either fixed (solid line) or parameterized (dashed lines). In the top row, we show the calculated energy, and in the bottom row, we show the energy difference, ΔE, between the classical and VQE calculations. Lighter colors indicate that more layers are used in the simulation. The results shown here are the best out of 100 samples.*

begin with, and since the starting values of the VQE come from the previous calculation, it overperforms when this crossing occurs.

The story is the same for the *i*SWAP gate, and we even see that the two-layer parameterized circuits perform better than fixed three-layer circuits. We are not capable of achieving chemical accuracy with just fixed gates. This time we see a sharp increase in ΔE around 0.75 Å for two of the excited states. Again it is due to the crossing; however, the algorithm finds the lowest and continues with this state. Finally, for the CZ gate, we find that it performs significantly worse than the two other gates, both for the fixed and parameterized versions. We only achieve chemical accuracy for the ground state for three layers of the parameterized gate. However, the CZ gate works surprisingly well for the fixed and parameterized versions for the first excited state, except for one layer, where the crossing is again the source of trouble. The CZ gate is better at approximating the excited state than the ground state is probably because the CZ gate mimics the structure of the first excited state better. In Appendix E we show similar results for LiH (Fig. E.1). We have also obtained results for BeH_2, however, with fewer samples. The result is the same: The parameterized gates perform better than the fixed gates in both cases.

In Fig. 6.6 we show results for the XXX Heisenberg model in Eq. (6.8) with six qubits. In the simulation, we take $B = 1$ and interate J in steps of 0.1. We note that the VQE model is very good at determining the energy when $J = 0$, which makes sense since the Hamiltonian is diagonal in the computational basis in this case. The ground state is also nicely determined until the crossing around $J/B = 0.3$, at which point the fixed gates start performing worse than the parameterized gates. Especially for the *i*SWAP

gate, we observe that the parameterized version outperforms the fixed version. The first excited state is more difficult for the VQE, and it generally performs poorly, although the parameterized version of the *i*SWAP performs best of all the gates. Here we also see that a two-layer PQC with parameterized gates is better than the three-layer fixed version, i.e., it is not just the increased number of parameters in the model that yields a better result. Altogether, the XXX Heisenberg model results confirm the results we found for the molecular Hamiltonian.

In Appendix E we show similar results for the pure swap Heisenberg model and the transverse-field Ising model, both for six qubits. These results agree with what is discussed here. We have also simulated these models for four, eight, and ten qubits; still, the conclusions are the same; however, we do not include these plots here due to the scope of this thesis.

6.6 Overlap fidelity

So far, we have only considered how well the VQE approximates the eigenvalue of the Hamiltonian, i.e., the energy. However, there are always two sides to an eigenvalue problem: the eigenvalue and the eigenstate. We, therefore, investigate how well the VQE algorithm approximates the eigenstates of the Hamiltonian. We do this by calculating the overlap fidelity between the classically found eigenstate, $|\psi_0\rangle$, and the one given by the VQE.

To make the calculation explicit, we consider an example. We chose the Heisenberg model in Eq. (6.8) with $J_x = J_y = J_z = B = 1$ and four qubits. To make sure that our VQE algorithm converges nicely, we pick the circuit ansatz in Fig. 6.4 with four layers. With this ansatz, we find an energy error of $\Delta E = 2 \times 10^{-4}$, which indicates that the energy obtained by the VQE simulation is close to the actual energy with a relative error of less than 0.01 %. However, when we calculate the overlap fidelity between the VQE state and the classically found, we find $|\langle\psi_0|\psi(\boldsymbol{\theta})\rangle|^2 = 0.078$ which is a very low overlap!

To gain further insight, we write out the states. First, the actual state, which consists of only six out of 16 basis states in the computational basis

$$\begin{aligned}|\psi_0\rangle =& 0.289e^{-0.581i}|0011\rangle + 0.577e^{2.561i}|0101\rangle + 0.289e^{-0.581i}|0110\rangle \\ &+ 0.289e^{-0.581i}|1001\rangle + 0.577e^{2.561i}|1010\rangle + 0.289e^{-0.581i}|1100\rangle ,\end{aligned} \tag{6.10}$$

and secondly the one found by VQE which consists of all possible basis states

$$\begin{aligned}|\psi(\boldsymbol{\theta})\rangle =& 0.387e^{-2.817i}|0000\rangle + 0.281e^{2.839i}|0001\rangle + 0.231e^{-2.953i}|0010\rangle \\ &+ 0.406e^{-0.146i}|0011\rangle + 0.17e^{-1.535i}|0100\rangle + 0.06e^{1.259i}|0101\rangle \\ &+ 0.135e^{1.811i}|0110\rangle + 0.162e^{2.843i}|0111\rangle + 0.496e^{2.836i}|1000\rangle \\ &+ 0.152e^{-1.821i}|1001\rangle + 0.304e^{2.366i}|1010\rangle + 0.05e^{-2.645i}|1011\rangle \\ &+ 0.131e^{0.826i}|1100\rangle + 0.25e^{-3.12i}|1101\rangle + 0.13e^{-3.13i}|1110\rangle \\ &+ 0.121e^{-1.272i}|1111\rangle .\end{aligned} \tag{6.11}$$

These states look pretty different, and apparently, all but the six states in Eq. (6.10) have minimal effect on the energy returned by the Hamiltonian.

Note that this is not an odd case. More often than not, we obtain a low fidelity despite good energy, especially when the number of qubits increases. One often obtains both good energy and overlap for two qubits, which is why this example is done for the more complex case of four qubits. It is important to note that this is also the case for classical variation. In other words, it is a consequence of the variation principle, and it is not necessarily a bad thing but a limitation to the procedure nevertheless [76, 343].

6.7 Summary and outlook

To summarize, we have used the VQE algorithm to find the ground state of multiple molecular Hamiltonians. We have also used the SSVQE and constrained VQE to find higher-lying states and discussed which methods are preferable depending on the aim of the investigation. By calculating the energy of the LiH molecule using VQE for PQCs with a different number of single-qubit rotations, we have confirmed the conclusions found in Chapter 5, stating that one can save a significant amount of single-qubit rotations when performing VQE.

We have also shown that parameterized entangling gates perform as well and often better than fixed entangling gates in VQE simulations. This could be exploited at no experimental cost in many VQE experiments as native gates in many quantum technology schemes often depend on some tunable driving parameter. For some reason, this has never been exploited in such experiments, to our knowledge. Especially the iSWAP gate performs well in its parameterized version, which occurs natively in superconducting circuits, see Section 1.8.2. Finally, we considered the overlap of VQE produced states and the actual states and showed that it was pretty low even for VQE states that approximate the system's energy quite well. This is an issue with the variational approach, and a point for further investigation could be to try to mend this problem.

CHAPTER 7

Quantum Generative Adversarial Networks

At some point during my PhD studies, I became interested in machine learning, and in particular, how to conceive quantum machine learning. Parameterized quantum circuits had already been dubbed the quantum neural network by some researchers [304–306] and many hybrid quantum-classical algorithms were considered quantum machine learning [342]. This chapter contains some unpublished work I have done on quantum generative adversarial networks.

In the last decade, machine learning has enjoyed great success worldwide. Machine learning is essentially the study of algorithms that can improve automatically by learning from data. Such algorithms have proved to be extraordinarily useful at recognizing patterns in existing data and using this insight for, e.g., classification (assigning the correct category to an example) and regression (estimating a numerical value based on a variety of inputs) [344, 345]. However, generation of data has been a weakness of machine learning. At least until 2014 when Generative adversarial networks (GANs) were invented [346]. Since then, GANs has proved a hugely successful generative machine learning technique. GANs was not the first computer program to generate data, but the realism and variety of the results have made GANs a tremendous success compared to other models [347].

The success of classical models have been a great source of inspiration within the quantum technology community, often posing the question: "Can we make this quantum?", and sure enough, the same has happened with GANs (and machine learning in general [348, 349]). In 2018 it was proposed to create a quantum version of a GAN, called a QuGAN [309]. At the same time, such a QuGAN was simulated and shown to be able to generate a single CNOT gate [308]. Before diving further into QuGANs, we will briefly introduce classical GANs.

7.1 Classical generative adversarial networks

The idea behind GANs is to pitch neural networks up against each other, in a way such that one network, called the *generator*, tries to generate some data (e.g., pictures, sounds, videos, text), while the other network, called the *discriminator* tries to tell whether the data it is receiving, is real or fake. In this sense, the networks become adversaries, which is why

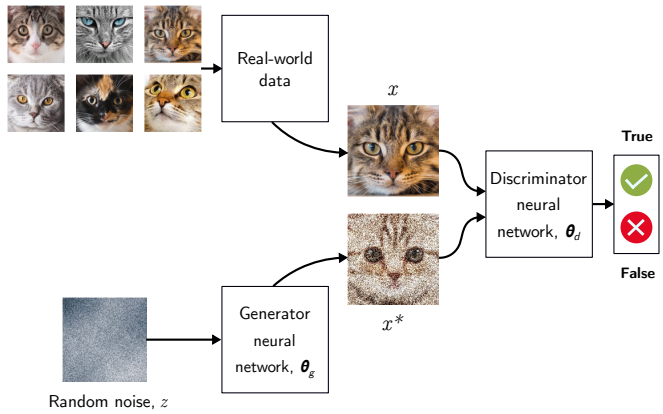

Figure 7.1: *Schematic representation of a generative adversarial network. A discriminative neural network is randomly fed with real world data or data generated by a generative network. The task of the discriminative network is then to determine what data is real and what data is fake.*

the networks are called adversarial networks[1] The network is set up in a zero-sum game, where one player's gain is the other player's loss. With this approach, the generator is trained indirectly through the discriminator, which is also updated dynamically.

The GAN training algorithm is as follows [344] (see Fig. 7.1 for a schematic representation):

1. Train the discriminator:
   a) Take a real random example, x, from the training dataset.
   b) Using a random noise vector, z, generate a fake example, x^*, using the generator.
   c) Use the discriminator network to classify x and x^*.
   d) Compute the classification errors and backpropagate the total error to update the discriminator's training parameters, $\boldsymbol{\theta}_d$, in order to *minimize* the classification errors, $\mathcal{E}$.
2. Train the generator:
   a) Using a random noise vector, z, generate a fake example, x^*, using the generator.
   b) Use the discriminator network to classify x^*.
   c) Compute the classification errors and backpropagate the total error to update the generator's training parameters, $\boldsymbol{\theta}_g$, in order to *maximize* the classification errors, $\mathcal{E}$.
3. Repeat the above steps until equilibrium is reached.

[1]Despite this seemingly antagonistic approach to GAN models there have been attempts at stopping this confrontational approach [350].

Mathematically we are updating the following minimax cost function

$$\max_{\boldsymbol{\theta}_g} \min_{\boldsymbol{\theta}_d} \mathcal{E}(\boldsymbol{\theta}_g, \boldsymbol{\theta}_d), \tag{7.1}$$

where $\mathcal{E}(\boldsymbol{\theta}_g, \boldsymbol{\theta}_d)$ is the cost function yielding unity when the discriminator correctly classifies all data and zero when it is wrong all the time. The above algorithm also means that GANs are implicit generative models implying that they do not explicitly model the likelihood function or provide ways of finding latent variables corresponding to a given sample [351].

As mentioned, this setup is a zero-sum game since the two networks are trying to minimize and maximize the same error simultaneously. All zero-sum games have Nash equilibriums, where neither player can improve their situation. GANs can reach a Nash equilibrium in two ways, in both cases $\mathcal{E}(\boldsymbol{\theta}_g, \boldsymbol{\theta}_d) = 0.5$

- The generator produces fake samples that are indistinguishable from the real data in the training dataset.

- The discriminator can at best randomly guess whether a particular example is real or fake.

In other words, once equilibrium is reached, we can either generate exceptional fake data or have trained an extremely poor discriminator. Of course, we are aiming for the first one.

However, there is no guarantee that a GAN will actually converge to the desired equilibrium. The convergence of GANs is an open problem, and it is well known that GANs are notoriously difficult to train [352]. The training has only become increasingly difficult as the depth of the neural networks has increased [353]. There are several proposed solutions to this problem, albeit none of the proposals completely solves the problem, they do remedy some of the shortcomings of the training [354]. We will not consider these approaches when considering QuGANs as we are still considering the most simple forms; however, these approaches could be used to improve the training of QuGANs.

Another common problem with GANs is mode collapse. Often we want GANs to produce a wide variety of outputs. For example, we would want the GAN to produce an output for each number of a dataset of handwritten digits. However, if the generator generates an especially plausible output, it may learn only to produce that output. However, if the generator starts to generate the same output all the time, the discriminator's best strategy is always to reject that output. If the discriminator gets stuck in a local minimum and does not find the optimal strategy, the generator can quickly learn to avoid that output. In other words, the generator can iterate through the remaining output types while the discriminator is trapped, always labeling the output the generator is avoiding as fake. Again there have been proposed ways to remedy this, but we will not discuss these further in the setting of QuGANs [355, 356].

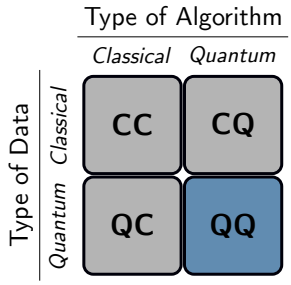

Figure 7.2: *Overview of the different approaches to combining classical and quantum machine learning. The first letter refers to the data type, while the second letter refers to the algorithm used. In this chapter, we consider the QQ approach to QuGANs. Figure inspired from Ref. [349].*

7.2 Quantum machine learning

Quantum generative adversarial networks are a type of quantum machine learning. Quantum machine learning is often used indiscriminately for any kind of machine learning related to quantum mechanics. We, therefore, start by defining the different kinds of quantum machine learning.

Classical machine learning considers classical machine learning models used on classical data, i.e., data we observe on an everyday basis, e.g., images, financial data, text. Due to the success of classical machine learning on classical data, these classical techniques have also been used on quantum mechanical data [357–360]. The opposite approach where quantum algorithms are used on classical data is also considered quantum machine learning. These approaches have also been seen within QuGANs, which have been applied to, e.g., financial data [310] and the MNIST dataset [361]. Finally, there is the fully quantum approach where we consider quantum algorithms on quantum data. We summarize the different approaches in Fig. 7.2.

Note that for the case of GANs, there are two distinct networks, meaning that we could, in principle, consider a system where either the generator or discriminator behaves quantum mechanically, while the other behaves classically [309]. In the following, we will consider the fully quantum mechanical approach to GANs.

7.2.1 Entangling quantum GAN

As with classical GANs, there are several approaches to QuGANs. Here we will consider an approach called Entangling Quantum Generative Adversarial Networks (EQ-GAN) [307]. The original work on QuGANs [308] proposed a direct analogy of the classical GAN architecture in the design of the generator and discriminator circuits. They proposed to exchange the neural networks of classical GANs with PQC. A simplified version of the proposal can be seen in Fig. 7.3(a). The input is either generated using a PQC, called $G(\boldsymbol{\theta}_g)$ or coming from a real source, R. The discriminator is also a PQC, $D(\boldsymbol{\theta}_d)$, that operates on the same qubits as the generator/real data, as well as an output qubit. Reference [308] successfully train this architecture to generate a CNOT gate using a total of five qubits and four layers.

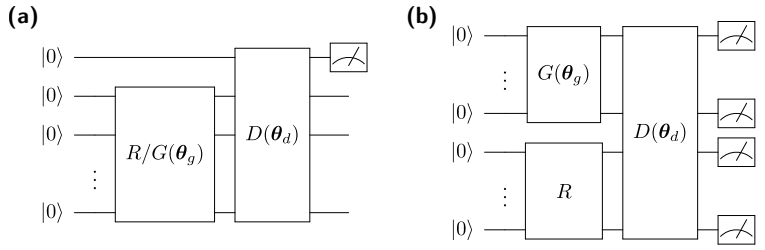

Figure 7.3: (a) *Original proposal for QuGANs [308].* **(b)** *Entangling Quantum GAN (EQ-GAN) [307]. Note that the EQ-GAN can also be configured using an ancilla qubit for measurement as for the QuGAN.*

However, this approach does not always converge but suffers from mode collapse. In some cases, it oscillates between a finite set of states and suffers from non-unique Nash equilibrium. This is due to the way the minimax cost function is defined using a positive operator-valued measurement [307].

To fix these problems, Ref. [307] proposed the Entangling Quantum GAN, which is operated more faithfully to the principles of quantum mechanics. The EQ-GAN algorithm does not pass the data to the discriminator as either fake or real, but rather, the discriminator is allowed to entangle the fake and real data. The schematic of this approach is seen in Fig. 7.3(b). In the proposal of the EQ-GAN, the authors verify both analytically and numerically that the EQ-GAN converges to the global optimal Nash equilibrium that the original QuGAN failed on.

In the EQ-GAN, we can, in principle, choose our generator how we like. However, similar to the VQE, it must be chosen realistically in relation to what is possible with near-term devices and what we are trying to generate. We will there use the same PQC ansatz as we did for the VQE simulation in Chapter 6.

The discriminator, on the other hand, is another story. In principle, we want some circuit that entangles the two states of the real data and the generated data in such a way that we can measure whether the discriminator deems it identical or different. The swap test does exactly this [362]. In Fig. 7.4(a), we show the destructive swap test, which, given two states, can be used to measure whether the two states are identical or not [363]. At the end of the circuit, we measure each qubit. Calling the bit strings O_1 and O_2 of the measurements related to O_1^i and O_2^i [see Fig. 7.4(a)] we say that the test succeeds if the bitwise AND operation of O_1 and O_2 is -1 while it fails if it is +1.

In the ideal world without noise, we would be done and not require any adversarial training of the discriminator circuit. However, noise is quite relevant for near-term quantum computing. The entangling two-qubit operation of the swap test introduces phase errors that make calibration difficult. We, therefore, resort to adversarial generative learning by choosing a different discriminator network. We, therefore, chose the discriminator network in Fig. 7.4(b). Its structure resembles that of the swap test, and it is indeed capable of learning the swap test. Reference [307] showed that this approach is more robust against noise and returns a more significant fidelity when trained on single-qubit gates. With this structure for our quantum GAN, we proceed to simulate one for approximating circuits and quantum states.

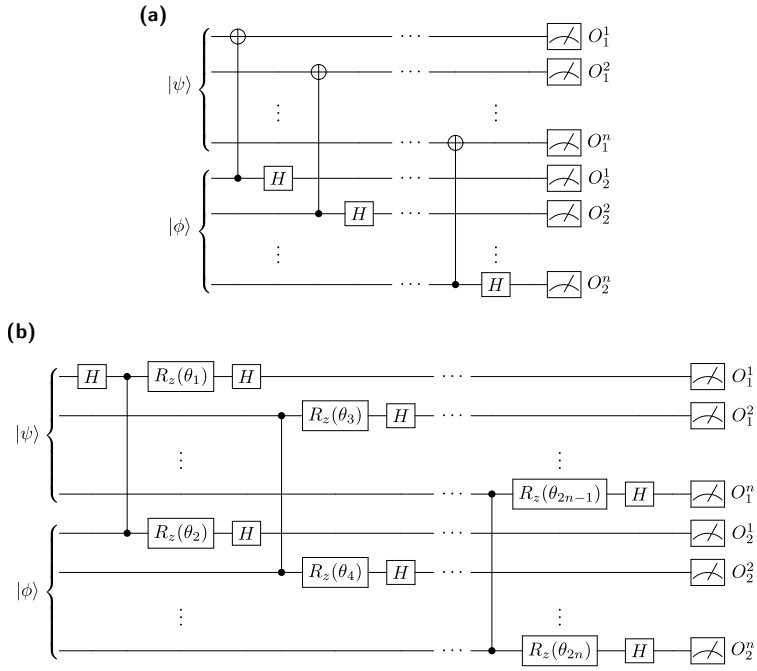

Figure 7.4: (a) *Perfect (destructive) swap test [363]* **(b)** *Adversarial swap test [307]. Note that the swap test can be done in a non-destructive fashion as well, see Ref. [362].*

7.3 Approximating simple circuits

We simulate our EQ-GAN following the approach described in Ref. [342]. We prepare our circuits using CIRQ and then add them as layers using TENSORFLOW QUANTUM. We compile the model using TENSORFLOW and optimize it using the ADAM optimizer, with learning rates of 0.01. We introduce noise in our system on the rotation angle of all of the gates. We do this by adding a gate after each gate with a random error. On the single qubit rotations we add an error to the rotation angle sampled from a normal distribution with $\mu = 0.06$ and $\sigma = 0.02$. On the two-qubit gates we sample from a normal distribution with $\mu = 0$ and $\sigma = 0.005$. These are chosen similarly with the errors in Ref. [307].

As a first approach, we consider a simple circuit consisting of two qubits and a single layer similar to the circuits used when we considered SSVQE in Fig. 6.4. The circuit can be seen in Fig. 7.5(a). We use a similar circuit with fixed predefined, randomly chosen rotation angles for the real data we want to generate. Having prepared our real circuit, we train the EQ-GAN using both the perfect swap test in Fig. 7.4(a) as the discriminator and the adversarial swap test in Fig. 7.4(b) as the discriminator. We train for 80 episodes and a batch size of 4, with learning rates of 0.01 for both networks, and the resulting fidelity can be seen in Fig. 7.5(b). As expected, the adversarial discriminator performs the perfect swap test. We present the maximal fidelities of the two cases in Table 7.1 where we also present the angles used in the simulation.

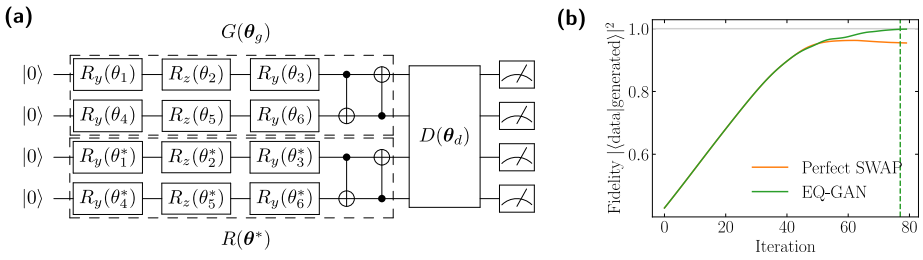

Figure 7.5: (a) *Parameterized quantum circuit representing the simple EQ-GAN model used in Section 7.3. The circuit should be compared to Fig. 7.3(a).* **(b)** *Fidelity of the generated circuit using the EQ-GAN model. The dashed line indicates where the generator loss is lowest.*

Table 7.1: *Parameters used in the EQ-GAN simulation and overlap fidelity of the states returned by the circuits.* True data *refers to the randomly chosen rotations angle $\boldsymbol{\theta}^*$ in Fig. 7.5(a).* Perfect angles *refer to the rotation angles obtained using the perfect swap test as the discriminator, while* adversarial angles *refer to the rotation angles obtained using the adversarial swap test as the discriminator. All angles are in radians.*

	Fidelity	θ_1	θ_2	θ_3	θ_4	θ_5	θ_6
True data, $\boldsymbol{\theta}^*$	1.0000	5.094	2.928	6.116	0.026	4.529	4.847
Perfect angles, $\boldsymbol{\theta}_p$	0.9811	0.519	0.063	0.519	5.646	0.438	5.65
Adversarial angles, $\boldsymbol{\theta}_a$	0.9992	0.51	6.018	0.494	5.631	0.051	5.47

Surprisingly, despite a fidelity less than 5×10^{-4} from unity in the overlap, we see that the generated rotation angles are far from the real ones. In order to investigate this peculiarity, we calculate the states produced by the different rotation angles:

$$\begin{aligned}
\hat{\mathcal{U}}(\boldsymbol{\theta}^*)\,|00\rangle &= 0.655e^{-0.609i}\,|00\rangle + 0.369e^{-0.841i}\,|01\rangle + 0.324e^{2.326i}\,|10\rangle + 0.575e^{2.558i}\,|11\rangle\,,\\
\hat{\mathcal{U}}(\boldsymbol{\theta}_p)\,|00\rangle &= 0.708e^{-0.306i}\,|00\rangle + 0.404e^{-0.27i}\,|01\rangle + 0.287e^{-3.141i}\,|10\rangle + 0.503e^{3.106i}\,|11\rangle\,,\\
\hat{\mathcal{U}}(\boldsymbol{\theta}_a)\,|00\rangle &= 0.654e^{-3.025i}\,|00\rangle + 0.355e^{3.105i}\,|01\rangle + 0.319e^{-0.005i}\,|10\rangle + 0.587e^{0.148i}\,|11\rangle\,.
\end{aligned}$$

Comparing the amplitudes of each state in the computational basis, we see that these match rather well. Especially the adversarial trained $\hat{\mathcal{U}}(\boldsymbol{\theta}_a)$ match the amplitudes of $\hat{\mathcal{U}}(\boldsymbol{\theta}^*)$ quite closely, as we should expect from a fidelity so close to unity. Thus we find that the fidelity measure of the swap test is only concerned with the amplitude and not the phase of the states. We obtain similar results using different entangling gates, more qubits, other rotation angles. Whenever we train a circuit to a high fidelity, only the amplitudes match, not the phases.

This discussion should be related to the discussion on the VQE overlap in Section 6.6. We found that an energy close to the real energy does not necessarily mean that we obtain a high overlap between the VQE state and the real state. As we will see in the next section, a good overlap is no guarantee of a matching energy.

In general, we can conclude that if one wants a precise energy, one should apply the VQE algorithm, and if one wants a good overlap, one should apply the EQ-GAN algorithm but still be mindful of the phases. Combining the EQ-GAN and VQE algorithm

might be tempting to find the full eigenstate. Nevertheless, doing so would require knowledge of both the real eigenstate (for the EQ-GAN) and the Hamiltonian (for the VQE), to which end we do not need any further information.

7.4 Approximating VQE states using EQ-GAN

In the previous section, we saw that an EQ-GAN could approximate a simple two-qubit circuit, or at least we found a high overlap fidelity, while the phase was estimated poorly.

Now we want to push the EQ-GAN. For that, we need some data. Luckily from the VQE simulation we have done in Section 6.5, we have plenty of data in the form of unitaries that an EQ-GAN could learn. We, therefore, chose our R in Fig. 7.3(b) as the circuits found using the VQE algorithm in Chapter 6. In other words, we set $R = \hat{\mathcal{U}}(\boldsymbol{\theta}_{\text{VQE}})$, where $\hat{\mathcal{U}}$ is a unitary representing a circuit on the form of Fig. 6.4 with a given number of layers and type of entangling gate. The parameters $\boldsymbol{\theta}_{\text{VQE}}$ are determined from a VQE simulation as performed in Section 6.5. To generate more data for the machine learning algorithm, we sample 100 circuit parameters from the original VQE parameters with a standard deviation of 0.01. We chose the generator identical to the VQE circuit, i.e., $G(\boldsymbol{\theta}) = \hat{\mathcal{U}}(\boldsymbol{\theta})$ and optimize the $\boldsymbol{\theta}$ parameters. This way, we could, in principle, learn the exact VQE circuit. We use both a perfect swap test and an adversarial swap test as the discriminator.

To sum up, what we are trying to do, we are trying to learn the eigenstates of a given system without knowing the Hamiltonian of the system. This could be useful for systems where one can only measure the states and energies of the system and not determine the Hamiltonian. We simulate the EQ-GAN algorithm equivalently to in Section 7.3[2]. As previously, we do the simulation for H_2, LiH, and BeH_2 for different entangling gates (CNOT, *i*SWAP, CZ, and their parameterized versions) for up to three layers. In Fig. 7.6 we present some typical results for H_2. For examples of other results, see Appendix F.

Considering the predicted energy in Fig. 7.6(a), we see that the perfect swap and adversarial swap predict roughly the same energy, and curiously enough, the excited state is predicted larger than the ground state energy. However, none of the predicted energies are close to the one found using VQE, both for the ground and excited state. The reason we do not obtain good energies is due to the lack of phase estimation as discussed in Section 7.3. If we consider the infidelity, $1 - |\langle \text{GAN}|\text{VQE}\rangle|^2$, on the other hand, we see that it is pretty good with infidelities around 0.05 and below. As expected, the adversarial swap test outperforms the perfect swap test.

We obtain similar results for other combinations of molecules, gates, and layers. See Appendix F for different results. It is worth noting that the results obtained here are done without optimizing the meta parameters, i.e., we are using the same 80 episodes, a batch size of 4, and learning rates of 0.01 as we did in Section 7.3. It is possible that optimizing these parameters could result in even higher fidelities, as is usually the case for classical machine learning algorithms [346].

[2]Some of the numerical results presented here were obtained at the Centre for Scientific Computing, Aarhus `http://phys.au.dk/forskning/cscaa/`.

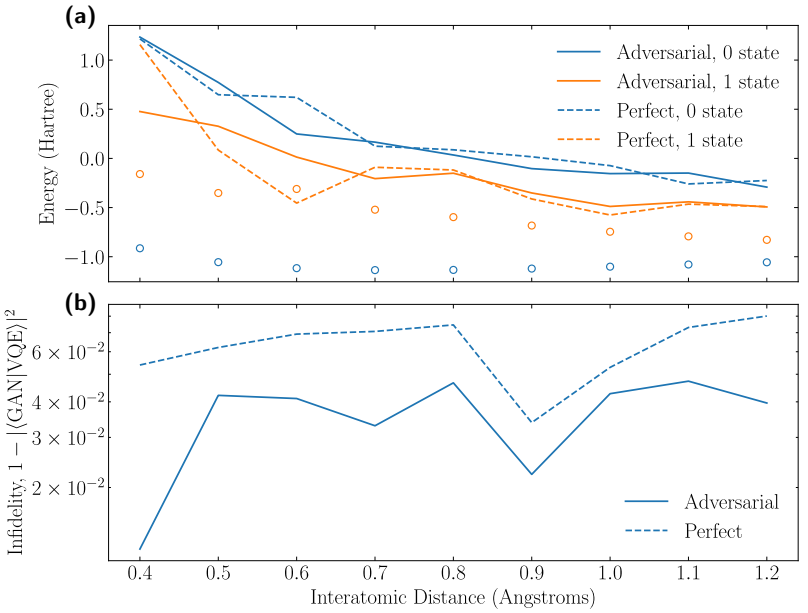

Figure 7.6: *Results of the EQ-GAN learning on VQE data for H_2 with three layers of Fig. 6.4.* **(a)** *Predicted energy of the EQ-GAN algorithm (lines) and SSVQE (circles). Solid lines indicates the adversarial swap test was used, while the dashed line indicate that the perfect swap test was used.* **(b)** *Infidelity of the state generated by the EQ-GAN, $|\text{GAN}\rangle = G(\boldsymbol{\theta})\,|0\rangle$, with the state generated by the VQE, $|\text{VQE}\rangle = \hat{\mathcal{U}}(\boldsymbol{\theta}_{\text{VQE}})\,|0\rangle$.*

7.5 Summary and outlook

In this chapter, we have introduced classical GANs and discussed how to make a fully quantum version of a GAN, i.e., a generative network based on a quantum algorithm working on quantum data. First, the original QuGAN proposal was introduced, and then the entangling quantum GAN. We then showed that using TensorFlow Quantum we could simulate an EQ-GAN, first on a simple two-qubit circuit and later on actual VQE data, from simulation done in Chapter 6. We showed that we achieved a rather good overlap fidelity, especially for the adversarial swap test, which outperforms the perfect swap test as expected. However, we also showed that the EQ-GAN lacks any phase estimation despite this excellent overlap fidelity. This means that the EQ-GAN simulation trying to generate molecular states, as approximated by the VQE, does not yield any good eigenvalues. In other words, it does not predict the energy of the given molecule very accurately. One could argue that this should not be surprising as we are trying to approximate an approximation.

To fix this problem, a point for further investigation could be to learn directly from the eigenstates of the molecular systems instead of learning from the states approximated by the VQE algorithm. This could improve the predicted energies, especially considering the magnitude of irrelevant states included in the VQE, as discussed in Section 6.6.

CHAPTER 8

Conclusion and outlook

The recurring theme throughout this thesis has been quantum technology based on a platform of superconducting circuits. We started by introducing superconducting circuits from a theoretical point of view, and we discussed the tools and methods needed to analyze a given circuit down to a qubit model. We then presented some examples of superconducting qubits from the general literature and discussed different coupling schemes.

In the following chapter, we presented three different controlled gates, which could all be implemented using the methods of superconducting circuits. First, we presented the n-bit iToffoli gate, and the related CNOT^n and Barenco gates, which we showed were more efficient in the number of operations needed to operate the gate. Next, we presented the controlled iSWAP gate and showed how it could exponentiate non-Hermitian gates. Finally, we discussed another way to implement a controlled swap gate using a linear coupled approach. This way, the opening and closing of the gate depended on a superposition state of the control qubits. All three gates could be used in near-term quantum chips, as they are high fidelity native gates in different quantum technology schemes, particularly in superconducting circuits.

In the last part of the thesis, we considered hybrid quantum-classical algorithms and simulated examples of these. The base for most HQC algorithms is parameterized quantum circuits. We showed that we could reduce the number of single-qubit rotations in these circuits without loss of expressibility or entanglement capability, and we showed that the placement of the single-qubit rotations could be arbitrary. We also showed that this reduction in single-qubit rotations did not affect the variational quantum eigensolver simulations as expected from the expressibility and entanglement analyses. We further used the VQE to find the eigenstates of different molecules and other Hamiltonians. We then discussed how parameterized entangling gates could improve variational quantum eigensolver results without any experimental cost. The last thing we discussed in the VQE chapter was the overlap fidelity of the approximate eigenstates. We showed that it was generally low, even for extremely good eigenvalues, possibly due to low-contributing states concerning the Hamiltonian.

Finally, we discussed quantum versions of the efficacious generative adversarial

networks in the last chapter. In particular, we considered the entangling quantum generative adversarial network, which we simulated to show that it yielded a high overlap fidelity. However, we also showed that it could not determine the phases of the states, which made it ineffective at determining the energies of a Hamiltonian despite a more considerable overlap fidelity with the eigenstates.

Where to go from here? One could continue to explore different ways to design superconducting circuits to obtain new gates and interactions. However, I believe that such analysis of superconducting circuits is most productive when objective with the analysis. It is my firm belief that any significant breakthrough within superconducting circuit engineering will probably be carried by experimental breakthroughs improving the lifetime of qubits and interactions between these. Such improvements are also what is needed for better superconducting quantum chips. Nonetheless, creative explorations of superconducting circuits may open up new ways to employ said circuits.

The variational quantum eigensolver is a well-proven algorithm that has already been shown to approximate eigenvalues quite well. However, there is room for improvement. As discussed, the approximate eigenstates are not that good, and improving these could be a valid point for further investigation.

The quantum generative adversarial networks, on the other hand, is much less proven; however, it has great potential, especially thinking of the success of their classical counter part. It is quite the opposite of the variational quantum eigensolver as it predicts the states rather well, without reproducing any possible eigenvalues. One possible application of the quantum GAN could be to generate states measured directly from, e.g., an actual molecule.

The final question of any thesis regarding any emerging technology such as quantum technology should be: When will it take over the world? The European Commission seems to think it is only 10-20 years away [364]; however, 10-20 years is a pretty standard answer that most scientists applying for funding will give you if you ask them when their research will revolutionize the world. On a more serious note, the question depends on what is meant; if by taking over the world, you are asking when we will be using quantum laptops to search the quantum internet while checking our quantum smartphones? Well, then the answer is never. Quantum computers may revolutionize the world, but the everyday private user will get their own quantum computer; they will probably not even notice the quantum revolution if it comes. There are several reasons for this: First, we live in a classical world, and therefore we need to interact with classical computers. Second, quantum computers are highly specialized in solving particular problems. Third, most people do not need improved computations when sending e-mails or surfing the internet.

Notwithstanding, this does not mean that quantum computers are a purely academic interest that will be useless in a commercial setting. Quantum computers could help speed up some computations needed by companies or researchers (Grover's algorithm, VQE, QAOA could potentially do this), but it is probably not something the end-user will ever notice. In other words, a quantum computer will become part of some backend, not visible to the end-users. Quantum computers may be available through cloud services as part of a computational suit. In fact, they are already available from, e.g., IBM Quantum, which offers a superconducting quantum computer [365], Amazon Braket, which offers both trapped-ion technology from IonQ and superconducting quantum processor

from Regetti, as well as quantum annealing from D-Wave through Amazon Web Services [366], or Microsoft Azure Quantum, which offers trapped-ion technology from IonQ and Quantinuum and superconducting quantum processor from Quantum Circuits, Inc and Regetti [367]. So if the question is: When will quantum computations be available? Then the answer is today.

To summarize, the real question is not when quantum computers will arrive, because they are already here. Instead, it is a question of when they will be useful for anything? Hopefully, some of the results presented in this thesis will help make quantum technologies useful in the near future, however long that may be.

APPENDIX A

Graph Theory of Electrical Networks

*This appendix is quoted from **[VIII]** with minor changes to fit the context of this thesis.*

In this appendix to Chapter 1, we present some useful graph theory for electrical circuits. The reason for this is that graph theory is the natural language of electromagnetic circuits where each circuit element can be represented as an edge on a graph.

A.1 Fundamental graph theory of electrical networks

In this appendix, we present some fundamental definitions from graph theory. The first three definitions are directly related to the discussion in Chapter 1, while the remaining definitions provide an alternative way of stating Kirchhoff's laws. We describe the quantities important to circuit analysis using the example circuit shown on Fig. A.1(a). The example circuit consists of a transmon qubit capacitively coupled to a resonator, which is a very common setup [80, 193]. For more material on graph theory see, e.g., Refs. [368, 369].

Definition 1 (Graph) *A **graph** $\mathcal{G} = (\mathcal{N}, \mathcal{B})$ is a set of **nodes** $\mathcal{N} = \{n_1, \ldots, n_N\}$ where N is the number of nodes, and a set of branches (sometimes called edges) $\mathcal{B} = \{b_1, \ldots, b_B\}$ where each*

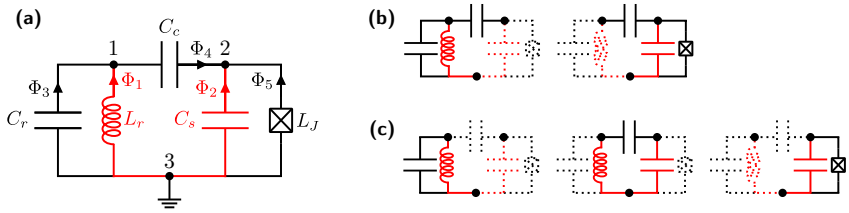

Figure A.1: ***(a)*** *Example transmon-resonator circuit. The chosen spanning tree (red) consists of the resonator L_r inductance and the shunting capacitance C_s.* ***(b)*** *Fundamental cutsets of the circuit (in solid) with respect to the chosen spanning tree.* ***(c)*** *Fundamental loops of the circuit (in solid) with respect to the chosen spanning tree.*

branch connects a pair of nodes and B is the number of branches. The number of nodes is called the ***order*** *of the graph and is denoted $|\mathcal{G}| = N$. We allow multiple branches to connect the same pair of nodes. Sometimes this is called a* ***multigraph*** *in order to distinguish it from* ***simple graphs*** *where only one branch can connect the same pair of nodes.*

Using this definition, we can consider each circuit as a graph where each component corresponds to a branch. The first step of any circuit analysis is to label every branch of the graph. These can be labeled in different ways, usually via the element or the flux through the current. These are equivalent, and often both are used as they complement each other.

Using the components as the labels, the set of branches in Fig. A.1(a) becomes $\mathcal{B} = \{L_r, C_s, C_r, C_c, L_J\}$. The order of the graph is $|\mathcal{G}| = 3$ and the nodes can be labeled arbitrarily, here we label them 1,2, and 3. The number of branches is $B = 5$, and we can thus write the flux over all branches as a vector with five elements

$$\mathbf{\Phi} = \begin{bmatrix} \Phi_1 & \Phi_2 & \Phi_3 & \Phi_4 & \Phi_5 \end{bmatrix}^T, \tag{A.1}$$

where the order of the fluxes corresponds to the number of the branches in $\mathcal{B}$. Note that we have indicated the direction of every branch in Fig. A.1(a) using arrows. We define positive branch currents $I_b > 0$ as the case where current flows through a branch in the direction of the arrow. Using the passive sign convention the voltage over a branch is then given by $V_b = V_b^{\text{start}} - V_b^{\text{end}}$, which ensures that the power $P_b = I_b V_b$ is positive if energy is being stored or dissipated in the branch element. Strictly speaking, this makes our graph a *directed* graph, but since all electrical network graphs are directed graphs, we are simply going to call them graphs. We are also going to assume that our graph is connected, meaning that there exists a path between every pair of nodes.

Definition 2 (Subgraph) *A graph $\mathcal{H} = (\mathcal{N}_\mathcal{H}, \mathcal{B}_\mathcal{H})$ is called a* ***subgraph*** *of $\mathcal{G} = (\mathcal{N}_\mathcal{G}, \mathcal{B}_\mathcal{G})$, written $\mathcal{H} \subseteq \mathcal{G}$, if $\mathcal{N}_\mathcal{H} \subseteq \mathcal{N}_\mathcal{G}$ and $\mathcal{B}_\mathcal{H} \subseteq \mathcal{B}_\mathcal{G}$. If $\mathcal{H}$ is a subgraph of $\mathcal{G}$ but $\mathcal{H} \neq \mathcal{G}$ it is called a proper subgraph.*

In the electrical circuit setting, the notion of subgraphs is often used to describe the capacitive and inductive subgraphs of the circuit. In the case of the example in Fig. A.1(a) the capacitive subgraph is defined to be the set of branches $\mathcal{B}_C = \{C_s, C_r, C_c\}$, while the inductive subgraph is defined by $\mathcal{B}_L = \{L_r, L_J\}$. Note that the set of nodes are identical for the capacitive and inductive subgraph as well as the full (super)graph, i.e., $\mathcal{N}_C = \mathcal{N}_L = \mathcal{N}$. Also, even though we assume our graph to be connected, its subgraphs are not necessarily connected.

The next step in the analysis is to specify a subgraph called a *spanning tree* for our graph.

Definition 3 (Spanning tree) *A* ***spanning tree*** *of a graph $\mathcal{G}$ is a connected subgraph $\mathcal{T}$ that contains the same nodes as $\mathcal{G}$ (i.e., $\mathcal{N}_\mathcal{T} = \mathcal{N}_\mathcal{G}$) and contains no loops.*

The branches of the spanning tree are called ***twigs*** *and branches of the complement of the spanning tree are called* ***links*** *(or* ***chords****). Note that there are $B_\mathcal{G} - (N_\mathcal{G} - 1)$ links.*

The spanning tree connects every pair of nodes through exactly one path. For our example, we choose branches 1 and 2 as our spanning tree as shown in red on Fig. A.1.

The linear inductor, together with the C_s shunting capacitor, constitutes the twigs of the tree, while the remaining capacitors (C_r, C_c) and Josephson junction (L_J) are links. Note that we are free to choose our spanning tree differently as long as it obeys the definition. We could, e.g., have chosen the inductive subgraph, as mentioned above, however, we can not choose the capacitive subgraph as it includes a loop. This freedom in choosing the spanning tree corresponds to a gauge freedom in the equations of motion.

Choosing a spanning tree also allows us to define fundamental cutsets and fundamental loops, which are useful when deriving the equations of motion for a circuit. The following definitions used in the main text but can be used for an alternative statement of Kirchhoff's laws. We start with the fundamental cutsets.

Definition 4 (Cut) *Given a graph $\mathcal{G} = (\mathcal{N}, \mathcal{B})$ a **cut** is a partitioning of nodes $\mathcal{N}$ into two disjoint sets $\mathcal{N}_A$ and $\mathcal{N}_B$. With every cut, we can associate a **cutset**, which is the set of branches that have endpoints in both $\mathcal{N}_A$ and $\mathcal{N}_B$.*

Note that removing a single twig cuts the spanning tree, $\mathcal{T}$, into two disjoint subgraphs with nodes $\mathcal{N}_A$ and $\mathcal{N}_B$. Such a cut is called a *fundamental cut*, and the branches that must be removed to complete the same cut on the full graph is called a *fundamental cutset*. More formally:

Definition 5 (Fundamental cut) *Given a graph $\mathcal{G}$ and a spanning tree $\mathcal{T}$ we define a **fundamental cut** or **f-cut** as a cut whose **cutset** contains only one twig.*

In practice, the fundamental cutsets can be found by removing one twig from the spanning tree. This creates two disjoint subgraphs of the spanning tree with nodes $\mathcal{N}_A$ and $\mathcal{N}_B$. Now remove the links of the full graph with endpoints in both partitions. The cutset is then the set of all the removed links and the single twig. We thus end up with a unique cutset with one twig and any number of links. This can be done for every twig, and the number of fundamental cutsets is thus equal to the number of twigs $|\mathcal{T}| = N - 1$. The fundamental cutsets of our example graph can be seen in Fig. A.1(b).

We now turn our attention to the loops. By taking the spanning tree and adding a single link from the full graph we form a unique loop. Such a loop contains exactly one link and one or more twigs. We call these loops the *fundamental loops* of the $\mathcal{G}$ with respect to the spanning tree $\mathcal{T}$.

Definition 6 (Fundamental loop) *Given a graph $\mathcal{G}$ and a spanning tree $\mathcal{T}$, we define a **fundamental loop** or **f-loop** as a loop consisting of exactly one link and one or more twigs.*

The number of fundamental loops that can be formed is equal to the number of links. The fundamental loops of our example graph can be seen in Fig. A.1(c).

As we shall see in the following section the fundamental loops and cuts allow us to write Kirchhoff's laws in a compact and useful way.

A.1.1 Circuit matrices

Using the notion of f-loops and f-cuts, we define two characteristic matrices for the network graphs, which can be used to write Kirchhoff's laws more compactly.

For every loop, we can define the orientation, i.e., clockwise or anti-clockwise. For an f-loop, we let the orientation be determined by the orientation of its link. We can then define the fundamental loop matrix.

Definition 7 (Fundamental loop matrix) *Given a graph $\mathcal{G} = (\mathcal{N}, \mathcal{B})$, with spanning tree $\mathcal{T}$, we define the **fundamental loop matrix**, or **f-loop matrix**, $\boldsymbol{F}^{(L)}$ as*

$$\boldsymbol{F}_{ij}^{(L)} = \begin{cases} +1 & \text{if } b_j \in f_i \text{ and } l_i, b_j \text{ same orientation} \\ -1 & \text{if } b_j \in f_i \text{ and } l_i, b_j \text{ opposite orientation} \\ 0 & \text{if } b_j \notin f_i \end{cases}, \tag{A.2}$$

where l_i is the link in the ith f-loop, f_i, with $1 \leq i \leq |\mathcal{G} \backslash \mathcal{T}| = B - (N-1)$ and b_j is the jth branch in $\mathcal{B}$ with $1 \leq j \leq B$.

In other words, we iterate through the branches and the set of f-loops. If the given branch is in the given f-loop, the matrix entry becomes ± 1, with a plus if the branch has the same orientation as the f-loop (which is determined by the link of the f-loop). If the branch is not in the given f-loop, the matrix entry is 0.

Consider our example circuit and its fundamental loops from Fig. A.1(c). The first fundamental loop consists of the link Φ_3 and the twig Φ_1. The orientation of the loop (determined by Φ_3) is clockwise, which means that the $\boldsymbol{F}_{11}^{(L)} = -1$, since the twig Φ_1 points in the anti-clockwise direction. The only other nonzero entry in the first row is $\boldsymbol{F}_{13}^{(L)} = 1$, corresponding to the link Φ_3 oriented in the clockwise direction. Following the same method for the other two f-loops, we find

$$\boldsymbol{F}^{(L)} = \begin{bmatrix} -1 & 0 & 1 & 0 & 0 \\ 1 & -1 & 0 & 1 & 0 \\ 0 & -1 & 0 & 0 & 1 \end{bmatrix}, \tag{A.3}$$

where the columns correspond to the branches in their respective order and the rows correspond to the loops in the same order as in Fig. A.1(c).

As with the loops, we can also choose an orientation for the cutsets. If a cut is oriented from $\mathcal{N}_A$ to $\mathcal{N}_B$, we say that a branch in the cutset has positive orientation if it begins in $\mathcal{N}_A$ and ends in $\mathcal{N}_B$. We choose to orient every f-cutset such that its twig in an f-cutset has positive orientation. We can then define the *fundamental cutset matrix*.

Definition 8 (Fundamental cut matrix) *Given a connected graph $\mathcal{G} = (\mathcal{N}, \mathcal{B})$, with spanning tree $\mathcal{T}$, we define the **fundamental cut matrix**, or **f-cut matrix**, $\boldsymbol{F}^{(C)}$ as*

$$\boldsymbol{F}_{ij}^{(C)} = \begin{cases} +1 & \text{if } b_j \in c_i \text{ and } t_i, b_j \text{ same orientation} \\ -1 & \text{if } b_j \in c_i \text{ and } t_i, b_j \text{ opposite orientation} \\ 0 & \text{if } b_j \notin c_i \end{cases}, \tag{A.4}$$

where t_i is the twig of the ith cutset, c_i, with $1 \leq i \leq |\mathcal{T}| = N - 1$ and b_j is the jth branch in $\mathcal{B}$ with $1 \leq j \leq B$.

In other words, we iterate through the branches and the set of cutsets. If the given branch is in the given cutset, the matrix entry becomes ± 1, with a plus if the branch has the same orientation as the cutset (which is determined by the orientation of the twig of the cutset). If the branch is not in the given f-cutset, the matrix entry is 0.

As an example take the first cutset from Fig. A.1(b). The twig Φ_1 and link Φ_3 both points towards the same node and thus have positive orientation. The final link Φ_4 points away from the node and has negative orientation. Thus the first row of the cutset matrix becomes $[1, 0, 1, -1, 0]$. By analyzing the other cutset, in the same manner, we find the fundamental cutset matrix

$$\boldsymbol{F}^{(C)} = \begin{bmatrix} 1 & 0 & 1 & -1 & 0 \\ 0 & 1 & 0 & 1 & 1 \end{bmatrix}, \tag{A.5}$$

where the columns correspond to the branches in their respective order, and the rows correspond to the cutsets in the same order as in Fig. A.1(b).

All branches of the graph are either twigs or links. Every f-cutset contains only one twig, and every f-loop contains only one link. Additionally, for every partition of nodes defined by an f-cut, every f-loop must begin and end in the same partition. Thus every f-cutset and f-loop share either 0 or exactly 2 branches. Now consider the elements

$$\left(\boldsymbol{F}^{(L)}(\boldsymbol{F}^{(C)})^T\right)_{ij} = \sum_k \boldsymbol{F}^{(L)}_{ik}\boldsymbol{F}^{(C)}_{jk}. \tag{A.6}$$

Evidently, the (i, j)th element depends only on the ith f-loop and the jth f-cut. If the f-cutset and f-loop share no branches, all the terms are zero, and in the case where they share exactly two branches, we get two nonzero terms with opposite signs. We thus have

$$\boldsymbol{F}^{(L)}(\boldsymbol{F}^{(C)})^T = \boldsymbol{0}. \tag{A.7}$$

Multiplying Eqs. (A.3) and (A.5) we see that this is exactly the case for the example graph, as it should be.

A.2 Method of electrical network graph theory

In this section, we present a more mathematical stringent method for obtaining the Hamiltonian of an electrical superconducting circuit. This method is based upon Ref. [48] and uses electrical network graph theory [368]. This method is a more advanced alternative to the method presented in Section 1.2, however, the resulting equations of motion are the same.

The first step is to label and order all the circuit components (branches) of the network graph and choose a spanning tree for the graph. Without loss of generality, we order the components such that the first $|\mathcal{T}|$ branches are the twigs, and we then write the fluxes and currents through all components as vectors

$$\boldsymbol{\Phi} = \begin{bmatrix} \boldsymbol{\Phi}_t \\ \boldsymbol{\Phi}_l \end{bmatrix}, \quad \boldsymbol{I} = \begin{bmatrix} \boldsymbol{I}_t \\ \boldsymbol{I}_l \end{bmatrix}, \tag{A.8}$$

where $\boldsymbol{\Phi}_t$ ($\boldsymbol{I}_t$) are the fluxes (currents) of all the twigs and $\boldsymbol{\Phi}_l$ ($\boldsymbol{I}_l$) are the fluxes (currents) of all the links. For the example circuit in Fig. A.1 we have $\boldsymbol{\Phi}_t = (\Phi_1, \Phi_2)^T$ and $\boldsymbol{\Phi}_l = (\Phi_3, \Phi_4, \Phi_5)^T$ and likewise for the current vector.

After all components have been labeled and a tree has been selected, we construct the fundamental matrices of the graph $\boldsymbol{F}^{(L)}$ and $\boldsymbol{F}^{(C)}$ following Definitions 7 and 8, respectively. In the following, we show how these matrices may be used to set up the equations of motion and reduce the number of free coordinates.

A.2.1 Kirchhoff's laws

Using Eq. (A.8) and the f-matrices, we reformulate Kirchhoff's laws as stated in Eq. (1.3).

Kirchhoff's current law

Kirchhoff's current law states that no charge may accumulate at a node. Mathematically we may write this as

$$\sum_{b \text{ incident on } n} s_{n,b} I_b = 0, \quad \text{for every node } n, \tag{A.9}$$

where we have $s_{n,b} = +1$ if the branch b ends at node n and $s_{n,b} = -1$ if b begins at n. This is equivalent to the definition in Eq. (1.3a), but with currents instead of charges, i.e., Eq. (A.9) is the time derivative of Eq. (1.3a). Recall that a cutset is the set of branches between two partitions of nodes. Thus if no charge has accumulated at a single node, the total current from one partition of nodes to another must be zero. We can write this using the f-cut matrix as

$$\boldsymbol{F}^{(C)} \boldsymbol{I} = \boldsymbol{0}. \tag{A.10}$$

If we calculate this matrix product for the example circuit using Eq. (A.5) we find

$$\boldsymbol{F}^{(C)} \boldsymbol{I} = \begin{bmatrix} 1 & 0 & 1 & -1 & 0 \\ 0 & 1 & 0 & 1 & 1 \end{bmatrix} \begin{bmatrix} I_1 \\ I_2 \\ I_3 \\ I_4 \\ I_5 \end{bmatrix} = \begin{bmatrix} I_1 + I_3 - I_4 \\ I_2 + I_4 + I_5 \end{bmatrix} = \begin{bmatrix} 0 \\ 0 \end{bmatrix},$$

which is equivalent to applying Kirchhoff's current law directly to nodes 1 and 2 in Fig. A.1.

Kirchhoff's voltage law

Kirchhoff's voltage law states that if we choose some oriented loop of branches l, the algebraic sum of voltages around the loop must equal the electromotive force induced by external magnetic flux, $\tilde{\Phi}_l$, through the face enclosed by the loop, i.e.,

$$\sum_{b \in l} s_{l,b} V_b = \dot{\tilde{\Phi}}_l, \quad \text{for all loops } l, \tag{A.11}$$

where $s_{l,b} = +1$ if b is oriented along l, and $s_{l,b} = -1$ if b is oriented against l. The external flux through the loop l is denotes $\tilde{\Phi}_l$. This is equivalent to the definition in Eq. (1.3b), but

with voltages instead of fluxes, i.e., Eq. (A.11) is the time derivative of Eq. (1.3b). Thus, the f-loops of the graph define a set of equations and using Eq. (1.2a) we may write Kirchhoff's voltage law as

$$\boldsymbol{F}^{(L)}\boldsymbol{\Phi} = \tilde{\boldsymbol{\Phi}}, \tag{A.12}$$

where $\tilde{\boldsymbol{\Phi}} = (\tilde{\Phi}_1, \ldots, \tilde{\Phi}_{B-N+1})^T$ is the vector external fluxes through the fundamental loops.

For the example circuit, we calculate the matrix product using Eq. (A.3) and find

$$\boldsymbol{F}^{(L)}\boldsymbol{\Phi} = \begin{bmatrix} -1 & 0 & 1 & 0 & 0 \\ 1 & -1 & 0 & 1 & 0 \\ 0 & -1 & 0 & 0 & 1 \end{bmatrix} \begin{bmatrix} \Phi_1 \\ \Phi_2 \\ \Phi_3 \\ \Phi_4 \\ \Phi_5 \end{bmatrix} = \begin{bmatrix} -\Phi_1 + \Phi_3 \\ \Phi_1 - \Phi_2 + \Phi_4 \\ -\Phi_2 + \Phi_5 \end{bmatrix} = \begin{bmatrix} \tilde{\Phi}_1 \\ \tilde{\Phi}_2 \\ \tilde{\Phi}_3 \end{bmatrix},$$

where each row is equivalent to applying Kirchhoff's voltage law directly to the corresponding loop. We assume external fluxes of $\tilde{\boldsymbol{\Phi}} = (\tilde{\Phi}_1, \tilde{\Phi}_2, \tilde{\Phi}_3)^T$ through the loops.

Reducing the number of coordinates

Using Kirchhoff's voltage law, we can reduce the number of free coordinates. We only need to specify the fluxes of the spanning tree to calculate the remaining fluxes. In order to do so, we write our f-cut matrix as

$$\boldsymbol{F}^{(C)} = \begin{bmatrix} \mathbb{1} & \boldsymbol{F} \end{bmatrix}, \tag{A.13}$$

where $\boldsymbol{F}$ is a $|\mathcal{T}| \times |\mathcal{G}\backslash\mathcal{T}| = (N-1) \times (B-N+1)$ matrix and the identity is a $(N-1) \times (N-1)$ matrix. Note that our specific ordering of the circuit components (twigs first, then links) allows for the simple block structure of Eq. (A.13). This structure is clearly seen in the example in Eq. (A.5), from which it is evident that

$$\boldsymbol{F} = \begin{bmatrix} 1 & -1 & 0 \\ 0 & 1 & 1 \end{bmatrix}, \tag{A.14}$$

for the example circuit in Fig. A.1.

Reordering the components shuffles the rows and columns of the fundamental cut matrix, and the following derivations can easily be generalized. From Eq. (A.7) and Definition 7 we find that we can write the f-loop matrix in a similar manner

$$\boldsymbol{F}^{(L)} = \begin{bmatrix} -\boldsymbol{F}^T & \mathbb{1} \end{bmatrix}, \tag{A.15}$$

where $\boldsymbol{F}$ is the same matrix as in Eq. (A.13), meaning that the identity is now $(B-N+1) \times (B-N+1)$. This structure is again seen in the example in Eq. (A.3) where the transpose of Eq. (A.14) occurs. We can then rewrite Kirchhoff's voltage law in Eq. (A.12) and isolate the fluxes of the links

$$\boldsymbol{\Phi}_l = \tilde{\boldsymbol{\Phi}} + \boldsymbol{F}^T\boldsymbol{\Phi}_t, \tag{A.16}$$

and use this to write our flux vector in Eq. (A.8) in terms of the twig and external fluxes

$$\boldsymbol{\Phi} = \begin{bmatrix} \boldsymbol{\Phi}_t \\ \boldsymbol{F}^T\boldsymbol{\Phi}_t + \tilde{\boldsymbol{\Phi}} \end{bmatrix} = (\boldsymbol{F}^{(C)})^T\boldsymbol{\Phi}_t + \begin{bmatrix} \boldsymbol{0} \\ \tilde{\boldsymbol{\Phi}} \end{bmatrix}, \tag{A.17}$$

meaning that we have eliminated the fluxes of the links. Using Eq. (A.17) on the example circuit in Fig. A.1 we can write the fluxes as

$$\boldsymbol{\Phi} = \begin{bmatrix} \Phi_1 \\ \Phi_2 \\ \Phi_1 + \tilde{\Phi}_1 \\ \Phi_1 - \Phi_2 + \tilde{\Phi}_2 \\ \Phi_2 + \tilde{\Phi}_3 \end{bmatrix}, \tag{A.18}$$

which means that we have eliminated the three fluxes on the links.

A.2.2 Equations of motion

In this section, we use Kirchhoff's current law, to set up the equations of motion for the system. For this purpose, it is convenient to introduce the species-specific vectors $\boldsymbol{I}_S$ and $\boldsymbol{\Phi}_S$

$$(\boldsymbol{I}_S)_i = \begin{cases} \boldsymbol{I}_i & \text{if the } i\text{th element is of species } S, \\ 0 & \text{otherwise,} \end{cases}, \tag{A.19a}$$

$$(\boldsymbol{\Phi}_S)_i = \begin{cases} \boldsymbol{\Phi}_i & \text{if the } i\text{th element is of species } S, \\ 0 & \text{otherwise,} \end{cases} \tag{A.19b}$$

where the species subscript, S, indicates the element species, i.e., capacitor, inductor, etc. This can be understood as the current and flux vectors with everything but S species removed. We use C for capacitors, L for linear inductors, and J for Josephson junctions. For the example circuit this yields

$$\boldsymbol{I}_C = (0, I_2, I_3, I_4, 0)^T, \tag{A.20a}$$

$$\boldsymbol{I}_L = (I_1, 0, 0, 0, 0)^T, \tag{A.20b}$$

$$\boldsymbol{I}_J = (0, 0, 0, 0, I_5)^T, \tag{A.20c}$$

and likewise for the fluxes.

The first step of the analysis is to express the current of every branch in terms of the tree fluxes $\boldsymbol{\Phi}_t$. The current flowing through a capacitor with capacitance C is given by Eq. (1.6), and we can thus write the current flowing through all capacitors as

$$\boldsymbol{I}_C = \boldsymbol{D}_C\ddot{\boldsymbol{\Phi}}, \tag{A.21}$$

where $\boldsymbol{D}_C$ is a diagonal matrix with the circuit capacitances on the diagonal. In this context, all other circuit components are counted as having zero capacitance. For the example circuit the capacitance matrix becomes $\boldsymbol{D}_C = \text{diag}(0, C_s, C_r, C_c, 0)$, which multiplied to $\ddot{\boldsymbol{\Phi}} = (\ddot{\Phi}_1, \ddot{\Phi}_2, \ddot{\Phi}_3, \ddot{\Phi}_4, \ddot{\Phi}_5)^T$ yields Eq. (A.20a).

The flux stored in the linear inductors is related to the currents through

$$\boldsymbol{L}\boldsymbol{I} = \boldsymbol{\Phi}_L, \tag{A.22}$$

where $\boldsymbol{L}$ is a symmetric matrix with diagonal elements $\boldsymbol{L}_{ii} = L_i$ where L_i is the inductance of the ith element. For all other components than linear inductors, we set $L_i = 0$. The off-diagonal elements are the mutual inductances $\boldsymbol{L}_{ij} = M_{ij} = k_{ij}\sqrt{L_i L_j}$ between the ith and jth inductor, with $-1 < k_{ij} < 1$ being the coupling coefficient. If a positive current in one inductor results in a positive magnetic flux contribution through another, we have $k_{ij} > 0$. If the contribution is negative, we instead have $k_{ij} < 0$. The numerical value of k_{ij} depends on the placement of the inductors relative to each other.

In the example circuit, there is only one inductor and thus no mutual inductance, which means that $\boldsymbol{L} = (L_r, 0, 0, 0, 0)^T$, which multiplied to $\boldsymbol{\Phi}$ gives Eq. (A.20b).

Note that all the rows and columns belonging to components not on the inductor subgraph are zero. By removing these zero rows and columns, we get a $N_L \times N_L$ matrix $\boldsymbol{L}'$, where N_L is the number of inductors. We can then rewrite Eq. (A.22) as

$$\boldsymbol{L}'\boldsymbol{I}'_L = \boldsymbol{\Phi}'_L, \tag{A.23}$$

where $\boldsymbol{I}'_L$ and $\boldsymbol{\Phi}'_L$ are the corresponding vectors found by removing all the noninductor entries of the full-size vectors $\boldsymbol{I}$ and $\boldsymbol{\Phi}$. In our example this becomes a single equation $L_r\Phi_1 = I_1$

The magnetic field energy stored in the inductors is

$$0 \leq E_L = \frac{1}{2}\boldsymbol{I}_L'^T\boldsymbol{L}'\boldsymbol{I}'_L, \tag{A.24}$$

which means that $\boldsymbol{L}'$ must be positive semi-definite. We further assume $\boldsymbol{L}'$ is positive definite, meaning that $0 < \boldsymbol{I}_L'^T\boldsymbol{L}'\boldsymbol{I}'_L$ for $\boldsymbol{I}'_L \neq 0$. This assumption is also physically sensible since any current through the inductors must store at least some magnetic field energy in a realistic configuration. It also ensures that the symmetric $\boldsymbol{L}'$ matrix is invertible, and we can write

$$\boldsymbol{I}'_L = \boldsymbol{L}'^{-1}\boldsymbol{\Phi}'_L. \tag{A.25}$$

We can expand the matrix $\boldsymbol{L}'^{-1}$ to work on the full flux vector by inserting zeros on the noninductor columns and rows. Similarly, we also build the corresponding full inductor current vector $\boldsymbol{I}_L$. The resulting equation can be written

$$\boldsymbol{I}_L = \boldsymbol{L}^+\boldsymbol{\Phi}, \tag{A.26}$$

where $\boldsymbol{L}^+$ is the matrix found by expanding $\boldsymbol{L}'^{-1}$ with the zero-columns and rows of the noninductor components. Formally, $\boldsymbol{L}^+$ is the Moore-Penrose pseudo-inverse [370] of the original full inductance matrix $\boldsymbol{L}$.

For our example we can easily invert $\boldsymbol{L}' = \begin{bmatrix} L_r \end{bmatrix}$ in order to find the psuedo-inverse $\boldsymbol{L}^+ = \mathrm{diag}(1/L_r, 0, 0, 0, 0)$, which fulfill Eq. (A.26).

Now we only need to include the current through the Josephson junctions, which follows from the Josephson relation

$$\boldsymbol{I}_J = \boldsymbol{D}_J \mathbf{sin}\boldsymbol{\Phi}, \tag{A.27}$$

where $\boldsymbol{D}_J$ is a diagonal matrix with the Josephson critical currents on the diagonal, see Eq. (1.11) for the case of a single Josephson junction. As with $\boldsymbol{L}$ and $\boldsymbol{C}$, all other components than Josephson junction are counted as having zero critical currents. The vector $\mathbf{sin}\boldsymbol{\Phi} = (\sin\Phi_1, \ldots, \sin\Phi_B)^T$ is understood as the vector of sines of the branch fluxes.

We have only one Josephson junction in the example circuit in Fig. A.1 which means that $\mathbf{sin}\boldsymbol{\Phi} = (0,0,0,0,\sin\Phi_5)^T$ and $\boldsymbol{D}_J = \mathrm{diag}(0,0,0,0,I_c)$, where $I_c = 1/L_J$ in our notation, see Section 1.1.2. Multiplying these two gives Eq. (A.20c).

Thus, the current through each branch can be written as a function of the branch flux and its derivatives as seen in Eqs. (A.21), (A.26), and (A.27), and Kirchhoff's current law thus gives a set of coupled second-order differential equations

$$\begin{aligned}\mathbf{0} &= \boldsymbol{F}^{(C)}\boldsymbol{I} = \boldsymbol{F}^{(C)}\left[\boldsymbol{I}_C + \boldsymbol{I}_L + \boldsymbol{I}_J\right] \\ &= \boldsymbol{M}\ddot{\boldsymbol{\Phi}}_t + \dot{\boldsymbol{Q}}_0 + \boldsymbol{K}\boldsymbol{\Phi}_t + \boldsymbol{I}_0 + \boldsymbol{F}^{(C)}\boldsymbol{D}_J\mathbf{sin}\left((\boldsymbol{F}^{(C)})^T\boldsymbol{\Phi}_t + \begin{bmatrix}\mathbf{0}\\ \tilde{\boldsymbol{\Phi}}\end{bmatrix}\right),\end{aligned} \tag{A.28}$$

where we define the "mass" and "spring constant" matrices (analogous to in Section 1.2.5)

$$\boldsymbol{M} = \boldsymbol{F}^{(C)}\boldsymbol{D}_{\boldsymbol{C}}(\boldsymbol{F}^{(C)})^T, \tag{A.29a}$$

$$\boldsymbol{K} = \boldsymbol{F}^{(C)}\boldsymbol{L}^{+}(\boldsymbol{F}^{(C)})^T, \tag{A.29b}$$

and the offset charges and flux induced currents

$$\boldsymbol{Q}_0 = \boldsymbol{F}^{(C)}\boldsymbol{D}_C\begin{bmatrix}\mathbf{0}\\ \dot{\tilde{\boldsymbol{\Phi}}}\end{bmatrix}, \tag{A.30a}$$

$$\boldsymbol{I}_0 = \boldsymbol{F}^{(C)}\boldsymbol{L}^{+}\begin{bmatrix}\mathbf{0}\\ \tilde{\boldsymbol{\Phi}}\end{bmatrix}. \tag{A.30b}$$

Note that these matrices are different from the capacitive and inductive matrices presented in Section 1.2.3.

Consider again the example circuit in Fig. A.1. The "mass" and "spring constant" matrices are in this case

$$\boldsymbol{M} = \begin{bmatrix}C_c + C_r & -C_c\\ -C_c & C_c + C_s\end{bmatrix}, \tag{A.31a}$$

$$\boldsymbol{K} = \begin{bmatrix}1/L_r & 0\\ 0 & 0\end{bmatrix}. \tag{A.31b}$$

Note how these are identical to how we constructed the capacitance matrix and the inductor matrix in Section 1.2.3, respectively. Thus we have derived how to formulate the capacitance and inductive matrices from the main text.

The offset charges and flux induces currents are

$$\boldsymbol{Q}_0 = \begin{bmatrix}C_r\dot{\tilde{\boldsymbol{\Phi}}}_1 - C_c\dot{\tilde{\boldsymbol{\Phi}}}_2\\ C_c\dot{\tilde{\boldsymbol{\Phi}}}_2\end{bmatrix}, \tag{A.32a}$$

$$\boldsymbol{I}_0 = \begin{bmatrix}0\\ 0\end{bmatrix}. \tag{A.32b}$$

The offset charges $\boldsymbol{Q}_0$ disappear if we assume the external fluxes to be time-independent. The offset flux induced currents are zero since no linear inductors are links, meaning that we have chosen no external fluxes over the linear inductors.

The final term of Eq. (A.28) reduces to

$$\boldsymbol{F}^{(C)}\boldsymbol{D}_J\mathbf{sin}\boldsymbol{\Phi} = \begin{bmatrix} 0 \\ I_c \sin(\Phi_2 + \tilde{\Phi}_3) \end{bmatrix}, \tag{A.33}$$

where we can move the external flux into the offset charges by choosing a spanning tree over the Josephson junction instead.

A.2.3 Voltage and current sources

Until now, we have assumed that external fluxes are our only control parameters, but we can also add current and voltage sources. Voltage sources can be added in series with existing components without introducing new constraints on the branch fluxes. This effectively transforms the external flux vector

$$\tilde{\boldsymbol{\Phi}}(t) \to \tilde{\boldsymbol{\Phi}}(t) - \int_{-\infty}^{t} \boldsymbol{V}_V(t')\,\mathrm{d}t', \tag{A.34}$$

where $(\boldsymbol{V}_V)_i$ is the voltage generated by the source on the ith branch, or 0 if the ith branch is not a voltage source, i.e., defined analogously to Eq. (A.19).

Similarly, we can add a current source in parallel with an existing element without introducing additional constraints on the free currents. This modifies $\boldsymbol{I}_0$ according to

$$\boldsymbol{I}_0 \to \boldsymbol{I}_0 + \boldsymbol{F}^{(C)}\boldsymbol{I}_B, \tag{A.35}$$

where $\boldsymbol{I}_B$ is the bias current vector with zeros on all entries except those belonging to a branch with a current source, where instead it has the applied current, i.e., as in Eq. (A.19a).

A.2.4 Lagrangian and Hamiltonian

One can show, using Eq. (1.27), that a Lagrangian fulfilling the equations of motion in Eq. (A.28) is

$$\begin{aligned} \mathcal{L} = \frac{1}{2}\dot{\boldsymbol{\Phi}}_t^T \boldsymbol{M}\dot{\boldsymbol{\Phi}}_t + \boldsymbol{Q}_0 \cdot \dot{\boldsymbol{\Phi}}_t - \frac{1}{2}\boldsymbol{\Phi}_t^T \boldsymbol{K}\boldsymbol{\Phi}_t - \boldsymbol{I}_0 \cdot \boldsymbol{\Phi}_t \\ + \boldsymbol{J}_C \cdot \mathbf{cos}\left((\boldsymbol{F}^{(C)})^T \boldsymbol{\Phi}_t + \begin{bmatrix} \mathbf{0} \\ \tilde{\boldsymbol{\Phi}} \end{bmatrix} \right), \end{aligned} \tag{A.36}$$

where we define the critical current vector

$$(\boldsymbol{J}_C)_i = (\boldsymbol{D}_J)_{ii}. \tag{A.37}$$

The conjugate momenta of the twig branches are then given by

$$\boldsymbol{Q}_t = \frac{\partial \mathcal{L}}{\partial \dot{\boldsymbol{\Phi}}_t} = \boldsymbol{M}\dot{\boldsymbol{\Phi}}_t + \boldsymbol{Q}_0, \tag{A.38}$$

and the Hamiltonian can be found performing a Legendre transformation

$$\begin{aligned}\mathcal{H} &= \boldsymbol{Q}_t \cdot \dot{\Phi}_t - \mathcal{L} \\ &= \frac{1}{2}\left(\boldsymbol{Q}_t - \boldsymbol{Q}_0\right)^T \boldsymbol{M}^{-1}\left(\boldsymbol{Q}_t - \boldsymbol{Q}_0\right) + \frac{1}{2}\boldsymbol{\Phi}_t^T \boldsymbol{K}\boldsymbol{\Phi}_t + \boldsymbol{I}_0 \cdot \boldsymbol{\Phi}_t \\ &\quad - \boldsymbol{J}_C \cdot \mathbf{cos}\left(\left(\boldsymbol{F}^{(C)}\right)^T \boldsymbol{\Phi}_t + \begin{bmatrix}\mathbf{0} \\ \tilde{\boldsymbol{\Phi}}\end{bmatrix}\right).\end{aligned} \tag{A.39}$$

This Hamiltonian can easily be quantized using the approach presented in Section 1.3.1, where this time the canonical variables are the branch fluxes Φ_b and Q_b of the twigs, with the commutator relation in Eq. (1.47).

APPENDIX B

Realistic Parameters for the *i*Toffoli Gate

*This appendix is quoted from [**V**] with minor changes to fit the context of this thesis.*

In this appendix to Chapter 2 we present parameters for the circuit model in Fig. 2.4(c), which yields the desired gate model of Fig. 2.4(a), i.e., a two-bit *i*Toffoli gate. The parameters are found by calculating the gate model parameters in Eq. (2.29) and then minimizing a cost function that returns a low value when the requirements of the gate model are met. The minimization is done using a simplex method, with randomized starting points, since many solutions exist. To judge the quality of the circuit parameters, we also calculate the relative anharmonicity of the two-level systems, i.e., the difference between the 01 and the 12 transitions and the ratio between the effective Josephson energy and the effective capacitive energy.

In order to simplify the numerical investigation, we have assumed that the parameters of the control qubits are identical. The parameters obtained are presented in Table B.1. As expected, we see that the capacitance of the coupling $C_{z,i}$ should be low compared to the other couplings as we wish to operate in the weak coupling regime. We note that we get Ising couplings in the range $|J^z| \in [25, 320]$ and in all cases dominating the cross-coupling J^x_{ij}. The swapping couplings J^x_i are all several factors lower than the detunings $\Delta_{i0} = |\Omega_i - \Omega_0|$.

We simulate all of the gates in Table B.1 and find that all result in a maximum fidelity above 0.99 when the driving is $\Omega = J^z_i/8$. The average fidelity as a function of time can be seen in Fig. B.1.

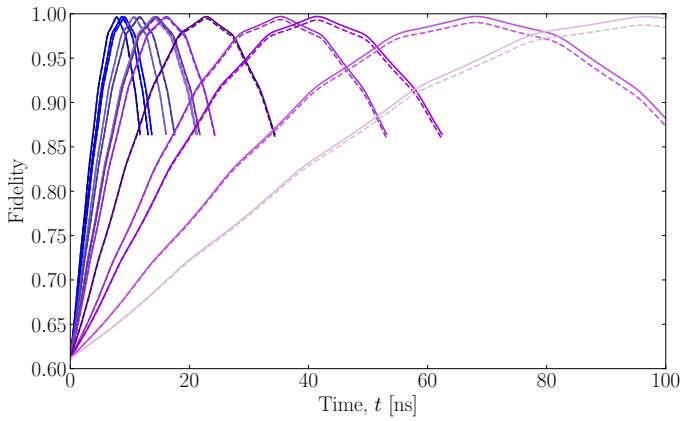

Figure B.1: *Average fidelity as a function of time for all the gate configurations presented in Table B.1. All simulations are done at a driving frequency of $\Omega = J^z/8$. The fidelity is expected to peak at $T = \pi/2\Omega$ The solid lines are simulations without decoherence, while the dashed line includes decoherence. The gate with the lowest gate time corresponds to gate #1 in Table B.1 and so forth. The color of the lines also corresponds to the colors in Table B.1.*

Table B.1: *Circuit and corresponding gate model parameters for possible Toffoli gates. Since the circuit parameter space is rather large, we have several possible solutions; some, but far from all, possible solutions are shown in the table. The different solutions are labeled and color-coded in the first column. The color coding corresponds to the simulation results seen in Fig. B.1. Column 2-7 show the circuit parameters for the circuit in Fig. 2.4(c). Here E_0, E_i, and $E_{z,i}$ indicate the Josephson junction of the target qubit, the control qubits, and the coupling between them, respectively; C_0, C_i, and $C_{z,i}$ indicate the capacitance of the target qubit, the control qubits and the coupling between them, respectively. Column 8-12 shows the obtained gate parameters, which can be seen in Eq. (2.29). Columns 13-16 show the quality parameters of the gate: α_0 and α_i are the anharmonicities of the target and control qubits, respectively, while E_0^J/E_0^C and E_i^J/E_i^C are the ratios between the effective Josephson energy and effective capacitive energy. The subscript i indicates $i = 1, 2$, i.e., the control qubits.*

	Circuit parameters						Gate parameters					Quality parameters			
#	E_0 [2πGHz]	E_i [2πGHz]	$E_{z,i}$ [2πGHz]	C_0 [fF]	C_i [fF]	$C_{z,i}$ [fF]	ω_0 [2πGHz]	ω_i [2πGHz]	J_i^z [2πMHz]	J_i^x [2πMHz]	J_{ij}^x [2πMHz]	α_0 [%]	α_i [%]	E_0^J/E_0^C	E_i^J/E_i^C
1	20.05	1.26	33.28	15.83	37.84	0.04	30.9	12.8	−320.1	452.6	27.8	−2.0	−2.0	71.1	67.5
2	0.61	0.02	29.30	22.19	44.89	0.03	21.9	10.8	−287.2	5.7	14.9	−2.0	−2.0	68.0	68.0
3	33.65	1.27	28.70	15.37	43.40	0.03	32.0	11.1	−274.0	453.3	22.5	−2.0	−2.0	72.6	67.2
4	31.29	0.71	24.10	16.96	53.10	0.03	28.4	9.2	−233.0	254.9	16.7	−2.0	−2.0	69.9	68.0
5	4.95	1.20	21.94	27.06	57.03	0.05	17.9	8.5	−214.0	433.7	15.0	−2.0	−2.0	68.5	68.2
6	1.58	1.27	17.14	41.71	56.41	0.09	12.5	7.6	−177.1	474.8	14.6	−1.9	−2.2	77.5	53.7
7	39.72	0.11	18.27	17.83	71.69	0.03	26.9	6.8	−176.0	38.3	9.8	−2.0	−2.0	70.4	68.0
8	0.56	0.03	17.53	35.36	77.67	0.08	13.4	6.4	−172.2	12.4	13.1	−2.0	−2.0	65.3	70.5
9	45.01	1.22	16.13	17.72	76.22	0.02	27.1	6.4	−154.6	437.1	7.8	−2.0	−2.0	70.9	68.3
10	19.87	1.22	11.35	31.88	105.46	0.04	15.1	4.6	−109.1	437.3	4.8	−2.0	−2.0	70.2	68.4
11	57.40	1.25	7.45	19.24	153.26	0.01	24.9	3.2	−70.6	444.1	1.7	−2.0	−2.0	71.9	68.8
12	23.81	0.80	6.30	37.75	187.62	0.02	12.7	2.6	−60.1	287.2	1.0	−2.0	−2.0	71.0	68.9
13	58.41	0.09	3.85	21.01	338.06	0.00	22.7	1.4	−36.6	31.3	0.0	−2.0	−2.0	71.7	68.7
14	0.01	0.19	2.50	299.11	386.88	0.37	1.7	1.1	−25.8	71.1	1.3	−1.9	−2.2	77.5	53.7

APPENDIX C

Realistic Parameters for the Controlled *i*SWAP Gate

*This appendix is quoted from **[VI]** with minor changes to fit the context of this thesis.*

In this appendix to Chapter 3 we present parameters for the circuit model in Fig. 3.3(c), which yields the desired gate model of Fig. 3.3(a). The parameters are found by calculating the gate model parameters presented in Section 3.2 and then minimizing a cost function that returns a low value when the requirements of the gate model are met. The minimization is done using a simplex method, with randomized starting points, since many solutions exist. To judge the quality of the circuit parameters, we also calculate the relative anharmonicity of the two-level systems, i.e., the difference between the 01 and the 12 transitions and the ratio between the effective Josephson energy and the effective capacitive energy.

The circuit parameters obtained are presented in Table C.1 and corresponding gate parameters can be seen in Table C.2. In Table C.3 we present quality parameters (anharmonicities, and effective Josephson junction and effective capacitance ratios) for the corresponding models. The parentheses in Tables C.2 and C.3 indicates the error on the parameters, when assuming fabrication error on the circuit parameters in Table C.1. The errors are found using Monte Carlo simulations, where circuit parameters are drawn from a normal distribution centered around the experimental values presented in Table C.1, with one standard deviation corresponding to a 5% error in the gate parameter. This corresponds to 95% of the drawn samples being within a 10% error. The resulting errors in Tables C.2 and C.3 corresponds one standard deviation.

Note that while it might look problematic that exchange coupling, J^x, is not significantly lower than the longitudinal coupling, J^z, this is not the case as the coupling of the gate is due to the first or second-order term in Eq. (3.25b). This means that we can lower the exchange coupling to a desirable level when operating the gate. It is, however, important that J^x is significantly lower than the detuning of the target qubit, which is indeed the case in all cases.

Note that all qubits have an anharmonicity above 2%, sufficient to suppress higher-order transitions in the anharmonic oscillator. We also note that the ratio between effective Josephson energy and effective capacitance is above 70, which is sufficient in order to

Table C.1: *Circuit parameters for implementing possible controlled i*SWAP *gates. Since the circuit parameter space is rather large we have several possible solutions; some, but far from all, possible solutions are show in the table. Here E_1, E_{T1}, E_{T2}, E_{TB}, and $E_{z,i}$ indicate the Josephson junction of the control qubit, target qubits, the tunable bus qubit, and the coupling between the target qubit and the control qubit, respectively; C_1, C_{T1}, C_{T2}, C_{TB}, C_z, and C_x indicate the capacitance of the control qubit, the target qubits, and the couplings between them, respectively. Corresponding gate parameters can be seen in Table C.2.*

#	E_1 [2πGHz]	E_{T1} [2πGHz]	E_{T2} [2πGHz]	E_{TB} [2πGHz]	$E_{z,1}$ [2πGHz]	C_1 [fF]	C_{T1} [fF]	C_{T2} [fF]	C_{TB} [fF]	C_z [fF]	C_x [fF]
1	44.22	12.63	11.44	0.41	14.70	1.00	1.00	68.32	100.00	54.26	27.16
2	24.88	21.28	53.12	1.46	9.18	41.84	31.47	12.39	27.92	6.74	7.46
3	8.10	33.93	44.86	5.09	58.93	16.63	16.93	29.69	8.35	10.01	1.00
4	0.09	0.01	13.27	0.41	33.39	8.28	19.38	36.98	99.30	60.64	35.75
5	32.32	20.14	35.10	0.51	24.50	4.80	1.00	1.00	82.82	79.21	20.58
6	20.48	0.01	17.14	1.03	50.65	1.01	23.85	61.90	39.50	45.53	10.27
7	52.99	45.93	29.78	1.04	6.44	8.21	3.06	27.90	39.54	70.97	9.79
8	29.58	7.72	21.40	0.71	28.64	26.54	32.89	33.37	56.54	1.00	16.55
9	9.50	26.92	31.10	2.90	8.08	72.77	37.09	30.97	12.31	49.03	7.34
10	10.77	10.58	17.51	1.59	16.70	56.66	7.18	61.71	23.92	52.22	10.16

Table C.2: *Gate model parameters for implementing possible controlled i*SWAP *gates corresponding to the circuit parameters in Table C.1. Since the circuit parameter space is rather large, we have several possible solutions; some, but far from all, possible solutions are shown in the table. Column 1-4 shows the dressed qubit frequencies. Column 5 and 6 shows the couplings seen in Eq.* (3.21) *and Eq.* (3.23b)*. The parentheses indicate the error in the parameters when assuming a fabrication error of 10% on the circuit parameters in Table C.1.*

#	ω_1 [2πGHz]	ω_{T1} [2πGHz]	ω_{TB} [2πGHz]	ω_{T2} [2πGHz]	J^z [2πMHz]	J^x [2πMHz]
1	16.61(43)	7.21(20)	1.08(4)	3.98(12)	$-90.7(52)$	8.2(8)
2	9.63(26)	8.90(37)	3.82(13)	17.65(52)	$-55.6(34)$	20.7(22)
3	16.37(50)	18.56(43)	13.37(46)	14.85(51)	$-299.6(107)$	27.3(193)
4	8.45(31)	4.82(18)	1.06(4)	4.51(12)	$-148.9(41)$	11.8(10)
5	14.66(32)	10.13(26)	1.34(5)	11.54(40)	$-123.9(63)$	11.1(9)
6	17.69(47)	10.28(1109)	2.70(9)	5.82(22)	$-252.8(73)$	14.3(16)
7	18.51(46)	15.92(45)	2.73(9)	10.18(25)	$-41.1(29)$	13.6(13)
8	15.84(55)	7.09(18)	1.88(6)	7.30(20)	$-141.6(59)$	12.2(13)
9	4.71(14)	2.90(281)	7.62(22)	10.64(35)	$-35.6(19)$	16.7(1107)
10	6.07(18)	7.41(18)	4.19(12)	5.87(20)	$-93.5(39)$	47.3(75)

suppress significant charge noise [80].

Table C.3: *Quality parameters for implementing possible controlled i*SWAP *gates corresponding to the circuit parameters in Table C.1. α are the relative anharmonicities of the qubits, while E^J/E^C are the ratios between the effective Josephson energy and effective capacitive energy. The parentheses indicate the error in the parameters when assuming a fabrication error of 10% on the circuit parameters in Table C.1.*

#	α_1 [%]	α_{T1} [%]	α_{TB} [%]	α_{T2} [%]	E_1^J/E_1^C	E_{T1}^J/E_{T1}^C	E_{TB}^J/E_{TB}^C	E_{T2}^J/E_{T2}^C
1	$-2.1(1)$	$-2.5(1)$	$-2.1(1)$	$-2.0(1)$	85.1(40)	77.1(45)	73.6(49)	71.4(39)
2	$-2.1(1)$	$-2.1(1)$	$-2.1(1)$	$-2.0(1)$	83.9(45)	81.4(39)	74.3(49)	73.7(39)
3	$-2.6(1)$	$-2.1(1)$	$-2.1(1)$	$-2.1(1)$	80.2(47)	120.6(62)	74.3(51)	73.3(46)
4	$-2.6(1)$	$-2.1(1)$	$-2.0(1)$	$-2.0(1)$	76.4(43)	164.4(103)	74.4(49)	72.4(39)
5	$-2.1(1)$	$-2.1(1)$	$-2.0(1)$	$-2.0(1)$	93.3(41)	104.9(57)	74.7(51)	74.3(45)
6	$-2.3(1)$	$-2.1(3)$	$-2.0(1)$	$-2.0(1)$	85.7(39)	117.1(70)	74.4(50)	72.4(42)
7	$-2.1(1)$	$-2.1(1)$	$-2.1(1)$	$-2.0(1)$	76.9(37)	79.6(38)	73.9(50)	72.1(39)
8	$-2.2(1)$	$-2.1(1)$	$-2.1(1)$	$-2.0(1)$	82.7(50)	123.6(67)	73.9(48)	72.2(39)
9	$-2.1(1)$	$-4.2(7)$	$-2.0(1)$	$-2.0(1)$	88.7(48)	144.9(71)	74.5(46)	71.9(40)
10	$-2.1(1)$	$-2.4(1)$	$-2.1(1)$	$-2.0(1)$	105.4(57)	75.7(34)	74.3(47)	73.3(42)

APPENDIX D

Realistic Parameters for the Linear Controlled Swapping Gate

*This appendix is quoted from **[III]** with minor changes to fit the context of this thesis.*

In this appendix to Chapter 4 we present parameters for the circuit model in Fig. 4.1(b), which yields the desired gate model of Fig. 4.1(a), i.e., linear controlled swapping gate. The parameters are found by calculating the gate model parameters and then minimizing a cost function which returns a low value when the requirements of the gate model are met. The minimization is done using a simplex method, with randomized starting points, since many solutions exist. In order to judge the quality of the circuit parameters, we also calculate the relative anharmonicity, α_r, (see Eq. (1.76)) of the two-level systems and couplings to higher-lying states $K^x_{2,3}$ and $M^x_{2,3}$. The parameters obtained are presented in Table D.1.

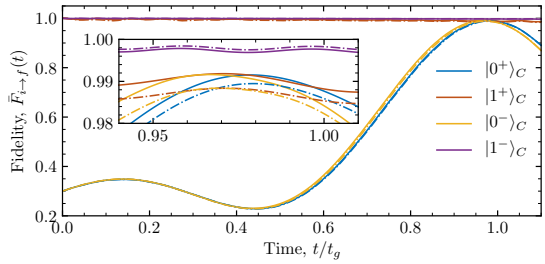

Figure D.1: *Average fidelity of the system with realistic parameters (row 6 of Table D.1) as a function of time. The simulations are done both for perfect control qubits (solid lines), i.e., perfect two-level systems, and for realistic control qubits, i.e., approximate two-level systems where the third level is included (dashed-dotted lines). The $|0^{\pm}\rangle_C$ indicates the choice of detuning $\delta_{\pm}$ and thus for which gates in Eq.* (4.2) *the simulation is done. The inset shows a zoom of the peak of the average fidelity in the open configuration $|0\rangle_C$, i.e., around $t \sim t_g$.*

Table D.1: *Circuit and corresponding spin model parameters. The parameters are found by minimizing a cost function which returns a low value when the spin parameters obey the requirement from the main text. The rather large parameter space (8 circuit parameters) yields several solutions to this, and some (but far from all) are shown below. Above the single line shows the case of $\delta_+ = 2(J_2^z + J_2^x)$, while below the line shows the case $\delta_- = 2(J_2^z - J_2^x)$. These numbers are shown in column $\delta_\pm$ and should be compared with the actual detuning, $\omega_2 - \omega_1$, identical for all cases. The circuit parameters can be seen in Fig. 4.1. The colored lines (numbers 6 and 11) corresponds to the parameters used in the simulation shown in Fig. D.1.*

	Circuit parameters								Spin model parameters							Second excited state			
#	E_1 [2πGHz]	E_2 [2πGHz]	$E_{1,2}$ [2πGHz]	$E_{2,3}$ [2πGHz]	C_1 [fF]	C_2 [fF]	$C_{2,3}$ [fF]	$L_{1,2}$ [nH]	ω_1 [2πGHz]	ω_2 [2πGHz]	J_1^x [2πMHz]	J_1^z [2πMHz]	J_2^x [2πMHz]	J_2^z [2πMHz]	$\delta_\pm$ [2πMHz]	$\alpha_r^{(1)}$ [%]	$\alpha_r^{(2)}$ [%]	$K_{2,3}^x$ [2πMHz]	$M_{2,3}^x$ [2πMHz]
1	532.0	464.1	187.9	410.4	729.4	65.6	279.4	36.7	10.7	11.3	42.0	42.0	−494.6	804.1	619.0	0.16	4.66	2680.3	−536.1
2	119.2	179.6	86.8	165.5	956.6	332.9	440.2	81.2	4.4	3.8	43.2	43.2	−764.3	453.7	−621.1	0.13	10.48	1512.5	−302.5
3	215.4	219.4	100.5	200.6	907.9	223.6	23.8	70.9	6.1	6.7	47.3	46.9	−552.1	844.6	585.0	0.19	10.28	2815.4	−563.1
4	310.2	371.2	74.9	272.4	183.5	25.8	649.2	93.9	16.1	19.2	44.9	44.9	962.1	562.8	3049.7	0.51	0.52	1876.0	−375.2
5	690.3	486.3	169.0	393.8	466.5	48.7	391.9	40.4	15.1	14.2	33.3	33.2	−987.4	498.0	−978.9	0.21	1.37	1660.0	−332.0
6	561.6	438.5	186.0	397.1	926.3	76.2	240.4	37.3	9.7	10.7	40.9	40.9	−540.4	1007.1	933.4	0.15	6.88	3357.1	−671.4
7	379.3	254.1	90.3	220.9	850.3	48.2	84.0	79.1	8.3	12.1	35.5	35.5	764.2	1107.6	3743.7	0.21	4.74	3692.0	−738.4
8	699.7	601.5	230.9	517.1	664.2	62.5	507.3	29.4	12.8	12.6	35.7	35.7	−696.6	582.7	−227.7	0.16	2.63	1942.3	−388.5
9	156.9	192.3	80.7	181.9	950.5	734.8	839.6	89.9	5.1	5.8	51.7	51.7	727.6	1081.2	707.2	0.21	14.39	3604.1	−720.8
10	699.8	611.2	236.7	547.7	676.7	64.1	185.7	29.0	12.7	12.9	45.4	45.4	857.1	965.2	216.1	0.15	4.73	3217.3	−643.5
11	313.1	199.6	78.3	185.2	994.4	152.6	302.3	92.1	7.0	7.4	34.7	34.7	936.2	1137.7	403.0	0.21	10.57	3792.2	−758.4
12	144.6	177.9	72.0	167.2	965.4	619.3	20.0	98.8	4.8	4.2	38.1	38.1	980.3	641.8	−677.1	0.22	11.29	2139.2	−427.8
13	113.3	277.9	118.7	264.2	987.7	706.6	583.2	58.8	4.3	3.6	51.9	51.9	852.9	538.2	−629.5	0.02	11.81	1793.9	−358.8
14	167.1	251.7	104.2	238.1	978.3	381.5	999.8	67.6	5.2	4.7	45.4	45.4	965.8	724.8	−482.0	0.15	11.73	2415.9	−483.2
15	178.4	352.0	144.2	324.9	953.8	230.0	488.4	47.7	5.4	5.0	41.4	41.4	661.6	446.5	−430.4	0.08	6.46	1488.2	−297.6
16	132.9	272.4	112.1	255.5	970.5	418.1	408.4	61.9	4.6	3.7	41.5	41.5	882.6	438.3	−888.5	0.07	8.73	1461.1	−292.2

We simulate the gate with the parameters of row 6 in Table B.1 and find that all result in a maximum fidelity above 0.99, when the driving is $\omega = J_i^z/8$. The average fidelity as a function of time can be seen in Fig. D.1. We simulate both perfect qubits and realistic qubits where we include the third state with the given anharmonicity. From the simulation, we see that the optimal gate time is just before t_g and that the inclusion of the third excited state does not change the fidelity significantly.

Appendix E

Additional Results for Entangling Gates in VQE

This appendix presents some additional results from the simulations discussed in Section 6.5.

Besides the results presented in Section 6.5 for H_2 and the full XXX Heisenberg model, we here present similar results for LiH (Fig. E.1), the pure swap model (Fig. E.2) and the transverse-field Ising model (Fig. E.3) with six qubits. The results in this appendix are consistent with the conclusion of the main text.

For LiH in Fig. E.1, we observe that the parameterized gates perform just as well

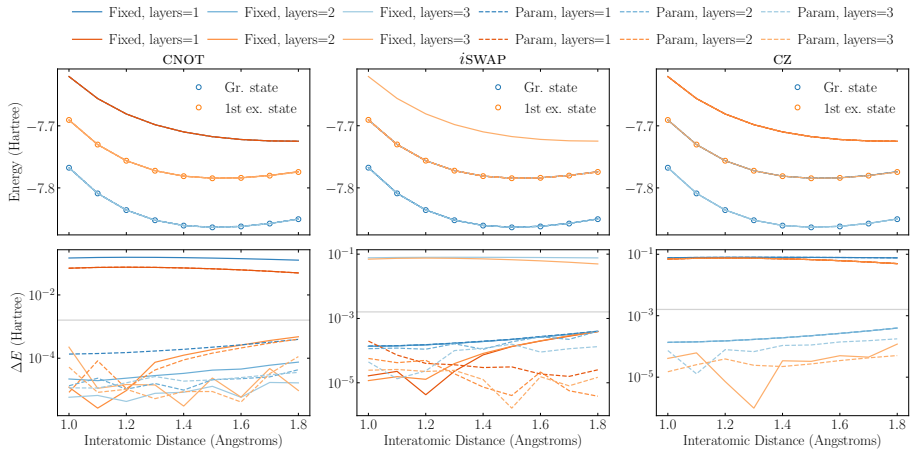

Figure E.1: *Potential energy surface for LiH calculated using SSVQE for the two lowest states. The title of each column indicates which entangling gate is used in the calculation, either fixed (solid line) or parameterized (dashed lines). In the top row, we show the calculated energy, and in the bottom row, we show the energy difference, ΔE, between the classical and VQE calculations. Lighter colors indicate that more layers are used in the simulation. The gray line indicates chemical accuracy at* 0.0016 *Hartree. The results shown here are the best out of 100 samples.*

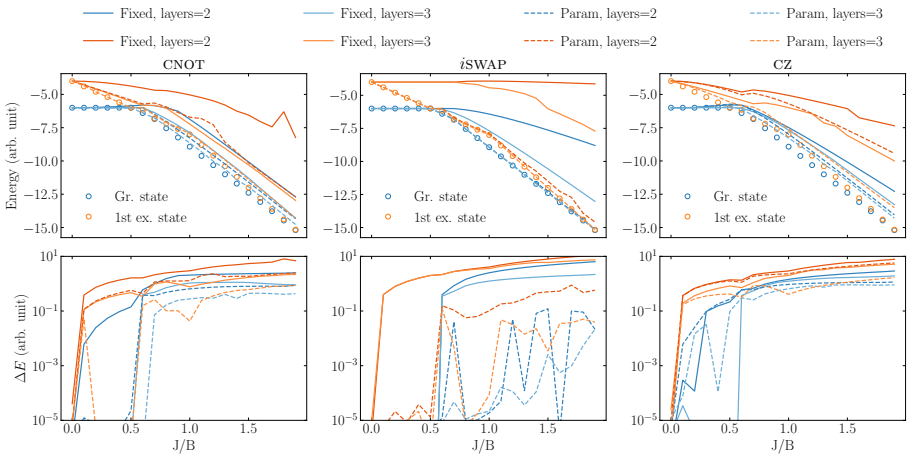

Figure E.2: *Potential energy surface for the pure swap Heisenberg model in Eq.* (6.8) *with six qubits calculated using SSVQE for the two lowest states. The title of each column indicates which entangling gate is used in the calculation, either fixed (solid line) or parameterized (dashed lines). In the top row, we show the calculated energy, and in the bottom row, we show the energy difference, ΔE, between the classical and VQE calculations. Lighter colors indicate that more layers are used in the simulation. The results shown here are the best out of 100 samples.*

or better than all the fixed gates. We also note that for the CNOT and CZ gate, the one layer PQC is having trouble finding the correct states. However, for the *i*SWAP gate, it is the three-layer fixed PQC that has the most trouble finding the correct state. This is quite peculiar and is probably due to some optimization difficulties. Nonetheless, the parameterized three-layer PQC performs quite well. Note that the third energy curve found by the SSVQE is probably the second excited state of LiH, i.e., the triplet state found in Fig. 6.1(b).

In Fig. E.2 we show results for simulations of the pure swap Heisenberg model, i.e., $J = J_x = J_y$ and $J_z = 0$ in Eq. (6.8), for six qubits. The simulation agrees with the conclusion for the full XXX Heisenberg model, i.e., the parameterized gates outperform the fixed gates. For both the CNOT and *i*SWAP gate, we see that the parameterized gate performs better than the fixed gates, even with fewer layers. The CZ gate, on the other hand, does not perform that well in the parameterized version.

In Fig. E.3 we show results for simulations of the transverse-field Ising model in Eq. (6.9). Again, the simulations are consistent with the previous conclusion. The main text results for four, six, and ten qubit yields the same conclusions but are omitted here.

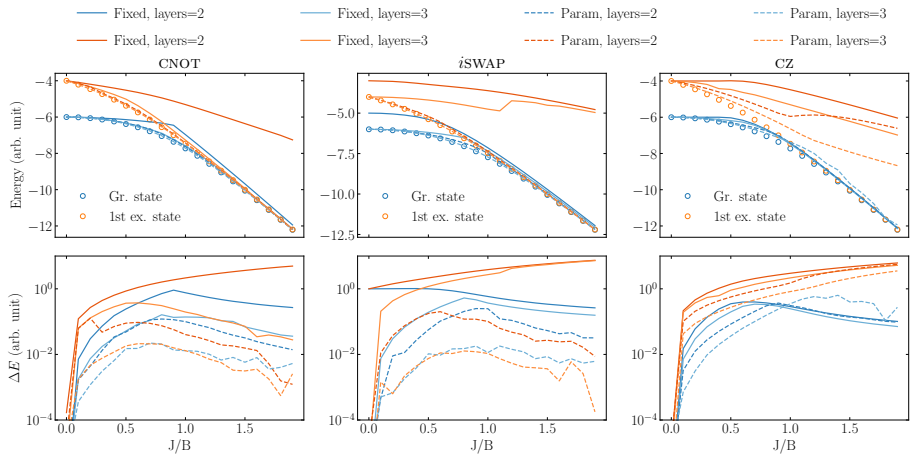

Figure E.3: *Potential energy surface for the transverse-field Ising model in Eq.* (6.9) *with six qubits calculated using SSVQE for the two lowest states. The title of each column indicates which entangling gate is used in the calculation, either fixed (solid line) or parameterized (dashed lines). In the top row, we show the calculated energy, and in the bottom row, we show the energy difference, ΔE, between the classical and VQE calculations. Lighter colors indicate that more layers are used in the simulation. The results shown here are the best out of 100 samples.*

APPENDIX F

Additional Results for Approximating VQE states using EQ-GAN

This appendix presents some additional results from the simulations discussed in Section 7.4.

In Fig. F.1 and Fig. F.2 we present the result of EQ-GAN simulations trying to learn the eigenstates o LiH and BeH_2, respectively, using the VQE results as data. The figures should be compared to Fig. 7.6 of the main text, and it is clear that the conclusion is the same. We obtain quite a good fidelity, especially for the adversarial training; however, the energies are not nearly as good as the VQE result.

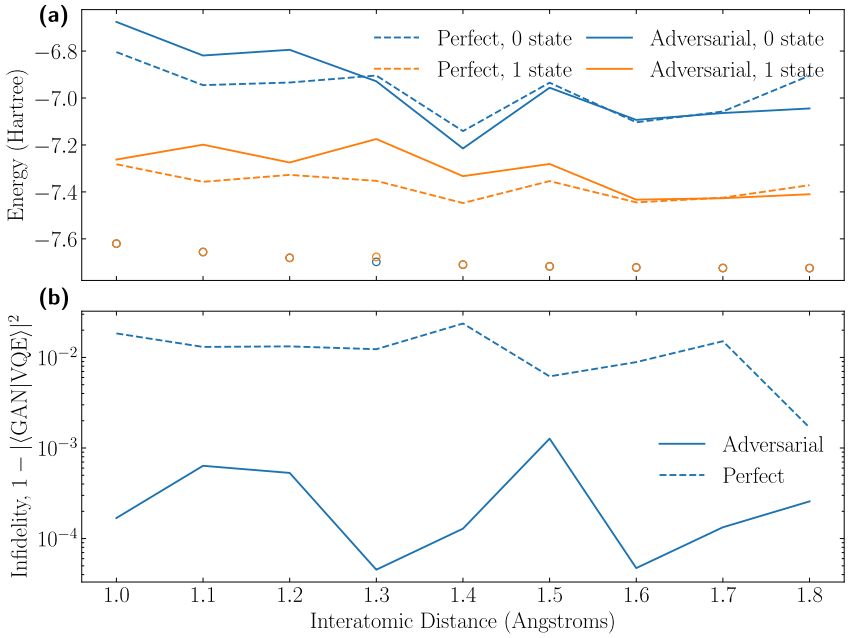

Figure F.1: *Results of the EQ-GAN learning on VQE data for LiH with one layer of Fig. 6.4.* **(a)** *Predicted energy of the EQ-GAN algorithm (lines) and SSVQE (circles). Solid lines indicates the adversarial swap test was used, while the dashed line indicate that the perfect swap test was used.* **(b)** *Infidelity of the state generated by the EQ-GAN,* $|\text{GAN}\rangle = G(\boldsymbol{\theta})\,|0\rangle$*, with the state generated by the VQE,* $|\text{VQE}\rangle = \hat{U}(\boldsymbol{\theta}_{\text{VQE}})\,|0\rangle$.

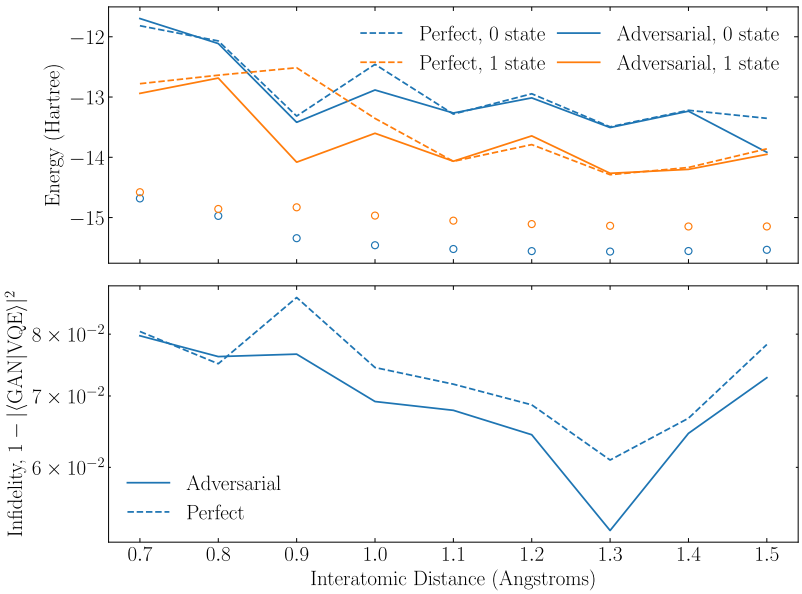

Figure F.2: *Results of the EQ-GAN learning on VQE data for BeH_2 with three layers of Fig. 6.4 but with* iSWAP *gates instead of* CNOT *gates.* **(a)** *Predicted energy of the EQ-GAN algorithm (lines) and SSVQE (circles). Solid lines indicates the adversarial swap test was used, while the dashed line indicate that the perfect swap test was used.* **(b)** *Infidelity of the state generated by the EQ-GAN, $|\mathrm{GAN}\rangle = G(\boldsymbol{\theta})\,|0\rangle$, with the state generated by the VQE, $|\mathrm{VQE}\rangle = \hat{\mathcal{U}}(\boldsymbol{\theta}_{\mathrm{VQE}})\,|0\rangle$.*

Bibliography

[1] Erwin Schödinger. *What is Life?* Cambridge, UK: Cambridge University Press, 1944.

[2] J. I. Cirac and P. Zoller. "Quantum Computations with Cold Trapped Ions". *Phys. Rev. Lett.* **74** (20 1995), 4091–4094.

[3] D. Leibfried, R. Blatt, C. Monroe, and D. Wineland. "Quantum dynamics of single trapped ions". *Rev. Mod. Phys.* **75** (1 2003), 281–324.

[4] D. Porras and J. I. Cirac. "Effective Quantum Spin Systems with Trapped Ions". *Phys. Rev. Lett.* **92** (20 2004), 207901.

[5] Rainer Blatt and David Wineland. "Entangled states of trapped atomic ions". *Nature* **453**.7198 (2008), 1008–1015. ISSN: 1476-4687.

[6] H. Häffner, C.F. Roos, and R. Blatt. "Quantum computing with trapped ions". *Physics Reports* **469**.4 (2008), 155–203. ISSN: 0370-1573.

[7] R. Blatt and C. F. Roos. "Quantum simulations with trapped ions". *Nature Physics* **8**.4 (2012), 277–284. ISSN: 1745-2481.

[8] D. Jaksch and P. Zoller. "The cold atom Hubbard toolbox". *Annals of Physics* **315**.1 (2005). Special Issue, 52–79. ISSN: 0003-4916.

[9] Maciej Lewenstein, Anna Sanpera, Veronica Ahufinger, Bogdan Damski, Aditi Sen(De), and Ujjwal Sen. "Ultracold atomic gases in optical lattices: mimicking condensed matter physics and beyond". *Advances in Physics* **56**.2 (2007), 243–379.

[10] Immanuel Bloch, Jean Dalibard, and Wilhelm Zwerger. "Many-body physics with ultracold gases". *Rev. Mod. Phys.* **80** (3 2008), 885–964.

[11] Christian Gross and Immanuel Bloch. "Quantum simulations with ultracold atoms in optical lattices". *Science* **357**.6355 (2017), 995–1001. ISSN: 0036-8075.

[12] Florian Schäfer, Takeshi Fukuhara, Seiji Sugawa, Yosuke Takasu, and Yoshiro Takahashi. "Tools for quantum simulation with ultracold atoms in optical lattices". *Nature Reviews Physics* **2**.8 (2020), 411–425. ISSN: 2522-5820.

[13] Daniel Loss and David P. DiVincenzo. "Quantum computation with quantum dots". *Phys. Rev. A* **57** (1 1998), 120–126.

[14] B. E. Kane. "A silicon-based nuclear spin quantum computer". *Nature* **393**.6681 (1998), 133–137. ISSN: 1476-4687.

[15] Rogerio de Sousa, J. D. Delgado, and S. Das Sarma. "Silicon quantum computation based on magnetic dipolar coupling". *Phys. Rev. A* **70** (5 2004), 052304.

[16] Rutger Vrijen et al. "Electron-spin-resonance transistors for quantum computing in silicon-germanium heterostructures". *Phys. Rev. A* **62** (1 2000), 012306.

[17] L. C. L. Hollenberg, A. D. Greentree, A. G. Fowler, and C. J. Wellard. "Two-dimensional architectures for donor-based quantum computing". *Phys. Rev. B* **74** (4 2006), 045311.

[18] Andrea Morello et al. "Single-shot readout of an electron spin in silicon". *Nature* **467**.7316 (2010), 687–691. ISSN: 1476-4687.

[19] A. Imamoglu, D. D. Awschalom, G. Burkard, D. P. DiVincenzo, D. Loss, M. Sherwin, and A. Small. "Quantum Information Processing Using Quantum Dot Spins and Cavity QED". *Phys. Rev. Lett.* **83** (20 1999), 4204–4207.

[20] Dirk Englund et al. "Controlling the Spontaneous Emission Rate of Single Quantum Dots in a Two-Dimensional Photonic Crystal". *Phys. Rev. Lett.* **95** (1 2005), 013904.

[21] J. R. Petta et al. "Coherent Manipulation of Coupled Electron Spins in Semiconductor Quantum Dots". *Science* **309**.5744 (2005), 2180–2184. ISSN: 0036-8075.

[22] R. Hanson, L. P. Kouwenhoven, J. R. Petta, S. Tarucha, and L. M. K. Vandersypen. "Spins in few-electron quantum dots". *Rev. Mod. Phys.* **79** (4 2007), 1217–1265.

[23] Floris A. Zwanenburg et al. "Silicon quantum electronics". *Rev. Mod. Phys.* **85** (3 2013), 961–1019.

[24] M. V. Gurudev Dutt et al. "Quantum Register Based on Individual Electronic and Nuclear Spin Qubits in Diamond". *Science* **316**.5829 (2007), 1312–1316. ISSN: 0036-8075.

[25] R. Hanson, O. Gywat, and D. D. Awschalom. "Room-temperature manipulation and decoherence of a single spin in diamond". *Phys. Rev. B* **74** (16 2006), 161203.

[26] E. Knill, R. Laflamme, and G. J. Milburn. "A scheme for efficient quantum computation with linear optics". *Nature* **409**.6816 (2001), 46–52. ISSN: 1476-4687.

[27] T. B. Pittman, B. C. Jacobs, and J. D. Franson. "Probabilistic quantum logic operations using polarizing beam splitters". *Phys. Rev. A* **64** (6 2001), 062311.

[28] J. D. Franson, M. M. Donegan, M. J. Fitch, B. C. Jacobs, and T. B. Pittman. "High-Fidelity Quantum Logic Operations Using Linear Optical Elements". *Phys. Rev. Lett.* **89** (13 2002), 137901.

[29] T. B. Pittman, M. J. Fitch, B. C Jacobs, and J. D. Franson. "Experimental controlled-NOT logic gate for single photons in the coincidence basis". *Phys. Rev. A* **68** (3 2003), 032316.

[30] F. Yan et al. "The flux qubit revisited to enhance coherence and reproducibility". *Nature Communications* **7**.12964 (2016).

[31] R. Barends et al. "Coherent Josephson Qubit Suitable for Scalable Quantum Integrated Circuits". *Phys. Rev. Lett.* **111** (8 2013), 080502.

[32] William D. Oliver and Paul B. Welander. "Materials in superconducting quantum bits". *MRS Bulletin* **38**.10 (2013), 816–825.

[33] A V Shcherbakova et al. "Fabrication and measurements of hybrid Nb/Al Josephson junctions and flux qubits withπ-shifters". *Superconductor Science and Technology* **28**.2 (2015), 025009.

[34] I. Tsioutsios et al. "Free-standing silicon shadow masks for transmon qubit fabrication". *AIP Advances* **10**.6 (2020), 065120.

[35] A.O Caldeira and A.J Leggett. "Quantum tunnelling in a dissipative system". *Annals of Physics* **149**.2 (1983), 374–456. ISSN: 0003-4916.

[36] Anthony J. Leggett. "Quantum mechanics at the macroscopic level". In: *Directions in Condensed Matter Physics*. Berlin: World Scientific, 1989, 187–248.

[37] Uri Vool and Michel Devoret. "Introduction to quantum electromagnetic circuits". *International Journal of Circuit Theory and Applications* **45**.7 (2017), 897–934.

[38] J. Q. You and F. Nori. "Superconducting Circuits and Quantum Information". *Physics Today* **58**.11 (2005), 42.

[39] Iulia Buluta and Franco Nori. "Quantum Simulators". *Science* **326**.5949 (2009), 108–111. ISSN: 0036-8075.

[40] Iulia Buluta, Sahel Ashhab, and Franco Nori. "Natural and artificial atoms for quantum computation". *Reports on Progress in Physics* **74**.10 (2011), 104401.

[41] J. Q. You and Franco Nori. "Atomic physics and quantum optics using superconducting circuits". *Nature* **474**.7353 (2011), 589–597. ISSN: 1476-4687.

[42] I. M. Georgescu, S. Ashhab, and Franco Nori. "Quantum simulation". *Rev. Mod. Phys.* **86** (1 2014), 153–185.

[43] T. Bækkegaard, L. B. Kristensen, N. J. S. Loft, C. K. Andersen, D. Petrosyan, and N. T. Zinner. "Realization of efficient quantum gates with a superconducting qubit-qutrit circuit". *Scientific Reports* **9**.1 (2019), 13389. ISSN: 2045-2322.

[44] S. Poletto et al. "Entanglement of Two Superconducting Qubits in a Waveguide Cavity via Monochromatic Two-Photon Excitation". *Phys. Rev. Lett.* **109** (24 2012), 240505.

[45] L. DiCarlo et al. "Preparation and measurement of three-qubit entanglement in a superconducting circuit". *Nature* **467**.7315 (2010), 574–578. ISSN: 1476-4687.

[46] M. H. Devoret. "Quantum fluctuations in electrical circuits". In: *Les Houches Session LXIII*. Oxford University Press, 1997.

[47] M. H. Devoret, A. Wallraff, and J. M. Martinis. "Superconducting Qubits: A Short Review". arXiv:cond-mat/0411174. 2004.

[48] Guido Burkard, Roger H. Koch, and David P. DiVincenzo. "Multilevel quantum description of decoherence in superconducting qubits". *Phys. Rev. B* **69** (6 2004), 064503.

[49] R. J. Schoelkopf and S. M. Girvin. "Wiring up quantum systems". *Nature* **451**.7179 (2008), 664–669. ISSN: 1476-4687.

[50] John Clarke and Frank K. Wilhelm. "Superconducting quantum bits". *Nature* **453**.7198 (2008), 1031–1042. ISSN: 1476-4687.

[51] S. M. Girvin. "Circuit QED: Superconducting Qubits Coupled to Microwave Photons". *Quantum Machines: Measurement and Control of Engineered Quantum Systems – Lecture Notes of the Les Houches Summer School* **96** (2014).

[52] Jay M. Gambetta, Jerry M. Chow, and Matthias Steffen. "Building logical qubits in a superconducting quantum computing system". *npj Quantum Information* **3**.1 (2017), 2. ISSN: 2056-6387.

[53] G Wendin. "Quantum information processing with superconducting circuits: a review". *Reports on Progress in Physics* **80**.10 (2017), 106001.

[54] Xiu Gu, Anton Frisk Kockum, Adam Miranowicz, Yu-xi Liu, and Franco Nori. "Microwave photonics with superconducting quantum circuits". *Physics Reports* **718-719** (2017). Microwave photonics with superconducting quantum circuits, 1–102. ISSN: 0370-1573.

[55] P. Krantz, M. Kjaergaard, F. Yan, T. P. Orlando, S. Gustavsson, and W. D. Oliver. "A quantum engineer's guide to superconducting qubits". *Applied Physics Reviews* **6**.2 (2019), 021318.

[56] Yvonne Y. Gao, M. Adriaan Rol, Steven Touzard, and Chen Wang. "Practical Guide for Building Superconducting Quantum Devices". *PRX Quantum* **2** (4 2021), 040202.

[57] D. J. Griffiths. *Introduction to Electrodynamics*. Boston: Pearson, 1981.

[58] A. O. Caldeira and A. J. Leggett. "Influence of Dissipation on Quantum Tunneling in Macroscopic Systems". *Phys. Rev. Lett.* **46** (4 1981), 211–214.

[59] J. C. Gallop. *SQUIDs, the Josephson Effect, and Superconducting Electronics*. New York: Taylor and Francis Group, 1991.

[60] L. N. Cooper. "Bound Electron Pairs in a Degenerate Fermi Gas". *Phys. Rev.* **104** (4 1956), 1189–1190.

[61] B.D. Josephson. "Possible new effects in superconductive tunnelling". *Physics Letters* **1**.7 (1962), 251–253. ISSN: 0031-9163.

[62] B. D. Josephson. "The discovery of tunnelling supercurrents". *Proceedings of the IEEE* **62**.6 (1974), 838–841.

[63] A. Barone and G. Paterno. *Physics and Applications of the Josephson Effect*. A Wiley-interscience publication. New York: Wiley, 1982. ISBN: 9780471014690.

[64] R. C. Jaklevic, John Lambe, A. H. Silver, and J. E. Mercereau. "Quantum Interference Effects in Josephson Tunneling". *Phys. Rev. Lett.* **12** (7 1964), 159–160.

[65] Bascom S. Deaver and William M. Fairbank. "Experimental Evidence for Quantized Flux in Superconducting Cylinders". *Phys. Rev. Lett.* **7** (2 1961), 43–46.

[66] R. Doll and M. Näbauer. "Experimental Proof of Magnetic Flux Quantization in a Superconducting Ring". *Phys. Rev. Lett.* **7** (2 1961), 51–52.

[67] Matti Hämäläinen, Riitta Hari, Risto J. Ilmoniemi, Jukka Knuutila, and Olli V. Lounasmaa. "Magnetoencephalography—theory, instrumentation, and applications to noninvasive studies of the working human brain". *Rev. Mod. Phys.* **65** (2 1993), 413–497.

[68] Cosimo Del Gratta, Vittorio Pizzella, Franca Tecchio, and Gian Luca Romani. "Magnetoencephalography - a noninvasive brain imaging method with 1 ms time resolution". *Reports on Progress in Physics* **64**.12 (2001), 1759–1814.

[69] D. Koelle, R. Kleiner, F. Ludwig, E. Dantsker, and John Clarke. "High-transition-temperature superconducting quantum interference devices". *Rev. Mod. Phys.* **71** (3 1999), 631–686.

[70] R. Kleiner, D. Koelle, F. Ludwig, and J. Clarke. "Superconducting quantum interference devices: State of the art and applications". *Proceedings of the IEEE* **92**.10 (2004), 1534–1548.

[71] Michel H. Devoret, John M. Martinis, and John Clarke. "Measurements of Macroscopic Quantum Tunneling out of the Zero-Voltage State of a Current-Biased Josephson Junction". *Phys. Rev. Lett.* **55** (18 1985), 1908–1911.

[72] Xinyuan You, J. A. Sauls, and Jens Koch. "Circuit quantization in the presence of time-dependent external flux". *Phys. Rev. B* **99** (17 2019), 174512.

[73] Roman-Pascal Riwar and David P. DiVincenzo. "Circuit quantization with time-dependent magnetic fields for realistic geometries". arXiv:2103.03577. 2021.

[74] John R. Taylor. *Classical Mechanics*. U.S.A.: University Science Books, 2005.

[75] Paul Dirac. *The Priciples of Quantum Mechanics*. 4th. UK: Oxford University Press, 1967.

[76] J. J. Sakurai and J. J. Napolitano. *Modern Quantum Mechanics*. 2nd. USA: Pearson, 2011.

[77] L. Allen and J. H. Eberly. *Optical Resonance and TwoLevel Atoms*. New York: Dover Publications, 1987.

[78] B. H. Bransden and C. J. Joachain. *Physics of Atoms and Molecules*. 2nd. Essex: Prentice Hall, 2003.

[79] Omar Gamel and Daniel F. V. James. "Time-averaged quantum dynamics and the validity of the effective Hamiltonian model". *Phys. Rev. A* **82** (5 2010), 052106.

[80] Jens Koch et al. "Charge-insensitive qubit design derived from the Cooper pair box". *Phys. Rev. A* **76** (4 2007), 042319.

[81] Simon E. Nigg et al. "Black-Box Superconducting Circuit Quantization". *Phys. Rev. Lett.* **108** (24 2012), 240502.

[82] Firat Solgun, David W. Abraham, and David P. DiVincenzo. "Blackbox quantization of superconducting circuits using exact impedance synthesis". *Phys. Rev. B* **90** (13 2014), 134504.

[83] Firat Solgun and David P. DiVincenzo. "Multiport impedance quantization". *Annals of Physics* **361** (2015), 605–669. ISSN: 0003-4916.

[84] Benjamin P. Lanyon et al. "Simplifying quantum logic using higher-dimensional Hilbert spaces". *Nature Physics* **5**.2 (2009), 134–140. ISSN: 1745-2481.

[85] A. Fedorov, L. Steffen, M. Baur, M. P. da Silva, and A. Wallraff. "Implementation of a Toffoli gate with superconducting circuits". *Nature* **481**.7380 (2012), 170–172. ISSN: 1476-4687.

[86] Niels Jakob Søe Loft et al. "Quantum interference device for controlled two-qubit operations". *npj Quantum Information* **6**.1 (2020), 47. ISSN: 2056-6387.

[87] M. A. Nielsen and I. L. Chuang. *Quantum Computation and Quantum Information*. Cambridge, UK: Cambridge University Press, 2010.

[88] Erik Lucero et al. "High-Fidelity Gates in a Single Josephson Qubit". *Phys. Rev. Lett.* **100** (24 2008), 247001.

[89] J. M. Chow et al. "Randomized Benchmarking and Process Tomography for Gate Errors in a Solid-State Qubit". *Phys. Rev. Lett.* **102** (9 2009), 090502.

[90] F. Motzoi, J. M. Gambetta, P. Rebentrost, and F. K. Wilhelm. "Simple Pulses for Elimination of Leakage in Weakly Nonlinear Qubits". *Phys. Rev. Lett.* **103** (11 2009), 110501.

[91] Erik Lucero et al. "Reduced phase error through optimized control of a superconducting qubit". *Phys. Rev. A* **82** (4 2010), 042339.

[92] Blake R Johnson, Marcus P da Silva, Colm A Ryan, Shelby Kimmel, Jerry M Chow, and Thomas A Ohki. "Demonstration of robust quantum gate tomography via randomized benchmarking". *New Journal of Physics* **17**.11 (2015), 113019. ISSN: 1367-2630.

[93] David C. McKay, Christopher J. Wood, Sarah Sheldon, Jerry M. Chow, and Jay M. Gambetta. "Efficient Z gates for quantum computing". *Phys. Rev. A* **96** (2 2017), 022330.

[94] J. M. Gambetta, F. Motzoi, S. T. Merkel, and F. K. Wilhelm. "Analytic control methods for high-fidelity unitary operations in a weakly nonlinear oscillator". *Phys. Rev. A* **83** (1 2011), 012308.

[95] Frederick W. Strauch, Philip R. Johnson, Alex J. Dragt, C. J. Lobb, J. R. Anderson, and F. C. Wellstood. "Quantum Logic Gates for Coupled Superconducting Phase Qubits". *Phys. Rev. Lett.* **91** (16 2003), 167005.

[96] David P. DiVincenzo. "The Physical Implementation of Quantum Computation". *Fortschritte der Physik* **48** (2000), 771–783.

[97] Alexandre Blais, Alexander Maassen van den Brink, and Alexandre M. Zagoskin. "Tunable Coupling of Superconducting Qubits". *Phys. Rev. Lett.* **90** (12 2003), 127901.

[98] E.T. Jaynes and F.W. Cummings. "Comparison of quantum and semiclassical radiation theories with application to the beam maser". *Proceedings of the IEEE* **51**.1 (1963), 89–109.

[99] Bruce W. Shore and Peter L. Knight. "The Jaynes-Cummings Model". *Journal of Modern Optics* **40**.7 (1993), 1195–1238.

[100] Christopher C. Gerry and Peter L. Knight. *Introductory Quantum Optics*. Cambridge, England: Cambridge University Press, 2005.

[101] A. Wallraff et al. "Strong coupling of a single photon to a superconducting qubit using circuit quantum electrodynamics". *Nature* **431**.7005 (2004), 162–167. ISSN: 1476-4687.

[102] L. Frunzio, A. Wallraff, D. Schuster, J. Majer, and R. Schoelkopf. "Fabrication and characterization of superconducting circuit QED devices for quantum computation". *IEEE Transactions on Applied Superconductivity* **15**.2 (2005), 860–863.

[103] A. Wallraff et al. "Sideband Transitions and Two-Tone Spectroscopy of a Superconducting Qubit Strongly Coupled to an On-Chip Cavity". *Phys. Rev. Lett.* **99** (5 2007), 050501.

[104] P. J. Leek et al. "Observation of Berry's Phase in a Solid-State Qubit". *Science* **318**.5858 (2007), 1889–1892. ISSN: 0036-8075.

[105] J. M. Fink, M. Göppl, M. Baur, R. Bianchetti, P. J. Leek, A. Blais, and A. Wallraff. "Climbing the Jaynes–Cummings ladder and observing its nonlinearity in a cavity QED system". *Nature* **454**.7202 (2008), 315–318. ISSN: 1476-4687.

[106] M. D. Reed, L. DiCarlo, B. R. Johnson, L. Sun, D. I. Schuster, L. Frunzio, and R. J. Schoelkopf. "High-Fidelity Readout in Circuit Quantum Electrodynamics Using the Jaynes-Cummings Nonlinearity". *Phys. Rev. Lett.* **105** (17 2010), 173601.

[107] Andrew J. Kerman. "Quantum information processing using quasiclassical electromagnetic interactions between qubits and electrical resonators". *New Journal of Physics* **15** (2013), 123011.

[108] Daniel Sank et al. "Measurement-Induced State Transitions in a Superconducting Qubit: Beyond the Rotating Wave Approximation". *Phys. Rev. Lett.* **117** (19 2016), 190503.

[109] Alexandre Blais, Steven M. Girvin, and William D. Oliver. "Quantum information processing and quantum optics with circuit quantum electrodynamics". *Nature Physics* **16**.3 (2020), 247–256. ISSN: 1745-2481.

[110] Alexandre Blais, Ren-Shou Huang, Andreas Wallraff, S. M. Girvin, and R. J. Schoelkopf. "Cavity quantum electrodynamics for superconducting electrical circuits: An architecture for quantum computation". *Phys. Rev. A* **69** (6 2004), 062320.

[111] A. Wallraff et al. "Approaching Unit Visibility for Control of a Superconducting Qubit with Dispersive Readout". *Phys. Rev. Lett.* **95** (6 2005), 060501.

[112] Maxime Boissonneault, J. M. Gambetta, and Alexandre Blais. "Dispersive regime of circuit QED: Photon-dependent qubit dephasing and relaxation rates". *Phys. Rev. A* **79** (1 2009), 013819.

[113] Sergey Bravyi, David P. DiVincenzo, and Daniel Loss. "Schrieffer–Wolff transformation for quantum many-body systems". *Annals of Physics* **326**.10 (2011), 2793–2826. ISSN: 0003-4916.

[114] D. I. Schuster et al. "ac Stark Shift and Dephasing of a Superconducting Qubit Strongly Coupled to a Cavity Field". *Phys. Rev. Lett.* **94** (12 2005), 123602.

[115] Jay Gambetta et al. "Qubit-photon interactions in a cavity: Measurement-induced dephasing and number splitting". *Phys. Rev. A* **74** (4 2006), 042318.

[116] D. I. Schuster et al. "Resolving photon number states in a superconducting circuit". *Nature* **445**.7127 (2007), 515–518. ISSN: 1476-4687.

[117] Chad Rigetti et al. "Superconducting qubit in a waveguide cavity with a coherence time approaching 0.1 ms". *Phys. Rev. B* **86** (10 2012), 100506(R).

[118] A. P. Sears et al. "Photon shot noise dephasing in the strong-dispersive limit of circuit QED". *Phys. Rev. B* **86** (18 2012), 180504(R).

[119] Gengyan Zhang, Yanbing Liu, James J. Raftery, and Andrew A. Houck. "Suppression of photon shot noise dephasing in a tunable coupling superconducting qubit". *npj Quantum Information* **3**.1 (2017), 1. ISSN: 2056-6387.

[120] Fei Yan et al. "Distinguishing Coherent and Thermal Photon Noise in a Circuit Quantum Electrodynamical System". *Phys. Rev. Lett.* **120** (26 2018), 260504.

[121] Howard M. Wiseman and Gerard J. Milburn. *Quantum Measurement and Control*. Cambridge: Cambridge University Press, 2009.

[122] Alexandre Blais, Jay Gambetta, A. Wallraff, D. I. Schuster, S. M. Girvin, M. H. Devoret, and R. J. Schoelkopf. "Quantum-information processing with circuit quantum electrodynamics". *Phys. Rev. A* **75** (3 2007), 032329.

[123] J. Majer et al. "Coupling superconducting qubits via a cavity bus". *Nature* **449**.7161 (2007), 443–447. ISSN: 1476-4687.

[124] Jonathan R. Friedman and D. V. Averin. "Aharonov-Casher-Effect Suppression of Macroscopic Tunneling of Magnetic Flux". *Phys. Rev. Lett.* **88** (5 2002), 050403.

[125] M. W. Johnson et al. "Quantum annealing with manufactured spins". *Nature* **473**.7346 (2011), 194–198. ISSN: 1476-4687.

[126] J. Q. You, Y. Nakamura, and Franco Nori. "Fast two-bit operations in inductively coupled flux qubits". *Phys. Rev. B* **71** (2 2005), 024532.

[127] M. Grajcar, Yu-xi Liu, Franco Nori, and A. M. Zagoskin. "Switchable resonant coupling of flux qubits". *Phys. Rev. B* **74** (17 2006), 172505.

[128] A. O. Niskanen, K. Harrabi, F. Yoshihara, Y. Nakamura, S. Lloyd, and J. S. Tsai. "Quantum Coherent Tunable Coupling of Superconducting Qubits". *Science* **316**.5825 (2007), 723–726.

[129] S. Ashhab et al. "Interqubit coupling mediated by a high-excitation-energy quantum object". *Phys. Rev. B* **77** (1 2008), 014510.

[130] Hanhee Paik et al. "Experimental Demonstration of a Resonator-Induced Phase Gate in a Multiqubit Circuit-QED System". *Phys. Rev. Lett.* **117** (25 2016), 250502.

[131] H.-P. Breuer and F. Peruccione. *The theory of open quantum systems*. New York, NY, US: Oxford University Press, 2002.

[132] Roald K. Wangsness. "Sublattice Effects in Magnetic Resonance". *Phys. Rev.* **91** (5 1953), 1085–1091.

[133] F. Bloch. "Generalized Theory of Relaxation". *Phys. Rev.* **105** (4 1957), 1206–1222.

[134] A.G. Redfield. "The Theory of Relaxation Processes". In: *Advances in Magnetic Resonance*. Ed. by John S. Waugh. **1**. Advances in Magnetic and Optical Resonance. Academic Press, 1965, 1–32.

[135] X. Y. Jin et al. "Thermal and Residual Excited-State Population in a 3D Transmon Qubit". *Phys. Rev. Lett.* **114** (24 2015), 240501.

[136] N. Wiener. "Generalized Harmonic Analysis". *Acta Mathematica* **55** (1930), 117–258.

[137] D. C. Champeney. *A handbook of Fourier theorems*. Cambridge: Cambridge University Press, 1987.

[138] C. P. Slichter. *Principles of Magnetic Resonance*. 3rd. Berlin: Springer, 1990.

[139] Norman F. Ramsey. "A Molecular Beam Resonance Method with Separated Oscillating Fields". *Phys. Rev.* **78** (6 1950), 695–699.

[140] Zijun Chen. "Metrology of Quantum Control and Measurement in Superconducting Qubits". PhD thesis. Santa Barbara: University of California, 2018.

[141] Jonas Bylander et al. "Noise spectroscopy through dynamical decoupling with a superconducting flux qubit". *Nature Physics* **7**.7 (2011), 565–570. ISSN: 1745-2481.

[142] G. Ithier et al. "Decoherence in a superconducting quantum bit circuit". *Phys. Rev. B* **72** (13 2005), 134519.

[143] Daniel Manzano. "A short introduction to the Lindblad master equation". *AIP Advances* **10**.2 (2020), 025106.

[144] J.R. Johansson, P.D. Nation, and Franco Nori. "QuTiP 2: A Python framework for the dynamics of open quantum systems". *Computer Physics Communications* **184**.4 (2013), 1234–1240. ISSN: 0010-4655.

[145] John M. Martinis, Michel H. Devoret, and John Clarke. "Energy-Level Quantization in the Zero-Voltage State of a Current-Biased Josephson Junction". *Phys. Rev. Lett.* **55** (15 1985), 1543–1546.

[146] Alexander Shnirman, Gerd Schön, and Ziv Hermon. "Quantum Manipulations of Small Josephson Junctions". *Phys. Rev. Lett.* **79** (12 1997), 2371–2374.

[147] V. Bouchiat, D. Vion, P. Joyez, D. Esteve, and M. H. Devoret. "Quantum coherence with a single Cooper pair". *Physica Scripta* **1998**.T76 (1998), 165.

[148] Y. Nakamura, Yu. A. Pashkin, and J. S. Tsai. "Coherent control of macroscopic quantum states in a single-Cooper-pair box". *Nature* **398**.6730 (1999), 786–788. ISSN: 1476-4687.

[149] Josef Meixner, Friedrich W. Schäfke, and Gerhard Wolf. *Mathieu Functions and Spheroidal Functions and Their Mathematical Foundations*. Germany: Springer, 1980.

[150] Yuriy Makhlin, Gerd Schön, and Alexander Shnirman. "Quantum-state engineering with Josephson-junction devices". *Rev. Mod. Phys.* **73** (2 2001), 357–400.

[151] J. A. Schreier et al. "Suppressing charge noise decoherence in superconducting charge qubits". *Phys. Rev. B* **77** (18 2008), 180502.

[152] R. Barends et al. “Superconducting quantum circuits at the surface code threshold for fault tolerance”. *Nature* **508**.7497 (2014), 500–503. ISSN: 1476-4687.

[153] J. Kelly et al. “State preservation by repetitive error detection in a superconducting quantum circuit”. *Nature* **519**.7541 (2015), 66–69. ISSN: 1476-4687.

[154] R. Barends et al. “Digital quantum simulation of fermionic models with a superconducting circuit”. *Nature Communications* **6**.1 (2015), 7654. ISSN: 2041-1723.

[155] R. Barends et al. “Digitized adiabatic quantum computing with a superconducting circuit”. *Nature* **534**.7606 (2016), 222–226. ISSN: 1476-4687.

[156] Hanhee Paik et al. “Observation of High Coherence in Josephson Junction Qubits Measured in a Three-Dimensional Circuit QED Architecture”. *Phys. Rev. Lett.* **107** (24 2011), 240501.

[157] T. W. Larsen, K. D. Petersson, F. Kuemmeth, T. S. Jespersen, P. Krogstrup, J. Nygård, and C. M. Marcus. “Semiconductor-Nanowire-Based Superconducting Qubit”. *Phys. Rev. Lett.* **115** (12 2015), 127001.

[158] L. Casparis et al. “Gatemon Benchmarking and Two-Qubit Operations”. *Phys. Rev. Lett.* **116** (15 2016), 150505.

[159] Christian Kraglund Andersen et al. “Repeated quantum error detection in a surface code”. *Nature Physics* **16**.8 (2020), 875–880. ISSN: 1745-2481.

[160] Ivan V. Pechenezhskiy, Raymond A. Mencia, Long B. Nguyen, Yen-Hsiang Lin, and Vladimir E. Manucharyan. “The superconducting quasicharge qubit”. *Nature* **585**.7825 (2020), 368–371. ISSN: 1476-4687.

[161] T. P. Orlando, J. E. Mooij, Lin Tian, Caspar H. van der Wal, L. S. Levitov, Seth Lloyd, and J. J. Mazo. “Superconducting persistent-current qubit”. *Phys. Rev. B* **60** (22 1999), 15398–15413.

[162] J. E. Mooij, T. P. Orlando, L. Levitov, Lin Tian, Caspar H. van der Wal, and Seth Lloyd. “Josephson Persistent-Current Qubit”. *Science* **285**.5430 (1999), 1036–1039.

[163] J. Q. You, X. Hu, S. Ashhab, and F. Nori. “Low-decoherence flux qubit”. *Phys. Rev. B* **75** (14 2007), 140515.

[164] M. Stern et al. “Flux Qubits with Long Coherence Times for Hybrid Quantum Circuits”. *Phys. Rev. Lett.* **113** (12 2014), 123601.

[165] J.-L. Orgiazzi et al. “Flux qubits in a planar circuit quantum electrodynamics architecture: Quantum control and decoherence”. *Phys. Rev. B* **93** (10 2016), 104518.

[166] Vladimir E. Manucharyan, Jens Koch, Leonid I. Glazman, and Michel H. Devoret. “Fluxonium: Single Cooper-Pair Circuit Free of Charge Offsets”. *Science* **326**.5949 (2009), 113–116.

[167] Ioan M. Pop, Kurtis Geerlings, Gianluigi Catelani, Robert J. Schoelkopf, Leonid I. Glazman, and Michel H. Devoret. “Coherent suppression of electromagnetic dissipation due to superconducting quasiparticles”. *Nature* **508**.7496 (2014), 369–372. ISSN: 1476-4687.

[168] Long B. Nguyen, Yen-Hsiang Lin, Aaron Somoroff, Raymond Mencia, Nicholas Grabon, and Vladimir E. Manucharyan. "High-Coherence Fluxonium Qubit". *Phys. Rev. X* **9** (4 2019), 041041.

[169] M. T. Bell, I. A. Sadovskyy, L. B. Ioffe, A. Yu. Kitaev, and M. E. Gershenson. "Quantum Superinductor with Tunable Nonlinearity". *Phys. Rev. Lett.* **109** (13 2012), 137003.

[170] Nicholas A. Masluk, Ioan M. Pop, Archana Kamal, Zlatko K. Minev, and Michel H. Devoret. "Microwave Characterization of Josephson Junction Arrays: Implementing a Low Loss Superinductance". *Phys. Rev. Lett.* **109** (13 2012), 137002.

[171] David Niepce, Jonathan Burnett, and Jonas Bylander. "High Kinetic Inductance NbN Nanowire Superinductors". *Phys. Rev. Applied* **11** (4 2019), 044014.

[172] T. M. Hazard, A. Gyenis, A. Di Paolo, A. T. Asfaw, S. A. Lyon, A. Blais, and A. A. Houck. "Nanowire Superinductance Fluxonium Qubit". *Phys. Rev. Lett.* **122** (1 2019), 010504.

[173] Joel I-Jan Wang and William D. Oliver. "An aluminium superinductor". *Nature Materials* **18**.8 (2019), 775–776. ISSN: 1476-4660.

[174] Lukas Grünhaupt et al. "Granular aluminium as a superconducting material for high-impedance quantum circuits". *Nature Materials* **18**.8 (2019), 816–819. ISSN: 1476-4660.

[175] Aaron Somoroff, Quentin Ficheux, Raymond A. Mencia, Haonan Xiong, Roman V. Kuzmin, and Vladimir E. Manucharyan. "Millisecond coherence in a superconducting qubit". arXiv:2103.08578. 2021.

[176] Giovanni Viola and Gianluigi Catelani. "Collective modes in the fluxonium qubit". *Phys. Rev. B* **92** (22 2015), 224511.

[177] N. E. Frattini, U. Vool, S. Shankar, A. Narla, K. M. Sliwa, and M. H. Devoret. "3-wave mixing Josephson dipole element". *Applied Physics Letters* **110**.22 (2017), 222603.

[178] N. E. Frattini, V. V. Sivak, A. Lingenfelter, S. Shankar, and M. H. Devoret. "Optimizing the Nonlinearity and Dissipation of a SNAIL Parametric Amplifier for Dynamic Range". *Phys. Rev. Applied* **10** (5 2018), 054020.

[179] V.V. Sivak, N.E. Frattini, V.R. Joshi, A. Lingenfelter, S. Shankar, and M.H. Devoret. "Kerr-Free Three-Wave Mixing in Superconducting Quantum Circuits". *Phys. Rev. Applied* **11** (5 2019), 054060.

[180] Benoit Dou çot and Julien Vidal. "Pairing of Cooper Pairs in a Fully Frustrated Josephson-Junction Chain". *Phys. Rev. Lett.* **88** (22 2002), 227005.

[181] L. B. Ioffe and M. V. Feigel'man. "Possible realization of an ideal quantum computer in Josephson junction array". *Phys. Rev. B* **66** (22 2002), 224503.

[182] Alexei Kitaev. "Protected qubit based on a superconducting current mirror". arXiv:cond-mat/0609441. 2006.

[183] Peter Brooks, Alexei Kitaev, and John Preskill. "Protected gates for superconducting qubits". *Phys. Rev. A* **87** (5 2013), 052306.

[184] Peter Groszkowski, A Di Paolo, A L Grimsmo, A Blais, D I Schuster, A A Houck, and Jens Koch. "Coherence properties of the 0-πqubit". *New Journal of Physics* **20**.4 (2018), 043053.

[185] András Gyenis et al. "Experimental Realization of a Protected Superconducting Circuit Derived from the 0–π Qubit". *PRX Quantum* **2** (1 2021), 010339.

[186] Joshua M. Dempster, Bo Fu, David G. Ferguson, D. I. Schuster, and Jens Koch. "Understanding degenerate ground states of a protected quantum circuit in the presence of disorder". *Phys. Rev. B* **90** (9 2014), 094518.

[187] David C. McKay, Stefan Filipp, Antonio Mezzacapo, Easwar Magesan, Jerry M. Chow, and Jay M. Gambetta. "Universal Gate for Fixed-Frequency Qubits via a Tunable Bus". *Phys. Rev. Applied* **6** (6 2016), 064007.

[188] Yinqi Chen, Konstantin N. Nesterov, Vladimir E. Manucharyan, and Maxim G. Vavilov. *Fast Flux Entangling Gate for Fluxonium Circuits*. 2021. arXiv: 2110.00632 [quant-ph].

[189] Charles J. Neill. "A path towards quantum supremacy with superconducting qubits". PhD thesis. Santa Barbara: University of California, 2017.

[190] Fei Yan et al. "Tunable Coupling Scheme for Implementing High-Fidelity Two-Qubit Gates". *Phys. Rev. Applied* **10** (5 2018), 054062.

[191] Youngkyu Sung et al. "Realization of High-Fidelity CZ and ZZ-Free iSWAP Gates with a Tunable Coupler". *Phys. Rev. X* **11** (2 2021), 021058.

[192] X. Li et al. "Tunable Coupler for Realizing a Controlled-Phase Gate with Dynamically Decoupled Regime in a Superconducting Circuit". *Phys. Rev. Applied* **14** (2 2020), 024070.

[193] M. Kounalakis, C. Dickel, A. Bruno, N. K. Langford, and G. A. Steele. "Tuneable hopping and nonlinear cross-Kerr interactions in a high-coherence superconducting circuit". *npj Quantum Information* **4**.1 (2018), 38. ISSN: 2056-6387.

[194] Yu Chen et al. "Qubit Architecture with High Coherence and Fast Tunable Coupling". *Phys. Rev. Lett.* **113** (22 2014), 220502.

[195] Michael R. Geller et al. "Tunable coupler for superconducting Xmon qubits: Perturbative nonlinear model". *Phys. Rev. A* **92** (1 2015), 012320.

[196] P. Roushan et al. "Chiral ground-state currents of interacting photons in a synthetic magnetic field". *Nature Physics* **13**.2 (2016), 146–151. ISSN: 1745-2481.

[197] Brian Vlastakis et al. "Deterministically Encoding Quantum Information Using 100-Photon Schrödinger Cat States". *Science* **342**.6158 (2013), 607–610. ISSN: 0036-8075.

[198] Mazyar Mirrahimi, Zaki Leghtas, Victor V Albert, Steven Touzard, Robert J Schoelkopf, Liang Jiang, and Michel H Devoret. "Dynamically protected cat-qubits: a new paradigm for universal quantum computation". *New Journal of Physics* **16**.4 (2014), 045014. ISSN: 1367-2630.

[199] Nissim Ofek et al. "Extending the lifetime of a quantum bit with error correction in superconducting circuits". *Nature* **536**.7617 (2016), 441–445. ISSN: 1476-4687.

[200] S. Rosenblum, P. Reinhold, M. Mirrahimi, Liang Jiang, L. Frunzio, and R. J. Schoelkopf. "Fault-tolerant detection of a quantum error". *Science* **361**.6399 (2018), 266–270.

[201] Yvonne Y. Gao et al. "Entanglement of bosonic modes through an engineered exchange interaction". *Nature* **566**.7745 (2019), 509–512. ISSN: 1476-4687.

[202] Jeffrey M. Gertler, Brian Baker, Juliang Li, Shruti Shirol, Jens Koch, and Chen Wang. "Protecting a bosonic qubit with autonomous quantum error correction". *Nature* **590**.7845 (2021), 243–248. ISSN: 1476-4687.

[203] Atharv Joshi, Kyungjoo Noh, and Yvonne Y Gao. "Quantum information processing with bosonic qubits in circuit QED". *Quantum Science and Technology* **6**.3 (2021), 033001.

[204] Weizhou Cai, Yuwei Ma, Weiting Wang, Chang-Ling Zou, and Luyan Sun. "Bosonic quantum error correction codes in superconducting quantum circuits". *Fundamental Research* **1**.1 (2021), 50–67. ISSN: 2667-3258.

[205] Shruti Puri, Samuel Boutin, and Alexandre Blais. "Engineering the quantum states of light in a Kerr-nonlinear resonator by two-photon driving". *npj Quantum Information* **3**.1 (2017), 18. ISSN: 2056-6387.

[206] Shruti Puri et al. "Stabilized Cat in a Driven Nonlinear Cavity: A Fault-Tolerant Error Syndrome Detector". *Phys. Rev. X* **9** (4 2019), 041009.

[207] A. Grimm et al. "Stabilization and operation of a Kerr-cat qubit". *Nature* **584**.7820 (2020), 205–209. ISSN: 1476-4687.

[208] Samuel L. Braunstein and Peter van Loock. "Quantum information with continuous variables". *Rev. Mod. Phys.* **77** (2 2005), 513–577.

[209] Hoi-Kwan Lau and Martin B. Plenio. "Universal Quantum Computing with Arbitrary Continuous-Variable Encoding". *Phys. Rev. Lett.* **117** (10 2016), 100501.

[210] Tommaso Toffoli. "Reversible computing". In: *Automata, Languages and Programming*. Ed. by Jaco de Bakker and Jan van Leeuwen. Lecture Notes in Computer Science Vol. 85. Berlin: Springer, 1980, 632–644. ISBN: 978-3-540-39346-7.

[211] D. G. Cory et al. "Experimental Quantum Error Correction". *Phys. Rev. Lett.* **81** (10 1998), 2152–2155.

[212] Philipp Schindler et al. "Experimental Repetitive Quantum Error Correction". *Science* **332**.6033 (2011), 1059–1061. ISSN: 0036-8075.

[213] Eric Dennis. "Toward fault-tolerant quantum computation without concatenation". *Phys. Rev. A* **63** (5 2001), 052314.

[214] Adam Paetznick and Ben W. Reichardt. "Universal Fault-Tolerant Quantum Computation with Only Transversal Gates and Error Correction". *Phys. Rev. Lett.* **111** (9 2013), 090505.

[215] Peter W. Shor. "Scheme for reducing decoherence in quantum computer memory". *Phys. Rev. A* **52** (4 1995), R2493–R2496.

[216] C. J. Ballance, T. P. Harty, N. M. Linke, M. A. Sepiol, and D. M. Lucas. "High-Fidelity Quantum Logic Gates Using Trapped-Ion Hyperfine Qubits". *Phys. Rev. Lett.* **117** (2016), 060504.

[217] J. P. Gaebler et al. "High-Fidelity Universal Gate Set for $^{9}Be^{+}$ Ion Qubits". *Phys. Rev. Lett.* **117** (2016), 060505.

[218] Y.-Y. Jau, A. M. Hankin, T. Keating, I. H. Deutsch, and G. W. Biedermann. "Entangling atomic spins with a Rydberg-dressed spin-flip blockade". *Nature Physics* **12** (2016), 71–74.

[219] K. M. Maller et al. "Rydberg-blockade controlled-NOT gate and entanglement in a two-dimensional array of neutral-atom qubits". *Phys. Rev. A* **92** (2015), 022336.

[220] R. Barends et al. "Superconducting quantum circuits at the surface code threshold for fault tolerance". *Nature* **508** (2014), 500–503.

[221] Vivek V. Shende and Igor L. Markov. "On the CNOT-Cost of TOFFOLI Gates". *Quantum Information and Computation* **9**.5&6 (2009), 461–486.

[222] T. C. Ralph, K. J. Resch, and A. Gilchrist. "Efficient Toffoli Gates Using Qudits". *Physical Review A* **75**.2 (2007), 022313.

[223] M. D. Reed, L. DiCarlo, S. E. Nigg, L. Sun, L. Frunzio, S. M. Girvin, and R. J. Schoelkopf. "Realization of three-qubit quantum error correction with superconducting circuits". *Nature* **482** (2012), 382.

[224] Y. Cao, G. C. Wang, H. D. Liu, and C. F. Sun. "Implementation of a Toffoli gate using an array of coupled cavities in a single step". *Scientific reports* **8**.1 (2018), 5813–5813. ISSN: 2045-2322.

[225] Ai Min Chen, Sam Young Cho, and Mun Dae Kim. "Implementation of a three-qubit Toffoli gate in a single step". *Phys. Rev. A* **85** (3 2012), 032326.

[226] Koen Groenland and Karel1 Schoutens. "Many-Body Strategies for Multiqubit Gates: Quantum Control through Krawtchouk-Chain Dynamics". *Physical Review A* **97**.4 (2018), 042321.

[227] Koen Groenland and Karel1 Schoutens. "Quantum Gates by Resonantly Driving Many-Body Eigenstates, with a Focus on Polychronakos' Model". *Journal of Statistical Mechanics: Theory and Experiment* **2019**.7 (2019), 073103. ISSN: 1742-5468.

[228] L. Isenhower, M. Saffman, and K. Mølmer. "Multibit CkNOT quantum gates via Rydberg blockade". *Quantum Information Processing* **10**.6 (2011), 755. ISSN: 1573-1332.

[229] Klaus Mølmer, Larry Isenhower, and Mark Saffman. "Efficient Grover search with Rydberg blockade". *Journal of Physics B: Atomic, Molecular and Optical Physics* **44**.18 (2011), 184016.

[230] Xiao-Feng Shi. "Deutsch, Toffoli, and cnot Gates via Rydberg Blockade of Neutral Atoms". *Phys. Rev. Applied* **9** (5 2018), 051001.

[231] Xiaoguang Wang, Anders Sørensen, and Klaus Mølmer. "Multibit Gates for Quantum Computing". *Phys. Rev. Lett.* **86** (17 2001), 3907–3910.

[232] I. I. Beterov et al. "Fast three-qubit Toffoli quantum gate based on three-body Förster resonances in Rydberg atoms". *Phys. Rev. A* **98** (4 2018), 042704.

[233] M. J. Gullans and J. R. Petta. "Protocol for a Resonantly Driven Three-Qubit Toffoli Gate with Silicon Spin Qubits". *Physical Review B* **100**.8 (2019), 085419.

[234] John Preskill. "Quantum Computing in the NISQ era and beyond". *Quantum* **2** (2018), 79. ISSN: 2521-327X.

[235] David P. DiVincenzo. "Two-bit gates are universal for quantum computation". *Phys. Rev. A* **51** (2 1995), 1015–1022.

[236] Michael J. Bremner et al. "Practical Scheme for Quantum Computation with Any Two-Qubit Entangling Gate". *Phys. Rev. Lett.* **89** (24 2002), 247902.

[237] Adriano Barenco. "A Universal Two-Bit Gate for Quantum Computation". *Proceedings of the Royal Society of London. Series A: Mathematical and Physical Sciences* **449**.1937 (1995), 679–683.

[238] Michał Horodecki, Paweł Horodecki, and Ryszard Horodecki. "General teleportation channel, singlet fraction, and quasidistillation". *Phys. Rev. A* **60** (3 1999), 1888–1898.

[239] Benjamin Schumacher. "Sending entanglement through noisy quantum channels". *Phys. Rev. A* **54** (4 1996), 2614–2628.

[240] J.R. Johansson, P.D. Nation, and Franco Nori. "QuTiP: An open-source Python framework for the dynamics of open quantum systems". *Computer Physics Communications* **183**.8 (2012), 1760–1772. ISSN: 0010-4655.

[241] Michael A Nielsen. "A simple formula for the average gate fidelity of a quantum dynamical operation". *Physics Letters A* **303**.4 (2002), 249–252. ISSN: 0375-9601.

[242] Benjamin P. Lanyon et al. "Simplifying quantum logic using higher-dimensional Hilbert spaces". *Nature Physics* **5** (2008), 134.

[243] M. Saffman. "Quantum Computing with Atomic Qubits and Rydberg Interactions: Progress and Challenges". *Journal of Physics B: Atomic, Molecular and Optical Physics* **49**.20 (2016), 202001. ISSN: 0953-4075.

[244] K. Kim, M.-S. Chang, R. Islam, S. Korenblit, L.-M. Duan, and C. Monroe. "Entanglement and Tunable Spin-Spin Couplings between Trapped Ions Using Multiple Transverse Modes". *Physical Review Letters* **103**.12 (2009), 120502.

[245] A. M. Steane. "Multiple-particle interference and quantum error correction". *Proc. R. Soc. Lond. A.* **452** (1954 1996), 2551–2577.

[246] A. M. Steane. "Error Correcting Codes in Quantum Theory". *Phys. Rev. Lett.* **77** (5 1996), 793–797.

[247] A. A. Houck, Jens Koch, M. H. Devoret, S. M. Girvin, and R. J. Schoelkopf. "Life after charge noise: recent results with transmon qubits". *Quantum Information Processing* **8**.2 (2009), 105–115. ISSN: 1573-1332.

[248] Andras Gyenis et al. "Experimental realization of an intrinsically error-protected superconducting qubit". arxiv.org/abs/1910.07542. 2019.

[249] J. Chiaverini et al. "Realization of quantum error correction". *Nature* **432**.7017 (2004), 602–605. ISSN: 1476-4687.

[250] D. Nigg et al. "Quantum computations on a topologically encoded qubit". *Science* **345**.6194 (2014), 302–305. ISSN: 0036-8075.

[251] Mohammadsadegh Khazali and Klaus Mølmer. "Fast Multiqubit Gates by Adiabatic Evolution in Interacting Excited-State Manifolds of Rydberg Atoms and Superconducting Circuits". *Phys. Rev. X* **10** (2 2020), 021054.

[252] Dongmin Yu, Yichun Gao, Weiping Zhang, Jinming Liu, and Jing Qian. *Scalability and high-efficiency of an $(n+1)$-qubit Toffoli gate sphere via blockaded Rydberg atoms*. 2020. arXiv: 2001.04599 [physics.atom-ph].

[253] Jeremy T Young, Przemyslaw Bienias, Ron Belyansky, Adam M Kaufman, and Alexey V Gorshkov. "Asymmetric blockade and multiqubit gates via dipole-dipole interactions". *Physical Review Letters* **127**.12 (2021), 120501.

[254] M Morgado and S Whitlock. "Quantum simulation and computing with Rydberg-interacting qubits". *AVS Quantum Science* **3**.2 (2021), 023501.

[255] Jin-Lei Wu et al. "Systematic-Error-Tolerant Multiqubit Holonomic Entangling Gates". *Phys. Rev. Applied* **16** (6 2021), 064031.

[256] Yucheng He et al. "Multiple-qubit Rydberg quantum logic gate via dressed-state scheme". *Optics Communications* **505** (2022), 127500.

[257] Koen Groenland, Freek Witteveen, Kareljan Schoutens, and Rene Gerritsma. "Signal processing techniques for efficient compilation of controlled rotations in trapped ions". *New Journal of Physics* **22**.6 (2020), 063006.

[258] Pranav Gokhale, Samantha Koretsky, Shilin Huang, Swarnadeep Majumder, Andrew Drucker, Kenneth R Brown, and Frederic T Chong. "Quantum fan-out: Circuit optimizations and technology modeling". In: *2021 IEEE International Conference on Quantum Computing and Engineering (QCE)*. IEEE. 2021, 276–290.

[259] Yosep Kim et al. *High-fidelity iToffoli gate for fixed-frequency superconducting qubits*. 2021. arXiv: 2108.10288 [quant-ph].

[260] Shengbin Wang, Zhimin Wang, Wendong Li, Lixin Fan, Guolong Cui, Zhiqiang Wei, and Yongjian Gu. *A quantum Poisson solver implementable on NISQ devices*. 2020. arXiv: 2005.00256 [quant-ph].

[261] Pradeep Niroula and Yunseong Nam. "A quantum algorithm for string matching". *npj Quantum Information* **7**.1 (2021), 1–5.

[262] John L. Orrell and Ben Loer. "Sensor-Assisted Fault Mitigation in Quantum Computation". *Phys. Rev. Applied* **16** (2 2021), 024025.

[263] Kodai Shiba, Chih-Chieh Chen, Masaru Sogabe, Katsuyoshi Sakamoto, and Tomah Sogabe. "Quantum-Inspired Classification Algorithm from DBSCAN–Deutsch–Jozsa Support Vectors and Ising Prediction Model". *Applied Sciences* **11**.23 (2021), 11386.

[264] Nilesh Goel and J. K. Freericks. *Native multiqubit Toffoli gates on ion trap quantum computers*. 2021. arXiv: 2103.00593 [quant-ph].

[265] Juan Diego Arias Espinoza, Koen Groenland, Matteo Mazzanti, Kareljan Schoutens, and Rene Gerritsma. "High-fidelity method for a single-step N-bit Toffoli gate in trapped ions". *Phys. Rev. A* **103** (5 2021), 052437.

[266] Aneirin J. Baker, Gerhard B. P. Huber, Niklas J. Glaser, Federico Roy, Ivan Tsitsilin, Stefan Filipp, and Michael J. Hartmann. *Single Shot i-Toffoli Gate in Dispersively Coupled Superconducting Qubits*. 2021. arXiv: 2111.05938 [quant-ph].

[267] Tetsufumi Tanamoto, Koji Maruyama, Yu-xi Liu, Xuedong Hu, and Franco Nori. "Efficient purification protocols using iSWAP gates in solid-state qubits". *Phys. Rev. A* **78** (6 2008), 062313.

[268] Tetsufumi Tanamoto, Yu-xi Liu, Xuedong Hu, and Franco Nori. "Efficient Quantum Circuits for One-Way Quantum Computing". *Phys. Rev. Lett.* **102** (10 2009), 100501.

[269] A. M. Zagoskin, S. Ashhab, J. R. Johansson, and Franco Nori. "Quantum Two-Level Systems in Josephson Junctions as Naturally Formed Qubits". *Phys. Rev. Lett.* **97** (7 2006), 077001.

[270] M. Benito, J. R. Petta, and Guido Burkard. "Optimized cavity-mediated dispersive two-qubit gates between spin qubits". *Phys. Rev. B* **100** (8 2019), 081412R.

[271] Hong-Fu Wang, Xiao-Qiang Shao, Yong-Fang Zhao, Shou Zhang, and Kyu-Hwang Yeon. "Scheme for implementing linear optical quantum iSWAP gate with conventional photon detectors". *J. Opt. Soc. Am. B* **27**.1 (2010), 27–31.

[272] Monika Bartkowiak and Adam Miranowicz. "Linear-optical implementations of the iSWAP and controlled NOT gates based on conventional detectors". *J. Opt. Soc. Am. B* **27**.11 (2010), 2369–2377.

[273] Clément Godfrin, Rafik Ballou, Edgar Bonet, Mario Ruben, Svetlana Klyatskaya, Wolfgang Wernsdorfer, and Franck Balestro. "Generalized Ramsey interferometry explored with a single nuclear spin qudit". *npj Quantum Information* **4**.1 (2018), 53. ISSN: 2056-6387.

[274] A. Dewes et al. "Characterization of a Two-Transmon Processor with Individual Single-Shot Qubit Readout". *Phys. Rev. Lett.* **108** (5 2012), 057002.

[275] Y. Salathé et al. "Digital Quantum Simulation of Spin Models with Circuit Quantum Electrodynamics". *Phys. Rev. X* **5** (2 2015), 021027.

[276] G. J. Milburn. "Quantum optical Fredkin gate". *Phys. Rev. Lett.* **62** (18 1989), 2124–2127.

[277] H. F. Chau and F. Wilczek. "Simple Realization of the Fredkin Gate using a Series Of Two-Body Operators". *Phys. Rev. Lett.* **75** (4 1995), 748–750.

[278] Jaromír Fiurášek. "Linear-optics quantum Toffoli and Fredkin gates". *Phys. Rev. A* **73** (6 2006), 062313.

[279] Jaromír Fiurášek. "Linear optical Fredkin gate based on partial-SWAP gate". *Phys. Rev. A* **78** (3 2008), 032317.

[280] Yan-Xiao Gong, Guang-Can Guo, and Timothy C. Ralph. "Methods for a linear optical quantum Fredkin gate". *Phys. Rev. A* **78** (1 2008), 012305.

[281] Raj B. Patel, Joseph Ho, Franck Ferreyrol, Timothy C. Ralph, and Geoff J. Pryde. "A quantum Fredkin gate". *Science Advances* **2**.3 (2016).

[282] Takafumi Ono, Ryo Okamoto, Masato Tanida, Holger F. Hofmann, and Shigeki Takeuchi. "Implementation of a quantum controlled-SWAP gate with photonic circuits". *Scientific Reports* **7** (2017). Article, 45353.

[283] John A. Smolin and David P. DiVincenzo. "Five two-bit quantum gates are sufficient to implement the quantum Fredkin gate". *Phys. Rev. A* **53** (4 1996), 2855–2856.

[284] Yvonne Y. Gao et al. "Programmable Interference between Two Microwave Quantum Memories". *Phys. Rev. X* **8** (2 2018), 021073.

[285] Hoi-Kwan Lau, Raphael Pooser, George Siopsis, and Christian Weedbrook. "Quantum Machine Learning over Infinite Dimensions". *Phys. Rev. Lett.* **118** (8 2017), 080501.

[286] Julia Kempe. "Quantum random walks: An introductory overview". *Contemporary Physics* **44**.4 (2003), 307–327.

[287] Danial Dervovic, Mark Herbster, Peter Mountney, Simone Severini, Naïri Usher, and Leonard Wossnig. "Quantum linear systems algorithms: a primer". arXiv:1802.08227. 2018.

[288] Andrew M. Childs, Richard Cleve, Enrico Deotto, Edward Farhi, Sam Gutmann, and Daniel A. Spielman. "Exponential Algorithmic Speedup by a Quantum Walk". In: *Proceedings of the Thirty-Fifth Annual ACM Symposium on Theory of Computing*. STOC '03. San Diego, CA, USA: Association for Computing Machinery, 2003, 59–68. ISBN: 1581136749.

[289] Iman Marvian and Seth Lloyd. "Universal Quantum Emulator". arXiv:1606.02734. 2016.

[290] W. Dür, G. Vidal, and J. I. Cirac. "Three qubits can be entangled in two inequivalent ways". *Phys. Rev. A* **62** (6 2000), 062314.

[291] Xiu Gu et al. "Fast Multiqubit Gates through Simultaneous Two-Qubit Gates". *PRX Quantum* **2** (4 2021), 040348.

[292] O. V. Marchukov, A. G. Volosniev, M. Valiente, D. Petrosyan, and N. T. Zinner. "Quantum spin transistor with a Heisenberg spin chain". *Nature Communications* **7** (2016), 13070.

[293] Mikko Möttönen, Juha J. Vartiainen, Ville Bergholm, and Martti M. Salomaa. "Quantum Circuits for General Multiqubit Gates". *Phys. Rev. Lett.* **93** (13 2004), 130502.

[294] Mikko Möttönen, Juha J. Vartiainen, Ville Bergholm, and Martti M. Salomaa. "Transformation of quantum states using uniformly controlled rotations". 2005.

[295] Ryan Babbush et al. "Encoding Electronic Spectra in Quantum Circuits with Linear T Complexity". *Phys. Rev. X* **8** (4 2018), 041015.

[296] Paolo Zanardi, Christof Zalka, and Lara Faoro. "Entangling power of quantum evolutions". *Phys. Rev. A* **62** (3 2000), 030301.

[297] Z. Wang, S. Shankar, Z.K. Minev, P. Campagne-Ibarcq, A. Narla, and M.H. Devoret. "Cavity Attenuators for Superconducting Qubits". *Phys. Rev. Applied* **11** (1 2019), 014031.

[298] Niels Jakob Søe Loft et al. "High-fidelity conditional two-qubit swapping gate using tunable ancillas". 2018.

[299] Edward Farhi, Jeffrey Goldstone, and Sam Gutmann. "A Quantum Approximate Optimization Algorithm". arXiv:1411.4028. 2014.

[300] J. S. Otterbach et al. "Unsupervised Machine Learning on a Hybrid Quantum Computer". 2017.

[301] Nikolaj Moll et al. "Quantum optimization using variational algorithms on near-term quantum devices". *Quantum Science and Technology* **3**.3 (2018), 030503.

[302] Jonathan Romero, Jonathan P. Olson, and Alan Aspuru-Guzik. "Quantum autoencoders for efficient compression of quantum data". *Quantum Sci. Technol.* **2** (2017), 045001.

[303] Peter D. Johnson, Jonathan Romero, Jonathan Olson, Yudong Cao, and Alán Aspuru-Guzik. "QVECTOR: an algorithm for device-tailored quantum error correction". arXiv:1711.02249. 2017.

[304] Edward Farhi and Hartmut Neven. "Classification with Quantum Neural Networks on Near Term Processors". arXiv:1802.06002. 2018.

[305] Vojtech Havlícek, Antonio D. Córcoles, Kristan Temme, Aram W. Harrow, Abhinav Kandala, Jerry M. Chow, and Jay M. Gambetta. "Supervised learning with quantum-enhanced feature spaces". *Nature* **567**.7747 (2019), 209–212. ISSN: 1476-4687.

[306] Maria Schuld, Alex Bocharov, Krysta M. Svore, and Nathan Wiebe. "Circuit-centric quantum classifiers". *Phys. Rev. A* **101** (3 2020), 032308.

[307] Murphy Yuezhen Niu, Alexander Zlokapa, Michael Broughton, Sergio Boixo, Masoud Mohseni, Vadim Smelyanskyi, and Hartmut Neven. *Entangling Quantum Generative Adversarial Networks*. 2021. arXiv: 2105.00080 [quant-ph].

[308] Pierre-Luc Dallaire-Demers and Nathan Killoran. "Quantum generative adversarial networks". *Phys. Rev. A* **98** (1 2018), 012324.

[309] Seth Lloyd and Christian Weedbrook. "Quantum Generative Adversarial Learning". *Phys. Rev. Lett.* **121** (4 2018), 040502.

[310] Christa Zoufal, Aurélien Lucchi, and Stefan Woerner. "Quantum Generative Adversarial Networks for learning and loading random distributions". *npj Quantum Information* **5**.1 (2019), 103. ISSN: 2056-6387.

[311] D. Zhu et al. "Training of quantum circuits on a hybrid quantum computer". *Science Advances* **5**.10 (2019).

[312] Alberto Peruzzo et al. "A variational eigenvalue solver on a photonic quantum processor". *Nature Communications* **5**.1 (2014), 4213. ISSN: 2041-1723.

[313] Jarrod R McClean, Jonathan Romero, Ryan Babbush, and Alán Aspuru-Guzik. "The theory of variational hybrid quantum-classical algorithms". *New Journal of Physics* **18**.2 (2016), 023023.

[314] P. J. J. O'Malley et al. "Scalable Quantum Simulation of Molecular Energies". *Phys. Rev. X* **6** (3 2016), 031007.

[315] A. Kandala, A. Mezzacapo, K. Temme, M. Takita, M. Brink, J. M. Chow, and J. M. Gambetta. "Hardware-efficient variational quantum eigensolver for small molecules and quantum magnets". *Nature* **549** (2017), 242.

[316] Yudong Cao et al. "Quantum Chemistry in the Age of Quantum Computing". *Chemical Reviews* **119**.19 (2019), 10856–10915.

[317] Panagiotis Kl. Barkoutsos et al. "Quantum algorithms for electronic structure calculations: Particle-hole Hamiltonian and optimized wave-function expansions". *Phys. Rev. A* **98** (2 2018), 022322.

[318] Alexander J. McCaskey, Zachary P. Parks, Jacek Jakowski, Shirley V. Moore, Titus D. Morris, Travis S. Humble, and Raphael C. Pooser. "Quantum chemistry as a benchmark for near-term quantum computers". *npj Quantum Information* **5**.1 (2019), 99. ISSN: 2056-6387.

[319] Bryan T. Gard, Linghua Zhu, George S. Barron, Nicholas J. Mayhall, Sophia E. Economou, and Edwin Barnes. "Efficient symmetry-preserving state preparation circuits for the variational quantum eigensolver algorithm". *npj Quantum Information* **6**.1 (2020), 10. ISSN: 2056-6387.

[320] Sukin Sim, Peter D. Johnson, and Alán Aspuru-Guzik. "Expressibility and Entangling Capability of Parameterized Quantum Circuits for Hybrid Quantum-Classical Algorithms". *Advanced Quantum Technologies* **2**.12 (2019), 1900070.

[321] Michael R. Geller. "Sampling and Scrambling on a Chain of Superconducting Qubits". *Phys. Rev. Applied* **10** (2 2018), 024052.

[322] Yuxuan Du, Min-Hsiu Hsieh, Tongliang Liu, and Dacheng Tao. "The Expressive Power of Parameterized Quantum Circuits". arXiv:1810.11922. 2018.

[323] Marcello Benedetti, Erika Lloyd, Stefan Sack, and Mattia Fiorentini. "Parameterized quantum circuits as machine learning models". *Quantum Science and Technology* **4**.4 (2019), 043001.

[324] Thomas Hubregtsen, Josef Pichlmeier, and Koen Bertels. "Evaluation of Parameterized Quantum Circuits: on the design, and the relation between classification accuracy, expressibility and entangling capability". arXiv:2003.09887. 2020.

[325] Marcello Benedetti, Delfina Garcia-Pintos, Oscar Perdomo, Vicente Leyton-Ortega, Yunseong Nam, and Alejandro Perdomo-Ortiz. "A generative modeling approach for benchmarking and training shallow quantum circuits". *npj Quantum Information* **5**.1 (2019), 45. ISSN: 2056-6387.

[326] David A. Meyer and Nolan R. Wallach. "Global entanglement in multiparticle systems". *Journal of Mathematical Physics* **43**.9 (2002), 4273–4278.

[327] Niels Jakob Søe Loft et al. "Quantum interference device for controlled two-qubit operations". *npj Quantum Information* **6**.1 (2020), 47. ISSN: 2056-6387.

[328] Colin William. *Explorations in Quantum Computing*. 2nd. Springer, 2011.

[329] Jonathan Romero, Ryan Babbush, Jarrod R. McClean, Cornelius Hempel, Peter Love, and Alán Aspuru-Guzik. *Strategies for quantum computing molecular energies using the unitary coupled cluster ansatz*. 2018. arXiv: 1701.02691 [quant-ph].

[330] Mateusz Ostaszewski, Lea M. Trenkwalder, Wojciech Masarczyk, Eleanor Scerri, and Vedran Dunjko. *Reinforcement learning for optimization of variational quantum circuit architectures*. 2021. arXiv: 2103.16089 [quant-ph].

[331] Raffaele Santagati et al. "Witnessing eigenstates for quantum simulation of Hamiltonian spectra". *Science Advances* **4**.1 (2018), eaap9646.

[332] J. I. Colless et al. "Computation of Molecular Spectra on a Quantum Processor with an Error-Resilient Algorithm". *Phys. Rev. X* **8** (1 2018), 011021.

[333] Ilya G. Ryabinkin, Scott N. Genin, and Artur F. Izmaylov. "Constrained Variational Quantum Eigensolver: Quantum Computer Search Engine in the Fock Space". *Journal of Chemical Theory and Computation* **15**.1 (2019), 249–255.

[334] Oscar Higgott, Daochen Wang, and Stephen Brierley. "Variational Quantum Computation of Excited States". *Quantum* **3** (2019), 156. ISSN: 2521-327X.

[335] Ken M. Nakanishi, Kosuke Mitarai, and Keisuke Fujii. "Subspace-search variational quantum eigensolver for excited states". *Phys. Rev. Research* **1** (3 2019), 033062.

[336] Jorge Nocedal and Stephen Wright. *Numerical Optimization*. New York, NY: Springer, 2006.

[337] Sergey B. Bravyi and Alexei Yu. Kitaev. "Fermionic Quantum Computation". *Annals of Physics* **298**.1 (2002), 210–226. ISSN: 0003-4916.

[338] P. Jordan and E. Wigner. "Über das Paulische Äquivalenzverbot". *Zeitschrift für Physik* **47**.9 (1928), 631–651. ISSN: 0044-3328.

[339] Qiming Sun et al. "PySCF: the Python-based simulations of chemistry framework". *WIREs Computational Molecular Science* **8**.1 (2018), e1340.

[340] Jarrod R. McClean et al. "OpenFermion: The Electronic Structure Package for Quantum Computers". arXiv:1710.07629. 2017.

[341] National Institute of Standards and Technology. *Computational Chemistry Comparison and Benchmark DataBase IV.D.8*. https://cccbdb.nist.gov/bondlengthmodel2.asp?method=12&basis=5. 2020.

[342] Michael Broughton et al. *TensorFlow Quantum: A Software Framework for Quantum Machine Learning*. 2021. arXiv: 2003.02989 [quant-ph].

[343] David J. Griffiths. *Introduction to Quantum Mechanics*. 2nd. Upper Saddle River, NJ: Pearson, 2005.

[344] Jakub Langr and Vladimir Bok. *GANs in action – Deep learning with Generative Adversarial Networks*. Shelter Island: Manning, 2019.

[345] Ian Goodfellow, Yoshua Bengio, and Aaron Courville. *Deep Learning*. Cambridge, MA: The MIT press, 2016.

[346] Ian Goodfellow et al. "Generative Adversarial Nets". In: *Advances in Neural Information Processing Systems*. Ed. by Z. Ghahramani, M. Welling, C. Cortes, N. Lawrence, and K. Q. Weinberger. **27**. Curran Associates, Inc., 2014.

[347] Facebook AI. *Papers with Code: Generative Adversarial Networks*. 2021.

[348] Maria Schuld, Ilya Sinayskiy, and Francesco Petruccione. "An introduction to quantum machine learning". *Contemporary Physics* **56**.2 (2014), 172–185. ISSN: 1366-5812.

[349] Maria Schuld and Francesco Petruccione. *Machine Learning with Quantum Computers*. 2nd. Schwitzerland: Springer, 2018.

[350] Samuel Albanie, Sébastien Ehrhardt, and João F. Henriques. *Stopping GAN Violence: Generative Unadversarial Networks*. 2017. arXiv: 1703.02528 [stat.ML].

[351] Shakir Mohamed and Balaji Lakshminarayanan. *Learning in Implicit Generative Models*. 2017. arXiv: 1610.03483 [stat.ML].

[352] Lars Mescheder, Andreas Geiger, and Sebastian Nowozin. *Which Training Methods for GANs do actually Converge?* 2018. arXiv: 1801.04406 [cs.LG].

[353] Alec Radford, Luke Metz, and Soumith Chintala. *Unsupervised Representation Learning with Deep Convolutional Generative Adversarial Networks*. 2016. arXiv: 1511.06434 [cs.LG].

[354] Tero Karras, Timo Aila, Samuli Laine, and Jaakko Lehtinen. *Progressive Growing of GANs for Improved Quality, Stability, and Variation*. 2018. arXiv: 1710.10196 [cs.NE].

[355] Martin Arjovsky, Soumith Chintala, and Léon Bottou. *Wasserstein GAN*. 2017. arXiv: 1701.07875 [stat.ML].

[356] Luke Metz, Ben Poole, David Pfau, and Jascha Sohl-Dickstein. *Unrolled Generative Adversarial Networks*. 2017. arXiv: 1611.02163 [cs.LG].

[357] Kelvin Ch'ng, Juan Carrasquilla, Roger G. Melko, and Ehsan Khatami. "Machine Learning Phases of Strongly Correlated Fermions". *Phys. Rev. X* **7** (3 2017), 031038.

[358] Peter Broecker, Fakher F. Assaad, and Simon Trebst. *Quantum phase recognition via unsupervised machine learning*. 2017. arXiv: 1707.00663 [cond-mat.str-el].

[359] Patrick Huembeli, Alexandre Dauphin, and Peter Wittek. "Identifying quantum phase transitions with adversarial neural networks". *Phys. Rev. B* **97** (13 2018), 134109.

[360] Mogens Dalgaard, Felix Motzoi, and Jacob Sherson. "Predicting quantum dynamical cost landscapes with deep learning". *Phys. Rev. A* **105** (1 2022), 012402.

[361] Samuel A. Stein et al. *QuGAN: A Generative Adversarial Network Through Quantum States*. 2021. arXiv: 2010.09036 [quant-ph].

[362] Harry Buhrman, Richard Cleve, John Watrous, and Ronald de Wolf. "Quantum Fingerprinting". *Phys. Rev. Lett.* **87** (16 2001), 167902.

[363] Juan Carlos Garcia-Escartin and Pedro Chamorro-Posada. "swap test and Hong-Ou-Mandel effect are equivalent". *Phys. Rev. A* **87** (5 2013), 052330.

[364] European Commission. *Quantum Technologies Flagship kicks off with first 20 projects*. `https://ec.europa.eu/commission/presscorner/detail/en/MEMO_18_6241`. 2018.

[365] IBM. *IBM Quantum*. `https://www.ibm.com/quantum-computing/`. 2022.

[366] Amazon Web Services. *Amazon Braket*. `https://aws.amazon.com/braket/`. 2022.

[367] Microsoft. *Azure Quantum*. `https://azure.microsoft.com/services/quantum/`. 2022.

[368] B. Peikari. *Fundamentals of Network Analysis and Synthesis*. Englewood Cliffs, NJ: Prentice-Hall, 1974.

[369] J. A. Bondy and U. S. R. Monty. *Graph Theory with Applications*. New York: Elsevier Science Publishing Co., 1976.

[370] R. Penrose. "A generalized inverse for matrices". *Mathematical Proceedings of the Cambridge Philosophical Society* **51**.3 (1955), 406–413.